AD-A111 827 PHYSICAL SCIENCES INC WOBURN MA F/G 17/5
LABCEDE AND COCHISE ANALYSIS II. VOLUME I.(U)
FEB 80 W T RAWLINS, L G PIPER, B D GREEN F19628-77-C-0089
UNCLASSIFIED PSI-TR-207A NL

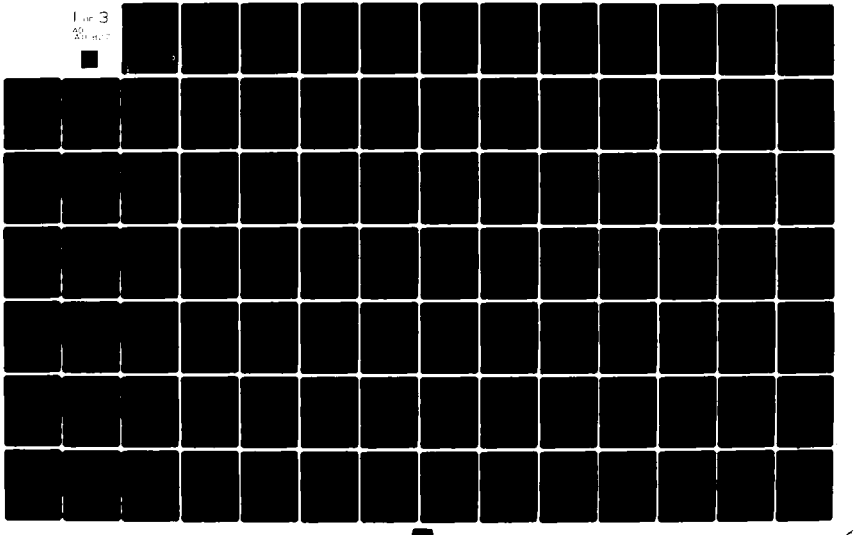

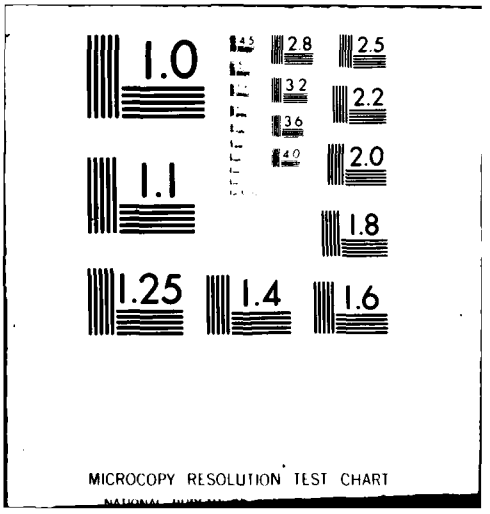
1.0
1.1
1.25
1.4
1.6
1.8
2.0
2.2
2.5
2.8
3.2
3.6
4.0
MICROCOPY RESOLUTION TEST CHART

(12)

AFGL-TR-80-0063(I)

AD A111827

LABCEDE AND COCHISE ANALYSIS II
Volume I

W.T. Rawlins
L.G. Piper
B.D. Green
G. Wilemski
J.S. Goela
G.E. Caledonia

Physical Sciences, Inc.
30 Commerce Way
Woburn, Massachusetts 01801

February 1980

Final Report
10 December 1976 - 10 February 1980

AIR FORCE GEOPHYSICS LABORATORY
AIR FORCE SYSTEMS COMMAND
UNITED STATES AIR FORCE
HANSCOM AFB, MASSACHUSETTS 01731

UNCLASSIFIED

SECURITY CLASSIFICATION OF THIS PAGE (When Data Entered)

REPORT DOCUMENTATION PAGE		READ INSTRUCTIONS BEFORE COMPLETING FORM
1. REPORT NUMBER AFGL-TR-80-0063(I)	2. GOVT ACCESSION NO. AD-A111827	3. RECIPIENT'S CATALOG NUMBER
4. TITLE (and Subtitle) LABCEDE and COCHISE Analysis II Volume I		5. TYPE OF REPORT & PERIOD COVERED Final Scientific Report 10 Dec. 1976 - 10 Feb. 1980 6. PERFORMING ORG. REPORT NUMBER PSI TR-207A
7. AUTHOR(s) W. T. Rawlins, L. G. Piper, B. D. Green, G. Wilemski, J. S. Goela, and G. E. Caledonia		8. CONTRACT OR GRANT NUMBER(s) F19628-77-C-0089
9. PERFORMING ORGANIZATION NAME AND ADDRESS PHYSICAL SCIENCES INC. 30 Commerce Way Woburn, MA 01801		10. PROGRAM ELEMENT, PROJECT, TASK AREA & WORK UNIT NUMBERS 61102F 2301G4AA
11. CONTROLLING OFFICE NAME AND ADDRESS Air Force Geophysics Laboratory Hanscom Air Force Base, MA 01730 Monitor/John P. Kennealy/OPR		12. REPORT DATE February 1980 13. NUMBER OF PAGES 247
14. MONITORING AGENCY NAME & ADDRESS(if different from Controlling Office)		15. SECURITY CLASS. (of this report) UNCLASSIFIED 15a. DECLASSIFICATION/DOWNGRADING SCHEDULE

16. DISTRIBUTION STATEMENT (of this Report)

Approved for public release; distribution unlimited.

17. DISTRIBUTION STATEMENT (of the abstract entered in Block 20, if different from Report)

18. SUPPLEMENTARY NOTES

19. KEY WORDS (Continue on reverse side if necessary and identify by block number)

NO	Chemiexcitation
O_3	Flowing Afterglow
$N_2(A)$	Surprisal
	Tritiates
	Remote Monitoring

20. ABSTRACT (Continue on reverse side if necessary and identify by block number)

The first volume of this report deals with studies related to the COCHISE facility which is a low temperature, low pressure device developed for the study of the spectrally resolved infrared fluorescence resulting from chemi-excitation reactions occurring under near single collision conditions. Several topics are discussed including (a) a study of the NO infrared fluorescence resulting from the reaction of metastable nitrogen atoms with oxygen molecules, (b) an examination of infrared fluorescence

DD FORM 1 JAN 73 1473 EDITION OF 1 NOV 65 IS OBSOLETE

UNCLASSIFIED

SECURITY CLASSIFICATION OF THIS PAGE (When Data Entered)

from chemi-excited O_3^*, (c) a proposed technique for implementing a nitrogen lamp resonance absorption diagnostic into the facility, (d) a preliminary examination of the COCHISE optical system, and (e) a review of a flow tube experiment directed towards the study of the products resulting from the reactions of $N_2(A^3\Sigma_u^+)$ with oxygen atoms and molecules.

The second volume of the report is concerned with studies related to the LABCEDE facility which is a device constructed to observe the fluorescence resulting from the electron irradiation of various atmospheric gases. Topics covered include an examination of CO and CO_2 infrared fluorescence occurring upon electron irradiation of mixtures of Ar/CO_2 and an examination of the SWIR radiation produced by irradiation of air-like mixtures.

TABLE OF CONTENTS

TABLE OF CONTENTS (CONT.)

LIST OF FIGURES

LIST OF FIGURES (CONT.)

LIST OF FIGURES (CONT.)

LIST OF FIGURES (CONT.)

LIST OF TABLES

I. INTRODUCTION

This report provides a comprehensive description of work performed on the subject contract over the past three years. During the course of this study a number of interim and special reports (Refs. 1-6) and journal articles (Refs. 7 and 8) have been published and much of the information in these documents has been directly incorporated into this report.

The report is divided into two volumes. The first volume is primarily dedicated to a review of studies provided in support of the COCHISE facility and the associated FAKIR facility. A study of the NO vibrational distribution produced in the chemi-excitation reaction between metastable nitrogen atoms and oxygen molecules is described in Section II along with preliminary observations on the ratio of NO fundamental to overtone band intensities and on O_3 chemiluminiscence. A description of the COCHISE facility is also provided in this section. A brief review of the COCHISE optical system, black body calibration techniques, and the definition of a proposed technique for implementing a resonance lamp diagnostic (for determining metastable nitrogen atom concentrations) may be found in Section III. Lastly, a description of a flow tube experiment for the study of the products of reactions between $N_2A\ ^3\Sigma_u^+$ molecules and oxygen atoms and molecules is provided in Section IV. The summary and conclusions of the report are presented in Section V. A number of appendices are also provided. These include, in order, (a) a review of the total data base for NO fundamental band observations, (b) a brief discussion of surprisal analysis, (c) a review of auroral production mechanisms for $N(^2D)$ atoms, (d) a description of the effect of slit width on black body intensities, (e) a discussion of the properties of F-center lasers, (f) a system description of COCHISE facility, and (g) a review of the potential of remote monitoring of selected tritiate molecules. The latter two appendices are direct reproductions of Refs. 8 and 3, respectively.

Volume II is dedicated to a review of studies performed in support of the LABCEDE facility, and provides a discussion of fluorescence phenomena observed upon electron irradiation of mixtures of CO_2/Ar and N_2/O_2.

II. NO CHEMI-EXCITATION STUDIES

A. Introduction

Because of its great importance as an infrared radiator in non-equilibrium air, particularly in the upper atmosphere, the chemistry, excitation, and relaxation of vibrationally excited nitric oxide is a subject of considerable interest. For quite some time the reaction between ground-state nitrogen atoms and molecular oxygen

$$N(^4S) + O_2 \overset{k_1}{\rightleftharpoons} NO + O \qquad \Delta H = -1.38 \text{ eV} \qquad (1)$$

was assumed to be the principal source of nitric oxide in the upper atmosphere,[9] despite the relatively slow rate constant for this process,[10]

$$k_1 = 1.1 \times 10^{-14} T\, e^{-3150/T} \text{ cm}^3/\text{sec} \quad .$$

Hushfar et al[11] and Whitson et al[12] have measured the infrared chemiluminescent efficiency of reaction (1) and have attempted to determine the relative efficiencies for production of nitric oxide in vibrational levels v=2 and above. Since infrared emission from the NO first overtone ($\Delta v=2$) band was the diagnostic used in all these experiments, no information was obtained about the relative rate of excitation for level v=1, the chemiluminescent efficiency in the fundamental band ($\Delta v=1$), or the total efficiency of the reaction towards producing vibrational excitation.

In the upper atmosphere, the principal processes responsible for producing $N(^4S)$ atoms are believed to be dissociative recombination of NO^+ and N_2^+ and photodissociation of N_2 and N_2O.[13,14] Above approximately 85 km, however, NO^+ dissociative recombination,

$$NO^+ + e \rightarrow N + O \qquad (2)$$

strongly predominates, and it is now rather well established[14,15] that $N(^2D)$, the first excited state of atomic nitrogen, is produced by reaction (2) at least as efficiently as is $N(^4S)$.

Black et al[16] were the first to report rapid "removal" of $N(^2D)$ by O_2 in laboratory studies, but Lin and Kaufman[17] unambiguously identified the "removal" process to be the reaction

$$N(^2D) + O_2 \xrightarrow{k_3} NO + O, \quad \Delta H = -3.77 \text{ eV} \quad , \tag{3}$$

rather than simply collisional relaxation. The room temperature rate constant determined for reaction (3) in these experiments was $\sim 6 \times 10^{-12}$ cm^3/sec, which is close to five orders of magnitude larger than that for reaction (1). Thus reaction (3) can clearly be a major source of nitric oxide in non-equilibrium air wherever there is a finite source for $N(^2D)$ atoms. In addition, the large exothermicity of (3) invites speculation about the distribution of that energy among the degrees of freedom of the products; for example, if the entire exothermicity were released into vibrational excitation of the product NO, levels up to v=18 could be excited by the reaction.

The principal objective of the work reported here has been to determine by experiment the relative rates of production of NO into individual vibrational levels by reaction (3); i.e., the determination of

$$R_3(v) \equiv \frac{k_3(v)}{\sum_{v'} k_3(v')}$$

Information of this type is fundamentally interesting in that it can be used to elucidate important quantum details of relatively basic chemical/physical processes, and thereby provides a broader foundation for the continuing development of quantum theoretical descriptions of reaction collisions. Equally important, however, the quantum details of processes such as reaction (3) are essential ingredients for the description of macroscopic phenomena such as atmospheric energy transport, particularly in those cases where

collisional relaxation rates and absorptivities are dependent on the identity of the quantum states involved. Furthermore, it should be pointed out that for studies of processes of this type it is highly desirable to obtain data on as many of the different quantum states involved as is possible. In the work to be reported here, data have been obtained on all significantly excited vibrational states of the nitric oxide product.

These measurements have been performed using a unique facility (COCHISE) which has recently been developed at the Air Force Geophysics Laboratory. This facility permits spectrally resolved measurements of the infrared radiation resulting from chemi-excitation processes such as (3) under conditions of low total pressure, 10^{-6} atm, typical of the upper atmosphere. A brief description of the COCHISE facility, including some details of its operation characteristics, diagnostics, and standard experimental conditions, is presented in Section B. The NO chemiluminescence data base and the analysis performed to convert the observed fluorescence into NO vibrational population distributions is reviewed in Section C, and a kinetic interpretation of the data relating the observations to the nascent vibrational distribution produced by reaction (3) is provided in Section D. The summary and conclusions of the study are given in Section E.

B. Experimental Description

Conventional infrared emission spectroscopic experiments designed to investigate gas phase chemi-excitation reactions generally have limited detection sensitivity, and, in order to sustain measurable steady-state concentrations of excited species, require pressures on the order of a torr, sufficiently high for collisional relaxation to occur. As a result, the initial product molecule vibrational distribution usually cannot be observed. In addition, for the flow rates associated with typical discharge flow and flowing afterglow experiments, excited species residence times can be sufficiently long to permit radiational relaxation to occur, again perturbing the observed product molecule vibrational distribution. Lastly, in ordinary flowing afterglow, discharge flow, and stirred reactor vacuum systems, surface effects can dominate in determining both the chemistry and the observed excited state distribution.

On the other hand, operation in a pressure regime where collisional vibrational relaxation is insignificant can reduce expected product molecule densities to as low as 10^6 cm^{-3}. The infrared chemiluminescent intensity associated with such low concentrations would be 8 orders of magnitude less than room temperature thermal emission. Since the limiting noise mechanism for infrared detectors in ordinary applications is the statistical fluctuation in the photon flux on the detector (these photons are the thermal radiation associated with the detector's optical and physical environment), a reduction of the detector temperature alone is insufficient to permit monitoring of the chemiluminescence arising at such low densities.

Various steps have been taken to minimize the effects of these limitations. Representative examples would be the experiments of McDonald and co-workers[18] and of Polanyi and co-workers.[19] In these systems, externally created reactant species mix in a relatively large reactant chamber held at low pressures, $\lesssim 10^{-3}$ torr, and the technique of arrested relaxation is utilized via rapid pumping of the excited species. Background radiation levels were decreased through cooling of the reaction chamber walls to either alcohol/dry ice[19] or liquid nitrogen[18] temperature, and Fourier transform spectroscopy was utilized in both systems, with the interferometer cooled to liquid nitrogen temperatures in McDonald's system.

The experimental direction taken in the COCHISE facility has been to reduce the temperatures of both the reaction volume and the detection system to near 20 K, resulting in a reduction of thermal emission to a level well below the anticipated intensities in chemiluminescent systems of interest. In addition, high speed cryopumping of the reaction vessel removes excited species from the detection system field-of-view before radiative relaxation can occur. Because there is negligible back-diffusion from the cryopumping walls, reaction contamination due to surface effects is eliminated. Consequently, "steady state" excited vibrational state distributions may be examined under nearly single collision conditions.

A schematic of the chemiluminescence reaction chamber is given in Fig. 1. Only the salient details of the apparatus will be described here; a more complete system description is being prepared for separate publication.[20] The reaction cell is cylindrically symmetric, 60 cm in length, 40 cm in diameter. Reagent gases are introduced through four sets of opposing inlet jets, equally spaced along the cylinder; microwave discharge excitation is possible in one of each pair of jets. Flow conditions in the reaction cell have been fluid dynamically modeled[21] for a range of experimental conditions; free expansion occurs in the reaction cell and the gas reaches a limiting velocity in which all of the thermal energy in the inlet tube is converted into kinetic energy. Near the cylinder axis, an axisymmetric stagnation point occurs, and the gas thermal energy returns to the inlet tube value. Because of the free expansion, gas density variations along the cylinder axis (reaction volume) are predicted to be $\lesssim$ 10%. Pressure in the reaction zone may be monitored through use of an MKS Baratron capacitance manometer.

The chemiluminescent reactions occur primarily in this stagnation region where the opposing flows meet, and only radiation occurring within $\approx$4 cm of the cylinder axis is monitored. The collection optics consist of a coated Ge lens matched to a f/7 grating monochromator; i.e., the detection system field-of-view is roughly columnar along the cylinder axis, and a mirror located at the far end of the cell is used to increase the collection efficiency. Reactant gas residence times in the field-of-view are predicted by the fluid dynamical modeling to be less than one msec.[21]

A schematic of the entire COCHISE apparatus is given in Fig. 2. The thermally insulating vacuum enclosure is maintained at 10^{-8} - 10^{-9} atm by a 20" diffusion pump with liquid nitrogen temperature baffles backed by a large two stage mechanical pump. The light-tight thermal shroud is cooled by a closed-cycle gaseous helium refrigeration system (Cryogenic Technology Inc.) and may be maintained at any temperature down to 20 K by varying the He coolant flow. The reaction cell temperature may be independently varied and has additional resistive heating elements to achieve temperature independence from the shroud. Temperature uniformity to 0.1 K over the copper

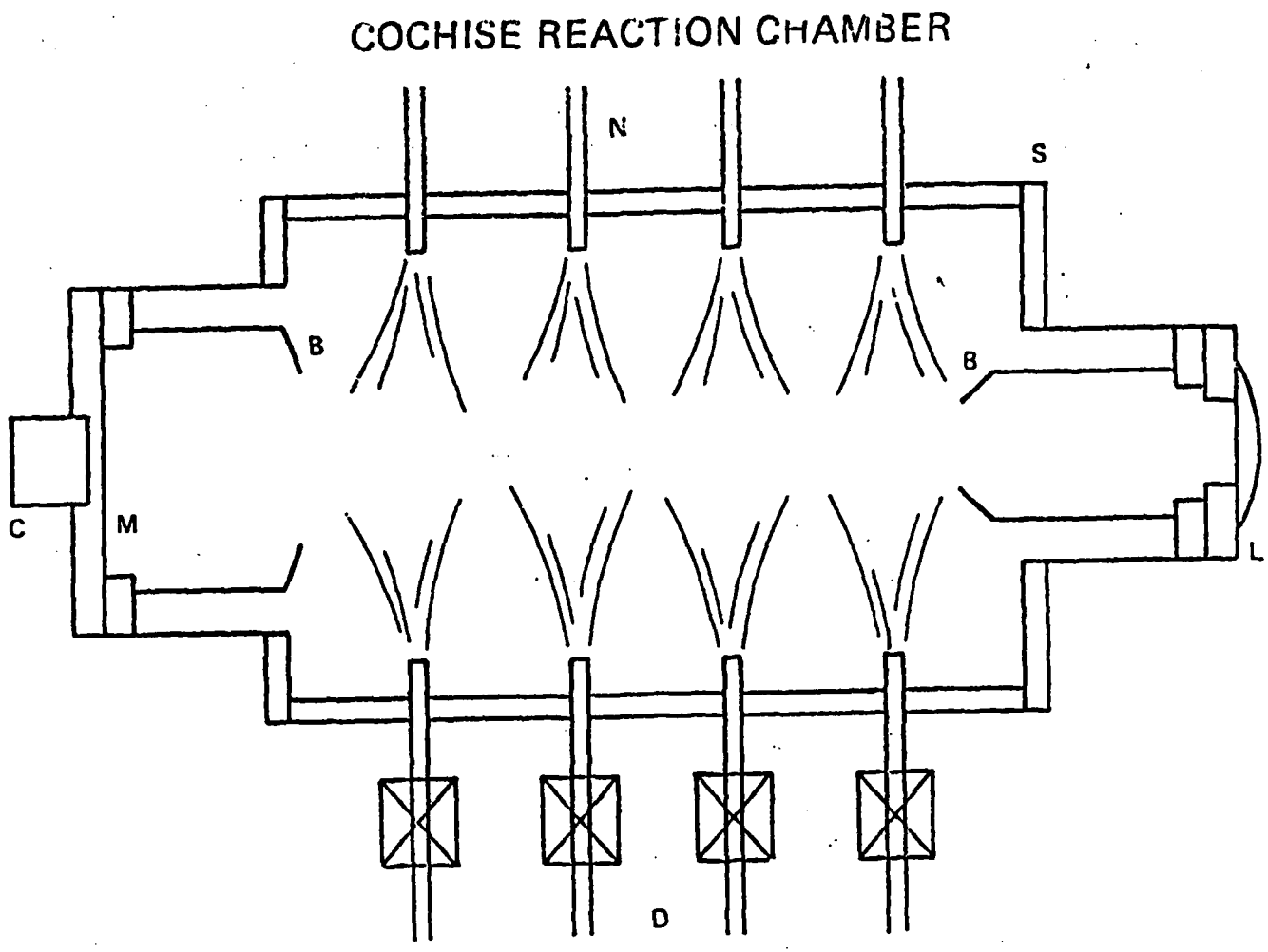

Fig. 1 Scale drawing of chemiluminescence reaction cell. Ar/N_2 mixtures are excited by microwave discharges, D, and mix with the counterflow of O_2 from nozzles N in an axisymmetric reaction zone at the chamber center. Baffles, B, restrict detection system field-of-view to the on-axis reaction volume. M is a plane mirror which increases the intensity of the radiation collected by lens L. Spectral response calibration is performed using blackbody source, C, embedded behind a small hole in the end mirror.

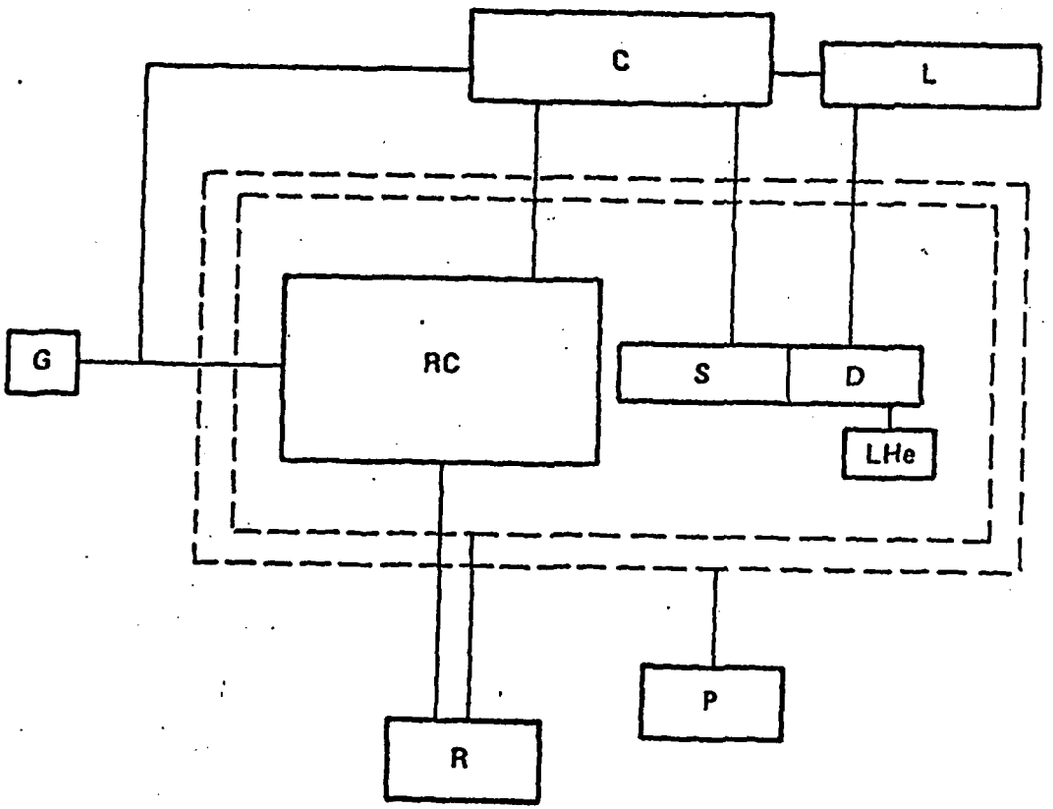

Fig. 2 Schematic of COCHISE experiment. RC is the reaction cell of Fig. 1. The radiation collected by the lens is dispersed by the spectrometer, S, and detected by a Si:As detector, D, maintained at liquid He temperatures. Phase-sensitive amplification, L, is followed by computer collection and processing of the signal. The computer, C, simultaneously monitors the detected wavelength, reaction cell temperature conditions, and flow rate of the gases, G. The pumping system, P, evacuates volume between the outer chamber walls and thermal shroud (dashed lines), permitting gaseous helium refrigeration system, R, to maintain cryogenic experimental conditions.

reaction cell surface is achieved through proper coolant flow line and heater element positioning. In order to minimize condensation, optical elements are maintained at a temperature slightly above wall temperature by resistive heating, ca. 80 K.

The gases used for this experiment are ultra-high purity Matheson Ar, N_2 and O_2. Each cylinder gas passes through a motorized, calibrated Granville-Phillips needle valve. Three gases may be mixed prior to introduction into the discharge cavities, and two gases may be separately mixed for the counterflow. After mixing, the discharge and counterflow gas mixtures are each split into four lines supplying the four sets of opposing jets. The gases undergo a two stage heat exchange process; the first copper-tubing exchanger is mounted on a plate maintained at liquid nitrogen temperature, and the second permits variable temperature selection over the range 30 K to 120 K. The cooled discharge gases then pass through inlet tubes where microwave excitation may occur, and then flow directly into the reaction cell. All inlet tubes are mounted in copper heat stations which are independently temperature controlled.

Typcial flow conditions for the present study were a discharge mixture of 90% argon and 10% nitrogen flowing at 1 standard liter/min. in each inlet tube, with an oxygen counterflow at the same rate, giving a total flow into the reaction cell of $\approx$8 standard liter/min. The measured pressure in the inlet jets was typically about a torr. These inlet jets are maintained at temperatures of 80 - 100 K.

The microwave discharges are in McCarroll[22] modified-Evenson electrodeless cavities[23] powered by Ratheon PGM 10 power supplies. Typical operation is at 50 - 90% of maximum power for a 50% duty cycle at 25 Hz, creating steady state conditions during the 20 milliseconds the discharge is on; all four discharges are driven by a single pulse generator, insuring synchronous operation to within a few microseconds. Atoms, ions, free radicals and electronically and vibrationally excited species are created in the discharge; however, by the time the gas has reached the low pressure reaction volume, many of these species will have disappeared (see Section D). Thus, the

number of possible reactant species will be less than that found in more typical discharge or afterglow experiments,[24] allowing for a more unambiguous interpretation of the data.

The collected infrared radiation is pre-filtered by an order sorting long pass filter, then dispersed by a 0.5m Czerny-Turner grating spectrometer (Minuteman #305CM) which is fabricated primarily from Invar in order to minimize defocussing and distortion during temperature cycling. Two replica gratings were employed, the first a 75 lines/mm grating blazed at 8μm, and the second a 150 lines/mm grating blazed at 3 μm. Use of a parabolic collector behind a cubic arsenic doped silicon photoconductive detector permits collection of nearly all radiation passed by the 20 mm high slits. This detector, when operated at liquid He temperatures, is sensitive to 1.2 to 22 μm radiation and has a peak Noise Equivalent Power of approximately 10^{-16} W/Hz$^{1/2}$. The detector signal is introduced into a preamplifier, which is separately maintained at 200 K. After leaving the vacuum enclosure, the AC signal is amplified (PARC Model 113 bandpass amplifier) and phase sensitively detected by a PARC Model 124 lock-in amplifier which is synchronized to the external pulse generator used to pulse the microwave discharges. A PDP-8/E (Digital Equipment) computer with both disk and tape storage is used for real time data collection, digital filtering, display, and storage. The computer also provides monitoring and control of experimental temperatures at many positions inside the shroud.

C. Measurements and Data Reduction

The NO vibrational band fluorescence has been observed over a range of both reaction zone total pressure and reactant concentrations. The reaction zone total pressure was varied between 2.7 - 5.8 mtorr, being limited by signal intensity at the lower end. The discharge gas mixture was varied from 0.8% N_2/99.2% Ar to pure N_2 with the resultant reaction zone partial pressure of nitrogen varying from 0.017 mtorr to 1.6 mtorr, and that of argon ranging from 0 to 2.1 mtorr. Similarly, the oxygen counterflow was varied from 3.2 to 6 standard liters/min corresponding to center line partial pressures of 1.1 - 2.1 mtorr. Additionally, helium could be added to the

reaction cell, but unlike the other reactant gases, helium is not cryo-pumped on the walls of the reaction cell. Partial pressures of up to 5 mtorr of helium were added in specific runs.

For a given monochromator slit width, an optimum lock-in amplifier integration time was determined, which balanced noise reduction against scan time. The monochromator scan rate was then set so that 3 to 5 time constants were spent on each spectral resolution element and, as a result, negligible data distortion occurred. Prior to analysis, all raw spectra were corrected for the detector's spectral response as determined by calibrations taken in situ, using a variable temperature blackbody source embedded in the end mirror.

A portion of a typical experimental spectrum is shown in Fig. 3. The dominant feature is this wavelength region is radiation from the NO fundamental vibration/rotation bands which will be shown to result from a highly non-Boltzmann vibrational distribution. The distribution corresponding to these spectral observations was deduced from comparisons with synthetically generated spectra. Specifically, sets of "basis functions" $\bar{\zeta}_v(\lambda)$ were generated, each of which is proportional to the spectrally resolved contribution of single quantum transitions from vibrational state v to the total signature. Combining these basis functions in a manner to best match the observed radiation signatures yielded weighting factors proportional to the desired vibrational populations. The details of the generation of the synthetic spectra and of the fitting technique are provided below.

It has been determined[25] that in NO the coupling of the spin and orbital angular momentum is very strong (Hund's coupling case a)[26] and remains strong for all rotational levels populated in the present experiment. The NO($^2\pi$) ground state has a separation of 121 cm^{-1} between the total angular momentum $\Omega = 1/2$ and 3/2 manifolds. Coupling between Ω and rotation is weak, and consequently, the Hönl-London line strength formulas are

$$S_J^R = (J' + \Omega)/J'$$

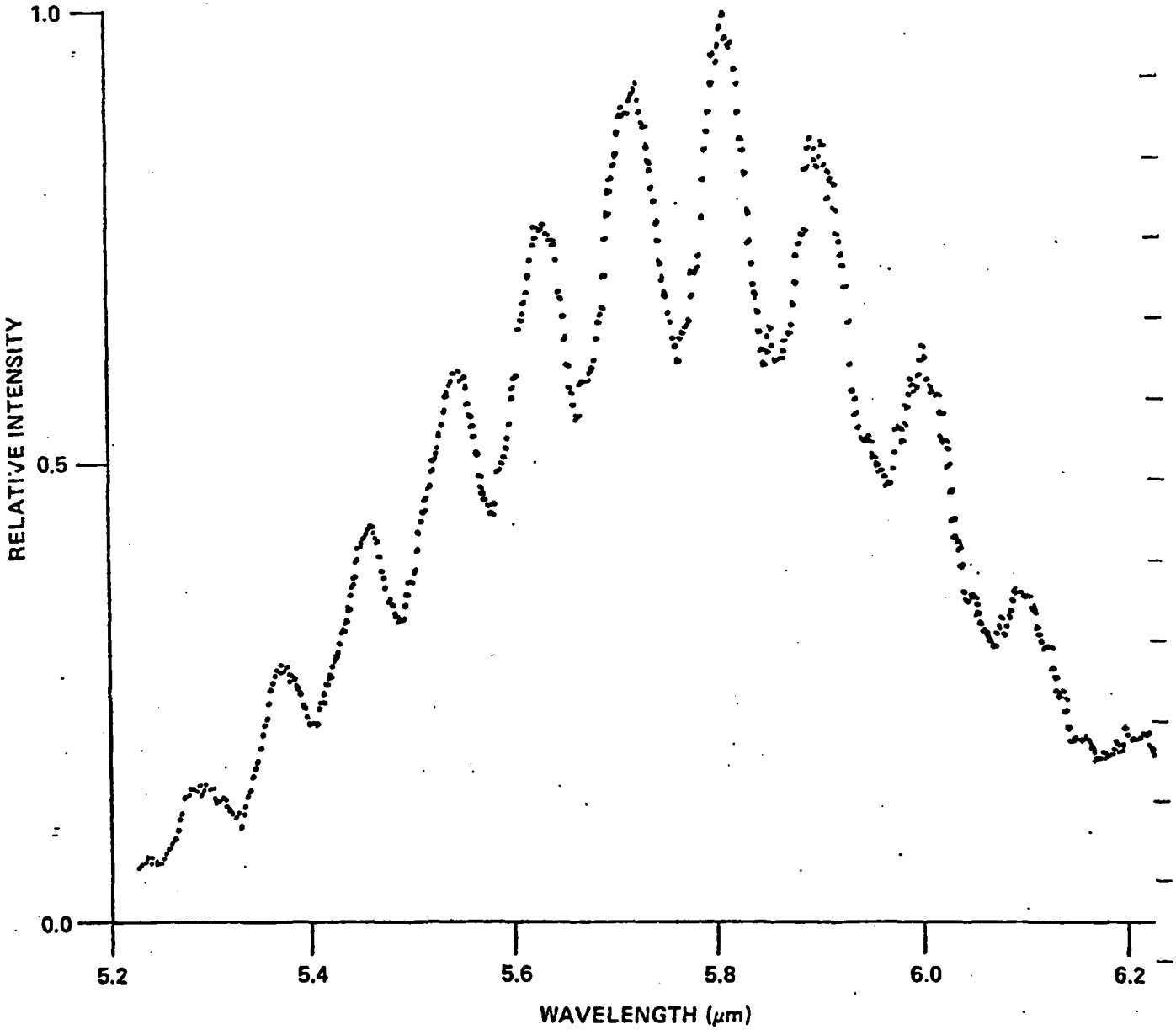

Fig. 3 Portion of a typical chemiluminescence spectrum showing resolved NO vibrational structure. The discharged mixture was 2.5% N_2/ 97.5% Ar, counterflowed with O_2. There was a background pressure of 0.43 Pa of He. The spectrum was taken with 0.027 μm resolution.

$$S_J^Q = (2J' + 1)\Omega^2/J'(J' + 1) \tag{4}$$

$$S_J^P = (J' + 1 + \Omega)(J' + 1 - \Omega)/(J' + 1)$$

where the J values are x/2, x = 1, 3, 5, ..., with $J \geq \Omega$. It can be seen from Eq. (4) that the Q branch lines will diminish rapidly in intensity with increasing J, and that the P branch lines will be more intense than the R branch lines.

The intensity of a single vibration/rotation transition is specified by:[26]

$$I^{v\rightarrow v-1}_{J\rightarrow J,J\pm1} = \frac{hc\ \nu_T^4\ S_J^{P,Q,R} A_{v\rightarrow v-1} N_{v,J}}{(2J + 1)\nu^3_{v\rightarrow v-1}} \tag{5}$$

where $A_{v\rightarrow v-1}$ is the Einstein coefficient, $\nu_{v\rightarrow v-1}$ is the band origin wavenumber, and ν_T is the frequency of the transition, defined as the difference in energy between the upper and lower states of the transition. These energies (in cm^{-1}) are calculated with the formula:

$$E_{v,J} = \omega_e(v+\tfrac{1}{2}) - \omega_e x_e(v+\tfrac{1}{2})^2 + B_v\, J(J+1) \tag{6}$$

using spectroscopic values (in cm^{-1}) of $\omega_e = 1903.6$, $\omega_e x_e = 13.97$, $B_e = 1.7042$, and $\alpha_e = 0.0178$. Higher order terms in v and J are negligible. B_v is the rotational constant for vibrational level v, and is defined as

$$B_v = B_e - \alpha_e(v + \tfrac{1}{2}) \tag{7}$$

The quantity $N_{v,J}$ in Eq. (5) is the population of the radiating vibration/rotation state and may be rewritten as

$$N_{v,J} = \frac{N_v}{Q_r} \; (2J + 1) \; \exp \left[-J(J + 1)B_v \, hc/kT\right] \qquad (8)$$

where Q_r is the rotational partition function, k is the Boltzmann constant and T is the temperature. N_v is the total number of molecules in vibrational state v.

The basis functions $\bar{\zeta}_v(\lambda)$ are representative of the spectrum arising from all possible rotational transitions occurring with the vibrational transition v→v-1. Specifically, the basis functions can be linearly related to the quantities $I^{v\to v-1}_{J\to J,J+1}/N_v$ by a convolution integral over the monochromator slit function; i.e., since the system has a finite spectral resolution, $\Delta\lambda$, the radiation observed at any wavelength will have a contribution from transitions occurring at wavelengths between $\lambda \pm \Delta\lambda$. In the present case, the system has been described by a triangular slit function with constant resolution in wavelength space. Fortunately, the Doppler broadened spectral lines are much narrower than the system resolution, and thus the convolution integral may be replaced by a sum. The quantity $\bar{\zeta}_v(\lambda)$ then merely becomes a summation over J of the quantities $I^{v\to v-1}_{J\to J,J\pm1}/N_v$, each properly weighted by the slit function fractional transmission corresponding to the difference between the wavelength of the specific transition and λ.

Finally, these radiation basis functions may be related to the observed intensity at any wavelength by the relation

$$I_p(\lambda) = \sum_v N_v \, \bar{\zeta}_v(\lambda) \qquad (9)$$

where the quantities N_v are directly proportional to the populations in level v of the excited NO molecules. Given the data $I(\lambda)$ and functions $\bar{\zeta}_v(\lambda)$, defined over some wavelength interval, the quantities N_v may be determined by requiring that the square of the differences $(I_p(\lambda) - I(\lambda))$ be minimized. Note that since the $\bar{\zeta}_v$'s are linearly proportional to the Einstein coefficients $A_{v\to v-1}$ the quantities actually determined by the least squares fit are the products $N_v \, A_{v\to v-1}$. Thus, the deduced values of N_v are only as accurate as the values of $A_{v\to v-1}$. The NO Einstein coefficients derived by Billingsley[25] were used in the present analysis.

A computer program has been developed to perform the fitting task. This code takes the data and basis functions as input and provides the relative vibrational populations as output. For a given resolution as defined by the slits, the rotational temperature is the only parameter which can be varied in order to optimize the fit. This temperature is also used to determine the relative populations of the two total angular momentum manifolds. Because similar transitions occurring with the two doublet states lie at the same frequencies (within the resolution of the experiment), the most obvious spectral effect of relative spin population changes is Q branch enhancement as the $\pi_{3/2}$ population is increased. (This effect is evident from Eq. (4).) The rotational temperature of the observed spectra may be considered a free variable to a limited extent. In the first place, the translational temperature in the reaction zone is not well defined. Although the reactant gas temperature at the inlets is initially 80 - 100 K, it may be increased by microwave discharge heating (efforts have been made to minimize this effect, e.g., sapphire discharge tubes for enhanced thermal conduction). Furthermore, any helium present in the reaction zone will be initially in translational equilibrium with the shroud walls, ca. 20 - 30 K. Lastly, the rotational distribution of the reaction products need not achieve equilibrium with translation before radiation occurs.

A synthetic spectrum generated with the aforementioned basis functions is shown in Fig. 4, fit to the data of Fig. 3. The experimental flow conditions were a 9:1 mixture of argon and nitrogen, flowing at 4 standard liters/min., discharged with inlet jet temperature maintained at 90 K and with a pure oxygen counterflow at the same rate and inlet temperature. Additionally, 3 millitorr of He was added as a background gas. The rotational temperature of the spectrum was determined to be 90 $\pm$ 10 K. For the resolution of this case, 0.027 μm, the vibrational band structure is well defined and some rotational line structure is evident in both the data and generated spectrum. The set of curves shown at the bottom of the spectrum are the properly weighted individual basis functions for v = 5, 6 and 7 which are components of the basis set utilized to produce the synthetic spectrum. The amplitude of individual basis functions represents the contribution of each

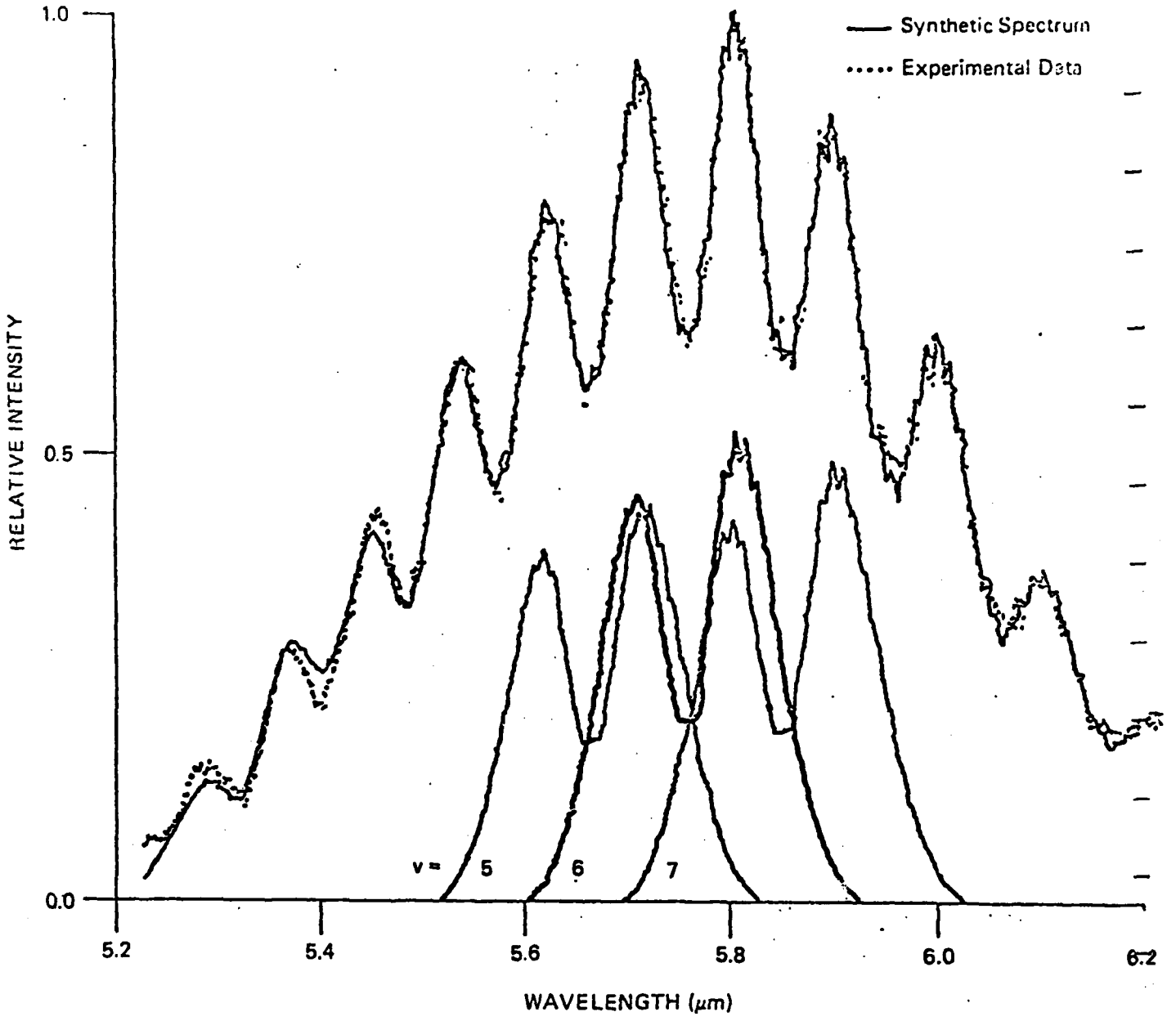

Fig. 4 Fit of the computer generated spectrum to the experimental data of Fig. 3 using 90°K rotational temperature. The standard deviation of this fit 0.019, the RMS deviation is 3.3%. The relative contributions to the synthetic spectrum of the basis function for vibrations 5, 6, and 7 are shown also. Some rotational structure in the vibrational band is visible under these conditions.

vibrational transition to the total intensity. The standard deviation of the fit is 0.019 with the peak radiation normalized to unity; the rms deviation is 3.3%. The relatively poor fit in the 5.2 - 5.5 μm region is due to the presence of underlying radiation, found to be present even when the oxygen counterflow is cut off (no NO fluorescence is observed in this case). Higher resolution scans (0.008 μm) reveal this underlying radiation spectrum to be similar to that of an inverted $^2\Pi$ hydrogenic molecule (the bandcenter, Q branch frequency, and rotational separation do not match calculated OH frequencies). Further investigation of this radiation is currently in progress.

A total of 24 distinct runs corresponding to various flow compositions and He partial pressures have been analyzed. Spectra taken in the absence of a helium background were best fit with higher rotational temperatures, typically around 180 K. Indeed, the experimental spectrum in these cases exhibit reproducible features which could be interpreted as indicating a non-Boltzmann rotational distribution. A representative "zero He" spectrum and computer fit are displayed in Fig. 5. The rotational temperature of the synthetic spectrum shown is 180 K. The fit of Fig. 5 is characterized by a standard deviation of 0.029 and a root mean square deviation of 4.3%. For these zero He runs, the temperature chosen for fitting is not as critical, i.e., fits with temperatures $\pm$ 20 K different from the best fit temperature still yield unchanged predicted population distributions.

The average relative population distribution for all analyzed spectra is shown in Fig. 6 normalized to the population of v=6. The error bar indicated for each population is one standard deviation. Note that the deduced population distribution does not vary significantly over the He pressure range 0 - 5 mtorr. The scatter in the populations of v=1, 2 is due primarily to the effect of the underlying band radiation while that observed for the populations of states v > 11 is a result of the low signal to noise in that wavelength region. These relative populations are also listed in Table I for convenience. A more detailed discussion of the data base is provided in Appendix A.

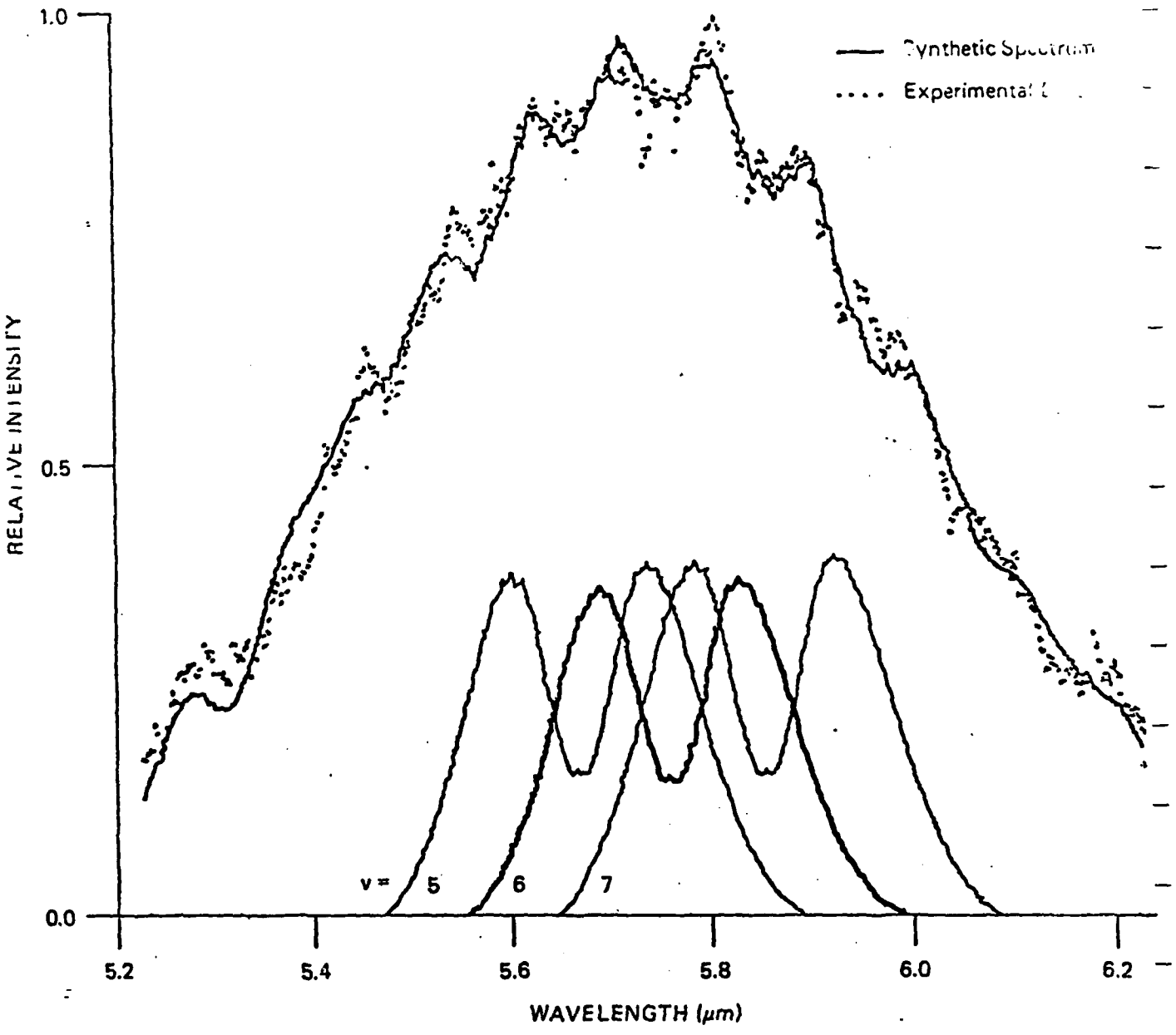

Fig. 5 Synthesized spectrum fit to experimental data for a case with no helium background. Flow composition and rates and instrumental resolution are the same as for Fig. 3. A rotational temperature of 180°K gave the best fit to the data. Standard deviation = 0.029, RMS deviation = 4.3%.

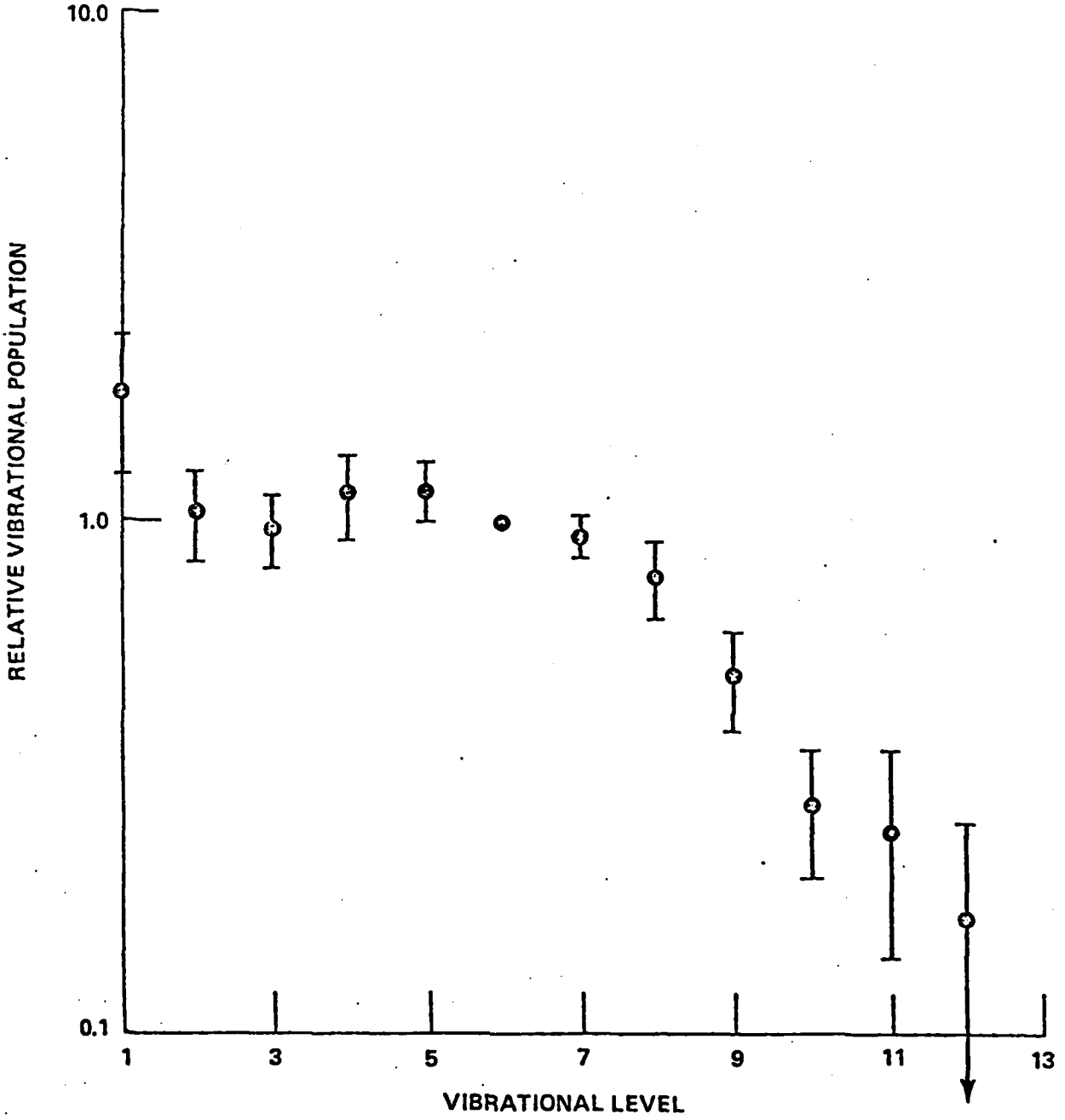

Fig. 6 Relative vibrational population distribution normalized to v = 6, shown with 1 standard deviation error bars. No significant variation of the distribution was observed as a function of helium background pressure over the range 0 - 0.5 Pa. The value shown for v=12 is an upper bound. The value for v = 1 is overestimated due to underlying spectral features.

TABLE I

AVERAGE RELATIVE POPULATIONS AND
FRACTIONAL EXCITATION RATE CONSTANTS

Vibrational Level	N(v)/N(6)*	$R_v = k_v/\Sigma k_v$
0	~ 1.0**	~0.1
1	≤ 1.8 ± 0.6	~0.1**
2	1.0 ± 0.2	0.1
3	1.0 ± 0.2	0.1
4	1.1 ± 0.2	0.11
5	1.2 ± 0.2	0.12
6	1.0	0.1
7	0.9 ± 0.1	0.09
8	0.8 ± 0.1	0.08
9	0.5 ± 0.1	0.05
10	0.3 ± 0.1	0.03
11	0.2 ± 0.1	0.02
12	<0.2 ± 0.1	<0.02

*Average for 24 experiments. The indicated uncertainty is one standard deviation.

** See text.

D. Data Analysis And Interpretation

1) Kinetic Considerations

The objective in this section is to attempt to unambiguously specify the production mechanism for the observed NO chemiluminescence, and further, to determine whether the observed distribution is that due to the excitation reaction alone or whether it has been affected by vibrational relaxation phenomena. The first step in this analysis involves identifying the chemical species (and their relative concentrations) which may be present in the reaction zone.

Active nitrogen is created via the passing of a microwave discharge through mixtures of N_2/Ar (typically 10/90) at a pressure of approximately one torr and temperatures near 100 K. While no diagnostics were available for the measurement of the concentrations of discharge produced species, the discharge conditions were purposely very similar to those of Lin and Kaufman[17] and it is assumed that the concentration of nitrogen atoms was roughly 1% of the N_2 density, with one to two percent of these in the $N(^2D)$ and $N(^2P)$ metastable states, and the remainder in the ground $N(^4S)$ state. Furthermore, the $N(^2D)$ concentration is anticipated to be roughly an order of magnitude larger than that of $N(^2P)$. The metastables $Ar(^3P_{0,2})$ and $N_2(A\ ^3\Sigma)$ will also be formed in the discharge; however, as will be shown, the concentration of these species will at least partially be controlled by collision processes occurring in the afterglow region of the flow; i.e., that region beyond the discharge but prior to the free jet expansion. A number of strongly radiative states, such as $N_2(B\ ^3\pi)$, will also be created in either the discharge or afterglow regions; however, such states will radiatively decay to ground or metastable states during the free jet expansion into the reaction zone. Lastly, vibrationally excited N_2 and modest levels of positive ions/electrons will also be formed in the discharge.

The afterglow region of the flow is several cm in length and for characteristic sonic velocities the gas residence time within this region will be approximately 200 μsec. The chemical reactions of interest occurring within this region include

$$Ar(^3P_{0,2}) + N_2 \rightarrow Ar(^1S) + N_2(C^3\pi) \quad k_{10} = 1.6 - 3.6 \times 10^{-11} \text{ cm}^3/\text{sec} \qquad (10)$$

$$N_2(A^3\Sigma) + N(^4S) \rightarrow N_2(x^1\Sigma) + N(^2P); \; k_{11} = 5 \times 10^{-11} \text{ cm}^3/\text{sec} \qquad (11)$$

$$N + N + Ar \rightarrow N_2 + Ar \; ; \; k_{12} = 8.2 \times 10^{-34} \, e^{500/T} \text{ cm}^6/\text{sec} \qquad (12)$$

$$N(^2D) + N_2 \rightarrow N(^4S) + N_2 \; ; \; k_{13} = 1 \times 10^{-13} \, e^{-510/T} \text{ cm}^3/\text{sec} \qquad (13)$$

$$N(^2P) + N_2 \rightarrow N(^4S) + N_2 \; ; \; k_{14} = 1 \times 10^{-16} \text{ cm}^3/\text{sec} \qquad (14)$$

$$N_2(v = 1) + N_2/Ar \rightarrow N_2 + N_2/Ar \; ; \; k_{15} = \text{slow} \qquad (15)$$

where all listed reaction rate constants are specific for a temperature of 300 K (only temperature for which data are available) unless a temperature dependence is explicitly shown. The listed rate constants are taken from Refs. 27, 28, 20, 29-31 respectively. Wall losses are negligibly small over the afterglow residence time.

From the prior discussion, it can be shown that the generic species concentrations in the afterglow region are $[Ar] \approx 10^{17}/\text{cm}^3$, $[N_2] \approx 10^{16}/\text{cm}^3$ and $[N] \approx 10^{14}/\text{cm}^3$. Thus, from reaction (10), the quenching of Ar metastables can be seen to occur immediately downstream of the discharge; i.e., $\tau_{10} \lesssim 6$ μsec assuming the listed rate constant is valid at 100 K. It should be noted that this quenching reaction can ultimately lead to production of the $N_2(A\ ^3\Sigma)$ state through $N_2(C \rightarrow B \rightarrow A)$ radiative cascade.[32,33] $N_2(A)$ state quenching by N_2/Ar is negligibly slow[34-36] and reaction (11) will provide the dominant loss

mechanism. The characteristic quenching time for $N_2(A\ ^3\Sigma)$ in the afterglow region is then $\tau_{11} \approx 200$ μsec, or approximately the same as the flow time, and thus a finite concentration of $N_2(A\ ^3\Sigma)$ will be found in the reaction zone. Lastly, the characteristic times for nitrogen atom loss and N_2 vibrational relaxation may be shown to be significantly longer than the flow time, and thus these species will flow undiminished into the reaction zone.

For the cases of zero helium background pressure presented in Section C, the reaction zone conditions ranged from P = 2.7 - 4.2 mtorr and $T \leq 200$ K. Thus, taking a typical case of T = 100 K, P = 4 mtorr, and a 90% Ar/10% N_2 jet mixing with a counterflow of pure oxygen, would result in species concentrations of $[O_2] = 2 \times 10^{14}/cm^3$, $[Ar] = 1.8 \times 10^{14}/cm^3$, $[N_2] = 2 \times 10^{13}/cm^3$, $[N] \approx 2 \times 10^{11}/cm^3$ and $[N(^2D, ^2P)] \approx 4 \times 10^9/cm^3$. Since the experiment is steady state, specific reactants will remain within the optical field-of-view (reaction zone) for a residence time which can be approximately defined from the measured steady gas flow rate into the system, i.e.,

$$\dot{m} = \rho V/\tau_R \tag{16}$$

where ρ is the gas density and V the volume of the optical field-of-view. As mentioned earlier, this volume is approximately cylindrical with length of 50 cm and radius of ≈ 4 cm; thus, for a typical $\dot{m}$ of 0.2 gm/sec, corresponding to a pressure of 4 mtorr,

$$\tau_R \sim 300\ \mu sec \tag{17}$$

Therefore, any NO created in the reaction zone will spend at most ~300 μsec within the field-of-view; thus, only NO quenching reactions which exhibit characteristic times of 10^{-3} seconds or smaller could affect the observed NO distribution.

The available production mechanisms for NO in the reaction zone are limited to

$$N(^4S) + O_2 \rightarrow NO + O\ ;\ k_1 = 1.1 \times 10^{-14}\ Te^{-3150/T}\ cm^3/sec \tag{1}$$

$$N(^2D) + O_2 \rightarrow NO + O \; ; \; k_3 = 7.4 \times 10^{-12} \; (T/300)^{1/2} \; cm^3/sec \qquad (3)$$

$$N(^2P) + O_2 \rightarrow NO + O \; ; \; k_{18} = 2.6 \times 10^{-12} \; cm^3/sec \qquad (18)$$

The temperature dependent rate constant listed for reaction (3) has been taken from Ref. 37 and is in reasonable agreement with other[16,17,30] measurements taken at room temperature. The rate constant listed for reaction (18) is from Ref. 30 and is specific for T = 300 K. The temperature dependence of reaction (1) is sufficiently great so that NO production due to $N(^4S)$ is unimportant relative to that due to $N(^2D, \; ^2P)$, even though the concentration of the latter species is some 10^2 lower than that of the former. The quenching of $N_2(A^3\Sigma)$ state by O_2 is known to be rapid,[38] but it is exceedingly unlikely that this reaction could form NO inasmuch as this would require the breaking of two bonds. To first order then, for the generic case, it is anticipated that $\lesssim 10^9/cm^3$ NO molecules (or oxygen atoms) can be produced by reactions (3) and (18) during the gas residence time. These densities are sufficiently small that the rates of any subsequent chemical reactions involving NO and O, such as

$$N + O + M \rightarrow NO + M \qquad (19)$$

$$NO + O + M \rightarrow NO_2 + M \qquad (20)$$

$$O + O_2 + M \rightarrow O_3 + M \qquad (21)$$

$$NO + O_3 \rightarrow NO_2 + O_2 \qquad (22)$$

will be insignificant over the gas residence time.

One additional source of vibrationally excited NO is the vibrational exchange reaction between N_2 and NO, i.e.,

$$N_2^* + NO \rightarrow N_2 + NO^* \tag{23}$$

Murphy et al[39] have determined this reaction to have a rate constant of $1.7 \times 10^{-16} e^{656/T}$ cm^3/sec (based upon a room temperature measurement) and, thus, if 10% of the N_2 were vibrationally excited, the maximum amount of NO* formed by reaction (23) during the residence time would be $< 10^6/cm^3$. This concentration is well below system detectability, and the effects of reaction (23) may be neglected.

It now remains to examine the possible loss mechanisms which could affect the NO vibrational distribution during the gas residence time. The shortest radiative lifetime for any vibrational level of NO is ~ 15 msec,[25] and radiative decay will not affect the NO vibrational distribution. NO(v) can also be destroyed by collisions with any of the reactants either by quenching

$$NO(v) + M \xrightarrow{k_Q} NO(v - 1) + M/M^* \tag{24}$$

or chemical reaction such as

$$NO(v) + N \rightarrow N_2 + O \tag{25}$$

Given the species concentrations within the reaction zone, one can determine the minimum rate constant required to provide a characteristic NO quenching time which is less than one msec (i.e., $\sim 3\ \tau_R$; any reaction with a characteristic time longer than this could not appreciably affect the NO vibrational distribution). From such considerations, it can be determined that quenching of NO(v) by O_2 or Ar would only be important if $k_{Q=O_2;\ Ar} \geq 5 \times 10^{-12}$ cm^3/sec, and that quenching by N_2 will be unimportant if $K_{Q=N_2} \geq 5 \times 10^{-11}$ cm^3/sec. The minimum quenching rate constants deduced for all other species in the flow are greater than the gas kinetic limit, and quenching effects due to these species may be neglected.

There are no available measurements on the quenching rate constants of NO(v=1-12) by O_2 or Ar at temperatures of 100 K. Room temperature measurements[12,39] for NO quenching by O_2 indicate that $k_{Q=O_2} \leq 1.4 \times 10^{-13}$ cm^3/sec for $v \leq 7$. The fractional populations exhibited in Fig. 6 were deduced from data taken over a range of argon densities of $0.0 - 2.1 \times 10^{14}$ molec./cm^3 and O_2 densities of $1.1 - 2.1 \times 10^{14}$ molec./cm^3, and no discernible changes in the vibrational population distribution were observed. Thus, one is led to conclude that the rate constants for de-activating NO(v=1-12) by O_2 and Ar at a temperature of 100 K are certainly less than 5×10^{-12} cm^3/sec. Similarly, the N_2 density was varied from $0.016 - 1.5 \times 10^{14}$ cm^3 with no apparent change in the NO vibrational distribution. Thus, it can be deduced that quenching by N_2 exhibits a rate constant of less than 6.7×10^{-12} cm^3/sec. Note that if the reaction zone temperature were 200 K, rather than 100 K, the deduced maximum quenching rate constants would increase by a factor of 4 because both species number density and residence time would decrease by a factor of two.

A number of the measurements presented in Fig. 6 were performed under conditions of finite helium background pressures of 3 - 5 mtorr. The flow characteristics of these runs are somewhat different from those discussed above, inasmuch as the helium will be dispersed uniformly across the test chamber (i.e., helium is not cryogenically pumped by the walls). The added reactant gases, N_2, O_2, etc. are still adsorbed by the walls, but their radial profiles are now controlled in part by diffusive interactions with the ambient helium as well as by pressure gradients. A crude estimate of the reactant residence time within the field-of-view for these cases may be provided by estimating the characteristic time for NO to diffuse four cm in helium at a pressure of 4 mtorr and nominal temperature of 100 K. Interestingly enough, this characteristic time is also on the order of 300 μsec. Since the deduced NO vibrational distributions for the cases taken with a non zero helium pressure are the same as those deduced from data taken in the absence of He, one can estimate to first order that $k_{Q=He}$ for NO(v=1-12) is $< 2 \times 10^{-12}$ cm^3/sec.

As alluded to earlier, there is one very significant difference between the NO spectra observed in the presence or absence of helium. A typical spectrum taken in the presence of helium was shown in Fig. 3. From the widths of individual peaks, as well as the intensity ratios of maxima to minima, it can be clearly discerned that the characteristic rotational temperature of the NO is of order 80 - 100 K. Measurements performed in the absence of helium, see Fig. 4, exhibit spectral features more appropriate to NO at rotational temperatures of 180 K (indeed, there is even some suggestion of non-Boltzmann rotational distributions, although all dominant spectral features are clearly identifiable as due to NO). Nonetheless, and very important, the vibrational populations deduced from these two limiting cases are virtually indistinguishable within the scatter of the data.

Although it is possible that the rotational temperature differences are related to actual differences in the translational temperatures in the reaction zone, there is no a priori reason to believe that the NO is created in rotational equilibrium. Indeed, the observations can be interpreted to imply that the NO is created in rotational disequilibrium and that helium more effectively relaxes the NO rotational states than $N_2/O_2/Ar$ does. A complete understanding of these details must await more refined studies. However, it can be pointed out that if rotational equilibration is to occur within the gas residence time, the rate constant for this process must be larger than $\sim 2 \times 10^{-11}$ cm^3/sec.

2) The Chemiluminescence Reactions

The results of the reaction zone kinetic analysis presented above lead one to conclude that the observed fluorescence results directly from the products of a chemiluminescent reaction without any effects due to collisional quenching (with the possible exception of rotational relaxation). Since this is so, the deduced vibrational populations corresponding to the fluorescence should be linearly proportional to the vibrational level dependent production rates for these levels. Thus, it is of some interest to examine the population distribution of Fig. 6 in some detail.

The observations are rather unusual for a chemiluminescent reaction in that the statistically averaged population distribution is approximately flat out to v=7, except for v=1, and then decays rapidly at higher vibrational levels. Attempts to artificially remove the contribution of the underlying radiation tend to reduce the v=1 populations deduced from the fitting procedure to the same level as those for v = 2 - 7. A number of chemiluminescent reactions or reaction paths could contribute to the observed radiation; these are

$$N(^2D) + O_2 \rightarrow NO(X^2\pi,\ v \leq 18) + O(^3P);\ \Delta H_F = -3.77\ eV \qquad (3)$$

$$N(^2D) + O_2 \rightarrow NO(X^2\pi,\ v \leq 8) + O(^1D);\ \Delta H_F = -1.8\ eV \qquad (26)$$

$$N(^2P) + O_2 \rightarrow NO(X^2\pi,\ v \leq 26) + O(^3P);\ \Delta H_F = -4.96\ eV \qquad (18)$$

$$N(^2P) + O_2 \rightarrow NO(X^2\pi,\ v \leq 14) + O(^1D);\ \Delta H_F = -3.00\ eV \qquad (27)$$

$$N(^2P) + O_2 \rightarrow NO(X^2\pi,\ v \leq 3) + O(^1S);\ \Delta H_F = -0.77\ eV \qquad (28)$$

where the exothermicities listed are for reaction at 100 K. As discussed earlier, the concentration of $N(^2P)$ in the reaction volume is expected to be an order of magnitude smaller than that of $N(^2D)$. Thus, although the relative quenching efficiencies of ^2D and ^2P are not known at 100 K, $N(^2D)$ atoms are more likely to be the dominant chemiluminescence precursor. Furthermore, the fact that excited vibrational levels with v > 8 are observed suggests that reaction (3) is at least partially contributing to the observed chemiluminescence, although reaction (26) may make intensity contributions at lower v.

Since the observed population distribution appears to be that initially formed by a chemical reaction, it is possible to examine these results in light of surprisal theory.[40-43] The surprisal of the observed population distribution is defined as

$$I(f_v') = - \ln \left[P(f_v')/P^o(f_v')\right] \tag{29}$$

$$\sum_v P(f_v') = 1 \tag{30}$$

$$\sum_v P^o(f_v') = 1 \tag{31}$$

where $P(f_v')$ is the observed relative vibrational population distribution and $P^o(f_v')$ is the prior nonspecific population distribution. The fraction of the total reaction exothermicity that is used for vibrational excitation is denoted by f_v'. A linear plot of $I(f_v')$ as a function of f_v' implies the existence of an exponential gap law, i.e.,

$$P(f_v') = P^o(f_v') \exp \left[-\lambda(f_v')\right] / \exp \lambda_o \quad , \tag{32}$$

where the parameter λ_v is a local measure of the deviation of $P(f_v')$ from the prior distribution of $P^o(f_v')$. A more detailed description of surprisal analysis is presented in Appendix B.

A prior distribution has been calculated using standard techniques (see Appendix B) under the assumption that reaction (3) is solely responsible for the observations. The population distribution calculated from the experimental data is plotted in Fig. 7 along with the prior distribution. Values of the surprisal, I, are also plotted in the figure. It is seen that

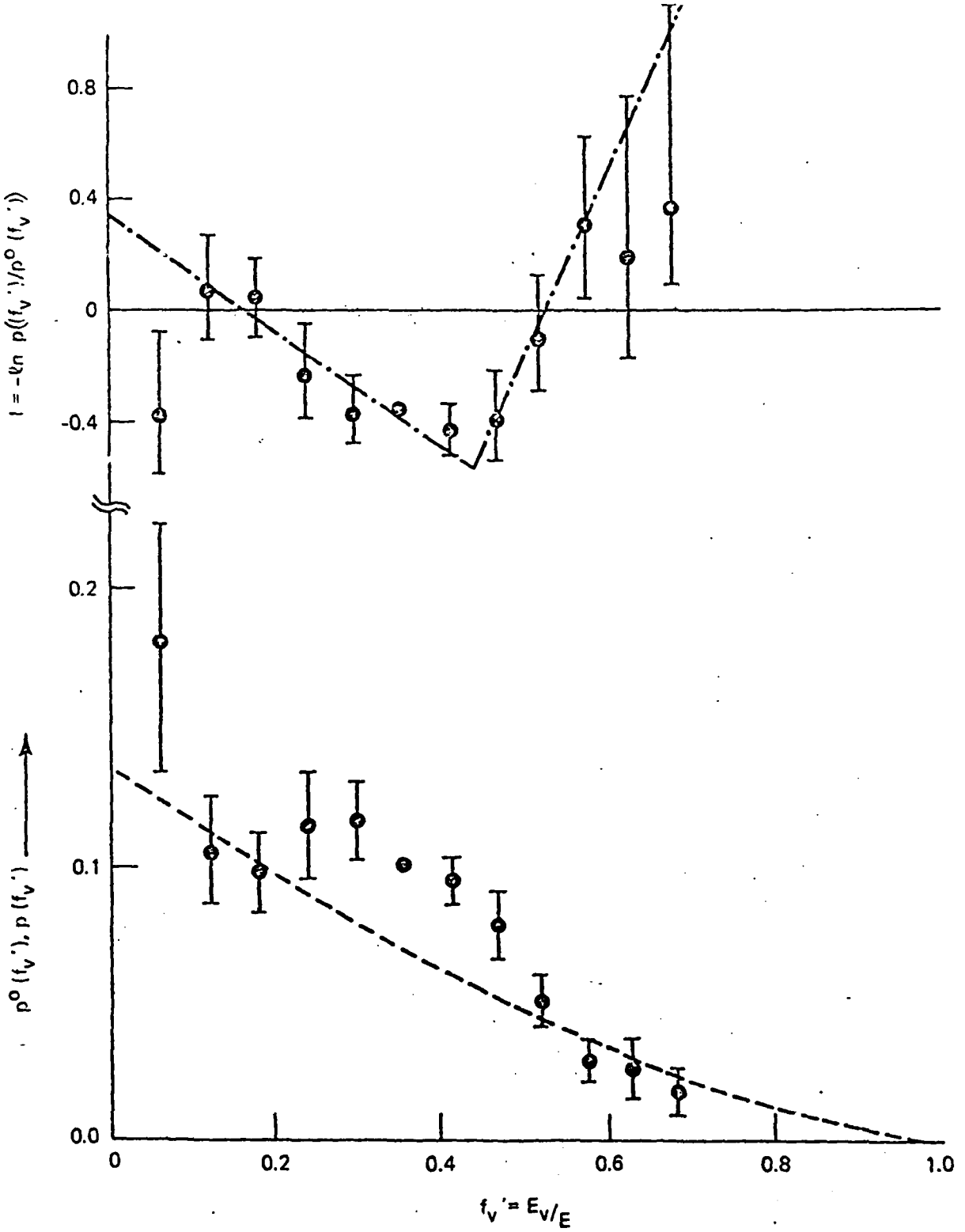

Fig. 7 Lower - population distribution as a function of the available energy plotted for both the prior distribution (dashed line) and the observed experimental distribution. Upper - the corresponding surprisal plot. A break in the surprisal appears to occur at v = 7, 8. The broken line fits to the data in the two regions have slopes of -2. 1 and +7. 0.

the surprisal plot is broken into two approximately linear regimes with a change in slope occurring at $v \approx 7 - 8$. In previous surprisal treatments where this behavior has been observed,[42,43] it has been attributed to the simultaneous occurrence of two reaction paths. It must be emphasized that a break in the surprisal plot does not by itself imply that two different mechanisms are occurring, but the fact that the maximum possible vibrational excitation for reaction (26) is in close agreement with the position of the experimentally observed break in λ_v supports a hypothesis that both $N(^2D) + O_2$ reaction branches, reactions (3) and (26), contribute to the chemiluminescence.

In one previous case,[43] a "two-slope" surprisal plot has been successfully interpreted to mean that the reaction had two branches. Specifically, that one of the reaction products was created in two distinct electronic states. When that experimental data was re-analyzed in terms of this mechanism, it was found that the resulting plot of the surprisal for each branch exhibited a linear behavior. Such an analysis does not work in the present case. Indeed, in the present case the calculated surprisal not only changes slope, but the slope also undergoes a change in sign from positive to negative. It can be readily shown mathematically that a reaction having two channels, each with a linear surprisal, cannot exhibit such a behavior.

Thus it is felt that some sort of constraint may be affecting the reaction dynamics. Reaction (3) may proceed along any of four adiabatic surfaces with different symmetries, one of which is the same symmetry as the only adiabatic surface for reaction (26).[44] The shared symmetry surface passes through the lowest energy intermediate for reaction (3), and thus is the most probable reaction path. At large $N\text{-}O_2$ distances where the reaction channel is decided, a great deal of mixing between the two surfaces is likely. Alternately, a non-adiabatic surface crossing may exist between the two paths.[45] In this case the reference energy of the reaction would be the energy at the interaction region as defined by the Landau-Zener formula.

If this interaction energy is postulated to occur at the energy of the break in the surprisal plot $[NO(v=7\text{-}8), O(^3P)]$, then the surprisal plot could be re-evaluated for these reaction energetics. The surprisal at low v for reaction (3) is expected to vary as $\lambda_{v=1-7} = -\lambda_{v=8-12}$.[46] With these

assumptions, the observed population distribution could perhaps be satisfactorily explained as arising from contributions from the two closely coupled reaction channels of reactions (3) and (26). A more accurate reaction path prediction would require a detailed reaction surface calculation of the $N(^2D) - O_2$ interaction.

If indeed $N(^2P)$ is present in sufficient quantities so that the observed chemiluminescence is due to both atom precursors, then the above interpretation of the results by surprisal analysis is not valid. But, if the surprisal were determined under the assumption that the fluorescence arose solely from reaction (18) rather than reaction (3), the surprisal plot would still exhibit two linear regimes. Furthermore, it can be shown[44] that there is no adiabatic pathway for reaction (18); i.e., the reactants of reaction (18) cannot be adiabatically coupled to the products. Thus some sort of surface crossing would be required for reaction (18) to proceed with a high probability.

E. Summary and Conclusions Concerning NO Fundamental Band Observations

In the preceding sections measurements of nitric oxide chemiexcitation have been described, and the observed emission has been shown to reflect the original vibrational distribution of NO produced in the reaction between metastable nitrogen atoms and oxygen molecules. To the authors' knowledge this is the first detailed study of a chemi-excitation reaction involving an electronically excited reactant. The measurements were performed under near single collision conditions, with total pressures of 5×10^{-6} atmospheres and temperatures of ~100 K, and the concentrations of vibrationally excited NO, which were monitored via infrared fluorescence, were estimated to be less than 10^9 particles/cm^3.

Although absolute rate constants have not been determined in this work, they can be inferred. Specifically, the apparent constancy of the relative rate constants for levels v=1-7 would seem to indicate that an extrapolation to v=0 is not unreasonable. This extrapolation is supported by results from the surprisal analysis of Section D, and yields a value of near unity for the relative population N(0)/N(6). It is worth re-emphasizing

in this context that a significant fraction of the total intensity in the vicinity of the NO v=1→0 band is due to an underlying source of radiation. Although this "background" radiation has not been explicitly accounted for in the data reduction, it is known that the derived population of NO(v=1) may be overestimated by as much as a factor of two. Thus the "true" population of the v=1 state is believed to be similar to those of v=2-7.

Using the extrapolated value for the population of the ground vibrational state of NO, the fractional efficiencies for production of NO into individual vibrational levels are easily computed and are presented in Table I. Note that even an error as large as a factor of two in the estimate for NO(v=0) would produce only a 5% error in the inferred production efficiencies of the other levels. From the results summarized in Table I it may be concluded that the average degree of vibrational excitation is about 4.5 vibrational quanta per NO molecule or, in terms of average vibrational energy, slightly more than 1.0 eV per molecule. If it is assumed that the nitric oxide has been created by the reaction of $N(^2D)$ atoms with O_2, this would imply that about 27% of the total reaction exothermicity is converted to vibrational excitation of the nitric oxide product. Furthermore, as discussed earlier, the location of the rather distinct discontinuity in the distribution, going from v=7 to v=8, occurs at the point where the simultaneous production of $O(^1D)$ could begin to limit the production of vibrationally excited nitric oxide.

Obviously, given the possible, and presently undefined, role of $N(^2P)$ atoms in producing vibrationally excited NO, there remains some degree of uncertainty in the mechanistic interpretations of the results presented here. Additional experimental diagnostics are presently being developed in order to address the most important unknowns; these include implementation of resonance absorption techniques for accurate determination of metastable atom concentrations and refinement of the techniques currently in use for the absolute calibration of the infrared measurement system. Unfortunately, it does not seem likely, at least not at the low total pressures for which the experiments are presently designed, that optical detection of the possible $O(^1D)$ product will be feasible.

The other intriguing aspect of the present data is, of course, the suggestion of non-equilibrium rotational anomalies in the spectra, perhaps reflecting details of the rotational kinematics associated with the reaction. It is believed that improvements currently being made to the optical system in the COCHISE facility will enable better definition of the rotational details in future work and, consequently, may provide enough information to more clearly specify many more of the quantum details of this and other reactions.

The ultimate goal of this work is to provide data for use in modeling upper atmospheric radiation signatures. The excitation distribution developed here may be used to predict NO fundamental and overtone band signatures occurring during an auroral event. Such predictions require specification of auroral $N(^2D)$ production rates and a model for these is provided in Appendix C.

F. Analysis of Additional Chemiluminescence Data

Preliminary studies of NO first overtone vibrational band chemiluminescence and O_3 - related emissions have also been performed. The NO ($\Delta v = 2$) chemiluminescence near 2.7 μm was excited in the reaction cell in the same manner as for the fundamental band; i.e., by the interaction between discharged N_2/Ar mixtures and O_2 as a counterflow gas. Radiation from the $O_3(\nu_3)$ band at 9.6 μm was observed when discharged O_2/Ar mixtures were introduced into the reaction cell with O_2 or Ar counterflows. In Part 1 below, the validity of the existing NO ($\Delta v = 2$) data base will be discussed, the results of spectral fitting calculations will be presented, and conclusions regarding improvement of the data base will be drawn. In Part 2, the O_3 data base will be described and compared to previous observations reported in the literature, and preliminary results, drawn both from trends in the observed spectra and from first-pass spectral fitting calculations, will be discussed.

1. NO Overtone Analysis

The emission from the NO ($\Delta v = 2$) band system near 2.7 μm observed in COCHISE experiments is most likely due to nascent NO (v) formed in the

reaction cell mixing region by reactions between metastable nitrogen atoms and oxygen molecules as was shown to be the case for NO ($\Delta v = 1$) radiation observed at 5.4 μm in similar experiments. Since the nascent vibrational population distribution must be identical for the two band systems, the resulting spectral data may be used to determine the ratio of the spontaneous emission coefficients for the two bands (these ratios have not been measured for $v \geq 2$; only theoretical estimates are available). Unfortunately, the existing data base cannot be used for this purpose, since the uncertainty in the temperature of the blackbody calibration source (cf. Section III) gives rise to an uncertainty of more than a factor of 2 in the relative system response between the wavelength regions of the two bands. Furthermore, contributions to the overall intensity of each band by unidentified radiation sources leads to additional ambiguity in the result. However, the effect of the calibration uncertainty on the spectral distribution of each band alone is negligible for the fundamental and only slight for the overtone; thus the spectral analysis of the existing NO ($\Delta v = 2$) spectra, coupled with the previously determined vibrational population distribution (see Table I), should at least allow the determination of the relative $\Delta v = 2$ Einstein coefficients for each vibrational level. Unfortunately, because of the presence of unidentified radiation in the same spectral range as the NO overtone emission, this result could only be achieved at high vibrational levels. The details of the analysis are provided below.

After thorough examination of the data base for NO ($\Delta v = 2$) fluorescence, eight spectra were found to be suitable for spectral analysis. The remaining measurements were found to be clouded by at least one of three experimental phenomena. First, some of the data were taken with the presence of large (> 8 mtorr) background levels of He in the reaction cell; it has been shown (see Appendix A) that such background He levels give rise to collisional relaxation of NO (v). Second, some data were taken under conditions where the RC time constant on the signal analyzer was sufficiently long such that the spectral resolution was significantly distorted; in future experiments, care should be taken that the electronic time constant

is less than ~30% of the time it takes for the grating to traverse one resolution element. Third, some of the spectra exhibit marked structure which should not have been observable with the stated slit width settings; this effect could be due to inadvertent misalignment of the slits, which is known to occur occasionally during adjustment of the slit width settings (cf. Appendix D). As a result of these experimental difficulties, the effective data base was limited to eight spectra of medium resolution (0.013 - 0.027 μm) and low He background (<4 mtorr); a typical observed spectrum is shown in Fig. 8.

The observed NO ($\Delta v = 2$) spectra were analyzed by the least squares spectral fitting procedure described in Section C. The NO spectrum was simulated using the high-precision spectral code developed for the analysis of high resolution data from the HIRIS rocket measurements; this spectral calculation is described in detail in Ref. 4. The band Einstein coefficients calculated by Billingsley[25] for the $\Delta v = 2$ transitions were used in the calculations. A comparison of the observed spectrum from Fig. 8 with a computed least squares fit is shown in Fig. 9. It can be seen from Fig. 9 that contributions from underlying radiation are significant at both the low and high wavelength ends of the spectrum; indeed, the $2 \rightarrow 0$ transitions of NO are completely obscured by this unidentified radiation source.

Relative vibrational state populations for the eight observed spectra, derived from the spectral fitting calculations, are plotted in Fig. 10. It can be seen that significant run-to-run variation exists, and the effect seems to occur primarily at lower vibrational levels. By comparison to the earlier results obtained from NO fundamental spectra, it is clear that the derived populations of the lower vibrational levels, especially of the $v = 2$ level, are strongly affected by the underlying radiation; the extent of this effect appears to vary during the course of a day's data gathering as well as from day to day or month to month. The source of this radiation may be species formed in the discharges from impurities either inherent in the gas or present as a result of air leaks in the gas lines. The temporal variability of the intensity of the radiation suggests the latter possibility; however, no such extensive effects were observed in the NO ($\Delta v = 1$) spectra obtained during

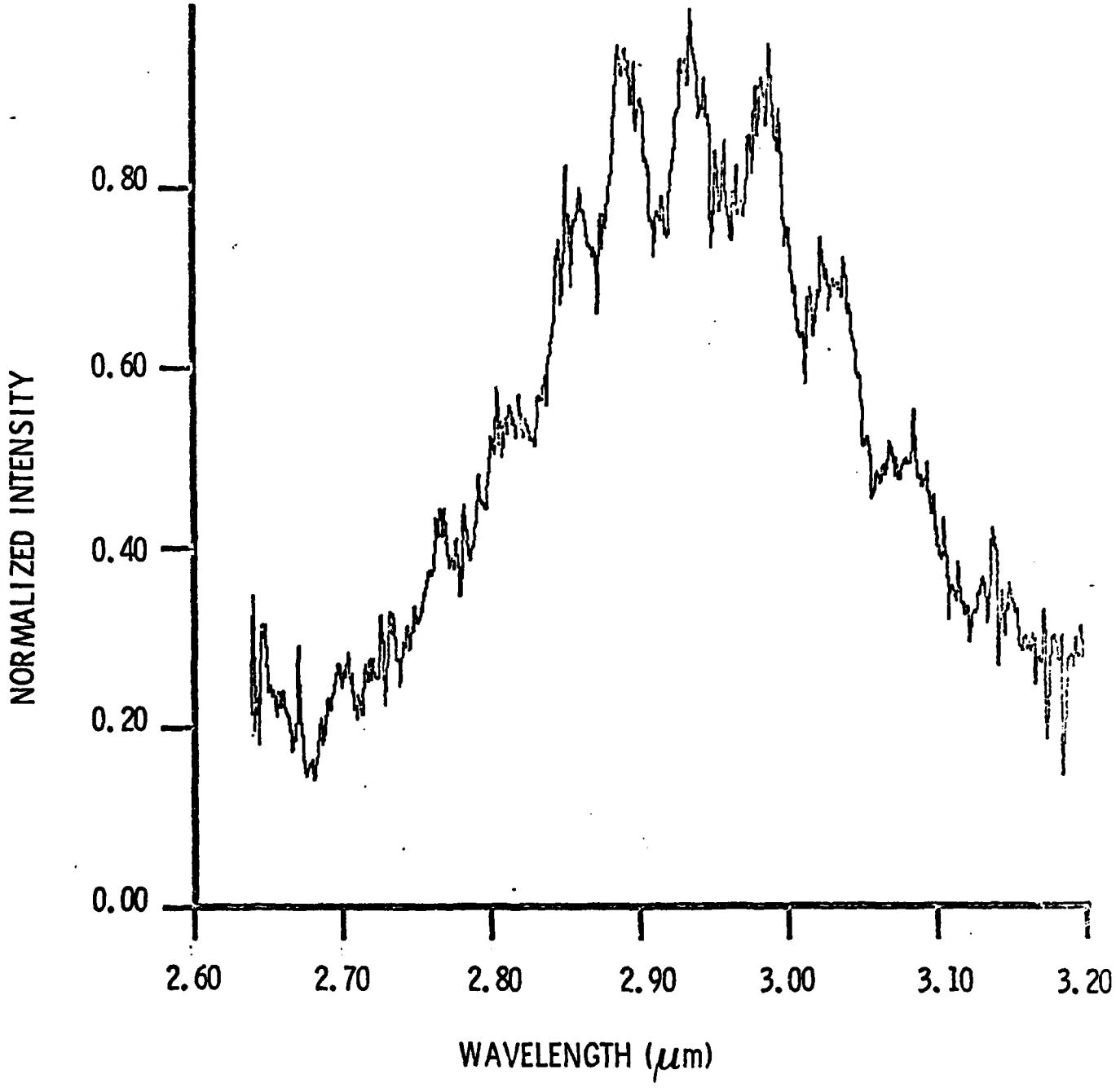

Fig. 8 Observed NO ($\Delta v = 2$) Spectrum. Experiment 283706, 1.5 mm slits, 0.0 mt He. Discharges Ar/N_2 = 3.6/0.4 std l/min; Counterflow: O_2, 4.0 std l/min.

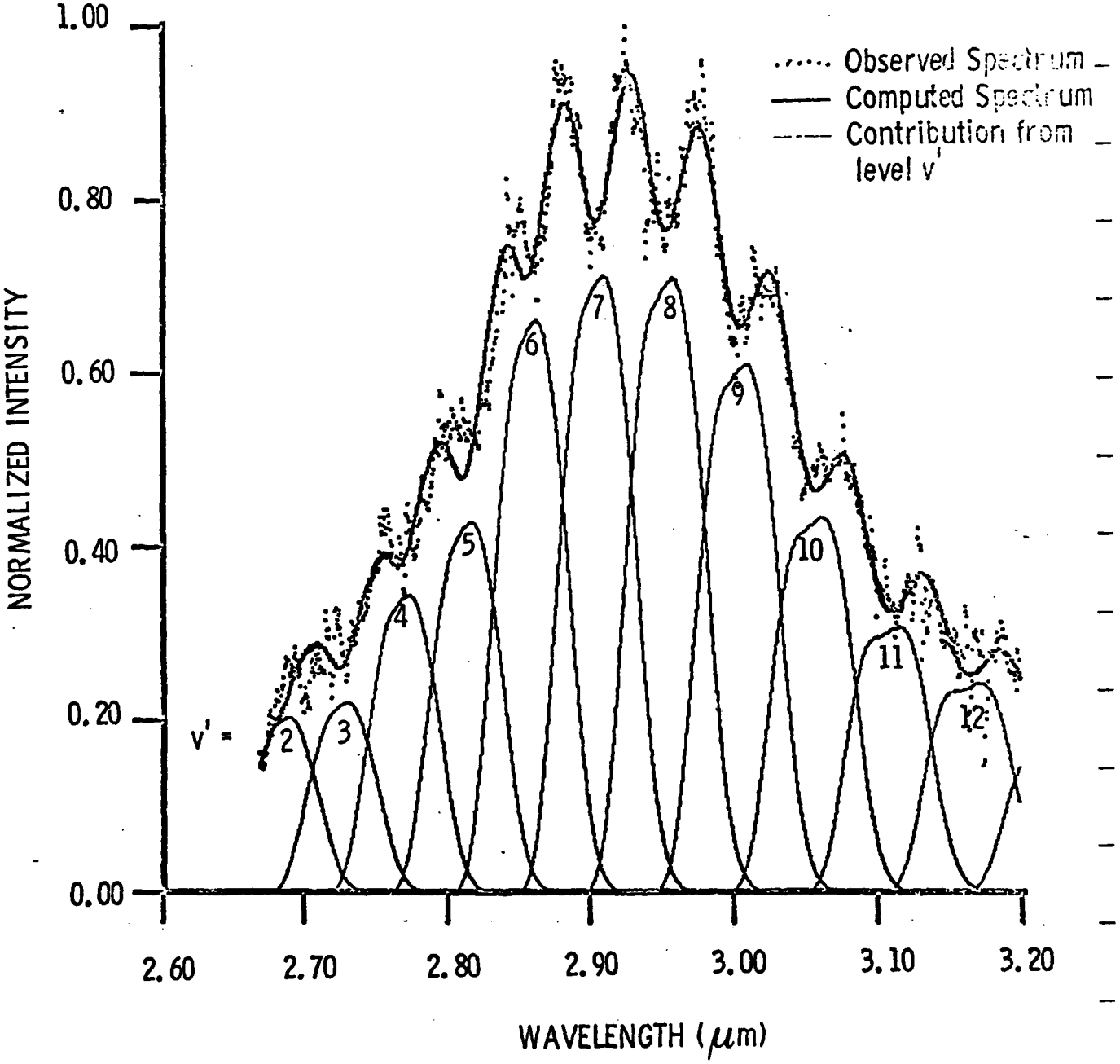

Fig. 9 Comparison of Computed and Observed Spectra, Experiment 283706. In the computed spectrum, the rotational temperature is 90 K and the resolution is 0.027 μm. The standard deviation of the least squares fit is 0.033.

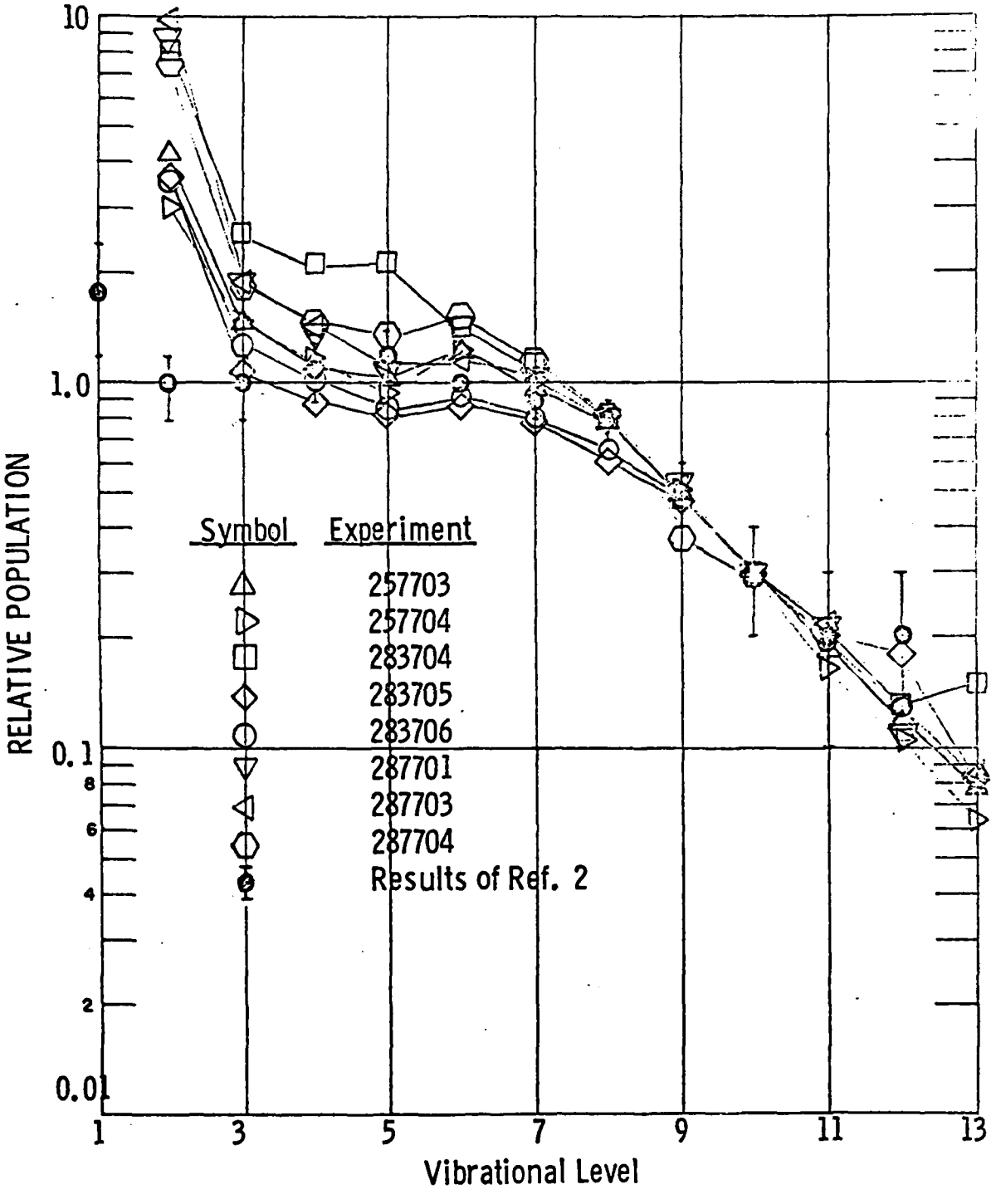

Fig. 10 Relative NO(v) Populations Derived from Overtone Spectra, compared to the results of Ref. 2 from fundamental spectra. The fundamental results are plotted as N(v')/N(6); the overtone results are adjusted to the same value of N(10) as given by the fundamental distribution.

the same time period. Although these effects are extremely difficult to correct for, further experiments could lead to more satisfactory results. An experimental approach to the problem would be to (1) eliminate system leaks and purify the gases entering the system, (2) use the best possible resolution for all scans, and (3) carry out a series of "blank" scans, in which a non-reactive counterflow gas is used in order to isolate the interfering radiation.

In an attempt to minimize the impurity effects, pairs of "matched" spectra, in each of which consecutive scans were taken of the overtone and fundamental bands, were selected from the data base. Due to the experimental difficulties outlined above, only three such pairs could be found. The relative values of $N_{v'}$, $A_{v'\rightarrow v'-n}$ determined in the spectral simulations for these scans were used to determine relative values of $A_{v'\rightarrow v'-1}/A_{v'\rightarrow v'-2}$. The relative Einstein coefficient ratios determined for these three cases are plotted in Fig. 11, together with the absolute ratios predicted by Billingsley[25] and Michels.[47] It can be seen that, although the experimental ratios are affected by impurity spectra below v' = 4, the observed ratios for $5 \leq v' \leq 12$ exhibit the same dependence on v' as the values predicted by Billingsley.[25] It must be emphasized that this observation is based on a very limited data base.

2. Observations of Emission From O_3

A preliminary study of O_3 chemiluminescence falling in the 2 to 15 μm wavelength region has also been performed. The observations were carried out through discharge excitation of O_2/Ar mixtures which were then mixed with counterflows of O_2 or Ar. The most clearly identifiable band system observed to date is the ν_3 band of O_3 near 9.6 μm; considerable data on the fluorescence of this band as observed in COCHISE have been inspected, and the results of a first-pass analysis will be described below. Two other bands which may be related to O_3 emission were observed near 4.8 μm and 6.4 μm; however, since the grating used in these experiments was blazed at 10 μm, the system response at the shorter wavelengths was sufficiently low that these measurements were signal-limited. More detailed, higher resolution

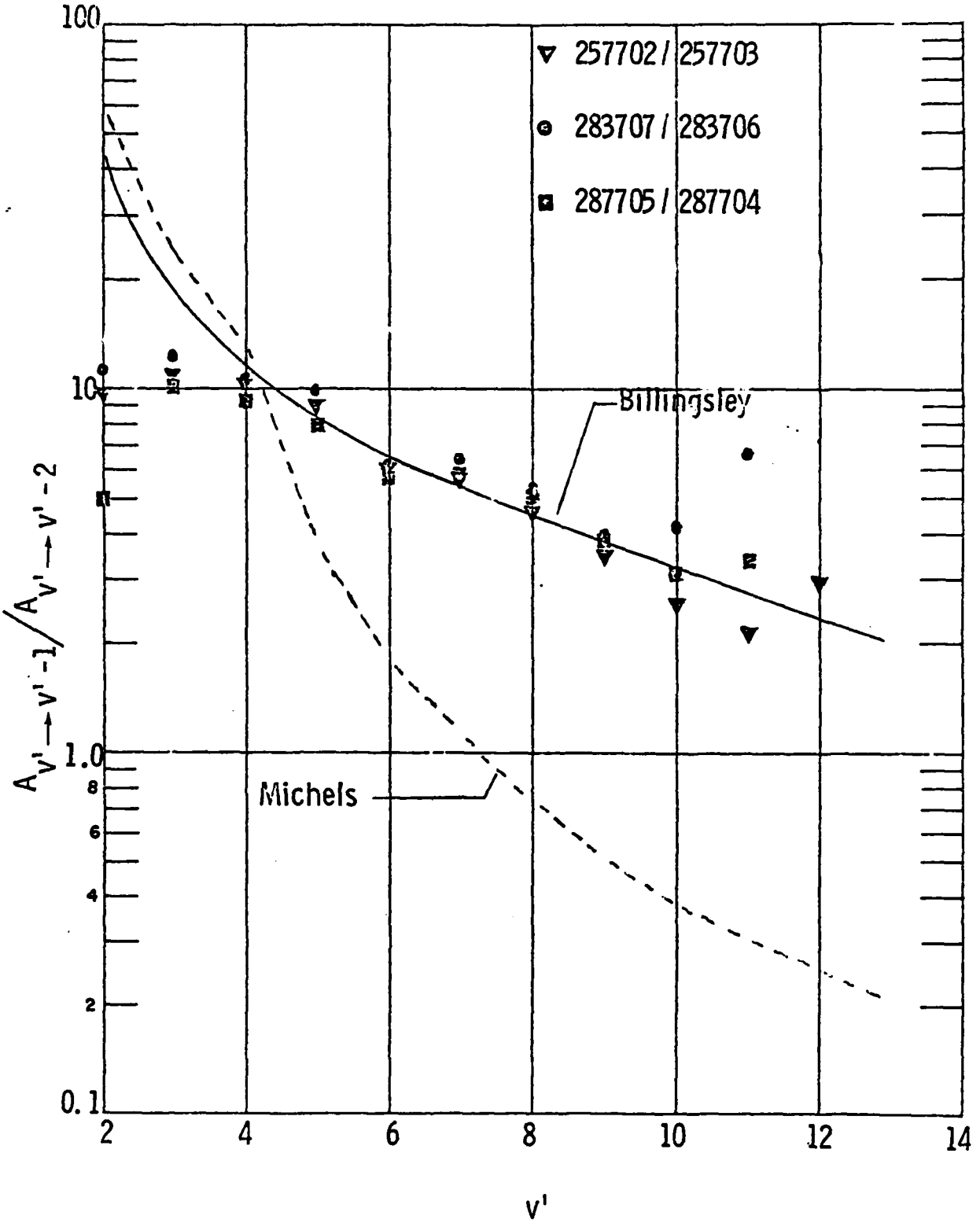

Fig. 11. Comparison of measured relative Einstein coefficient ratios (arbitrary scale) to predicted values.

measurements using the 3 μm grating will be required for a reliable determination of the origin of these bands.

Von Rosenberg and Trainor[48] have observed infrared chemiluminescence from O_3 formed by recombination of O and O_2 in flash-photolyzed mixtures of O_2/O_3 held at pressures of 100 - 400 torr. These investigators used interference filters to isolate different spectral bandpasses between 2 and 15 μm. Their spectral observations and interpretations may be summarized as follows: emission in the 8 - 12 μm region due to ν_3 and/or ν_1 radiation; emission in the 10 - 12 μm region due to high vibrational levels of the ν_3 band system; emission in the 13 - 16 μm region from the ν_2 band; emission at 4.5 - 5.0 μm, possibly from the $\nu_1 + \nu_3$ combination band; emission in the 5.5 - 7.5 μm region, tentatively assigned to the $^3B_2 \rightarrow {}^1A_1$ transition; and weak emission at 7.5 - 8.5 μm, possibly from vibration - rotation bands of the $^3B_2$ state. The COCHISE observations are consistent with these except that the ν_2 (14 μm), ν_1 (9 μm), and 8 μm bands were not observed.

A representative spectral scan of the ν_3 band observed in the COCHISE experiments is shown in Fig. 12. The 001 → 000 transition, centered at 9.6 μm, is responsible for most of the observed intensity. However, $\Delta\nu_3 = 1$ transitions for higher vibrational levels can be seen extending to ~11 μm. To the best of our knowledge, these data represent the first spectrally resolved laboratory observations of emission from higher vibrational levels of the ν_3 band of O_3. The emission observed in the COCHISE experiments may arise from some combination of the following processes:

$$O + O_2 \rightleftarrows O_3^* \tag{33}$$

$$O_3^* \rightarrow O_3\ (v') + h\nu \tag{34}$$

$$O_3^* + M \rightarrow O_3\ (v') + M \tag{35}$$

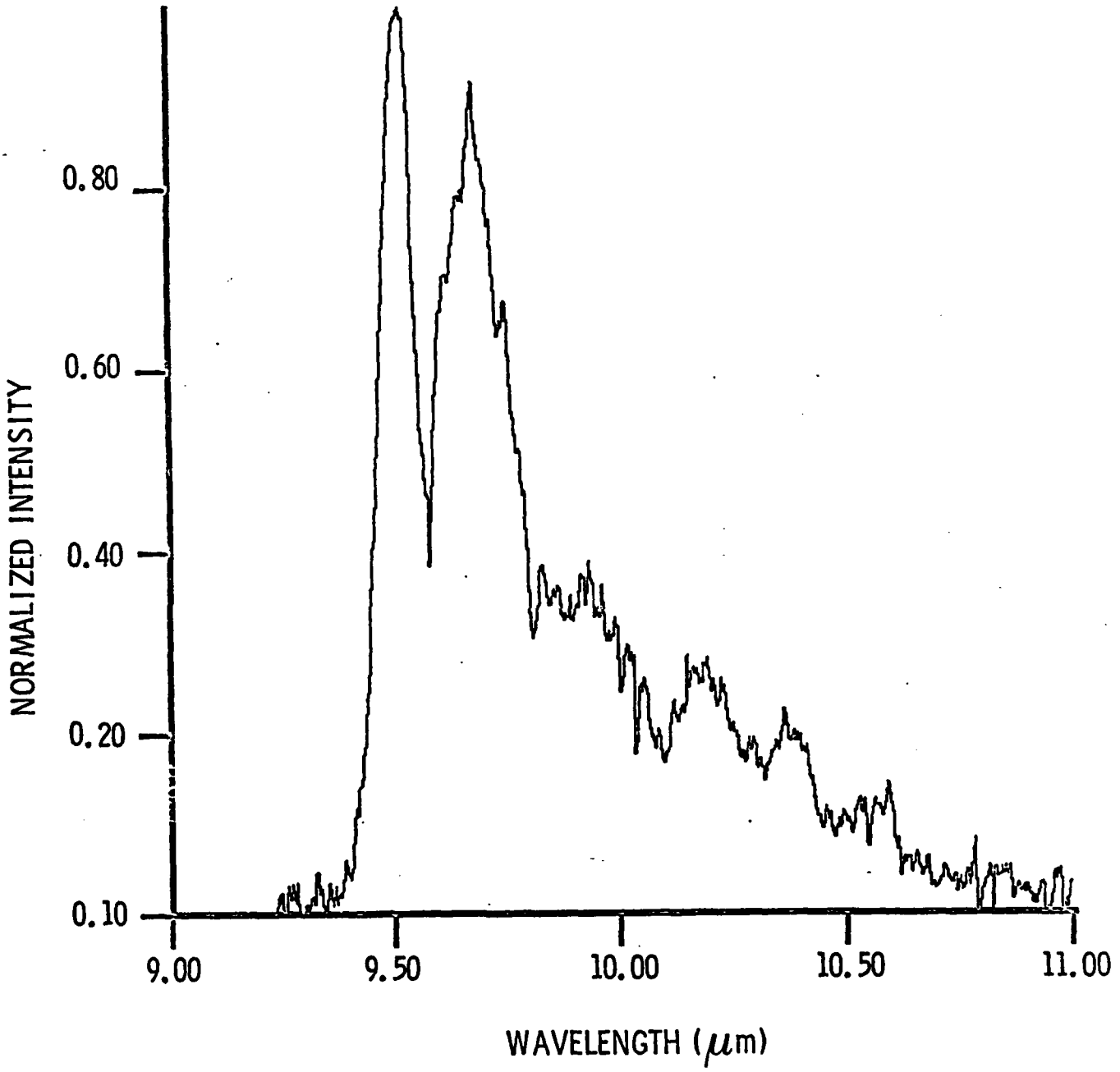

Fig. 12. Observed spectrum of O_3 ν_3 band. Experiment 107016, 1.5 mm slits, 3 mt He background. Discharge 0.7% O_2/Ar; Counterflow: O_2.

$$O_3(v') \rightarrow O_3\ (v' - 1) + h\nu\ (9.6\ \mu m) \qquad (36)$$

$$O_3\ (v') + M \rightarrow O_3\ (v'') + M \qquad (37)$$

These processes may occur both in the interaction region and in the discharge tubes. It is anticipated that more detailed analysis of the existing data, coupled with further experiments which may be defined thereby, will serve to illuminate the relative importance of the above processes.

The preliminary analysis of the ν_3 data has included an inspection of the effects of various experimental parameters on the observed spectra and the initial development of a spectral simulation code. In the former case, it was found that the observed spectral intensities and distributions were affected by the use of Ar instead of O_2 as a counterflow gas, by the concentration of O_2 in the discharge gas, and by the temperature of the discharge gas. Switching from an O_2 to Ar counterflow for a given O_2/Ar discharge mixture consistently gave a spectrum of roughly the same spectral distribution but about a factor of two lower in overall intensity (see Fig. 13). This result, coupled with the further effects of discharge mixture and temperature to be described below, strongly implies that the majority of the observed excitation results from processes occurring in the microwave discharges. However, the implications of the reduction in intensity in the viewing region for Ar counterflows are not yet understood, and may be related to chemical or fluid dynamic processes occurring in the mixing zone.

Reduction of the fraction of O_2 in the O_2/Ar discharge mixture from 13% to 0.5% gave rise to a corresponding decrease in overall spectral intensity and also to an enhancement of the fractional intensity of emission from the higher vibrational levels relative to that from the 001 → 000 transition (see Fig. 14), as if the presence of less O_2 in the discharge mixture causes less vibrational relaxation of the O_3 formed in the discharges (or

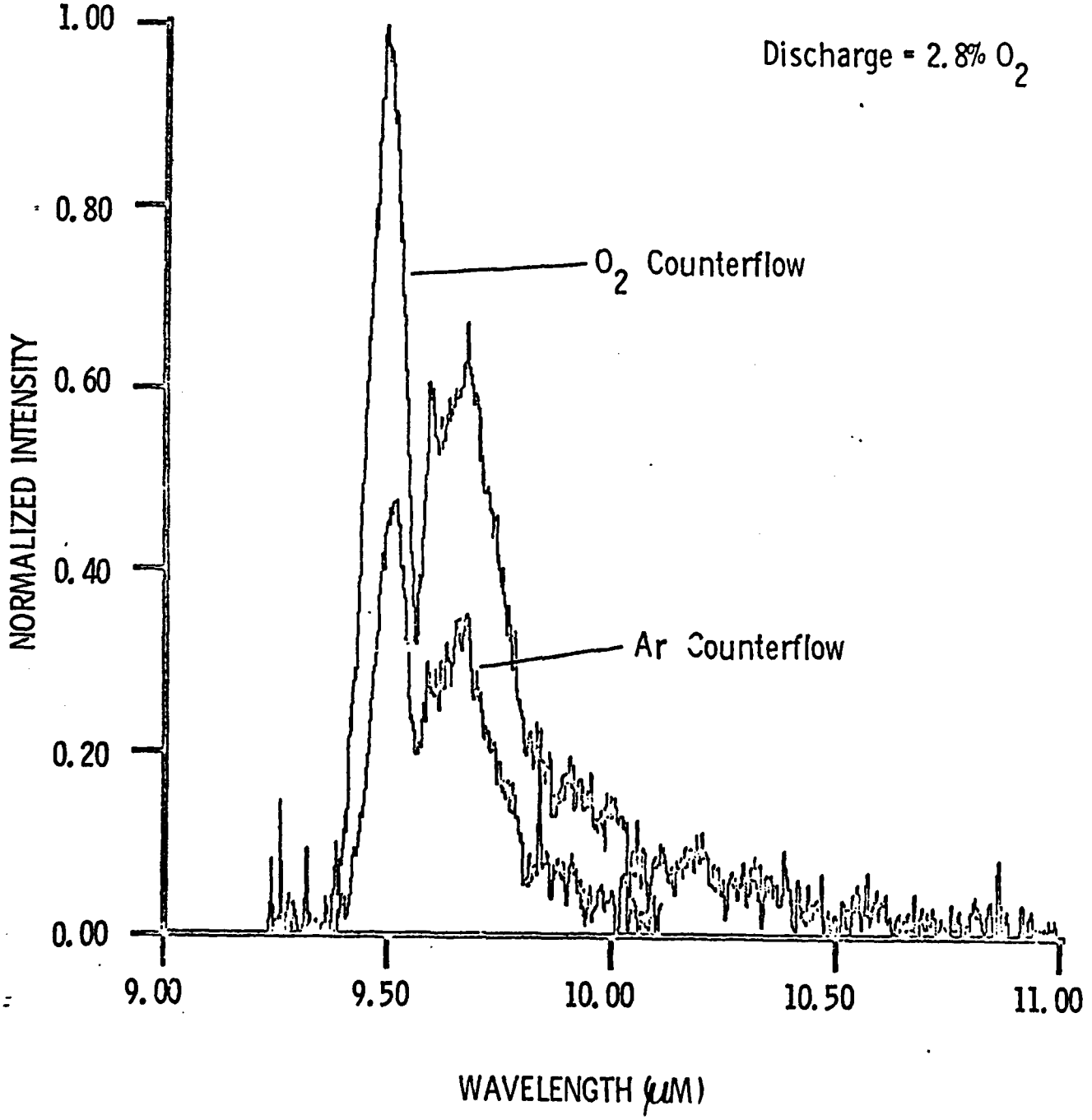

Fig. 13 Effect of Ar Counterflow.

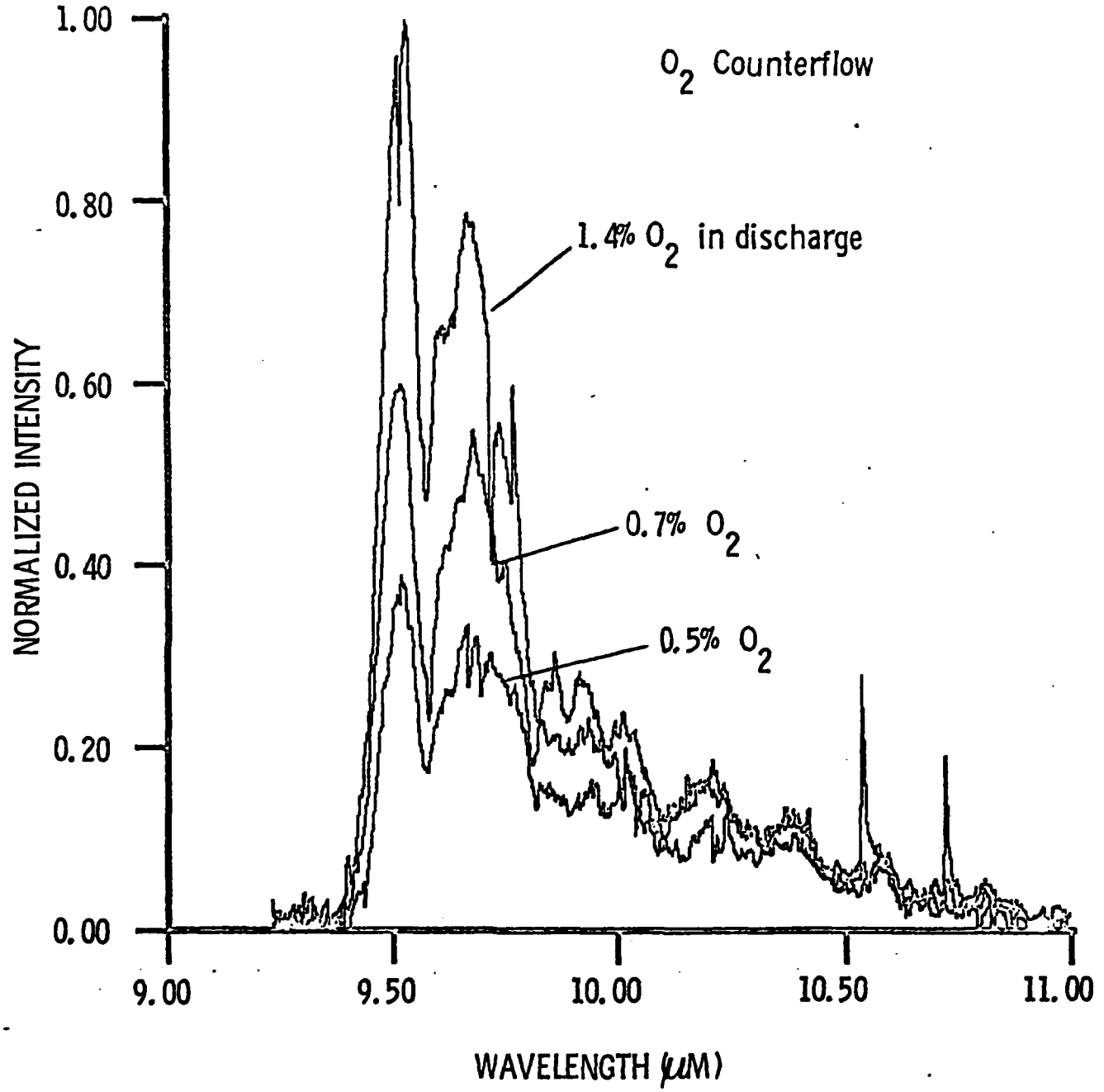

Fig. 14 Effect of O_2 Level in Discharge.

alternately less production of v = 1 relative to v > 1). However, the use of 73% O_2 in the discharge mixture gave rise to spectra with a distinct bimodal distribution as shown in Fig. 15. The cause of the spectral distribution shown in Fig. 15 is not yet understood, but may be related to pumping of the higher vibrational levels by collisions between O_3 and excited O_2 in the discharge region. Finally, it was found that the observed spectral intensity displayed a strong inverse temperature dependence for discharge region temperatures of 80 - 120 K (see Fig. 16); the observed temperature dependence of the intensity was found to scale directly with the exp (510/T) dependence reported for the three-body recombination rate constant.[49] While this observation suggests that the overall three-body process is the major route for the production of O_3 (v'), it does not necessarily mean that the entire process occurs within the discharge region. In any event, it is clear from the above discussion that a more rigorous kinetic and spectral analysis is required before any definitive conclusions can be made regarding the mechanism for the production of the observed radiation.

To this end, a code has been initiated for least squares analysis of the O_3 spectral data using theoretically computed spectra in a method analogous to that used for NO. Since relatively little spectroscopic data exists for high vibrational levels of the ν_3 band, some simplifying assumptions were used in order to provide an estimate of the contributions from the higher levels. The rotational line positions and line strengths for the 001 → 000 transitions were obtained from the AFGL absorption line parameters compilation,[50] which contains an extrapolated version of the results of Clough and Kneizys.[51] More recent rotational analyses of the 000 → 001 transition give line frequencies[52,53] and line strengths[53] in reasonable agreement with the results of Ref. 51. The band centers of the $\Delta v = 1$ transitions from higher vibrational levels of the ν_3 mode were calculated from the formula[54]

$$\omega_o\ (v' \rightarrow v' - 1) = \nu_{01} + 2(v' - 1)\ x_{33} \qquad (38)$$

where v' is the vibrational quantum number (ν_3 mode) of the emitting state, ν_{01} is the band center of the 001 → 000 transition, and x_{33} is the first-order

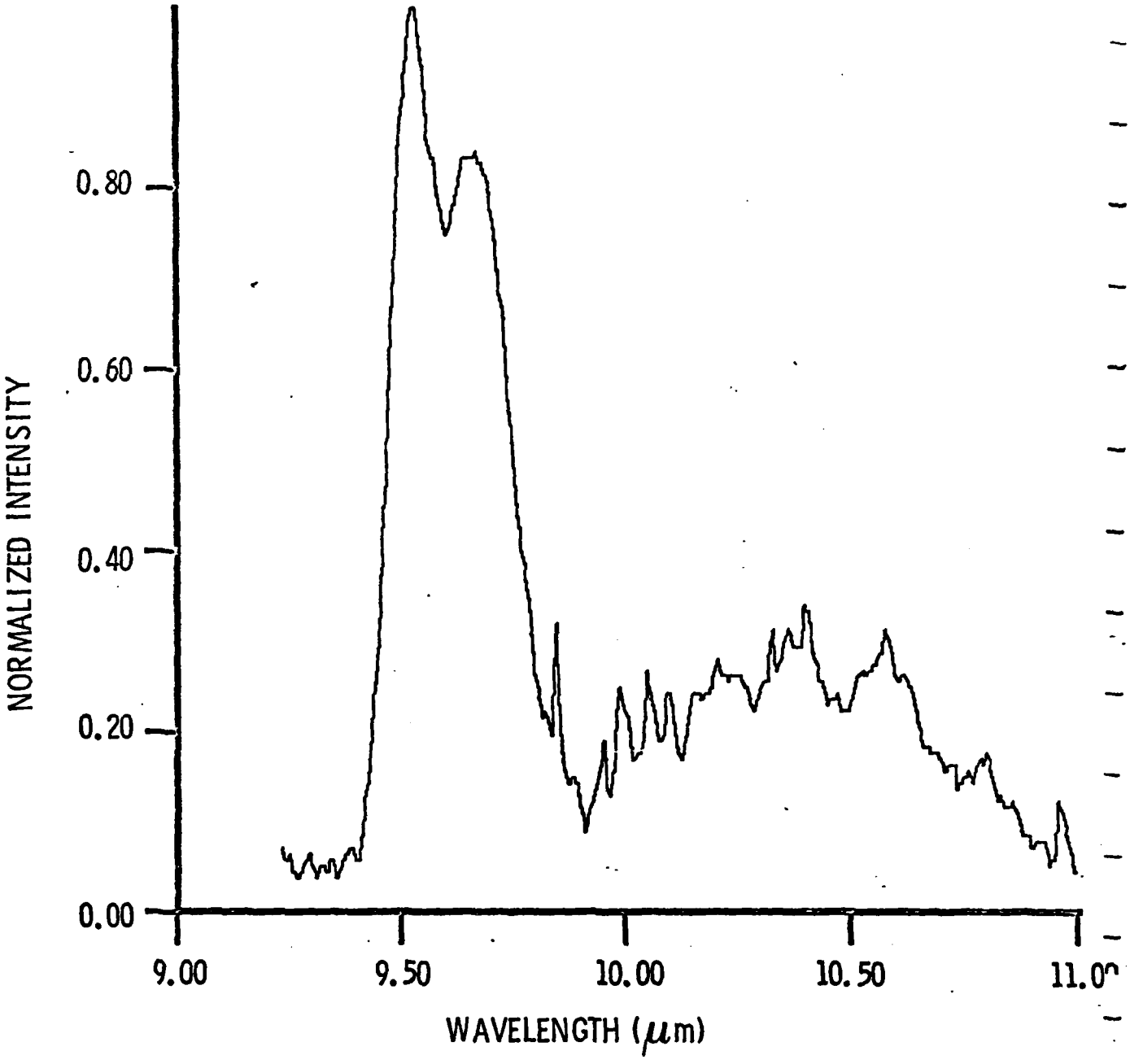

Fig. 15 Observed O_3 spectrum for O_2-rich discharge mixture. Experiment 138001, 3 mm slits, 3 mt He background. Discharge: 73% O_2/Ar; Counterflow: O_2.

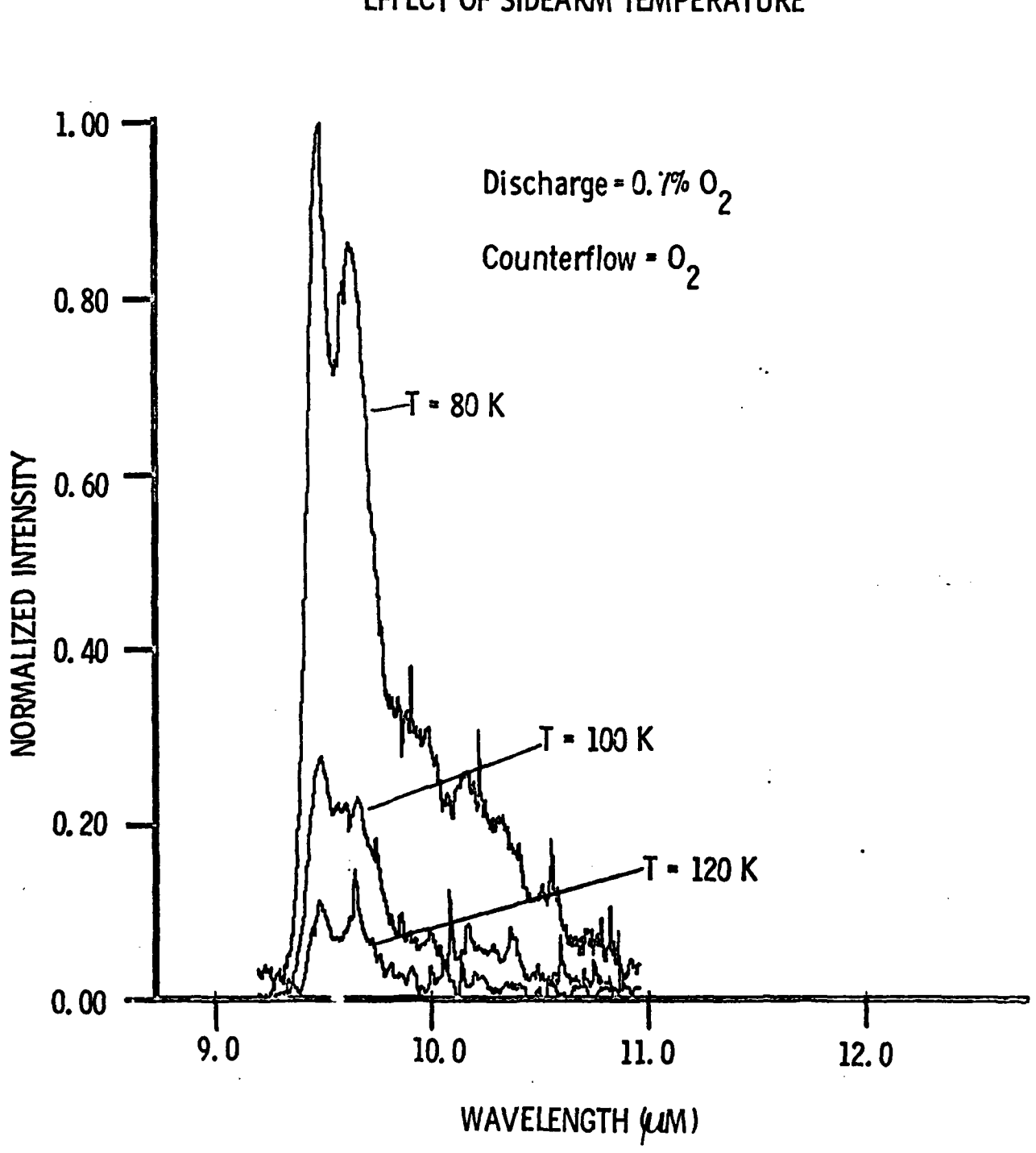

Fig. 16 Effect of Gas Temperature on Observed O_3 Spectrum.

anharmonicity constant. The value of ν_{01} is well known[50-55] to be ν_{01} = 1042.1 cm^{-1}. Values of x_{33} in the literature are -15 cm^{-1} [54] and -12.3 cm^{-1};[55] since the measurements of Ref. 55 extended to v' = 4, the latter value of x_{33} was used in the initial calculations. The rotational spacings and relative line strengths obtained from Ref. 50 for the 001 → 000 transition were assumed to hold for all higher v', thus neglecting the effects of vibration-rotation interactions. The band Einstein coefficients were estimated from the scaling law

$$A_{v'\rightarrow v'-1} = v' A_{10} \left(\frac{\nu_{v'\rightarrow v'-1}}{\nu_{10}} \right)^3 \qquad (39)$$

where the Einstein coefficient of the 001 → 000 band is, from the data of Ref. 50, A_{10} = 10.6 s^{-1}. The contribution to the total spectral intensity due to each v' → v' - 1 transition was then given by

$$I_{v'v'-1}(\nu) \propto hc\nu N_{v'} A_{v'\rightarrow v'-1} . \qquad (40)$$

The sum of the spectrally resolved contribution of all vibrational levels was matched to each observed spectrum by use of the least squares method previously applied to the NO data.

The computed fit to the spectrum of Fig. 12 is shown, compared to the data, in Fig. 17; the contributions to the computed spectrum by the transitions from different vibrational levels are shown, compared to the overall synthetic spectrum, in Fig. 18. The corresponding derived population distribution is plotted in Fig. 19. Contributions to the observed spectral intensity can be identified for vibrational levels up to v' = 6; it can be seen from Fig. 17 that the anharmonicity constant of Ref. 55 appears to be incorrect for high v'. Further analysis using the x_{33} value of Ref. 54 yields a similar result. Indeed, it may be necessary to use higher order corrections in order to more accurately match the positions of the features observed at higher v'.

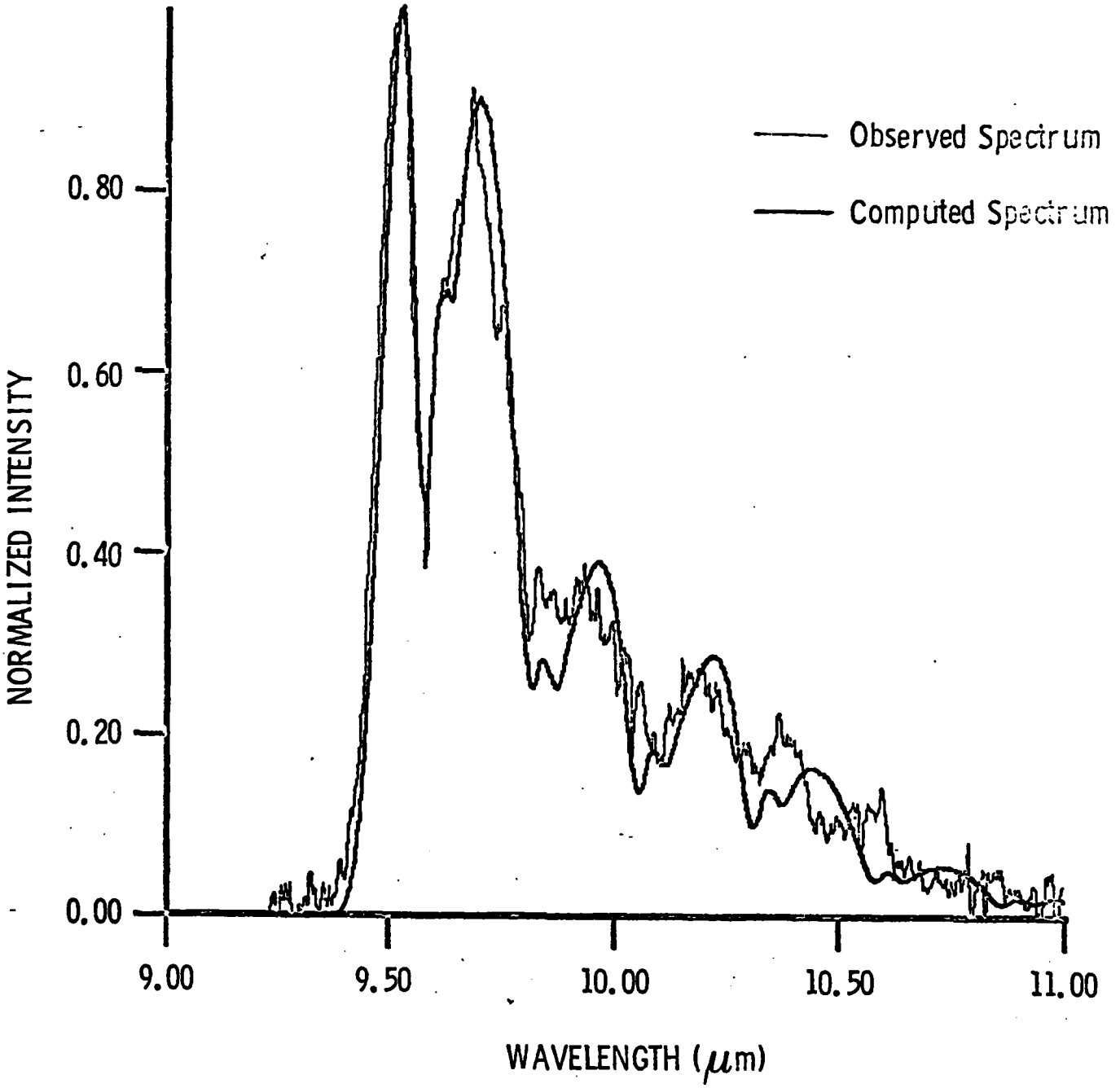

Fig. 17 Comparison of computed and observed spectra, Experiment 107016. In the computed spectrum, the rotational temperature is 90 K and the resolution is 0.04 μm. The standard deviation of the least squares fit is 0.051.

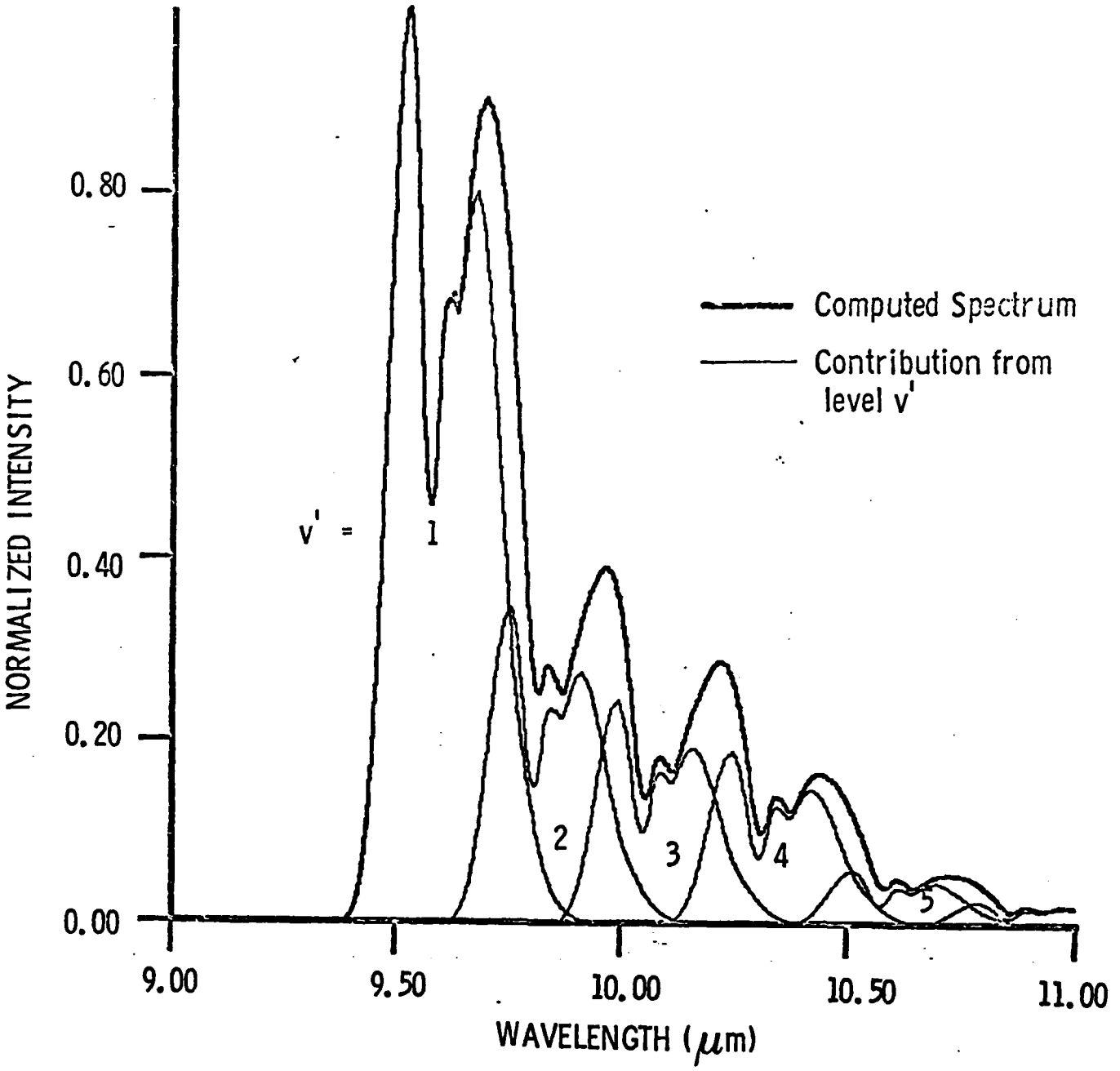

Fig. 18 Contributions of Vibrational Basis Sets to Overall Computed O_3 Spectrum of Fig. 17.

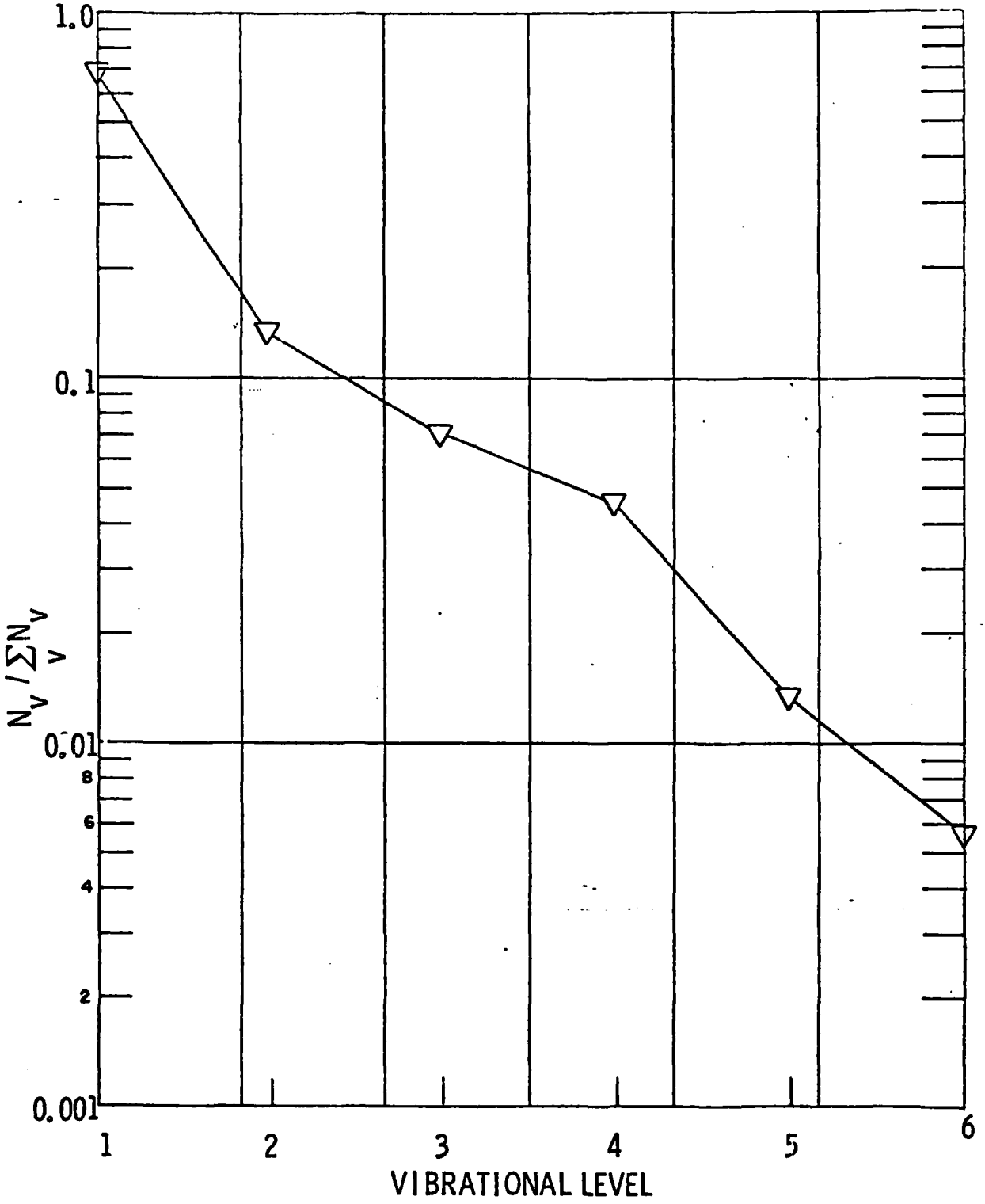

Fig. 19 Relative Vibrational Populations for the O_3 ν_3 Mode, Derived for Experiment 107016 from the Least Squares Fit Shown in Fig. 17.

A more sophisticated spectral analysis would include contributions from difference bands of the type $\nu_i + \nu_k - \nu_i$, where $\Delta v_3 = 1$ and the ν_1 and/or ν_2 modes are also excited. However, in view of the lack of spectroscopic information on these transitions and the extreme difficulty of resolving the extensively overlapped bands, such a detailed treatment is not feasible for the present data. Some preliminary spectral fits, in which only the difference bands (101) → (100) and (011) → (010) are included[50] with the ($00v_3$) sequence, give an improved spectral match to the data in the 9.7 - 10.0 μm region. The populations derived from these fits suggest that the (101) state is significantly populated while the (011) state is not; however, this deduction is clouded by the uncertainty in x_{33}, which introduces uncertainty into the degree of overlap between the (011) and (002) transitions. Clearly, direct spectral measurements of the $\nu_1 + \nu_3$ summation band at 4.7 μm would greatly elucidate the analysis of the ν_3 spectra reported here.

Due to the assumptions which had to be made in order to carry out these calculations, the relative populations reported here cannot be expected to represent ground truth, but they can be used to identify trends induced by changing experimental conditions. For example, the trends in spectral distribution with different O_2/Ar discharge mixtures described above are reflected in the derived population distributions as shown in Figs. 20 and 21. Figure 20 exhibits the effects on the derived relative populations resulting from variation of the O_2 fraction by over an order of magnitude in O_2 - lean discharge mixtures; the enhancement of the relative populations of the higher levels with decreasing O_2 fraction is clearly indicated. The derived relative populations for an experiment using an O_2 - rich discharge mixture are shown in Fig. 21; the bimodal nature of this distribution is characteristic of those obtained from complicated chemical mechanisms. In general, the distributions shown here exhibit an average excitation of ~1.6 quanta in the ν_3 mode; this is similar to that given by a vibrational temperature of 1200 - 2000 K.

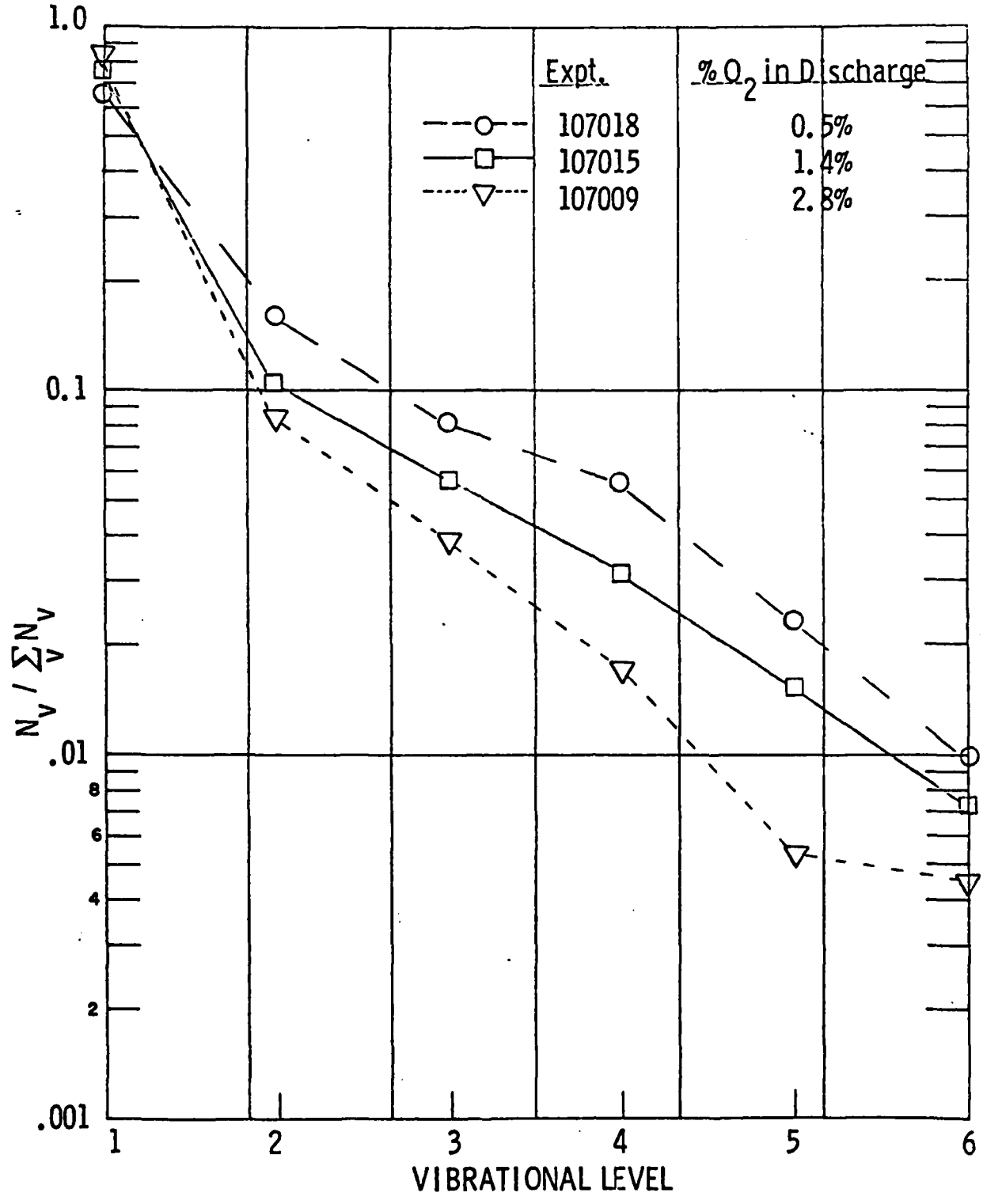

Fig. 20 Effect of Fraction of O_2 in O_2/Ar Discharge Mixture Upon Derived O_2 Population Distributions.

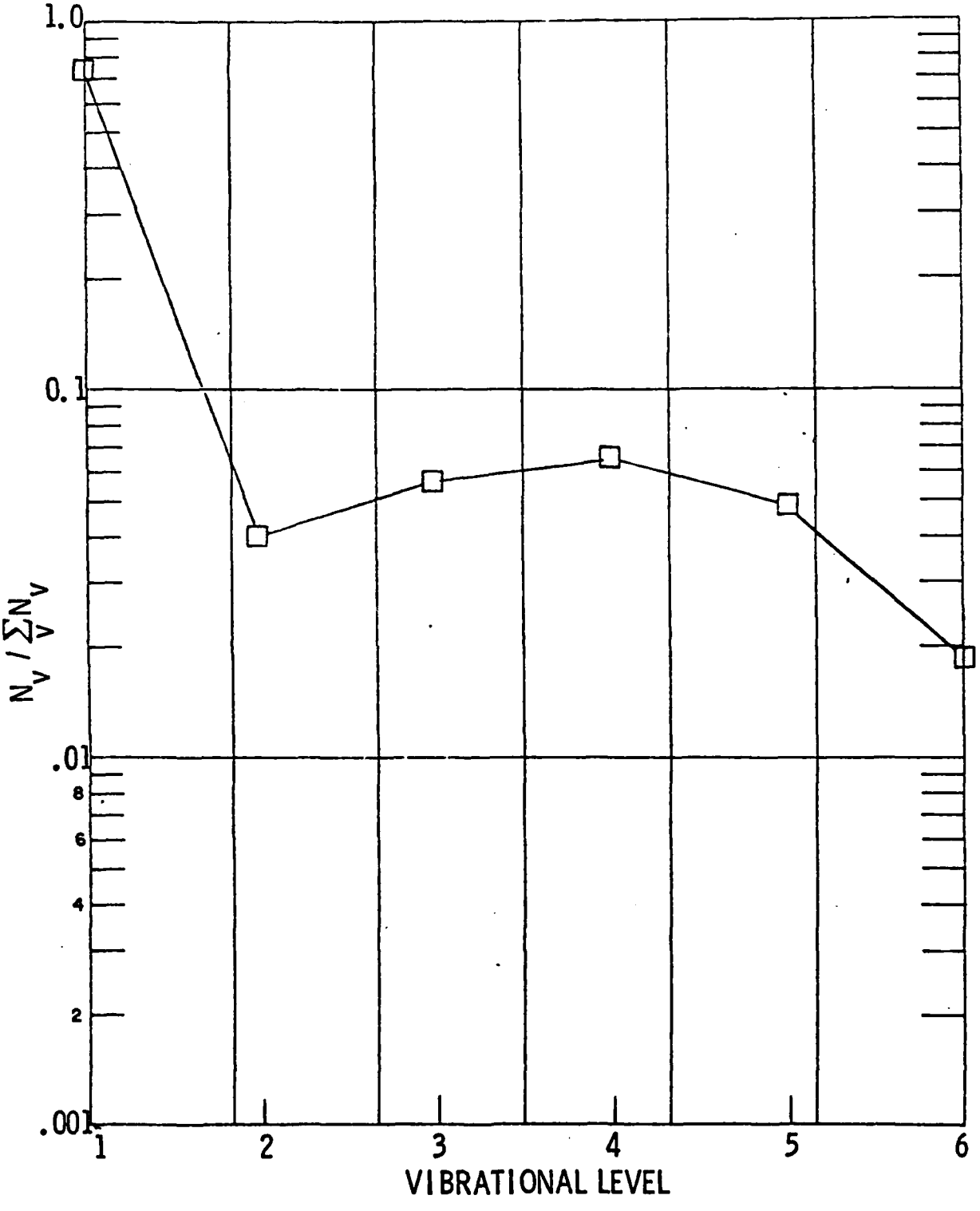

Fig. 21 Derived Population Distribution for O_2-rich Discharge Mixture (Experiment 138001).

The spectral calculations presented here were performed assuming rotational temperatures of 90 K and using the nominal instrument resolution; as such, they represent only first-generation efforts. The temperatures and resolutions need to be optimized and sensitivity calculations need to be carried out in order to determine the "noise level" of the results. Further work on all phases of the O_3 data analysis is required.

III. COCHISE DIAGNOSTIC STUDIES

As was pointed out in Section II certain improvements or adaptations to the COCHISE system would be useful in providing a more detailed examination of the NO chemiluminescence reaction, reaction (3). These include the development of a diagnostic for measuring the absolute concentrations of metastable nitrogen atoms within the reaction zone and the development of an absolute intensity calibration for the system. Preliminary efforts have been directed towards the completion of these goals and these are described below.

A. COCHISE Resonance Absorption Diagnostic

The immediate purpose of a vacuum-ultraviolet (VUV) resonance absorption diagnostic for the COCHISE apparatus is to measure the absolute concentrations of $N(^2D)$ and $N(^2P)$ in the reaction zone in order to relate those quantities to the NO infrared chemiluminescence observed in the reaction of active nitrogen with oxygen. The establishment of a working diagnostic for these species may allow longer range development of similar diagnostics for other atomic species such as $N(^4S)$, $O(^3P)$, and $H(^2S)$.

It is well-known that the metastable species $N(^2D)$ and $N(^2P)$ can be detected by absorption in their resonance multiplets at 149 nm and 174 nm, respectively.[17,21] The purpose of this section is to outline the means by which this method can be applied to the COCHISE experiment. In the following pages, a general design of a proposed optical system will be presented, the resonance absorption method will be briefly reviewed, and the feasibility of this application will be examined. Finally, techniques for examining the spectral and line shape characteristics of the resonance line source will be discussed.

The most desirable diagnostic configuration for COCHISE is one which does not compromise the infrared detection system, yet which symmetrically samples through the center of the reaction zone. These criteria are met by

the arrangement shown in Fig. 22. Radiation from a resonance line source mounted on the infrared (IR) mirror flange is directed through the reaction cell, reflected from a plane MgF_2 - coated mirror mounted on the IR lens baffle, and viewed by a photomultiplier (PM) tube at the mirror flange. Baffle arrangements on the line source and PM detector would be used to eliminate the effects of scattered light. The 149 and 174 nm resonance multiplets would be separated by means of a rotating filter wheel in front of the photomultiplier tube, using filter materials selected according to their low wavelength cutoffs at 100 K.[56] The $N(^2P)$ 174 nm multiplet would be selected by a suprasil cutoff window while the $N(^2D)$ 149 nm multiplet would be isolated from the 174 nm lines and from the OI 130 nm triplet (which may be produced by the line source) using a special dielectric stack coating upon a high-grade quartz, sapphire, or BaF_2 substrate. The use of such filters eliminates the need for a monochromator. The line source will be either a simple flow system or a sealed, gettered bulb in which the NI resonance radiation is excited by microwave or radio frequency discharge of 1 - 5 torr of He or Ar containing trace amounts of N_2.[17] A MgF_2 window can be used to isolate the line source gas from the reaction cell.

The 149 nm and 174 nm radiation emanating from the source lamp will be absorbed by $N(^2D)$ and $N(^2P)$, respectively, in the reaction zone. Over the range of conditions encountered in COCHISE, the absorption line shapes will be virtually entirely determined by Doppler broadening. For a single resonance line with frequency ν_0 and absorber optical depth $k_o\ell$ (absorption coefficient k_o and path length ℓ), the fractional absorption of resonance radiation is given by[57]

$$A = \frac{\int_{-\infty}^{\infty} f(\omega)\left(1 - e^{-k_o \ell e^{-\omega^2}}\right) d\omega}{\int_{-\infty}^{\infty} f(\omega)\, d\omega} \qquad (41)$$

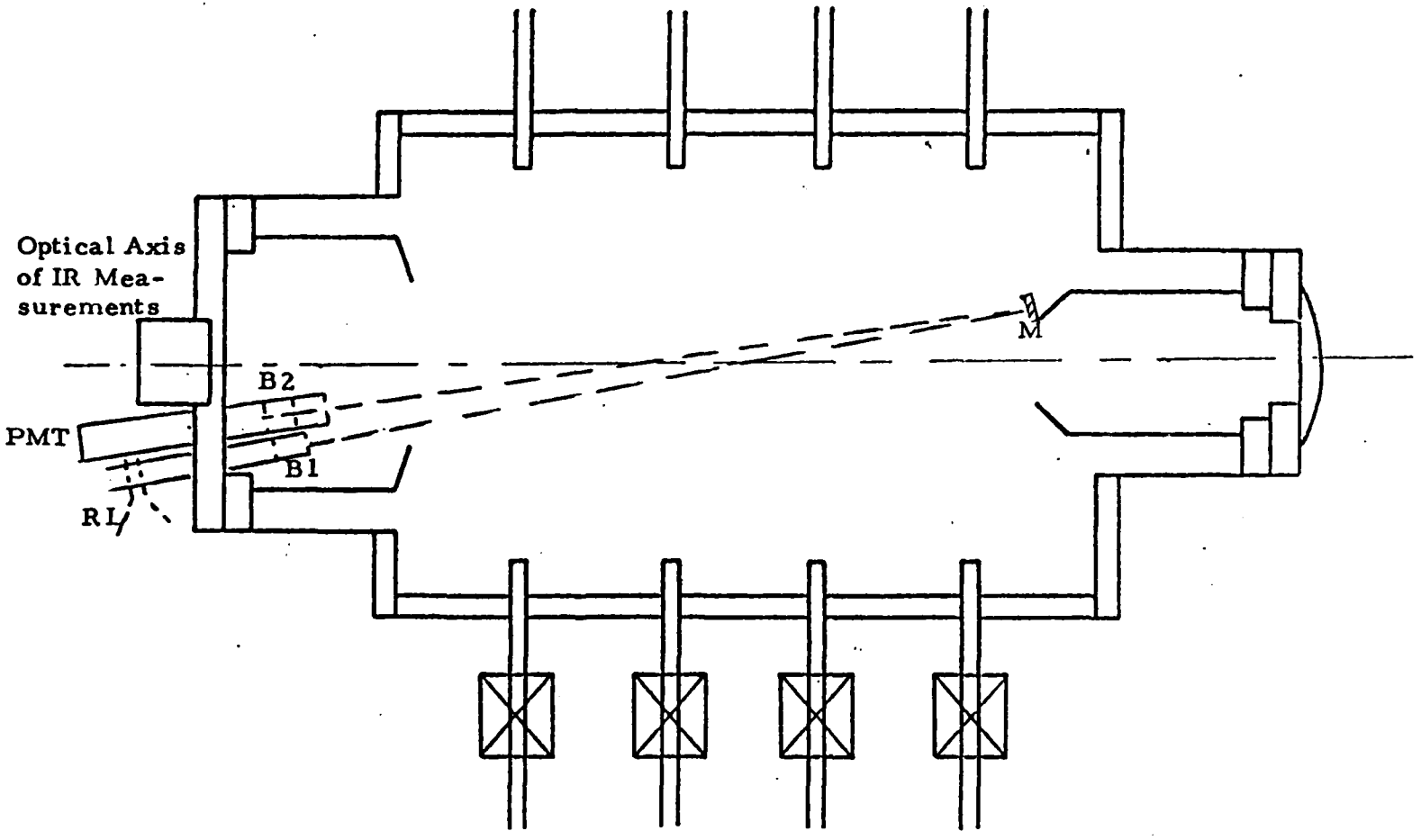

Fig. 22 Diagram of proposed optical system for resonance absorption diagnostic. M = MgF_2-coated mirror, B1 and B2 = baffles, PMT = photomultiplier tube, RL = discharge resonance lamp.

where $\omega = 2(\ln 2)^{1/2} (\nu - \nu_0)/\Delta\nu_D$, $\Delta\nu_D = 2(2R \ln 2)^{1/2} \nu_0/c(T_A/M)^{1/2}$, $\Delta\nu_D$ is the Doppler width of the absorption line in sec^{-1}, R is the gas constant, c is the speed of light, M is the molecular weight, and T_A is the kinetic temperature of the absorbing species. The function $f(\omega)$ describes the shape of the resonance line emitted by the source. It has been shown that $f(\omega)$ can be affected by self-absorption in the source[58] and/or by excitation processes in the discharge plasma;[59] these effects can be experimentally tested as discussed at the end of this section. For the purposes of the following discussion, it will be assumed that $f(\omega)$ is affected only by Doppler broadening corresponding to a source kinetic temperature T_E:

$$f(\omega) \propto e^{-(\omega/\alpha)^2} \tag{42}$$

where $\alpha = (T_E/T_A)^{1/2}$. Substitution of Eq. (42) into Eq. (41) and integration gives

$$A_\alpha = \sum_{n=1}^{\infty} (-1)^{n-1} \frac{(k_o \ell)^n}{n!(1 + n\alpha^2)^{1/2}} \tag{43}$$

or for small $k_o \ell$,

$$A_\alpha \cong \frac{k_o \ell}{(1 + \alpha^2)^{1/2}} \tag{44}$$

For the NI 149 nm and 174 nm multiplets at $T_E \approx T_A = 100$ K, overlap of the lines is negligible and the absorption in the unresolved multiplet is simply the weighted sum of absorptions in each line:

$$A_{TOT} = \frac{\sum_i C_i A_\alpha (k_{oi} \ell)}{\sum_i C_i} \qquad (45)$$

where the C_i are the relative source emission intensities of each line and the k_{oi} are the absorption coefficients of each line.

The spectroscopic properties of the $N(^2D)$ and $N(^2P)$ resonance multiplets are given in Tables II and III, respectively. The lower state for each transition is actually a multiplet, where the $^2D_{5/2}$ and $^2D_{3/2}$ states are separated by 9.2 cm^{-1} and the $^2P_{1/2}$ and $^2P_{3/2}$ states are separated by 0.25 cm^{-1}. The lower state degeneracy g_L is given by $g_L = (2J + 1)$ and the relative intensities I are given by L - S sum rules.[17] Values of the absorption oscillator strength f_{LU} are obtained from radiative lifetime measurements.[60] The oscillator strength is related to the absorption coefficient by:

$$f_{LU} = \left(\frac{\pi}{4 \ln 2}\right)^{1/2} \frac{mc}{\pi e^2} \Delta\nu_D \frac{k_o}{N_L} \qquad (46)$$

where m and e are the electronic mass and charge, respectively, and N_L is the number density of atoms in the lower state of the transition. Thus the relative k_{oi} values within each multiplet are determined by ratios of $f_{LU}N_L$, where $N_L = g_L e^{-\Delta E_L/kT} / \sum_i g_{Li} e^{-\Delta E_{Li}/kT}$. From combining Eqs. (44), (45), and (46) using the values of Tables II and III for T_A = 100 K and ℓ = 110 cm, $[N(^2D)]_{TOT} = (5.81 \times 10^{10}\ cm^{-3})A_{TOT}$ and $[N(^2P)]_{TOT} = (7.00 \times 10^{10}\ cm^{-3})A_{TOT}$ for $\alpha^2 = 1$ (i.e., for $T_E \approx T_A = 100$ K), or $[N(^2D)]_{TOT} = (7.12 \times 10^{10}\ cm^{-3})A_{TOT}$ and $[N(^2P)]_{TOT} = (8.57 \times 10^{10}\ cm^{-3})A_{TOT}$ for $\alpha^2 = 2$ (i.e., T_E = 200 K, T_A = 100 K). If a minimum fractional absorption of $A_{TOT} = 0.005$ can be detected, the lower detection limit for $N(^2D, {}^2P)$ will be (3 - 4) x 10^8 cm^{-3}. This concentration is near that expected for $N(^2P)$, and is roughly an order of magnitude lower than that expected for $N(^2D)$ (see Section II).

TABLE II

$N(^2D)$ RESONANCE LINES[a]

Wavelength, nm	Upper State	Lower State	g_L	Relative Intensity	f_{LU}[b]
149.2615	$^2P_{3/2}$	$^2D^o_{5/2}$	6	9	0.078
149.2812	$^2P_{3/2}$	$^2D^o_{3/2}$	4	1	0.013
149.4668	$^2P_{1/2}$	$^2D^o_{3/2}$	4	5	0.065

[a]Ref. 17

[b]Ref. 60

TABLE III

$N(^2P)$ RESONANCE LINES[a]

Wavelength, nm	Upper State	Lower State	g_L	Relative Intensity	f_{LU}[b]
174.2717	$^2P_{3/2}$	$^2P^o_{1/2}$	2	1	0.021
174.2725	$^2P_{3/2}$	$^2P^o_{3/2}$	4	5	0.053
174.5246	$^2P_{1/2}$	$^2P^o_{1/2}$	2	2	0.043
174.5255	$^2P_{1/2}$	$^2P^o_{3/2}$	4	1	0.011

[a]Ref. 17

[b]Ref. 60

There can also be some signal attenuation due to absorption by O_2 in the dissociative Schumann-Runge continuum. The O_2 absorption cross-section is 1.24×10^{-17} cm^2 and 2×10^{-19} cm^2 at 149 nm and 174 nm, respectively,[61] corresponding to Beer's-law absorption of 0.38 and 0.006 at the two wavelengths for an O_2 concentration of 2×10^{14} cm^{-3}. While the $N(^2D, ^2P)$ measurements must be corrected for this attenuation, the effect can be turned to advantage as a diagnostic for O_2.

For the optical system shown in Fig. 22, the number of photons/sec impinging on the PM photocathode is $I_o TA_c/x^2$, where I_o is the number of photons/sr-sec emitted by the source in a given resonance multiplet, T is the net fractional transmission of the lamp window, mirror, and filter, A_c is the area of cathode, and x is the total optical path length. Past experience with similar microwave-powered line sources has shown that emission intensities of $\sim 10^{13}$ photons/sr-sec can be readily attained for each NI multiplet.[59] For this radiant intensity, $T \sim 0.1$, $A_c \sim 0.5$ cm^2, and x = 155 cm, conditions appropriate to the COCHISE facility, approximately 2×10^7 photons/sec will be intercepted by the photocathode. For a photomultiplier tube with a quantum efficiency of 10% and a gain of 10^6, the resulting current will be $\sim 3 \times 10^{-7}$ Amp, which is at least four orders of magnitude above the probable dark current of the tube. Because of the short radiative lifetime of the emission, background radiation from the reaction zone due to atoms excited in the system discharges will be negligibly small.

These absorption measurements can be made with the reaction cell discharges in either the cw or pulsed mode. In the cw mode, the O_2 and $N(^2D, ^2P)$ absorption should each be measured in the absence of the other absorbing species. However, in the pulsed mode, the fractional intensity absorbed by $N(^2D, ^2P)$ is directly obtained even in the presence of O_2. Since the absorbed intensity is determined in volts as the rms value of a pulsed signal and the unabsorbed lamp intensity is a cw current measurement, their ratio (i.e., A_{TOT}) cannot be determined without making assumptions about the signal waveform. For this reason, it may be desirable to measure the unabsorbed lamp intensity in the pulsed mode using a mechanical chopper operating at the same frequency as the atom modulation. In normal practice, measurements of the concentrations of $N(^2D, ^2P)$ and O_2 need only be made when flow or pressure conditions are altered, so that the VUV and IR observations can be made separately.

The performance of the resonance lamp can be optimized and characterized in separate observations not involving the COCHISE facility. By observing the lamp emission with a VUV monochromator, flow and discharge conditions can be adjusted to maximize the intensity of the NI lines, minimize the intensities of impurity lines which could interfere with the measurements, and minimize the self-absorption in the NI multiplets (indicated by deviations of intensity ratios within the multiplet from the values in Tables II and III).

The possibility of non-thermal broadening of the emission lines can be tested by making absorption measurements of $N(^2D)$ produced in a discharge-flow apparatus similar to that of Lin and Kaufman.[17] One method is to vary the temperature of the lamp body while measuring a given concentration of $N(^2D)$ and compare the results to predictions of models based on Eqs. (41) - (45). Another method is to kinetically remove $N(^2D)$ in the flow tube by titration with a fast reactant under second-order conditions, as was done for $N(^4S)$ in Refs. 17 and 59; however, the kinetic analysis required for such a titration is complicated by the very fast first-order removal at the flow tube wall which is the dominant $N(^2D)$ loss process.

B. COCHISE Optics And Observed Intensities

The observed infrared chemiluminescence signals can be related to absolute intensities and average species concentrations in the field-of-view of the detector by means of blackbody calibrations and knowledge of the collection efficiency of the optical system for all radiation within the field-of-view. The purpose of the following discussion is to show the relationships between blackbody and chemiluminescence intensities, to examine the method of determining the intensity of the blackbody radiation, to discuss methods for determining the overall detector collection efficiency and field-of-view, and finally to provide estimates for the observed chemiluminescence intensity.

1. Method of Calibration

As pointed out in Section II a blackbody source is built into one end of the COCHISE reaction cell. The spectral radiance in watts cm^{-2} sr^{-1}

μm^{-1}, N_λ, emitted by the blackbody is given by $N_\lambda = 11909\ \lambda^{-5}\ [\exp(14388/\lambda T) - 1]^{-1}$ where λ is the wavelength in μm. The observed detector signal, S_B volts, corresponds to a detected power density of $(4\pi N_\lambda\ A_B\ \varepsilon_B\ T_\lambda)$ watts μm^{-1}, where A_B is the area of the blackbody, ε_B is the fractional collection efficiency of the optical system for radiation from the blackbody, and T_λ is the overall transmission of the optical system. Similarly, the infrared chemiluminescence signal S_c in volts corresponds to a detected power density of $(4\pi\ I_\lambda\ A_c\ \varepsilon_c\ T_\lambda)$ watts μm^{-1}, where ε_c is the effective collection efficiency of the optical system for radiation in the field-of-view, A_c is the effective cross-sectional area of the viewing region, and I_λ is the spectral radiance in watts $cm^{-2}\ sr^{-1}\ \mu m^{-1}$ (here, the viewing region is approximated to be cylindrically symmetric about the optical axis, with a uniform distribution of emitters throughout the emitting volume. The details of the actual field-of-view will be examined in Section 3). The quantity I_λ is then given by $I_\lambda = S_c/F_\lambda$ where the calibration factor F_λ is

$$F_\lambda = \frac{S_B}{(A_B/A_c)(\varepsilon_B/\varepsilon_c)N_\lambda} = \frac{S_B}{C\ N_\lambda} \qquad (47)$$

Experimentally, $S_B(\lambda)$ is measured for a given blackbody temperature. That temperature is used to determine N_λ and the value of the constant C is obtained by characterization of the optical geometry; these values are then used to compute F_λ from Eq. (47). Note that the optical transmission T_λ cancels out in Eq. (47) because it is present in both the blackbody and the chemiluminescence measurements.

The quantity F_λ can be used to convert the observed chemiluminescence signal into the spectral radiance I_λ, which is directly related to the number density of the emitting species averaged over the field-of-view. In the following discussion, Section 2 deals with the determination of N_λ and ε_B, Section 3 discusses the dimensions of the viewing region and the determination of ε_c, and Section 4 shows how the characterization of the optical system is used to relate observed intensities to concentrations of NO in the viewing region.

2. Determination of Blackbody Parameters

The key to defining the absolute response of the COCHISE optical system is a blackbody calibration source imbedded in the end mirror of the reaction cell. During the course of the NO studies reported in Section II, this source was an Electro Optical Industries (EO) Model LT1521 blackbody with a factory-installed chromed-constantan thermocouple potted into the casing. Unfortunately, it has been found that the blackbody temperatures, as indicated by the thermocouple for given power settings, were considerably lower under COCHISE cryopumping conditions than under vented conditions, and a preliminary radiometric analysis of a somewhat limited data base indicated that the temperatures characteristic of the source radiation were consistent with the thermocouple readings. The purpose of this section is to: (a) describe further interpretation of a more extensive blackbody response data base developed to elucidate the appropriate blackbody source temperatures (b) present analysis of extra-COCHISE measurements designed to evaluate blackbody performance under a variety of conditions, and (c) detail the selection of an alternate blackbody source for future use.

The temperature-vs.-power characteristics observed for the EO blackbody under various conditions are shown in Fig. 23. The minor difference between the manufacturer's curve and the room-condition curve taken with the blackbody installed in COCHISE is probably the result of the additional voltage drop in the latter case resulting from the longer leads required to connect the blackbody to the power source. The 100 - 130^{o}K difference in apparent temperatures between the room-and cryopumped-condition measurements was eventually found to be due to a pressure effect, as will be described below. The COCHISE blackbody response data base was used to test these two "calibration" curves as follows. Ratios of the observed spectrally resolved radiative output of the blackbody for two power settings (in the COCHISE apparatus, this output can only be observed under cryopumping conditions) were compared to ratios predicted for those two settings from each temperature curve using the relationship

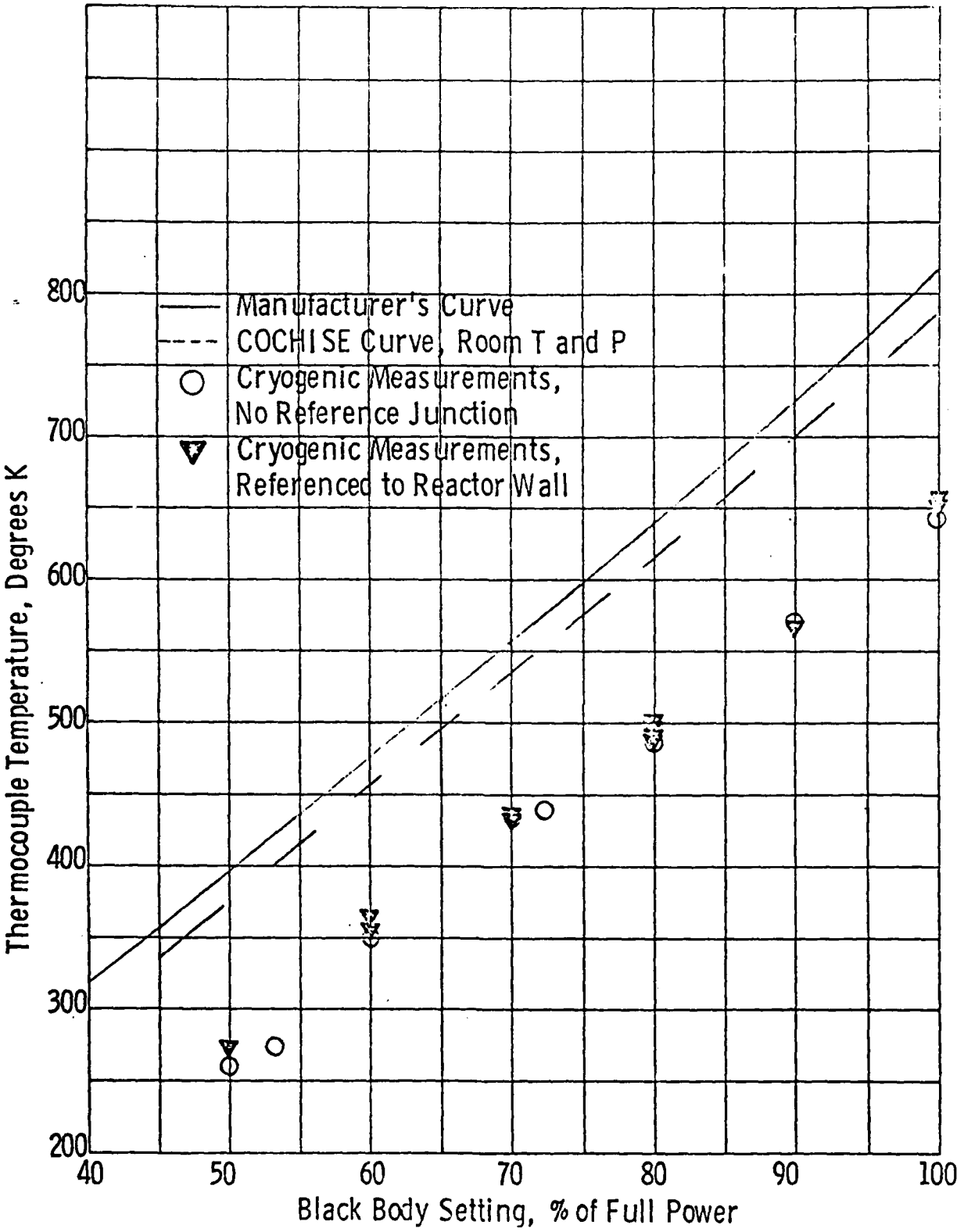

Fig. 23 Apparent Temperature - Power Characteristics of Electro-Optics Black Body Source as Determined by Thermocouple Measurements.

$$N_\lambda = 11909\lambda^{-5} \left[\exp\left(14388/\lambda T\right) - 1\right]^{-1} \qquad (48)$$

where N_λ is the spectral radiance of the blackbody in watts cm^{-2} sr^{-1} μm^{-1}, λ is the wavelength in μm, and T is the apparent temperature (obtained from the appropriate "calibration" curve) in K. This analysis was performed over the spectral range of 2 - 8 μm for nine different sets of blackbody spectra; although considerable scatter was found in the 2 - 4 μm region, all data obtained prior to 12-23-77 were clearly consistent with lower temperature values while all data obtained subsequent to that date (a date when the blackbody was temporarily removed from the apparatus for recalibration testing) were equally consistent with the upper of the two curves. These results suggested that the temperature of the blackbody components within the field-of-view of the detector was not uniform and that the relative contributions of the nonuniformities to the observed radiative output were very sensitive functions of the handling and/or orientation of the device.

The EO blackbody source was further tested through use of the FAKIR facility (see description in Section IV) so that the apparent temperature and spectrally resolved radiative output of the blackbody could be monitored as functions of pressure over the range 0 - 760 torr. Specifically, the blackbody was inserted into the quartz flow reactor via a vacuum feedthrough adapter, and the radiative output in the 2-4 μm region was observed through the reactor wall by a scanning monochromator equipped with a liquid nitrogen-cooled infrared detector. The pressure was varied by controlled addition of Ar to the static system. It was found that, as the pressure was increased from $<10^{-3}$ torr to 1 atm, the temperature indicated by the thermocouple reading for a given power setting varied smoothly from the value obtained in COCHISE under cryopumped conditions to the value obtained in COCHISE in room air, even though the power supplied to the cavity remained constant. The radiant intensity of the blackbody was found to behave in a similar manner. These observations, coupled with the COCHISE measurements, clearly demonstrated that the thermocouple was not in good mechanical contact with the radiating element, and that either or both components could give rise

to radiation within the field-of-view of the detector. On the basis of this interpretation, it was concluded that the EO blackbody device was inadequate as a calibration source for low pressure environments such as that used in the COCHISE facility.

Further analysis was carried out on similar tests conducted with an alternate blackbody source fabricated by AFGL/OPR personnel. This device, which has now been integrated into the COCHISE apparatus, consists of a 25W, 2kΩ, 1% resistive heater (Dale, 7243) with a flat-black-painted emitting surface; the temperature is monitored by a platinum resistance thermometer epoxied to the back of the heat sink. Pressure tests performed on the FAKIR facility established that the temperature probe was well coupled to the heating element.

The crucial test of the suitability of the alternate blackbody as a calibration source is to determine whether the wavelength and temperature dependence of its radiant intensity is the same as given by Eq. (48). It can be seen from Eq. (48) that, for the wavelengths and temperatures of interest, plots of $\ln (1/S_B\lambda^5)$ vs $1/T$ should give straight lines of slope $\lambda/14388$ if the observed relative emission intensity S_B is truly "black". Measurements of S_B vs. $1/T$, made on the FAKIR facility over the ranges 2.8 - 4.0 μm and 340-400 K, were analyzed to give the results plotted in Fig. 24. The points represent the experimental values; the solid lines indicate the behavior at each wavelength predicted from Eq. (48). It can be seen that, over the range of wavelength and temperature available in the FAKIR measurements, the emission intensity follows the Planck radiation law within the scatter of the data.

Additional measurements were made on the COCHISE facility over a larger range of wavelength (2-8 μm) and blackbody temperature (250-400K), with more precise regulation of the blackbody temperature ($\pm$ 0.3°K, as opposed to the $\pm$ 2°K uncertainty in the FAKIR results shown in Fig. 24. Preliminary analysis of these data provides further indication that the observed radiation follows the Planck formula.

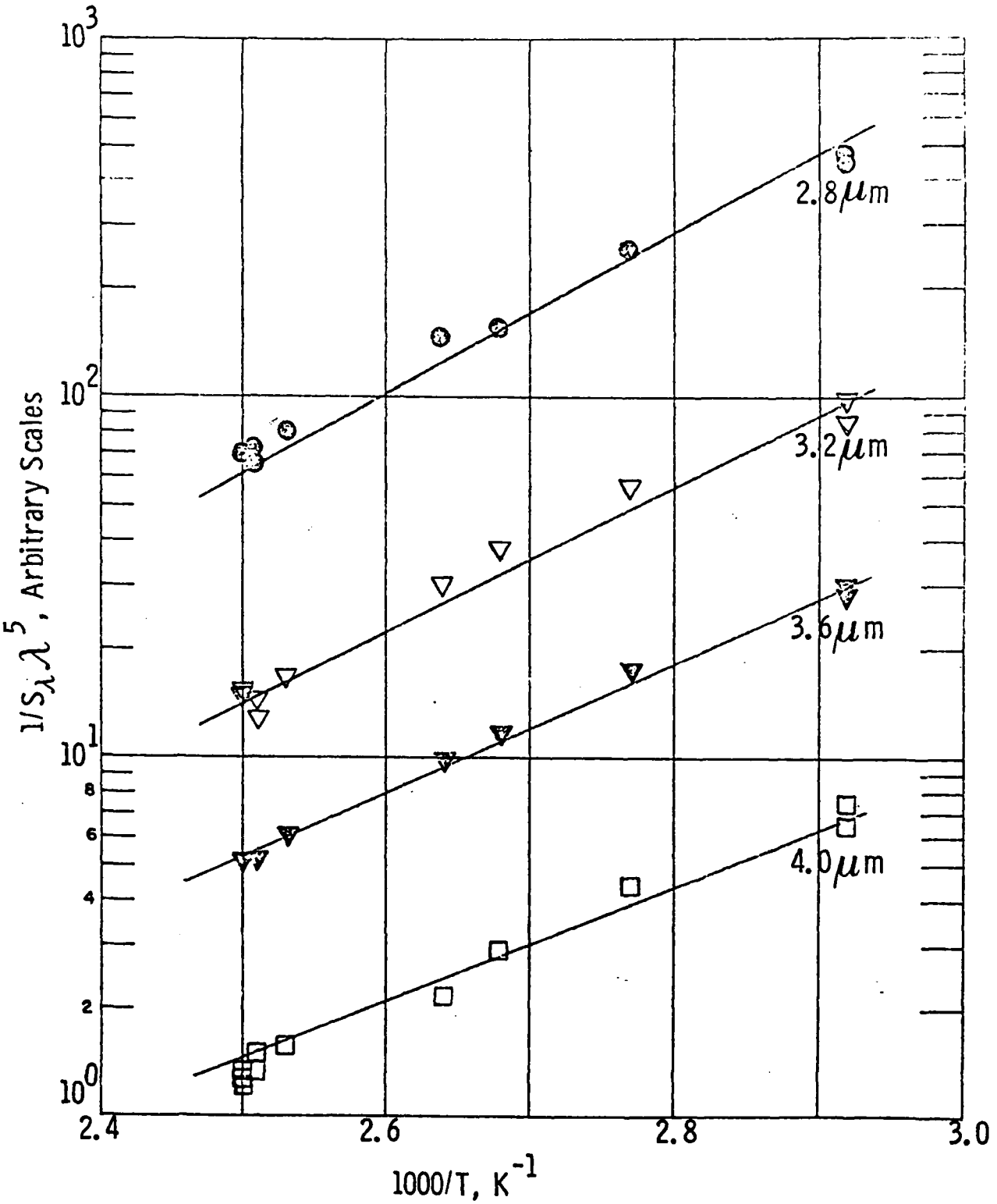

Fig. 24 Temperature Dependence of Emission from New Black Body Source as Observed on FAKIR Facility. The points are the experimental data; the slopes of the lines were computed for the indicated wavelengths from Eq.

In conclusion then, it appears that data taken to date in the COCHISE facility will exhibit an uncertainty in absolute intensity resulting from the inability to appropriately define the blackbody temperature. Future calibrations should be more reliable now that an improved blackbody source has been inserted into the system. The NO fundamental band discussed in Section II was taken prior to 1978, and thus, it has been assumed that the thermocouple temperature should be used in evaluating Eq. (48). The remainder of this discussion will be specific to the Electro Optical Industries blackbody with thermocouple definition of temperature.

The collection efficiency of the optical system for radiation from the blackbody can be determined by consideration of the COCHISE optical system diagrammed in Fig. 25. The blackbody, which is embedded in an aluminum mirror, is located beyond the focal point of the lens at a distance x_{oB} from the center of the lens. The radius of the blackbody aperture, R_{oB} (0.1 cm) is sufficiently small so that the extreme rays emerging from the lens underfill the window aperture (which is equal to that of the lens), overfill the entrance slit (2 cm tall) of the monochromator, underfill the grating (6 cm x 6 cm, here represented schematically for what is actually an f/6.9 Czerny-Turner mount of 50 cm focal length), and converge to an image of radius R_{iB} at a distance x_{iB} from the center of the lens. The net collection efficiency of the system is then the product of collection efficiencies of the lens for blackbody radiation and of the slit for light passing through the lens. (The detector is designed with a parabolic reflector so as to have unit collection efficiency for light collected by the lens-monochromator system.) The blackbody collection efficiency of the lens of radius R_L is approximately $(R_L/2\ x_{oB})^2 = 4.1 \times 10^{-4}$ for $R_L = 3.8$ cm and $x_{oB} = 94.4$ cm. The slit efficiency is given by the ratio of the slit area to the area illuminated in the plane of the slit. The radius of the illuminated region was determined from geometrical optics to be 3.3 cm (for a lens focal length of 1.2 cm and a distance of 43.2 cm from the lens to the 2 cm tall slit), so the slit efficiency is $(5.9 \times 10^{-3})W_B$ where W_B is the slit width in mm. The overall collection efficiency is then $\epsilon_B = (2.4 \times 10^{-6})W_B$.

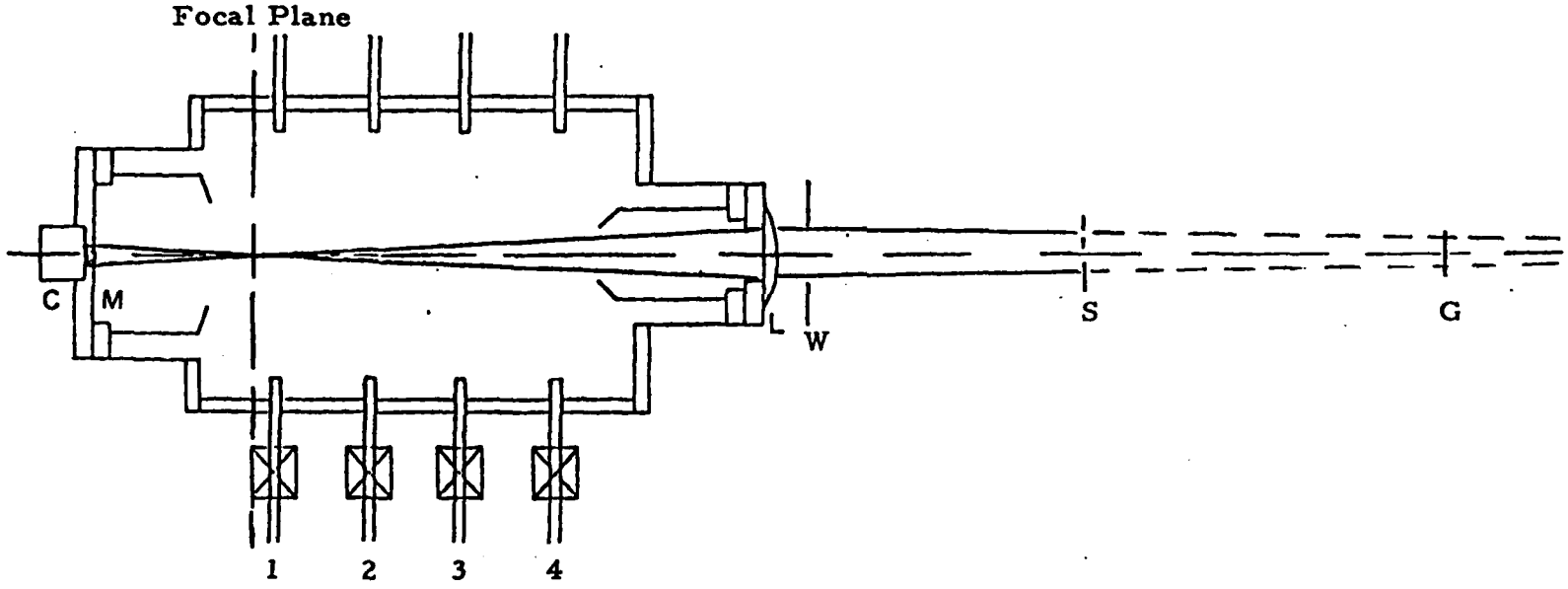

Fig. 25 COCHISE Optical System. The numbers 1-4 indicate the inlet positions along the axis. C = blackbody source, M = Al mirror, L = lens, W = window, S = entrance slit of monochromator, G = grating. The relative size of the blackbody source is exaggerated; the vertical slit aperture is shown.

3. Detection of Chemiluminescence*

The emitting volume is divided into two regions by the focal plane of the lens. The collection efficiency for radiation originating from beyond the focal point is greatly enhanced by reflection from the aluminum end mirror. The extrema of the field-of-view in the vertical and horizontal directions are determined by the extreme rays which pass through the lens according to the lens equation ($1/x_i + 1/x_o = 1/f$, where the subscripts i and o designate image and object respectively), pass through the various stops of the system, and strike the edge of the grating. Figures 26 and 27 illustrate the determination of the field-of-view for the two regions. For points between the lens and its focal plane, virtual images are formed beyond the source radiation as shown in Fig. 26. The maximum observable radial extent of the virtual image is shown by the dashed arrow in Fig. 26, and is determined by the intersection of the plane of the virtual image with the solid line, which is the extreme acceptable ray from the reaction chamber (as limited by the apertures of the lens baffle, lens, slit, and grating, i.e., in the absence of refraction by the lens itself). The solid arrow in Fig. 26 represents the maximum radial extent of the detected chemiluminescence from the source plane in either the vertical (slit height) or horizontal (slit width) direction, and is determined by the intersection of the plane of the source radiation with the dashed line connecting the virtual image extent and the center of the lens.

For radiation arising from points beyond the focal plane of the lens, real images are formed well past the monochromator, as shown in Fig. 27. In this case, the maximum image extent, represented by the dashed arrow in Fig. 27 is determined by the intersection of the image plane with the solid line, which is the extreme acceptable ray following refraction by the lens. The radial extent of the observed chemiluminescence in the source plane, shown by the solid arrow, is then determined as before by the intersection of the source plane with the dashed line from the maximum image extent through the center of the lens.

---

*This section is concerned with the definition of the optical system field-of-view and collection efficiency. See Ref. 62 for a detailed discussion of out-of-focus photometry.

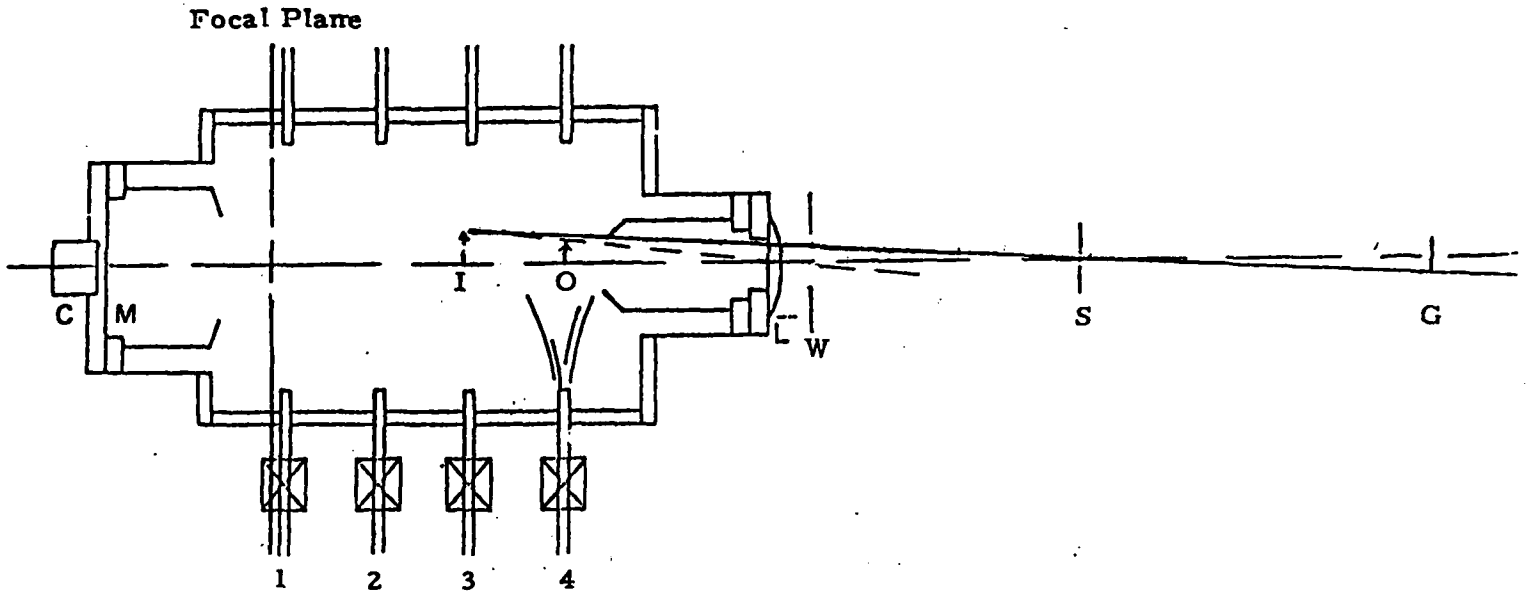

Fig. 26 Determination of field of view for radiation arising between the focal plane and the lens. I = image position, O = source position. See Fig. 25 for explanation of other labels.

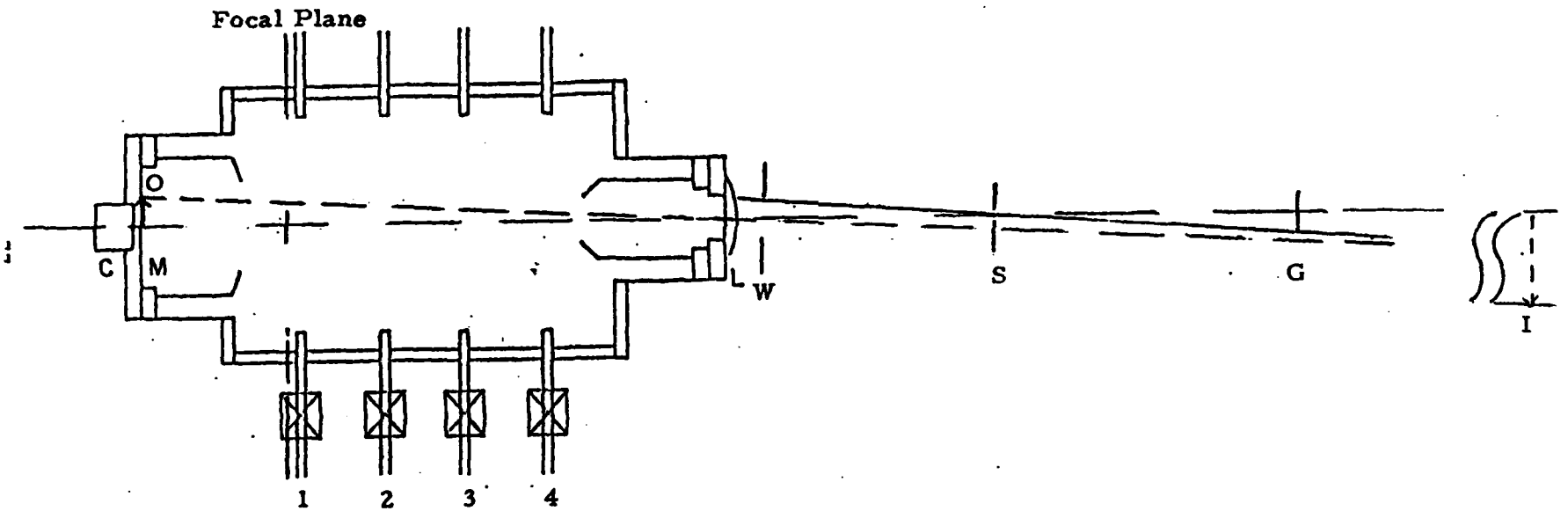

Fig. 27 Determination of field of view for radiation arising beyond the focal plane. I = image position, O = source position. See Fig. 25 for explanation of other labels.

This procedure was carried out graphically for both direct and reflected radiation from the plane of each pair of inlet jets; the results are presented in Table IV. In the vertical direction, the viewing region has an inner portion for which the entrance slit is vertically filled and an outer portion for which the slit is only partially illuminated; the radial gradient of the collection efficiency is greater beyond the inner boundary. In the horizontal direction, the separation between inner and extreme boundaries is negligible.

The overall collection efficiency for all radiation in the field-of-view is the product of the efficiencies of the lens, window aperture, slit, and grating, each of which depends on both the radial and axial position of the emitter. Although the complete calculation is somewhat complicated, a simpler calculation may be made for emission arising on the optical axis. The radial collection efficiency will be a maximum along this axis of symmetry where the slit is fully illuminated and the grating is underfilled. The determination of the collection efficiency for the two optical regions on either side of the focal plane is illustrated in Figs. 28 and 29. For points nearer than the focal point of the lens, the on-axis collection efficiency is the product of the efficiencies of the lens, window, and slit, as shown by the solid lines in Fig. 28. For the lens (area A_L), the collection efficiency is $\varepsilon_L = A_L/(4\pi x_o^2)$. For the window aperture (also of area A_L and at a distance δ_W from the lens), the collection efficiency is $\varepsilon_w = x_i^2/(\delta_w - x_i)^2$ (note that x_i is a negative number in this case). The slit efficiency is simply the ratio of the slit area to the area illuminated in the slit plane (which is a distance δ_s from the lens); the illuminated area is given by $A = A_L (\delta_s - x_i)^2/(\delta_w - x_i)^2$. For points beyond the focal length of the lens (diagrammed in Fig. 29), the rays emerging from the lens are converging and the window aperture is no longer a stop. The on-axis collection efficiency is then the product of only the lens and slit efficiencies, defined as before except that the illuminated area at the slit plane is $A = A_L (x_i - \delta_s)^2/x_i^2$.

The parameters of the optical system are: f = 71.2 cm, δ_s = 43.2 cm, δ_w = 5 cm, $R_w = R_L$ = 3.81 cm, and slit height = 2 cm. Using these values, on-axis collection efficiencies for both direct and reflected radiation were

TABLE IV

EXTREMA OF DETECTOR FIELD-OF-VIEW[a]

Discharge Position[b]	Slit Vertically Filled, cm	Vertical Extreme, cm	Horizontal Extreme, cm
4	4.0	4.5	3.6
3	4.5	5.6	3.6
2	5.3	6.6	3.8
1	5.8	7.6	3.8
1'	4.4	5.6	5.3
2'	4.4	5.8	5.6
3'	4.6	6.1	6.1
4'	4.5	6.1	6.3

[a] Extrema are expressed as radial extent of the viewing region from the optical axis, ± 0.5 cm.

[b] Discharge positions are numbered starting with the one closest to the mirror. Primes indicate reflected radiation.

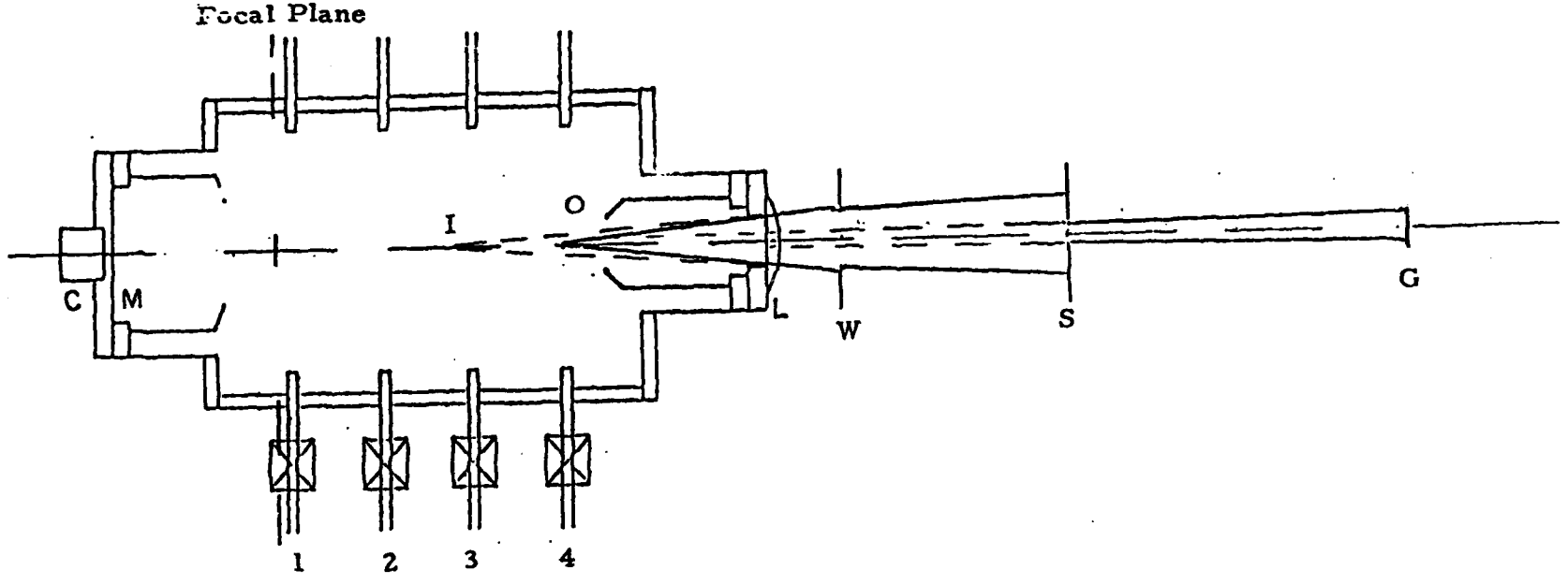

Fig. 28 Illumination of grating by on-axis radiation arising between the focal point and the lens. I = image position, O = source position. The solid lines indicate the extreme rays transmitted by each aperture. See Fig. 25 for explanation of other labels.

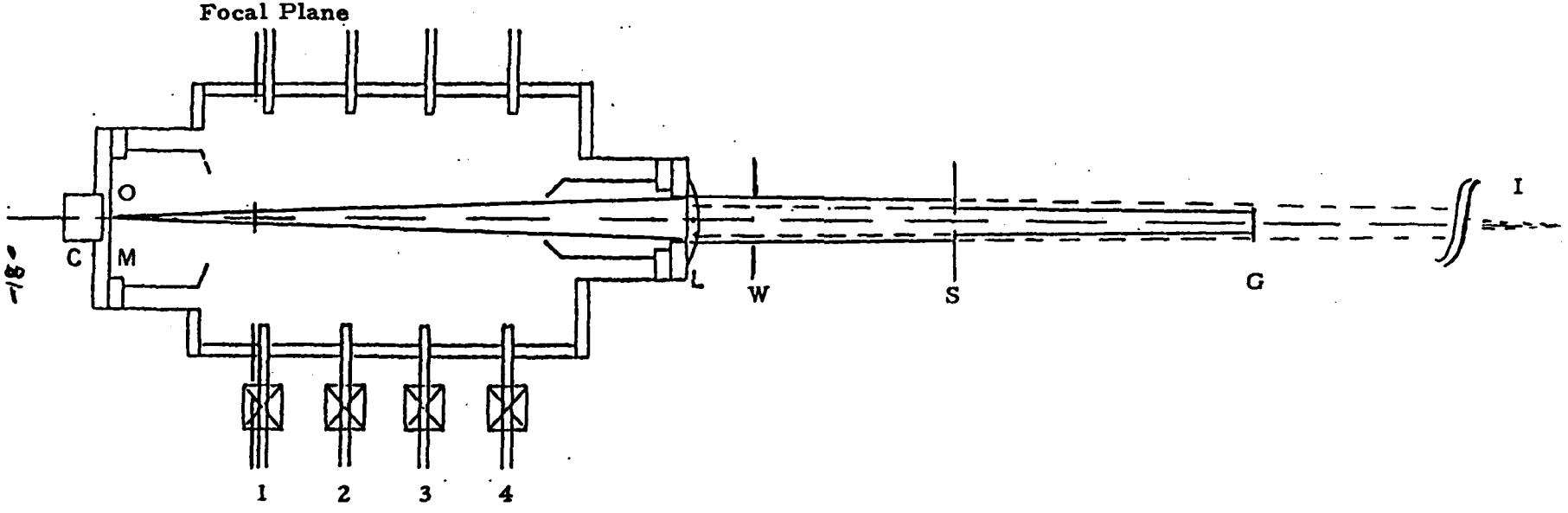

Fig. 29 Illumination of grating by on-axis radiation arising beyond the focal point. I = image position, O = source position. The solid lines indicate the extreme rays transmitted by each aperture. See Fig. 25 for explanation of other labels.

calculated for the plane of each pair of inlet jets; the results are shown in Fig. 30. The sum of the values for direct and reflected radiation from each point represents the total system collection efficiency for on-axis radiation. This value varies from $(7.4 \times 10^{-6})W_c$ at the end of the reaction zone nearest the lens to $(5.1 \times 10^{-6})W_c$ at the end of the reaction zone nearest the mirror, where W_c is the slit width in mm. The average value is $(6 \times 10^{-6})W_c$, which corresponds to emission from the vicinity of jet position 3 (cf. Figs. 28, 29). Note that the effect of the mirror is to increase the on-axis collection efficiencies by factors of 1.2 to 1.7. It should also be pointed out that the reflectivity of the mirror as a function of wavelength is not sampled in the blackbody calibration, and is taken to be 100% in the preceding discussion.

Due to the small slit width (0.1 - 3 mm) and near-collimation of the incoming radiation, the grating is not horizontally filled; this can be expected to have some effect upon the apparent resolution of the monochromator. The nominal resolution of the instrument, as determined from the linear dispersion of the grating in the plane of the slit, is given by[63] $\delta\lambda_s = WD/nf_M$, where W is the exit (and entrance) slit width in mm, D is the groove spacing of the grating in mm, n is the diffraction order of the grating, f_M is the focal length of the monochromator in meters, and $\delta\lambda_s$ is in μm. For the grating used in the most recent experiments, $D = (150 \text{ lines/mm})^{-1}$, $n = 1$, and $f_M = 0.5$ m, so the nominal resolution for 2 mm slits is $\delta\lambda_s = 0.027$ μm. This value should be equal to the observed resolution if all the grating lines are illuminated, i. e., if the grating is horizontally filled. However, if relatively few grating rulings are illuminated, the overall instrument resolution is degraded due to a low grating resolving power $\lambda/\delta\lambda_G$, where $\lambda/\delta\lambda_G = nN$, n is the grating diffraction order, and N is the number of lines illuminated.

For example, for the case of collimated incoming light and geometrical imaging of a 2 mm entrance slit, 300 rulings are illuminated and the "resolution" of the grating in the first order is $\delta\lambda_G \sim 0.017$ μm at $\lambda = 5$ μm, which is comparable to the nominal value $\delta\lambda_s$. If the slit is sufficiently narrow to produce a significant diffraction pattern at the grating, it can be shown[63] that the width of the central diffraction maximum at its base is

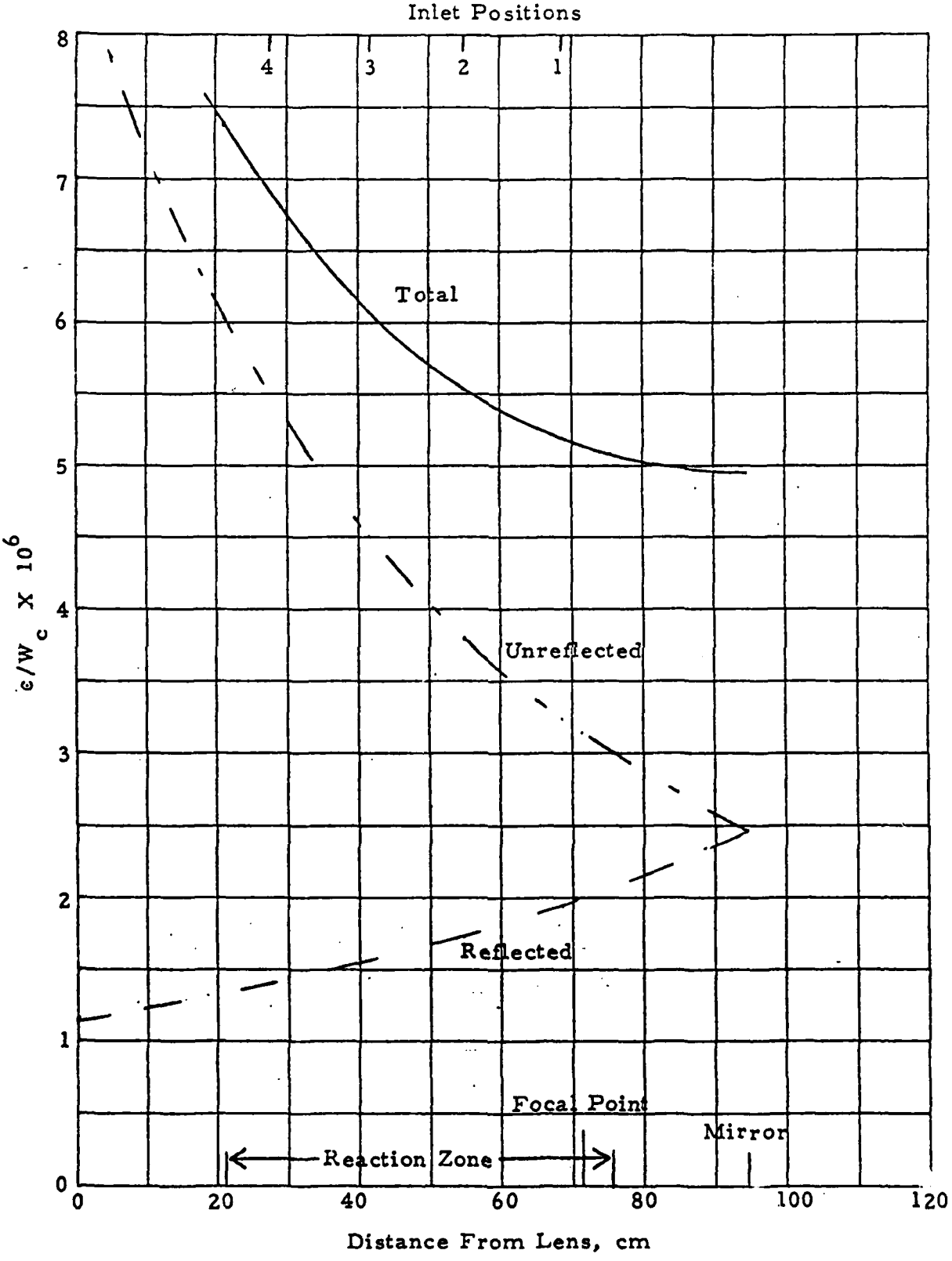

Fig. 30 Collection Efficiency of Optical System for On-axis Radiation.

2 $\lambda f_M/W$ for collimated incoming light; for a 2 mm entrance slit, the illuminated width of the grating is then about 2.5 mm, which corresponds to $\delta\lambda_G \sim 0.013$ mm.

In reality, the available slit widths (0.1 - 3 mm) clearly lie in a transition region for which the pattern of illumination of the grating through the entrance slit may have significant contributions from both geometrical imaging and diffraction by the slit. In any event, the result is that, due to contributions from both $\delta\lambda_G$ and $\delta\lambda_s$, the actual wavelength uncertainty will be somewhat larger than that which can ultimately be provided by the monochromator. This is in qualitative agreement with the results of the analysis of NO chemiluminescence, where the resolution giving the best matches between computed and experimental NO spectra is 0.035 μm for 2 mm slits (see Appendix A). Furthermore, the actual observed radiation is not collimated but is convergent or divergent to varying degrees, depending upon its point of origin; this leads to the speculation that the effective resolution may be slightly different for radiation originating from different axial regions of the field-of-view.

In connection with the above discussion, it should be pointed out that it has been empirically observed that the blackbody signal at a given wavelength increases roughly as $W^{3/2}$. Although a complete understanding of this result requires a larger data base for both blackbody and chemiluminescent radiation, the effects of incomplete illumination of the grating may provide a partial explanation.

The preceding discussion has merely provided an approximate description of the properties of the COCHISE optical system. A detailed characterization of the system would clearly require a significant theoretical/experimental effort, which could conceivably be provided in a future effort.

4. Absolute Specific Intensity

From Eq. (47), the ratio of blackbody to chemiluminescence geometric factors is $C = A_B \varepsilon_B/(A_c \varepsilon_c)$. Using the results of the preceding sections, A_c can be approximated as the area of an elliptical cross section of the viewing region in the plane of the "average emitter" near jet 3 (cf. Fig. 30,

Table IV): $A_c \approx 80$ cm^2. Using the average on-axis collection efficiency for ε_c gives $C = 1.57 \times 10^{-4}\ W_B/W_c$. The on-axis value for C, which should provide the minimum estimate for I_λ, will be used throughout the following discussion, but the empirical $W_B^{1.5}$ result mentioned earlier will be used to correct the blackbody signal observed for one W_B to that corresponding to $W_B = W_c$.

The total NO chemiluminescent intensity is $\int I_\lambda\, d\lambda$ in watts cm^{-2} sr^{-1} and is related to the average NO number density (assuming a uniform cross section) by

$$\int I_\lambda\, d\lambda \approx \frac{h\nu \sum_{v=0}^{\infty} A_v N_v}{4\pi \sum_{v=0}^{\infty} N_v} [NO]\, \ell \qquad (49)$$

where $h\nu$ is the number of joules/photon at frequency ν, A_v is the rotationally averaged Einstein coefficient for emission from level v to level v - 1, N_v is the relative population of level v, and ℓ is the length of the reaction zone. From the Einstein coefficients of Ref. 25 and the average relative populations deduced in Section II and Appendix A, $\sum_{v=0}^{12} A_v N_v / \sum_{v=0}^{12} N_v \cong 34\ s^{-1}$. For $\ell = 54.4$ cm and $\lambda \cong 5$ μm, Eq. (49) gives

$$[NO] = 1.7 \times 10^{17} \int I_\lambda\, d\lambda \qquad (50)$$

Graphical integration of the spectrum from experiment 286706 (cf. Table A-I) gives $\int I_\lambda\, d\lambda \approx 1.7 \times 10^{-8}$ watt sr^{-1} cm^{-2} after making the empirical correction for the relative slit widths of the blackbody (calibration experiment 286701, $W_B = 1.5$ mm) and chemiluminescence ($W_c = 2.0$ mm) observations. Thus the total NO density averaged over the viewing region is estimated to be $[NO] \approx 3 \times 10^9$ cm^{-3}, which is consistent with that predicted in Section II on the basis of kinetic arguments.

IV. FAKIR STUDIES

A. Introduction

It has been suggested that reactions of N_2 ($A^3\Sigma_u^+$) with O and O_2 could be significant sources of odd nitrogen and of vibrationally excited NO in the upper atmosphere.[64] The possible reactions of $N_2(A)$ with oxygen atoms are summarized as follows:

$$N_2(A^3\Sigma_u^+)_{v'=0} + O\ (^3P) \rightarrow N_2(X^1\Sigma_g^+) + O\ (^3P) + 6.2\ eV \quad (51a)$$

$$\rightarrow N_2(X^1\Sigma_g^+) + O\ (^1D) + 4.2\ eV \quad (51b)$$

$$\rightarrow N_2(X^1\Sigma_g^+) + O\ (^1S) + 2.0\ eV \quad (51c)$$

$$\rightarrow NO(X^2\pi) + N\ (^4S) + 2.9\ eV \quad (51d)$$

$$\rightarrow NO(X^2\pi) + N\ (^2D) + 0.5\ eV \quad (51e)$$

Reactions (51d) and (51e) may be major sources of NO and $N(^2D)$ in auroras and in the quiet daytime E-region;[64] in addition, some of the exothermicity of these reactions may appear as vibrational energy in the product NO molecules. The further reaction of $N(^2D)$, formed in reaction (51e), with ambient O_2 can also give rise to vibrationally excited NO.

The rate constant for quenching $N_2(A^3\Sigma_u^+)$ by oxygen atoms has been reported as 2.2×10^{-11} cm^3/sec[28] and 1.5×10^{-11} cm^3/sec.[65] However, Meyer et al's[28] measurement is indirect and could be in error by a factor of three to four, while the determination of Dunn and Young[65] was made in a complicated system which could provide reactive species, in addition to $N_2(A)$, which might complicate the kinetics. Aeronomic estimates[64] have favored a value closer to 10^{-10} cm^3/sec. Recent rocket measurements by Sharp et al[66] and O'Neil et al[67] are in conflict on this. Sharp et al[66] favor the high value, while O'Neil et al[67] support the earlier laboratory measurements.

AD-A111 827 PHYSICAL SCIENCES INC WOBURN MA F/G 17/5
LABCEDE AND COCHISE ANALYSIS II. VOLUME I.(U)
FEB 80 W T RAWLINS, L G PIPER, B D GREEN F19628-77-C-0089
UNCLASSIFIED PSI-TR-207A NL

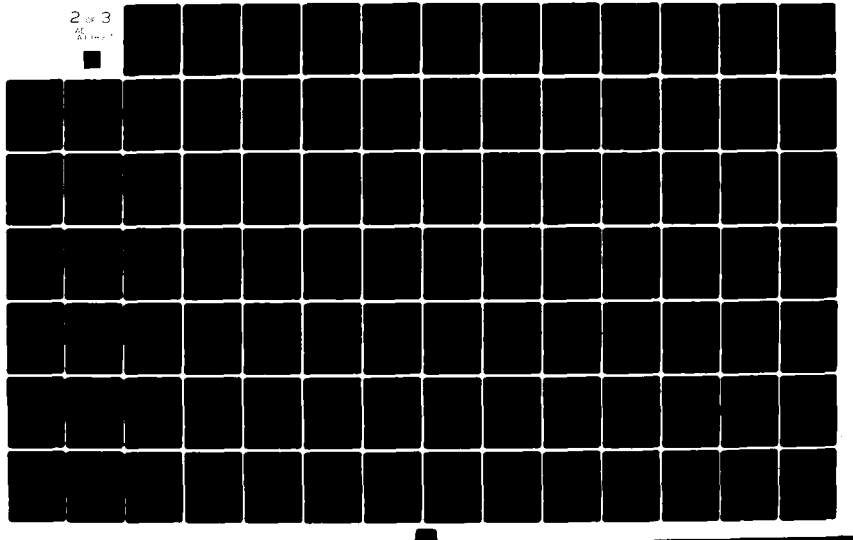

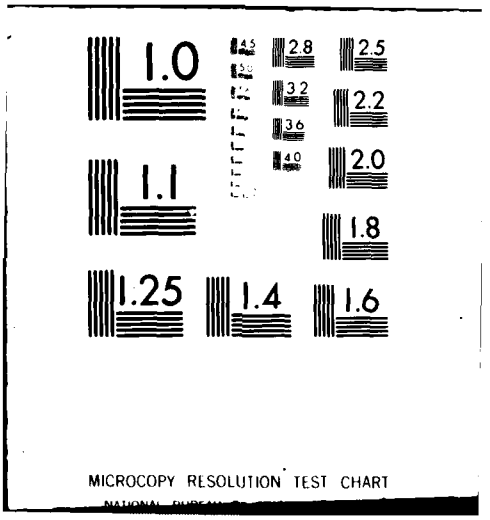
1.0
1.1
1.25
1.4
1.6
1.8
2.0
2.2
2.5
2.8
3.2
3.6
4.0
MICROCOPY RESOLUTION TEST CHART

Only Meyer et al[28,68] have investigated the products of the reaction between $N_2(A)$ and oxygen atoms. They observed excitation of $O(^1S)$ by its characteristic emission at 557.7 nm, and estimated that 15-50% of the total $N_2(A)$ quenching by oxygen atoms occurs via this path. Their system was not sufficiently free from extraneous NO contamination to rule out the possibility of NO product formation as well.

The possible reaction channels for the interaction of $N_2(A)$ with molecular oxygen are as follows:

$$N_2(A^3\Sigma_u^+)_{v'=0} + O_2(X^3\Sigma_g^-) \rightarrow N_2\ (X^1\Sigma_g^+) + O_2(X^3\Sigma_g^-) + 6.2\ eV \qquad (52a)$$

$$\rightarrow N_2\ (X^1\Sigma_g^+) + 2O(^3P) + 1.1\ eV \qquad (52b)$$

$$\rightarrow N_2O + O(^3P) + 3.0\ eV \qquad (52c)$$

$$\rightarrow N_2O + O(^1D) + 1.0\ eV \qquad (52d)$$

$$\rightarrow 2NO\ (X^2\pi) + 4.2\ eV \qquad (52e)$$

Since O_2 is the main deactivator of $N_2(A^3\Sigma_u^+)$ in the atmosphere below 100 km,[64] significant amounts of atmospheric N_2O could be formed via reactions (52c) and (52d), with possible vibrational excitation of the product. Further reactions of N_2O with $N(^2D)$ and $O(^1D)$ can lead to the formation of NO.[64] Direct formation of NO via reaction (52e) is expected to be extremely slow due to the dynamic constraints which inhibit such four-center exchange reactions.

Measurements of the room-temperature rate constants for this reactions vary between 1.9 and 7.6 x 10^{-12} cm^3/sec.[28,38,65,68-74] (Table V). Some of this scatter probably results in the variation in deactivation rate constant with vibrational level, although there is some controversy over the importance of this variation for v' = 0 and 1, the two main vibrational levels populated

TABLE V. Rate Constants for Reactions of $N_2(A\,^3\Sigma_u^+)$ v = 0,1 with O and O_2[a]

k_{O_2}	k_O	Comments	Reference
6.0	22	$Hg(6\,^3P_1)$ tracer k_O from k_O/k_{O_2} = 3-4 and listed number for k_{O_2} claim $k_{v=1}/k_{v=0} \approx 1.3$	28
2.9 (v = 0)	15	claimed $k_{v=1} = k_{v=0}$ Looked at VK 0,6 and 1,5 with interference filters. Probably some interference from NO γ - bands	65
3.8		NO γ - band tracer	69
3.3		NO γ - band tracer	70
3.7		$Hg(6\,^3P_1)$ tracer claim $k_{v=1} = k_{v=0}$	71
6.5		Hg $(6\,^3P_1)$ tracer	72
7.6		Hg $(6\,^3P_1)$ tracer - This value was measured relative to $k_{N_2(A)+N} = 5 \times 10^{-11}$ cm^3 molecule^{-1}s^{-1}	73
1.9 (v = 0) 7.6 (v = 1)		Measured $N_2(A)$ with absorption on nitrogen 1^+ system	38
3.5 4.5 (v = 0) 5.1 (v = 1)		Broadband filter - "mostly v = 0". Could have been contaminated with NO γ - bands. v = 0 and v = 1 with monochromator. Could have large uncertainty in reaction time.	74

a. The listed rate constants are for T = 300K. They are in units of 10^{-12} cm^3 molecule^{-1}s^{-1}.

in most laboratory experiments. The data of Dreyer, Perner and Roy[38] indicate that for reaction (52) $k_{v'=1}/k_{v'=0} = 3.9$. On the other hand Dunn and Young[65] and Callear and Wood[71] claim both levels are deactivated with equal probability, Meyer, Setser and Stedman[28] claim only a 30% greater rate constant for quenching v' = 1 by O_2 compared to v' = 0, and Clark and Setser[74] claim $k_{v'=1}/k_{v'=0} = 1.13$. A number of the experiments were done using tracers or broad band filters, hence the lack of specificity in vibrational level.

Only Meyer et al[28] have investigated product formation in this reaction. They indicated that oxygen atoms are a significant product of the reaction, but did not make a quantitative estimate of the yield. The determination of a quantitative yield of O from the reaction between $N_2(A)$ and O_2 could give insight into the other products of the reaction. For example, if the yield were two O atoms per $N_2(A)$ deactivated, then clearly, the only important product channel would be reaction (52b). If, however, the yield were significantly less than one atom per deactivation, then it would be clear that either reactions (52a) or (52e) were important. The importance of reaction (52e), which is considered to be unlikely, could of course be checked by looking for NO.

The above discussion indicates that for reactions (51) and (52) neither the overall reaction rate constants nor the branching into various product channels can be considered to be known to even an accuracy of a factor of two; although Setser thinks a value of 3.5×10^{-12} cm^3 $molecule^{-1}s^{-1}$ for the rate constant for reaction (52) is probably correct to within 30%.[74] The situation is even worse for temperatures other than 300 K, since there is only one published study[70] of the rate constant for reaction (52) over the limited temperature range of 245-365°K, and no such studies at all for reaction (51). Initial experiments were carried out in the FAKIR facility to test the feasibility of modifying this apparatus to allow for studying the $N_2(A)/O,O_2$ system.[5] The tests indicated that the apparatus could be used to study $N_2(A)$ reactions and the necessary modifications have nearly been completed. Initial calibrations and performance tests are now being done.

B. Description of Experimental Facility

The FAKIR facility, which is shown schematically in Fig. 31 consists of a two-inch diameter quartz flow reactor which is pumped by a Roots blower capable of producing linear flow velocities of 8×10^3 cm s^{-1} at pressures of 1 torr. A 0.5 m monochromator is mounted upon a set of rails parallel to the flow tube which permits spectral observations of luminous gases within the flow tube as a function of linear distance down the tube. Distances are converted to reaction times by dividing by the flow velocity.

A hollow-cathode source of metastable argon atoms is at the upstream end of the flow tube. Nitrogen metastables are produced in the electronic energy transfer reaction between metastable $Ar(^3P_{2,0})$ and N_2.[32,75] This transfer results in the production of nearly equal populations of the $C^3\pi_u$ and $B^3\pi_g$ states of N_2 which quickly cascade radiatively to the metastable $A^3\Sigma^+_u$ state.[76] The hollow-cathode metastable source is clean and free from other reactive species such as ions or energetic electrons, so that $N_2(A^3\Sigma^+_u)$ is produced in the absence of significant concentrations of other reactive species such as ground-state or electronically excited nitrogen atoms, and vibrationally excited ground electronic-state nitrogen molecules. The concentrations of $N_2(A)$ produced by this technique are reported[72] to be on the order of 1-10 $\times 10^9$ cm^{-3}.

A microwave discharge in argon was used initially to try to produce the argon metastables which were subsequently to be mixed with nitrogen to make the nitrogen metastables. Under no conditions were the nitrogen metastables positively identified by observation of the Vegard-Kaplan, $A^3\Sigma_u^+ - X^1\Sigma_g^+$, emission in the 250-350 nm region. Some indirect evidence for small concentrations of $N_2(A)$ came from the observation of NO γ-band emission in the 220-300 nm region; this emission has been shown to be excited efficiently in the interaction of $N_2(A)$ with NO.[73,75] In the present case, the NO had been produced in the microwave discharge from impurities in the argon. The inability to obtain useful concentrations of metastables by this technique was probably a result of the failure to purify further the commercial UHP argon prior to flowing it through the discharge. In addition, the microwave source is efficient over only a very limited range of operating conditions[77]

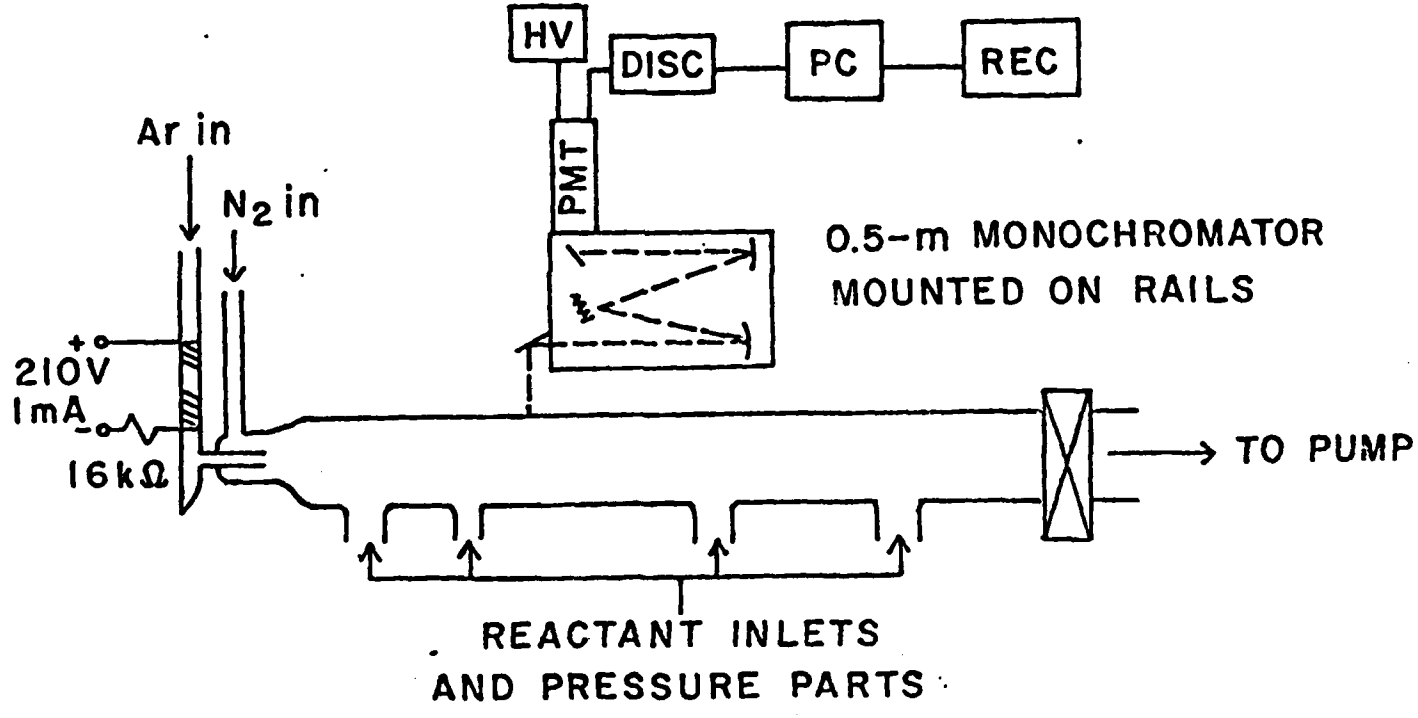

Fig. 31. FAKIR Facility Modified for N_2 ($A^3\Sigma_u^+$) Studies

which may not have matched those of the early experiments.

A hollow-cathode discharge source was built to produce metastable argon. Most experimenters have used tantalum for the electrodes,[75,78] but other materials have also been found to be suitable.[78,79] For the FAKIR experiments, 0.005 inch aluminum shim was used for the electrode material. The shim was rolled into a cylinder whose diameter was the same as the inside diameter of the glass tubing through which the gas flowed (13 mm). The cathode (the down-stream electrode) is 40 mm long, the anode 15 mm long, and the two electrodes are separated by 45 mm. The discharge is operated in the dc mode with the anode biased at +210 volts. A load resistor of 10 kΩ gives the discharge stability and limits the current. The current in the present experiments is about 3 mA. For the discharge to produce metastables efficiently, it is crucial to take some care with gas purity. A helical trap, made from 3/8 inch copper tubing filled with 5Å molecular sieve and cooled to liquid nitrogen temperature, is placed on the low-pressure side of the regulating needle valve on the argon line (argon freezes with a vapor pressure of about 200 torr at liquid nitrogen temperature; thus, the trap must not appear on the high pressure side of the feed line). These traps are adequate for producing argon metastables down-stream from the discharge. The metastables may be detected by the appearance of the characteristic reddish-violet flame which obtains upon the addition of nitrogen down-stream from the discharge. At the concentrations of N_2 at the point of addition, ~10^{15} cm^{-3}, the flame length is about 2 cm. This length is just governed by diffusional mixing of the two streams of gas, since at these nitrogen concentrations the collisional quenching times for nitrogen on argon are on the order of tens of microseconds.[27] Typically, the argon flow rate is ~1500 μmols s^{-1}, the nitrogen flow rate ~250 μmols s^{-1}, and the flow-tube pressure about 1.5 torr. When only the forepump is pumping on the flow tube, the flow velocity is about 1100 cm s^{-1} at 1.5 torr, thus giving a resolution of 0.9 ms/cm along the flow tube axis.

Spectroscopic observations made about 27 cm (27 ms) down-stream from the Ar^*/N_2 mixing region showed Vegard-Kaplan and nitrogen second-positive emission. The spectrum is shown in Fig. 32. The Vegard-Kaplan emission is completely free from interference from NO γ-band emission, and shows that the first three vibrational levels of the $A^3\Sigma_u^+$ state of N_2 are populated. The

relative populations of the three levels are approximately 100:53:38 for v' = 0, 1, 2, respectively. This is in contrast to the relative populations reported by Stedman and Setser of 100:95:10 for the same levels, respectively.[32,75] This difference may arise in part from differences in the transition probabilities used to estimate the populations, from differences in transit time from the discharge to the observation region, and from differences in total pressure.

From the intensities observed in the spectrum, it is possible to make a crude estimate of the number density of nitrogen metastables in the flow tube. The number density is just the ratio of the fluorescence intensity, corrected for collection and transmission losses in the detection system, and the transition probability of the band of interest. The monochromator has an effective aperture of f/6.9, resulting in a collection efficiency of 1.3×10^{-3}. Further losses in detection arise from transmission through the flow tube wall (T ≈ 90%), reflections off of four mirrors (T ≈ 90% each), grating losses (≈ 85% efficient at 260 nm) and photomultiplier quantum efficiency ($\eta \approx 20\%$). Thus the total loss of photons, the product of losses from each optical component, the collection efficiency, and the quantum efficiency, is $\approx 1.3 \times 10^{-4}$. The relevent transition probabilities have been tabulated by Shemansky.[80] The total density of nitrogen metastables in all vibrational levels is calculated to be about 3×10^{8} cm^{-3}. This is about an order of magnitude less than the estimates from Setser's group;[72] however, their measurements were performed over a shorter flow time than the 27 ms in the present experiments. One expects some reduction in the $N_2(A)$ number density resulting from diffusion to the walls with subsequent deactivation, and perhaps some quenching by impurities which were not efficiently trapped from the gases. In addition, some uncertainty exists in the present estimation of the losses in the detection system. More precise quantitative estimates will be possible after the apparatus has been calibrated using standard lamps and O/NO air afterglow.[81]

The signal from the nitrogen second positive bands seen in Fig. 32 results in part from energy pooling of the $N_2(A)$:[74,82-84] reactions between two $N_2(A)$ molecules have been shown to produce excitation of the $N_2C^3\pi_u$,

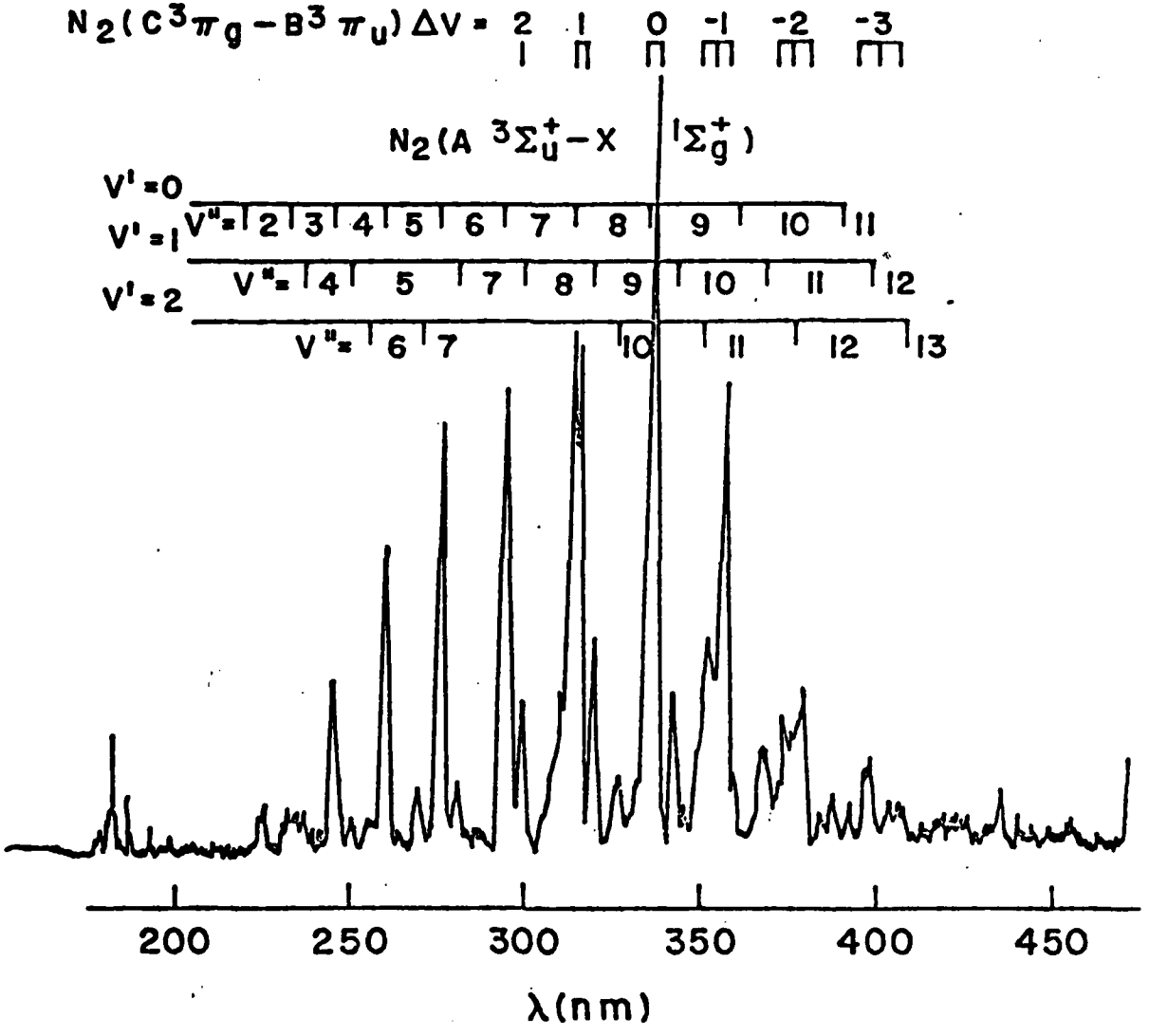

Fig. 32 Observed Fluorescence upon Mixing N_2 with Active Ar

and perhaps $C'^3\pi_u$ and $B^3\pi_g$ states. The rate constant for the process producing the $N_2C^3\pi_u$ state, the upper level of the second-positive system, has been reported to be 1.8×10^{-10} cm^3 s^{-1} [74] and 2.6×10^{-10} cm^3 s^{-1} [83,84]. Crude estimates of the second positive emission intensity expected in the FAKIR system, based upon estimates of the $N_2(A)$ state concentration, are consistent with these values. It is difficult to make a very accurate assessment of the energy pooling rate constant at this time however, because some of the observed second-positive emission probably comes from scattered light from Ar^*/N_2 interaction region.

It is clear from the spectrum in Fig. 32 that there is sufficient Vegard-Kaplan intensity to allow kinetic measurements of $N_2(A)$ reactions in the FAKIR facility. Necessary modifications to proceed further with the experiments are to provide a gas purification and handling line to allow introduction of high purity gases in trace quantities. This is necessary to provide accurate calibrations of the sensitivity of the various methods outlined below for the detection of potential product species at the level of 10^9 cm^{-3}. In addition, it is necessary to calibrate the spectroscopic system so that accurate determinations of the $N_2(A^3\Sigma_u^+)$ number density will be possible.

C. Experimental Plans

The main goal of the FAKIR experiments is to determine the products of the reactions under study and to determine rate constants for product formation. These experiments are difficult because the products from the $N_2(A)$ reactions will appear at concentrations no greater than the initial $N_2(A)$ number density, approximately 10^9 molecules cm^{-3}. Such sensitivity is difficult to achieve in systems. Potential techniques for monitoring expected signal levels are described below.

As mentioned previously, $O(^1S)$ has already been observed in emission as a product of reaction (51). A more precise determination of its relative importance compared to other possible exit channels should be made, however. If any atomic nitrogen is produced in the reaction, it cannot be measured except by means of atomic resonance fluorescence in the vacuum ultraviolet. However, if it can be shown that NO has been produced in the reaction, it

can be inferred that nitrogen atoms are also a product. Since $N(^2D)$ reacts rapidly with O_2 to produce NO,[17] the NO yield from reaction (51e) will be twice that from reaction (51d). The detection of NO at fairly low concentrations can be accomplished in a variety of ways: molecular resonance fluorescence using either a microwave discharge lamp source, or a tunable dye laser, operating on the NO γ-bands in the uv, O/NO air afterglow intensities resulting from the addition of known concentrations of O atoms in a calibrated system,[81] and NO γ-band fluorescence excitation from electronic energy transfer from $N_2(A^3\Sigma_u^+)$ sensitization.[73,75] Because transition probabilities of the NO γ-bands are similar to those for uv transitions of OH and NH,[85-87] laser-induced fluorescence would be expected to provide similar detection sensitivity for NO as it does for OH and NH. These latter two radicals have been shown to be detectable at concentrations on the order of 10^8 cm^{-3} or less by this technique.[88] However, a tunable dye laser is not available for the experiments. The O/NO air afterglow technique can provide detection sensitivities on the order of 10^9 cm^{-3},[89] but this technique is more difficult to use for detection of NO than it is for O atom detection because conventional microwave discharge sources of oxygen atoms are usually contaminated with traces of NO which complicate the measurements. However, given initial concentrations of O atoms on the order of 10^{14} cm^{-3}, it may be possible to monitor the buildup of NO formed in reaction (52d, e) provided the impurity NO emanating from the discharge can be kept below 10^9 cm^{-3}. The most sensitive and readily accessible technique, however, seems to be excitation of the NO γ-bands by energy transfer from $N_2(A)$.

The NO γ-band fluorescence will be in steady state in the reactor so that the NO* photon-emission rate will be proportional to the NO excitation rate, i.e. $I \propto k_{ex} [NO] [N_2(A)]$. The rate constant k_{ex} has been measured to be 1.5×10^{-10} cm^3/sec.[74] Roughly 25% of the excitation will appear as emission of the (0, 1) band.[90] As mentioned above, the total fluorescence is reduced further by a factor of 1.3×10^{-4} prior to being detected by the photon counting system. For concentrations of both NO and $N_2(A)$ of 10^8 cm^{-3}, the (0, 1) band is calculated to produce a detected signal of ~50 Hz. As presently configured, the counting system on the apparatus is capable of detecting signals as low as 5- Hz, we below the anticipated signal.

As mentioned earlier, Meyer et al[28] have determined that one of the products of reaction (52) is atomic oxygen. They did not, however, make any quantitative estimate of yield. The O/NO air afterglow should provide sufficient sensititivity to determine O-atom yields from this reaction, i.e. a detection limit of about 10^9 atoms cm^{-3}. If reaction (52e) is an important channel, the product NO can be detected by NO γ-band excitation from $N_2(A)$. Product N_2O from reactions (52c, d) will prove very difficult to measure. It was suggested previously that N_2O might be detectable by observation of N_2 first positive emission following photolysis of N_2O by Kr resonance radiation in the vacuum ultraviolet. In view of the difficulties of Young et al[91] and the failure of Okabe[92] to observe the first positive emission from photolysis of N_2O with Kr resonance radiation, it would seem that this approach would be marginal when applied to the detection of N_2O at concentrations on the order of 10^{10} cm^{-3}. It would appear from the report of Okabe[92] that NO β-band fluorescence would be more intense than the N_2 1+ emission following N_2O photolysis at 123.6 nm. Okabe estimates the quantum yield for NO β-band fluorescence to be only about a half percent. For an absorption cross section at 124 nm of about 10^{-17} cm^2,[91] a Kr resonance lamp flux[91] of about 10^{14} photons s^{-1} and an N_2O number density of 10^{10} cm^{-3}, <5 Hz of β-band fluorescence will be detectable in the FAKIR facility. Thus, this approach is marginal at best. However, sufficient uncertainty exists in the reports of Okabe[92] and of Young et al[91] so that an experimental test of this approach might be warranted.

In summary, it appears that the O and NO product from reactions (51) and (52) should be detectable in the FAKIR facility without serious modification of the present apparatus. Nitrogen atoms should be detectable if the apparatus is modified to permit the use of vacuum uv resonance lamps. The detection of N_2O product is marginal at best, even if the apparatus is modified to give vacuum uv capability.

D. Preliminary Experimental Observations

Some preliminary experiments have been run in the FAKIR apparatus. These have, for the most part, resulted in qualitative observations on apparatus performance and on the interactions of $N_2(A)$ with O_2 and O. Preliminary conclusions which may be drawn are that O is a more efficient quencher of

$N_2(A)$ than is O_2; $O(^1S)$ is excited efficiently in the interaction between $N_2(A)$ and O; and $N_2(A)$ v=1 is quenched more rapidly than $N_2(A)$, v'=0.

Metastable nitrogen molecules decay exponentially in the flow reactor. In the absence of added reagent, the decay is the result of diffusion to the wall followed by quenching of the molecules by collisions with the wall. If a quenching gas is added to the reactor in concentrations significantly greater than the concentration of the metastable nitrogen, the decay is still exponential. The change in concentration of $N_2(A)$ as a function of distance down the flow tube, and of reagent concentration Q is given as follows:

$$\ln \frac{[N_2(A)]}{[N_2(A)]_0} = -(k_w + k_q [Q]) \quad z/\bar{v} \tag{53}$$

where, k_q is the rate constant for the bimolecular reaction of interest, k_w is the rate for first-order removal by the wall (this rate varies inversely with pressure because it depends upon diffusion to the reactor walls), $\bar{v}$ is the average flow velocity, and z is the effective distance from the reagent inlet to the point of observation. If the decay of the $N_2(A)$ is measured as a function of distance down the reactor at fixed pressure and $[Q]$, a pseudo first-order decay is observed whose rate equals $k_w + k_q \cdot [Q]$. If one measures a number of pseudo first-order decay rates at various $[Q]$ but fixed total pressure, and then plots these decay rates versus $[Q]$, a straight line whose slope equals the rate constant, k_q is obtained. This procedure is demonstrated in the pseudo first-order decays and second-order plot of Figs. 33 and 34 respectively. The rate constant obtained from the second-order plot for k_{52} is 1.3×10^{-12} cm^3 $molecule^{-1}$ s^{-1}. This value must be corrected by a factor of 1.6 to account for the coupling of the radial density gradient of $N_2(A)$ caused by wall removal and the parabolic velocity profile of fully developed laminar flow,[93] thus giving a corrected rate constant of 2.1×10^{-12} cm^3 $molecule^{-1}$ s^{-1}. This value is about 50% lower than the values commonly accepted for k_2, (see Table I). There is some curvature

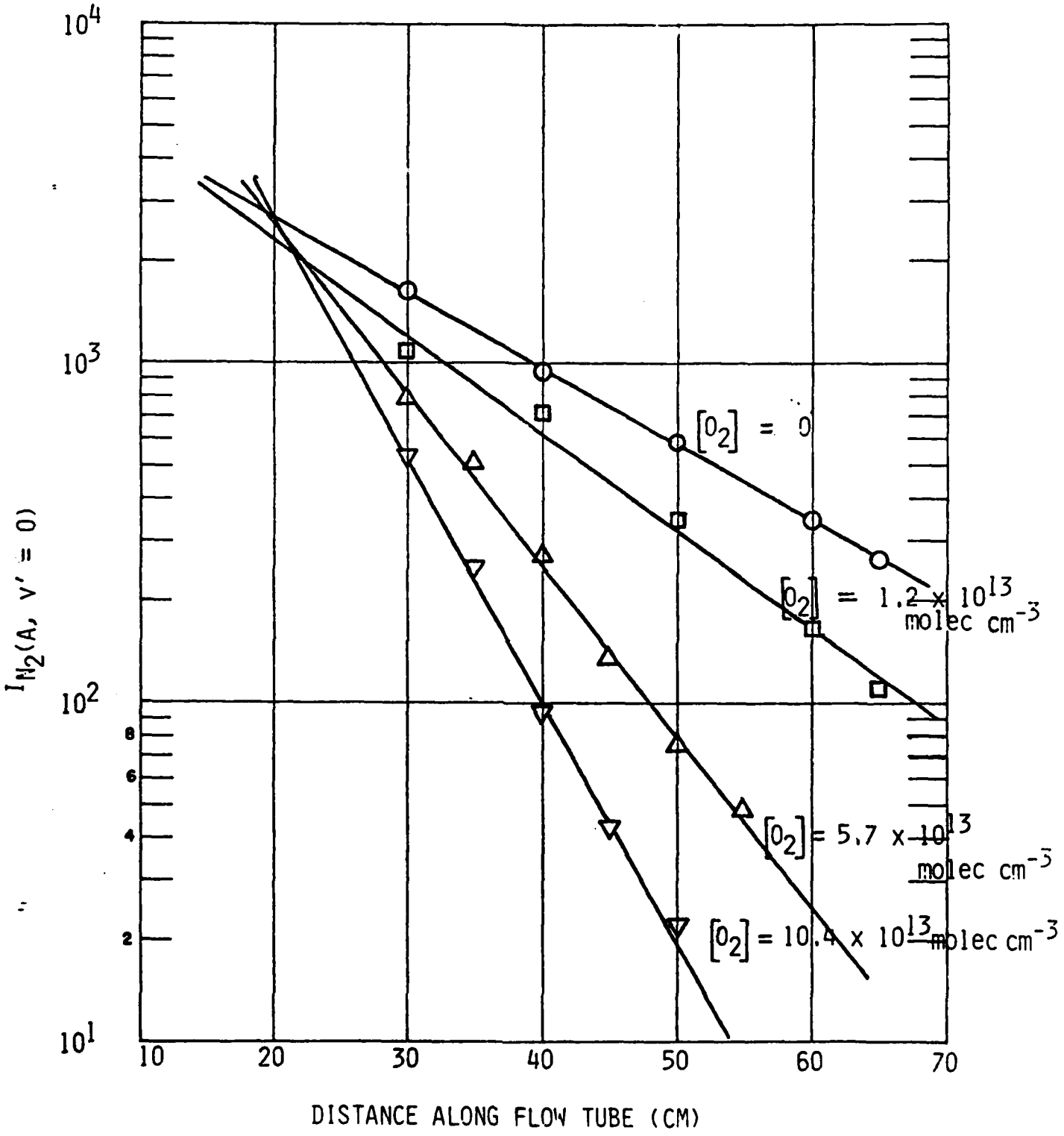

Fig. 33 Decay of $N_2(A^3\Sigma_u^+, v' = 0)$ as a function of distance down the flow tube at several different O_2. ($\bar{v}$ = 1108 cm s^{-1})

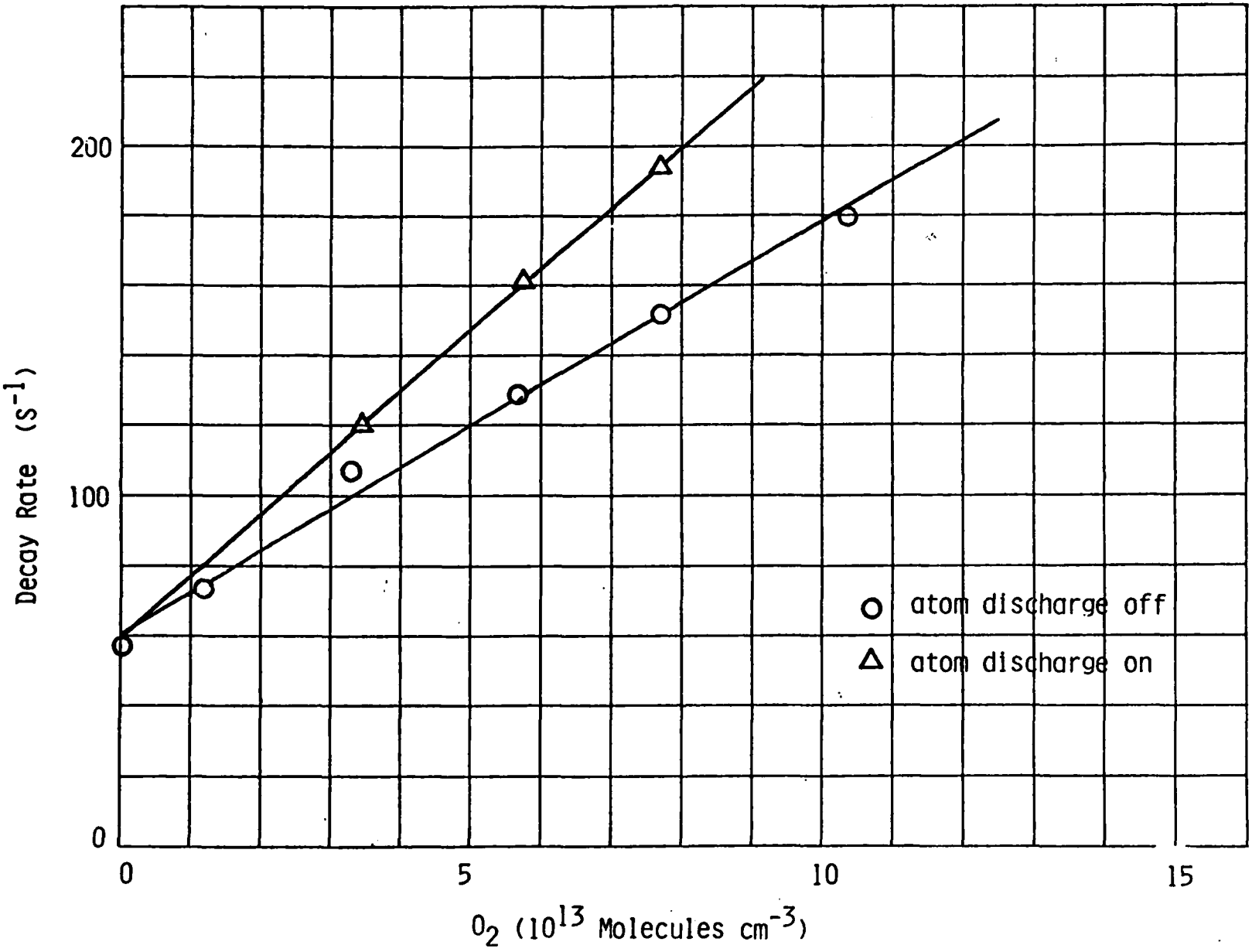

Fig. 34 Decay of $N_2(A^3\Sigma_u^+, v'=0)$ as a function of O_2 concentration in the presence and absence of oxygen atoms.

in both the first-order and second-order plots which combine to lower the rate constant from the value which would be obtained by taking initial slopes. We are currently investigating the causes of this curvature.

The triangles in Fig. 54 represent the decay rates obtained when the oxygen is discharged prior to entry into the flow tube. The discharge creates some atoms, so that both oxygen atoms and molecules are present in the reactor to quench the $N_2(A)$. Clearly, the presence of atoms enhances the decay of $N_2(A)$. As we were not set up to measure atom concentrations in that experiment, we cannot extract a rate constant for quenching $N_2(A)$ by atoms. In future work, this information will be obtained.

Shown in Fig. 35 is the decay for both $N_2(A)$ $v'=0$ and $v'=1$ as a function of $[O_2]$ at a fixed reaction distance. These preliminary data show that $v'=1$ is removed about 50% faster by O_2 than is $v'=0$.

The variation in the 557.7 nm emission from $O(^1S)$ as a function of intensity from the 0, 6 and 1,8 bands of the Vegard-Kaplan system is shown in Fig. 36. These data show that the green line is indeed excited by energy transfer between $N_2(A)$ and oxygen atoms. A careful calibration of the spectral system will allow determination of a rate constant for this process (reaction (51c)) in future measurements.

The preliminary data presented indicate that the FAKIR facility is capable of generating data of the quality necessary for the present program. Future work should be aimed at resolving the few experimental difficulties which remain, doing the careful calibrations necessary for the rate constant measurements, and in performing the desired experiments.

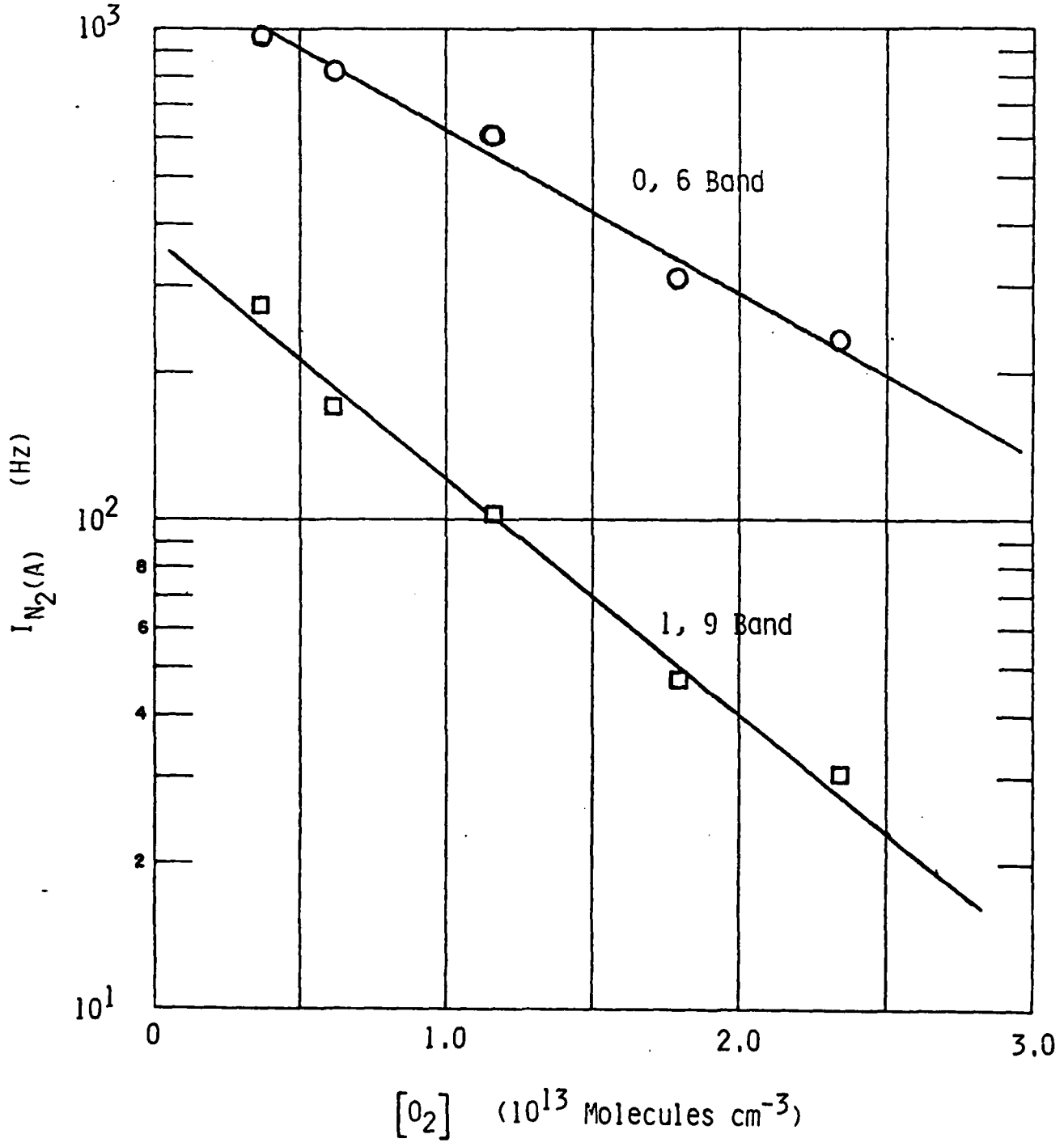

Fig. 35 Variation in intensity of 0, 6 and 1, 9 Bands of the Vegard-Kaplan system as a function of oxygen concentration for a mixing time of about 17 ms.

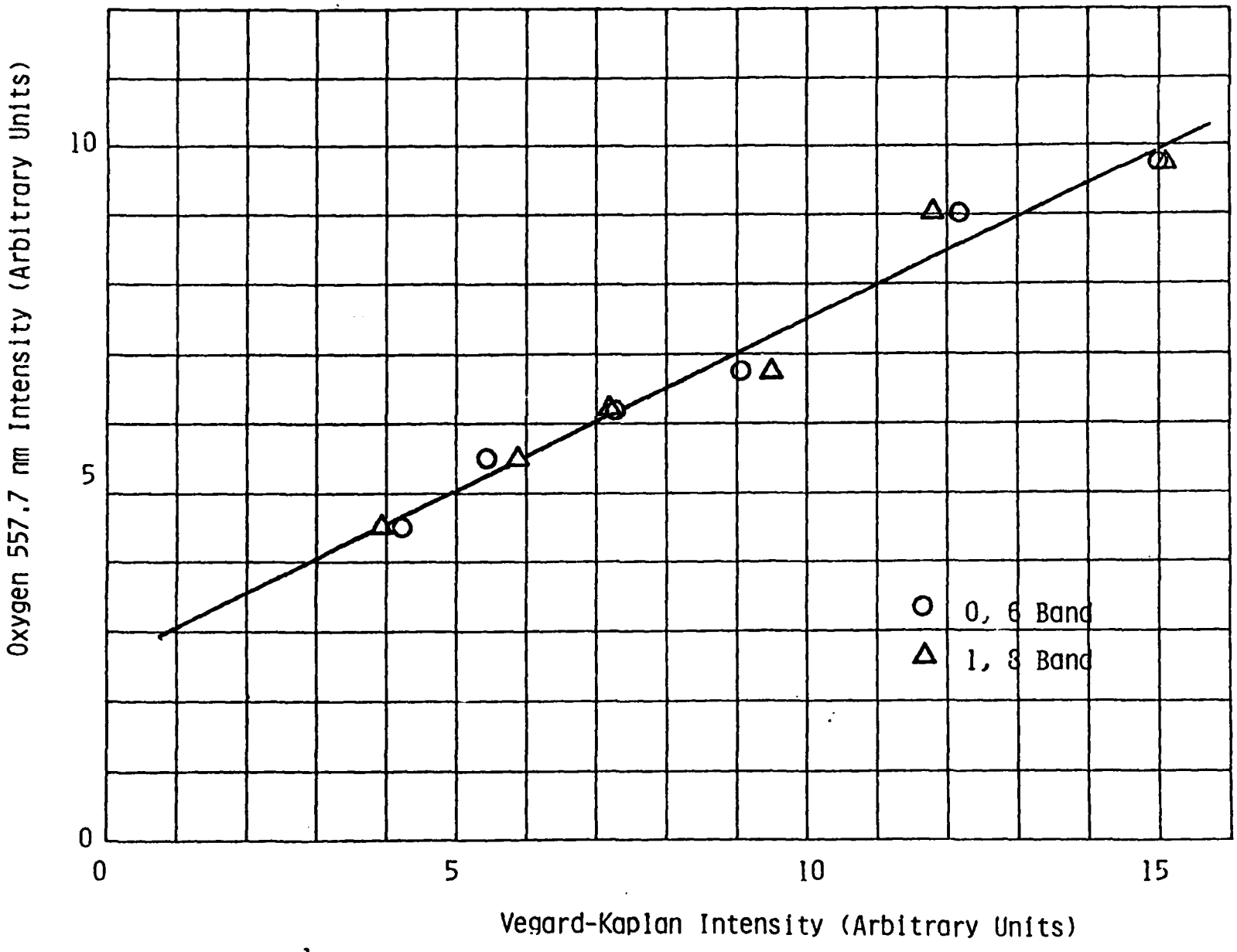

Fig. 36 Variation in $O(^1S)$ emission intensity as a function of $N_2(A)$ emission intensity

V. SUMMARY AND CONCLUSIONS

The primary study performed on the COCHISE facility was the examination of the NO infrared fluorescence resulting from the chemi-excitation reaction between metastable nitrogen atoms and oxygen molecules. It has been concluded that the observed NO vibrational populations were directly proportional to the relevant chemical production rates; i.e., collisional and radiational losses of vibrationally excited nitric oxide were unimportant during the gas residence time. Therefore the relative rate constants for production of NO in various vibrational levels could be defined from the data; it was found that the average level of excitation of NO was ~4.5 quanta, which would correspond to ~27% of the available reaction exothermicity if the NO precursor was an $N(^2D)$ atom.

It became evident during the data analysis that additional diagnostic information would be valuable in developing a mechanistic interpretation of the observations. Examples of such information would include concentrations of $N(^2D)$ and $N(^2P)$ atoms and the absolute intensities of the infrared emission. A possible method for implementation of a nitrogen lamp resonance absorption diagnostic has been described and estimates of minimum detectable $N(^2D, ^2P)$ concentrations have been provided. Furthermore, an examination of the COCHISE optical system has also been undertaken and a crude estimate of the absolute concentration of NO has been developed. The full development of an absolute calibration must await a more detailed study which would specify the spatial variation of both the radiation source and the local optical collection efficiency over the volumetric field-of-view.

Preliminary measurements of NO first overtone band emissions and ozone infrared chemiluminescence have also been performed. The NO overtone signal exhibited effects due to underlying radiation from an unknown source at the shorter wavelengths; nonetheless, the deduced NO population distribution at higher vibrational levels was in agreement with that determined from NO fundamental band observations. The ozone chemiluminescence indicated a high level

of vibrational excitation in the ν_3 band, and intriguing changes in spectral shape and signal strength were observed upon variation of experimental parameters such as temperature and gas mixture. Additional measurements will be required in order to elucidate the appropriate mechanisms responsible for this behavior.

The last topic discussed involved a review of a flow experiment for the study of the reactions between $N_2(A^3\Sigma_u^+)$ and oxygen molecules and atoms. In this experiment the $N_2(A^3\Sigma_u^+)$ molecules are produced through collisions with $Ar(^3P_{0,2})$ metastables formed in a DC hollow cathode discharge in Ar. Oxygen atoms can be created either via N + NO titration or by discharge of O_2/rare gas mixtures. The primary purpose of the experiments is to determine the reaction products, and various ultraviolet fluorescence techniques have been proposed as possible diagnostics. Emission from the nitrogen Vegard-Kaplan bands is used as a diagnostic for the $N_2(A^3\Sigma_u^+)$ concentration. The feasibility of the experiment has been demonstrated, and preliminary observations of $N_2(A^3\Sigma_u^+)$ decay have been analyzed to estimate the relevant rate constants.

REFERENCES

1. G. E. Caledonia, B. D. Green, W. T. Rawlins and J. S. Goela, "LABCEDE and COCHISE Analysis II. Vol. I: COCHISE Studies," Physical Sciences Inc. Report PSI TR-116, February, 1978.

2. B. D. Green and G. E. Caledonia, "LABCEDE and COCHISE Analysis II: Vol. II: LABCEDE Studies," Physical Sciences Inc. Report PSI TR-116, February, 1978.

3. B. D. Green, G. Wilemski and G. E. Caledonia, "Remote Infrared Monitoring of Selected Tritiated Molecules," Physical Sciences Inc. Report PSI TR-110, December, 1977.

4. W. T. Rawlins and G. E. Caledonia, "Preliminary Analysis of HIRIS NO Spectral Data," Physical Sciences Inc. Report PSI TR-157, December, 1978.

5. W. T. Rawlins, L. G. Piper, B. D. Green and G. E. Caledonia, "LABCEDE and COCHISE Analysis II: Interim Scientific Report," Physical Sciences Inc. Report TR-164, February, 1979.

6. B. D. Green, G. E. Caledonia and R. E. Murphy, "SWIR-MWIR Electron Fluorescence Measurements in N_2/O_2 and Air," Air Force Geophysics Laboratory Report AFGL-TR-78-0083, April, 1978.

7. J. P. Kennealy, F. P. DelGreco, G. E. Caledonia and B. D. Green, "Nitric Oxide Chemi-excitation Occurring in the Reaction between Metastable Nitrogen Atoms and Oxygen Molecules," J. Chem. Phys. 69, 1574 (1978).

8. J. P. Kennealy, F. P. DelGreco, G. E. Caledonia and W. T. Rawlins, "COCHISE Laboratory Spectroscopic Studies of Atmospheric Phenomena with High-Sensitivity Cryogenic Instrumentation," in Proc. Soc. Photo-Opt. Instrumentation Eng. V. 191, ed. G. A. Vanasse, August, 1979, pp. 151-158.

9. A. Dalgarno "Infrared Day and Night Airglow of the Earths Upper Atmosphere," Phil. Trans. Roy. Soc. (London) A 264, 153 (1969).

10. D. L. Baulch, D. D. Drysdale, D. G. Horne and A. C. Lloyd, Evaluated Kinetic Data for High Temperature Reactions. II. Homogeneous Gas Phase Reactions of the $H_2 - N_2 - O_2$ System. (Butterworths, London, 1973).

11. F. Hushfar, J. W. Rogers and A. T. Stair, "Infrared Chemiluminescence of the Reaction $N + O_2 \rightarrow NO + O$," Appl. Opt. 10, 1843 (1971); also "Further Comments on the Chemiluminescent Reaction $N + O_2 \rightarrow NO + O$ and its Overtone Photon Efficiency," Appl. Opt. 11, 1656 (1972).

12. M. E. Whitson, Jr., L. A. Darnton and R. J. McNeal, "Vibrational Energy Distribution in the NO Produced by the Reaction of $N(^4S)$ with O_2," Chem. Phys. Lett. 41, 532 (1976).

13. E. S. Oran, P. S. Julienne and D. F. Strobel, "The Aeronomy of Odd Nitrogen in the Thermosphere," J. Geophys. Res. 80, 3068 (1975).

14. T. Ogawa and T. Shimazaki, "Diurnal Variations of Odd Nitrogen and Ionic Densities in the Mesophere and Lower Thermosphere; Simultaneous Solution of the Photochemical-Diffusive Equations," J. Geophys. Res. 80, 3945 (1975).

15. D. Kley, G. M. Lawrence and E. J. Stone, "The Yield of $N(^2D)$ Atoms in the Dissociative Recombination of NO^+," J. Chem. Phys. 66, 4157 (1977).

16. G. T. Black, T. G. Slanger, G. A. St. John and R. A. Young, "Vacuum UV Photolysis of N_2O. IV. Deactivation of $N(^2D)$" J. Chem. Phys. 51, 116 (1969).

17. C. L. Lin and F. Kaufman, "Reactions of Metastable Nitrogen Atoms," J. Chem. Phys. 55, 3760 (1971).

18. J. G. Moehlmann, J. T. Gleaves, J. W. Hudgens and J. D. McDonald, "Infrared Chemiluminescence Studies of the Reaction of Fluorine Atoms with Monosubstituted Ethylene Compounds," J. Chem. Phys. 60, 4790 (1974).

19. P. E. Charters, R. C. MacDonald and J. C. Polanyi, "Formation of Vibrationally Excited OH by the Reaction H + O_3," Appl. Opt. 10, 1747 (1971).

20. J. P. Kennealy, in preparation.

21. G. E. Caledonia, B. D. Green, G. A. Simons, J. P. Kennealy, F. X. Roberts, A. Corman and F. P. DelGreco, "COCHISE Studies I: Fluid Dynamical and Infrared Spectral Analysis," Air Force Geophysics Laboratory TR-77-0281, Environmental Research Paper #619, 9 December 1977.

22. B. McCarroll, "An Improved Microwave Discharge Cavity for 2450 MHz," Rev. Sci. Instr. 41, 279 (1970).

23. F. C. Fehsenfeld, K. M. Evenson and H. P. Broida, "Microwave Discharge Cavities Operating at 2450 MHz." Rev. Sci. Instr. 36, 294 (1965).

24. F. Kaufman, "The Production of Atoms and Simple Radicals in Glow Discharges," in Advances in Chemistry Series No. 80 (American Chemical Society, 1969), pp. 29-47.

25. F. P. Billingsley II, "Calculated Vibration Rotation Intensities for NO($X^2\pi$)," J. Molec. Spectrosc. 61, 53 (1976).

26. G. Herzberg, Molecular Spectra and Molecular Structure I, Spectra of Diatomic Molecules (D. Van Nostrand Co., New York, 1951), 2nd ed.

27. L. G. Piper, J. E. Velazco and D. W. Setser, "Quenching Cross Sections for Electronic Energy Transfer Reactions between Metastable Argon Atoms and Noble Gases and Small Molecules," J. Chem. Phys. 59, 3323 (1973).

28. J. A. Meyer, D. W. Setser and D. H. Stedman, "Energy Transfer Reactions of $N_2(A^3\Sigma_u^+)$. II. Quenching and Emission by Oxygen and Nitrogen Atoms," J. Phys. Chem. 74, 2238 (1970).

29. T. G. Slanger and G. Black, "Quenching of $N(^2D)$ by N_2 and H_2O," J. Chem. Phys. 64, 4442 (1976).

30. D. Husain, S. K. Mitra and A. N. Young, "Kinetic Study of Electronically Excited Nitrogen Atoms, $N(2\ ^2D_J, 2\ ^2P_J)$, by Attenuation of Atomic Resonance Radiation in the Vacuum Ultra-violet," J. Chem. Soc. Far. Trans. II 70, 1721 (1974).

31. R. C. Millikan and D. R. White. "Systematics of Vibrational Relaxation," J. Chem. Phys. 39, 3209 (1963).

32. D. W. Setser, D. H. Stedman and J. A. Coxon, "Chemical Applications of Metastable Argon Atoms. IV. Excitation and Relaxation of Triplet States of N_2," J. Chem. Phys. 53, 1004 (1970).

33. J. LeCalve and M. Bourene, "Pulse Radiolysis Study of Argon-Nitrogen Mixtures. Measurement of the Rate Constant of Metastable Argon Deexcitation by Nitrogen," J. Chem. Phys. 58, 1446 (1973).

34. J. W. Dreyer and D. Perner, "Deactivation of $N_2(A\ ^3\Sigma_u^+, v=0\text{-}7)$ by Ground State Nitrogen, Ethane, and Ethylene Measured by Kinetic Absorption Spectroscopy," J. Chem. Phys. 58, 1195 (1973).

35. C. R. Roy, J. E. Dreyer and D. Perner, "Rate Constants for Quenching of $N_2(A\ ^3\Sigma_u^+; v_A = 1 - 6,8)$ by Rare Gases," J. Chem. Phys. 63, 2131 (1975).

36. P. H. Vidaud, R. P. Wayne, M. Yaron and A. von Engel, "Collisional Quenching on $N_2(A\ ^3\Sigma_u^+; v = 0, 1)$ by N atoms, Ground State N_2 and a Pyrex Surface," J. Chem. Soc. Far. Trans. II 72, 1185 (1976).

37. T. G. Slanger, B. J. Wood and G. Black, "Temperature Coefficients for $N(^2D)$ Quenching by O_2 and N_2O," J. Geophys. Res. 76, 8430 (1971).

38. J. W. Dreyer, D. Perner and C. R. Roy, "Rate Constants for the Quenching of $N_2(A\ ^3\Sigma_u^+, v_A = 0 - 8)$ by CO, CO_2, NH_3, NO and O_2," J. Chem. Phys. 61, 3164 (1974).

39. R. E. Murphy, E. T. P. Lee and A. M. Hart, "Quenching of Vibrationally Excited Nitric Oxide by Molecular Oxygen and Nitrogen," J. Chem. Phys. 63, 2919 (1975).

40. R. B. Bernstein and R. D. Levine, "Role of Energy in Reactive Molecular Scattering: An Information-Theoretic Approach" in Advances in Atomic and Molecular Physics II, ed. by D. R. Bates and B. Bederson (Academic Press, New York 1975), pp. 216-297.

41. R. D. Levine and R. B. Bernstein, "Thermodynamic Approach to Collision Processes," in Modern Theoretical Chemistry, Vol. II: Dynamics of Molecular Collisions Part B, ed. by W. H. Miller (Plenum Publishing Co., New York, 1975) Chapter 7.

42. A. Ben-Shaul, R. D. Levine and R. D. Bernstein, "Entropy and Chemical Change, II. Analysis of Product Energy Distributions; Temperature and Entropy Deficiency," J. Chem. Phys. 57, 5427 (1972).

43. U. Dinur, R. Kosloff, R. D. Levine and M. J. Berry, "Analysis of Electronically Nonadiabatic Chemical Reactions: An Information Theoretic Approach," Chem. Phys. Let. 34, 199 (1975).

44. R. J. Donovan and D. Husain, "Recent Advances in the Chemistry of Electronically Excited Atoms," Chem. Rev. 70, 489 (1970).

45. J. I. Steinfeld, private communication.

46. I. Procaccio and R. D. Levine, "Vibrational Energy Transfer in Molecular Collisions: An Information Theoretic Analysis and Synthesis," J. Chem. Phys. 63, 4261 (1975).

47. H. H. Michels, "Calculation of the Integrated Band Intensities of NO," JQSRT 11, 1735 (1971).

48. C. W. von Rosenberg and D. W. Trainor, "Observations of Vibrationally Excited O_3 Formed by Recombination," J. Chem. Phys. 59, 2142 (1973); "Vibrational Excitation of Ozone Formed by Recombination," J. Chem. Phys. 61, 2442 (1974); "Excitation of Ozone Formed by Recombination II," J. Chem. Phys. 63, 5348 (1975).

49. R. F. Hampson, Jr. and D. Garvin, eds., Reaction Rate and Photochemical Data for Atmospheric Chemistry - 1977, NBS Spec. Pub. 513, U.S.G.P.O., 1978.

50. R. A. McClatchey, W. S. Benedict, S. A. Clough, D. E. Burch, R. F. Calfee, K. Fox, L. S. Rothman, and J. S. Garing, "AFCRL Atmospheric Absorption Line Parameters Compilation," Air Force Geophysics Laboratory Report AFCRL-TR-73-0096, 26 January 1973.

51. S. A. Clough and F. X. Kneizys, "Coriolis Interaction in the ν_1 and ν_3 Fundamentals of Ozone," J. Chem. Phys. 44, 1855 (1966); "Ozone Absorption in the 9.0 Micron Region," Air Force Geophysics Laboratory Report AFCRL-TR-65-862, November 1965.

52. M. J. C. Depannemaecker, B. Duterage and M. J. Bellet, "Systematic Calculations of Rotational Spectra of Normal and Substituted (^{18}O in Place of ^{16}O) Ozone Molecules," J. Quant. Spectrosc. Radiat. Transfer 17, 519 (1977); J. C. Depannemaecker and J. Bellet, "Rotational Spectra of $^{16}O_3$ and of the Five $^{18}O_3$ Isotopic Species," J. Mol. Spectrosc. 66, 106 (1977).

53. A. Barbe, C. Secroun, and P. Jouve, "Infrared and Microwave High-Resolution Spectrum of the ν_3 Band of Ozone," J. Mol. Spectrosc. 64, 343 (1977).

54. D. J. McCaa and J. H. Shaw, "The Infrared Spectrum of Ozone," J. Mol. Spectrosc. 25, 374 (1968).

55. A. Barbe, C. Secroun, and P. Jouve, "Spectre d'Absorption Infrarouge de l'Ozone Gazeux," Compte Rendue Acad. Sci. Paris 274, 615 (1972).

56. W. R. Hunter and S. A. Malo, "The Temperature Dependence of the Short Wavelength Transmittance Limit of Vacuum Ultraviolet Window Materials - I. Experiment," J. Phys. Chem. Solids 30, 2739 (1969).

57. A. C. G. Mitchell and M. W. Zemansky, Resonance Radiation and Excited Atoms (Cambridge Univ. Press, New York, 1934).

58. F. Kaufman and D. A. Parkes, "Sources of Error in Using Resonance Light Absorption to Measure Atomic Concentration," Trans. Faraday Soc. 66, 1579 (1969).

59. W. T. Rawlins and F. Kaufman, "Characteristics of OI and NI Resonance Line Broadening in Low Pressure Helium Discharge Lamps," JQSRT 18, 561 (1977).

60. G. M. Lawrence and B. D. Savage, "Radiative Lifetimes of UV Multiplets in Boron, Carbon and Nitrogen," Phys. Rev. 141, 67 (1966).

61. S. Ogawa and M. Ogawa, "Absorption Cross Sections of $O_2(a\ ^1\Delta_g)$ and $O_2(X\ ^3\Sigma_g^-)$ in the Region from 1087 to 1700 Å," Can. J. Phys. 53, 1845 (1975).

62. D. E. Spencer, "Out of Focus Photometry," J. Opt. Soc. Amer. 55, 396 (1965).

63. R. A. Sawyer, Experimental Spectroscopy (Dover, New York, 1963).

64. W. Swider, "Atmospheric Formation of NO from $N_2(A\ ^3\Sigma)$," Geophys. Res. Lett. 3, 335 (1976).

65. O. J. Dunn and R. A. Young, "Quenching of $N_2(A\ ^3\Sigma_u^+)$ by O_2, O, N and H," Int. J. Chem. Kin. 8, 161 (1976).

66. W. E. Sharp, M. H. Rees and A. I. Stewart, "Coordinated Rocket and Satellite Measurements of an Auroral Event 2. The Rocket Observations and Analysis," J. Geophys. Res. 84, 1977 (1979).

67. R. R. O'Neil, E.T.P. Lee, and E. R. Huppi, "Auroral $O(^1S)$ Production and Loss Processes: Ground-Based Measurements of the Artificial Auroral Experiment Precede," J. Geophys. Res. 84, 823 (1979).

68. J. A. Meyer, D. W. Setser and D. H. Stedman, "Excitation of the Auroral Green Line of Atomic Oxygen ($^1S \rightarrow {}^1D$) by $N_2(A\ ^3\Sigma_u^+)$, Astrophys. J. 157, 1923 (1969).

69. R. A. Young, G. Black, and T. G. Slanger, "Vacuum-Ultraviolet Photolysis of N_2O. II. Deactivation of $N_2(A\ ^3\Sigma_u^+)$ and $N_2(B^3\pi_g)$," J. Chem. Phys. 50, 303 (1969).

70. T. G. Slanger, B. J. Wood, and G. Black, "Temperature-Dependent $N_2(A\ ^3\Sigma_u^+)$ Quenching Rate Coefficients," J. Photochem. 2, 63 (1974).

71. A. B. Callear and P. M. Wood, "Rates of Energy Transfer from N_2 $(A\ ^3\Sigma_u^+)$ to Various Molecules. Initial and Final Quantum States in the Transfer to NO $X^2\pi$ and Hg (6^1S_0) and Vibrational Relaxation of N_2 $(A\ ^3\Sigma_u^+)$ (v=1) in Helium," Trans. Faraday Soc. 67, 272 (1971).

72. J. A. Meyer, D. H. Klosterboer, and D. W. Setser, "Energy Transfer Reactions of $N_2(A\ ^3\Sigma_u^+)$. IV. Measurement of the Radiative Lifetime and Study of the Interaction with Olefins and Other Molecules," J. Chem. Phys. 55, 2084 (1971).

73. J. A. Meyer, D. A. Setser and W. G. Clark, "Rate Constants for Quenching of N_2 $(A\ ^3\Sigma_u^+)$ in Active Nitrogen," J. Phys. Chem. 76, 1 (1972).

74. W. G. Clark and D. W. Setser, "Energy Transfer Reactions of N_2 $(A\ ^3\Sigma_u^+)V$: Quenching by Hydrogen Halides, Methyl Halides and Related Molecules," J. Phys. Chem. to be published (1980).

75. D. H. Stedman and D. W. Setser, "Chemical Applications of Metastable Argon Atoms II. A Clean System for the Formation of N_2 $(A\ ^3\Sigma_u^+)$." Chem. Phys. Lett. 2, 542 (1968).

76. J. H. Kolts, H. C. Brashears, and D. W. Setser, "Redetermination of the $N_2(C)$ and $N_2(B)$ Branching Ratio from the Ar $(^3P_{0,2})$ + N_2 Reaction," J. Chem. Phys. 67, 2931 (1977).

77. J. M. Cook, T. A. Miller, and V. E. Bondybey, "Production of Metastable Rare Gas Atoms in Microwave and DC Discharges," J. Chem. Phys. 68, 2001 (1978).

78. D. H. Stedman and D. W. Setser, "Chemical Applications of Metastable Rare Gas Atoms," Prog. React. Kinet. 6, 193 (1971).

79. M. F. Golde and B. A. Thrush, "Vacuum UV Emission from Reactions of Metastable Inert Gas Atoms: Chemiluminescence of ArO and ArCl," Chem. Phys. Lett. 29, 486 (1974).

80. D. E. Shemansky, "N_2 Vegard-Kaplan System in Absorption," J. Chem. Phys. 51, 689 (1969).

81. A. Fontijn, C. B. Meyer, and H. I. Schiff, "Absolute Quantum Yield Measurements of the NO - O Reaction and Its Use as a Standard for Chemiluminescent Reactions," J. Chem. Phys. 40, 64 (1964).

82. D. H. Stedman and D. W. Setser, "Energy Pooling by Triplet Nitrogen ($A\ ^3\Sigma_u^+$) Molecules," J. Chem. Phys. 50, 2256 (1969).

83. G. N. Hays, C. J. Tracy, A. R. deMonchy, and H. J. Oskam, "Production of $N_2(C^3\pi_u)$ and $N_2\ (C'^3\pi_u)$ by Mutual Collisions of $N_2\ (A\ ^3\Sigma_u^+)$ Metastable Molecules," Chem. Phys. Lett. 14, 352 (1972).

84. G. N. Hays and H. J. Oskam, "Population of $N_2(B^3\pi)$ by $N_2\ (A\ ^3\Sigma_u^+)$. During the Nitrogen Afterglow," J. Chem. Phys. 59, 1507 (1973).

85. A. J. D. Farmer, V. Hasson, and R. W. Nicholls, "Absolute Oscillator Strength Measurements of the (v"=0, v'=0-3) bands of the ($A^2\Sigma - X^2\pi$) γ-system of Nitric Oxide," J. Quant. Spectro. Radiat. Transfer 12, 627 (1972).

86. R. A. Sutherland and R. A. Anderson, "Radiative and Predissociative Lifetimes of $A^2\Sigma^+$ state of OH," J. Chem. Phys. 58, 1226 (1973).

87. W. H. Smith and H. S. Liszt, "Franck-Condon Factors and Absolute Oscillator Strengths for NH, SiH, S_2, and SO," J. Quant. Spectrosc. Radiat. Transfer 11, 45 (1971).

88. L. G. Piper, R. H. Krech, and R. L. Taylor, "Investigation of Concept of Efficient Short Wavelength Laser," PSI TR-128 under ERDA Contract No. ES-77-C-02-4223.A002 (1978).

89. L. G. Piper, Unpublished results (1978).

90. H. Bubert, "Population and Predissociation of Vibronic States of Nitric Oxide," J. Chem. Phys. 56, 1113 (1972).

91. R. A. Young, G. Black, and T. G. Slanger, "4000 - 8000 Å Emission from the Far Ultraviolet Photolysis of N_2O, NO, NO_2, CO, CO_2 and O_2," J. Chem. Phys. 48, 2067 (1968).

92. H. Okabe, "Excited Species and Their Contribution to NO (ß, γ) Fluorescence in the Photodissociation of N_2O," J. Chem. Phys. 47, 101 (1967).

93. E. E. Ferguson, F. C. Fehsenfeld, and A. L. Schmeltekopf, "Flowing Afterflow Measurements of Ion-Neutral Reactions," in Adv. Atom. Molec. Phys. V, 1-56 (1970), ed. D. R. Bates.

APPENDIX A

NO DATA ANALYSIS

1) Experimental Data

Spectra of the NO fundamental band near 5.2 μm were analyzed for experiments from series 335600 - 387700 (11/30/76 - 10/14/77). In all, 29 spectra with acceptable signal-to-noise were analyzed. Prior to the spectral simulation procedure, all observed spectra were corrected for the relative system spectral response by the appropriate black body calibrations. Some spectra were also edited in order to remove occasional large transient noise spikes which were clearly not associated with the observed infrared emission. No cases were included in the analysis where resolution degradation occured as a result of signal amplification.

The observed spectra can be divided into three classes on the basis of their structural features; each class corresponds to a different range of static helium pressure in the reaction cell. Representative experimental spectra for these classes are shown in Figs. A-1 → A-3. When no helium is present in the reaction cell, the spectrum is characteristically broad and exhibits little rotational structure (i.e., Fig. A-1). For the spectrum in Fig. A-2, 3 mtorr of helium was present as a background gas; in this case, considerable structure is apparent. This spectrum is characteristic of those observed in the presence of low pressures of helium (1 - 5 mtorr), except that the structure is enhanced somewhat with increasing helium pressure. Spectra observed in the presence of relatively large amounts of helium (8 - 15 mtorr) exhibit very pronounced structure, as shown in Fig. A-3 for 10 mtorr of helium. Note also that the spectral intensity distribution drops more rapidly at longer wavelengths than in the previous cases; this indicates that in this case the relative populations of the higher vibrational levels are considerably lower than those observed at lower helium pressures.

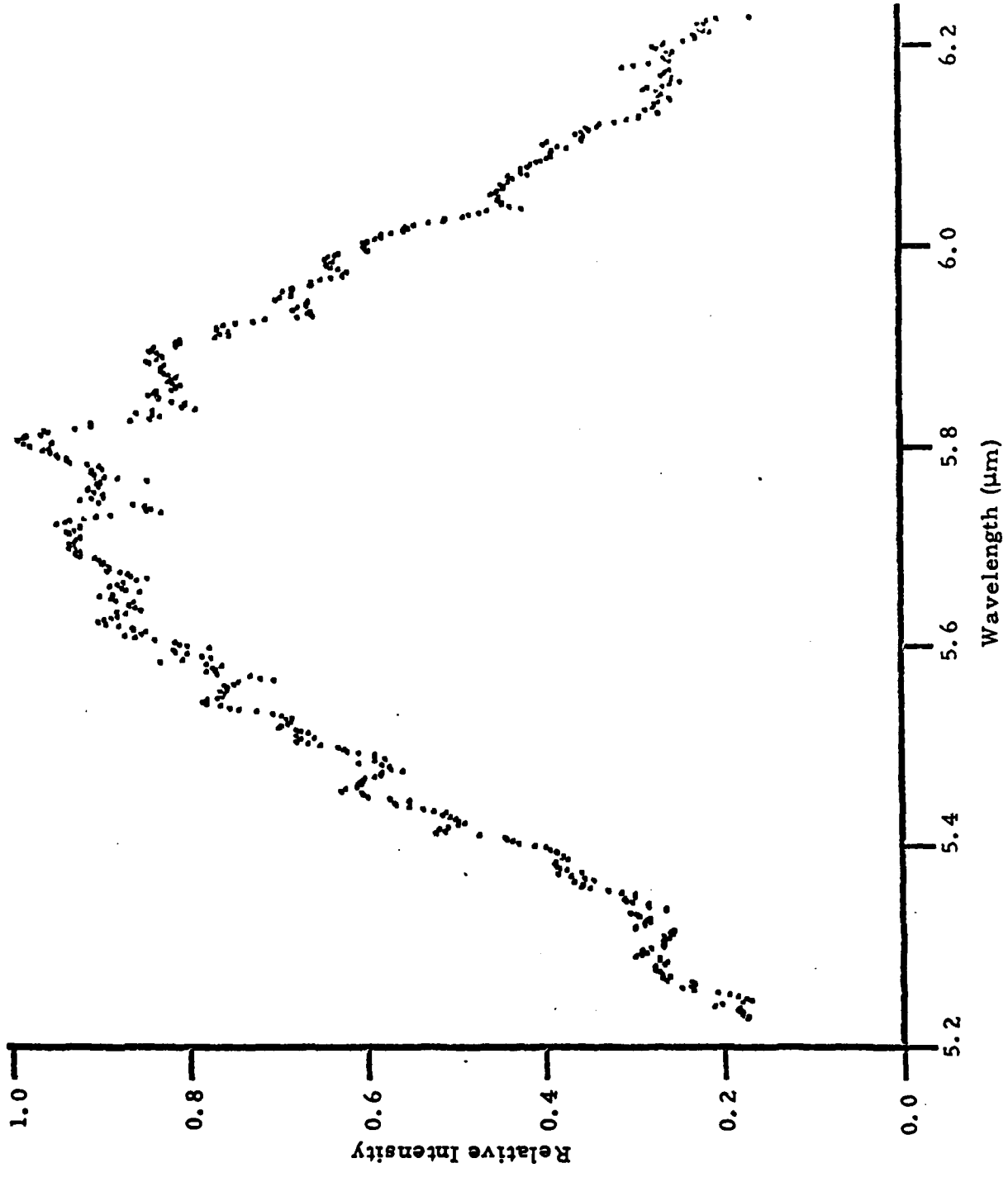

Fig. A-1 Observed spectrum for experiment 286706 (see Table A-I).

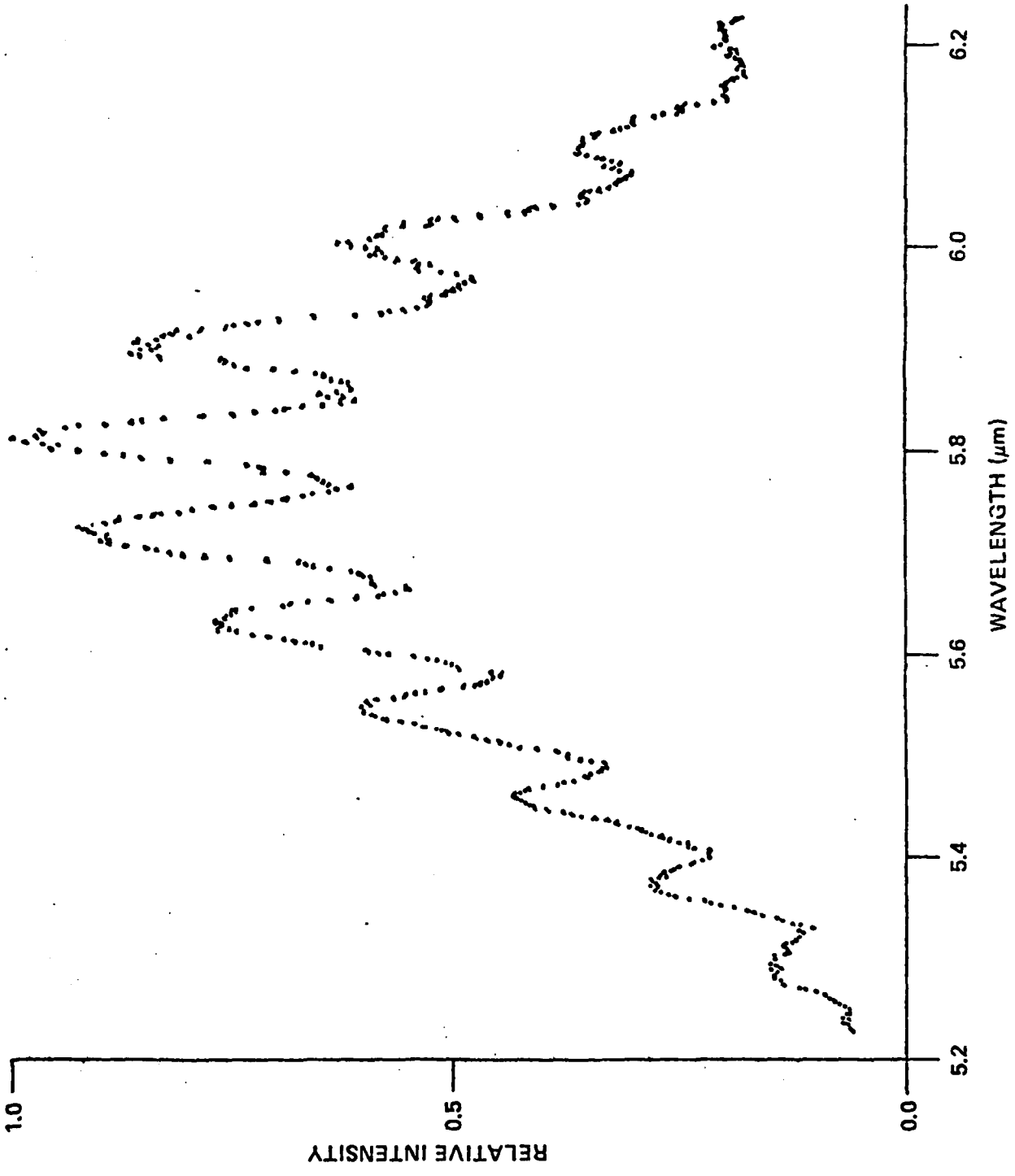

Fig. A-2 Observed spectrum for experiment 287706 (see Table A-I).

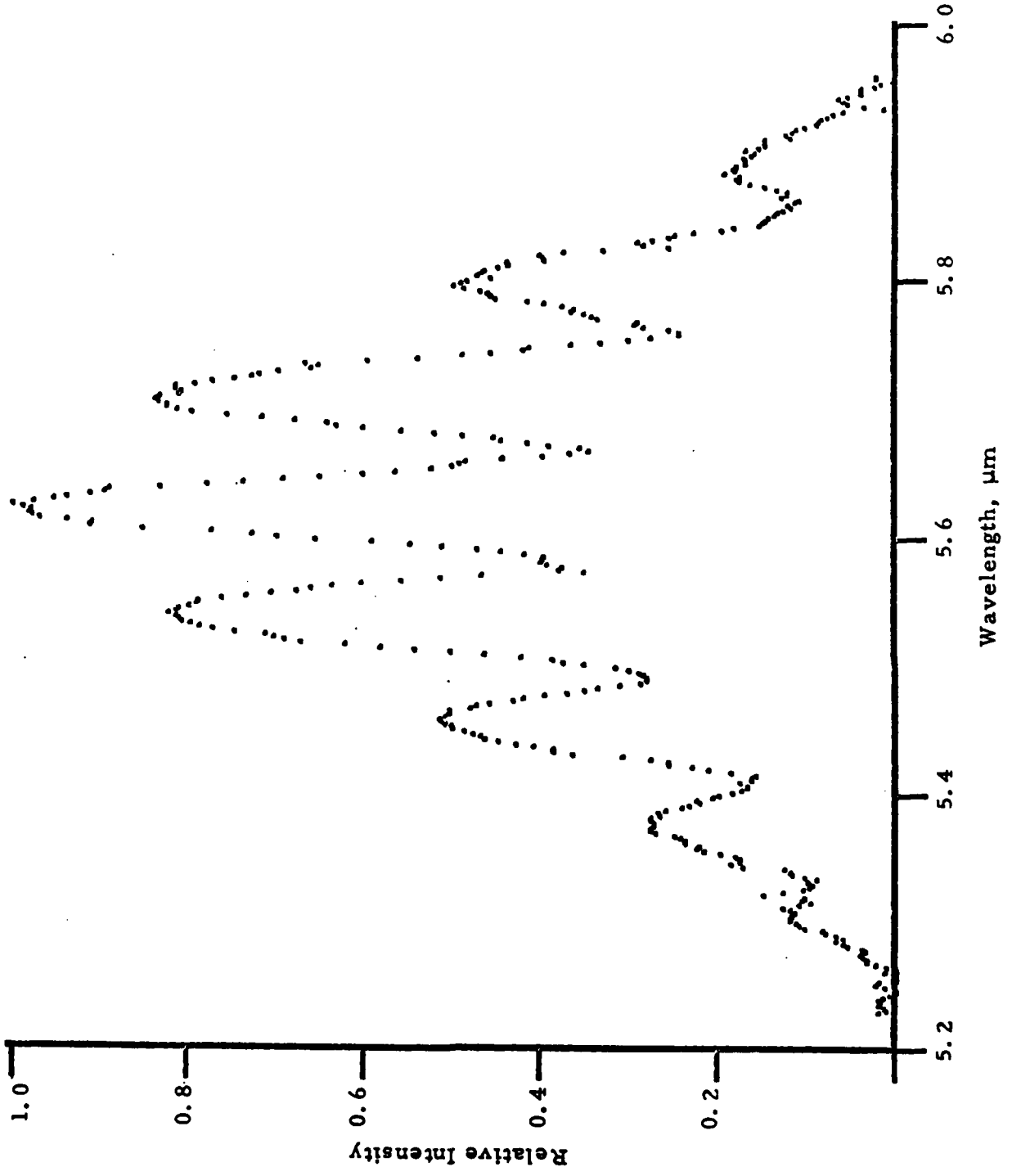

Fig. A-3 Observed spectrum for experiment 269706 (see Table A-I).

2) Spectral Fitting Procedure

The direction taken in the spectral simulation analysis was to first determine the sensitivity of the derived vibrational population distributions to the parameters and fine details of the spectral match. When a systematic approach to the parameterization was established, relative population distributions were obtained for all the spectra. These distributions were then compared to determine the level of consistency and reproducibility of the experiments. The ultimate goal of the analysis was to determine a relative population distribution which was unaffected by collisions. A complete listing of the results, with the experimental conditions and the derived relative population distributions, is given in Tables A-I and A-II.

The variable parameters in the spectral fitting routine are the instrument resolution (full width at half maximum of the triangular slit function), the rotational temperature (assuming a Boltzmann rotational distribution), and the relative populations of the $\Omega = 1/2, 3/2$ total angular momentum states (which may be either determined by the rotational temperature or varied separately). In general, reduction of the values of the resolution, rotational temperature, or effective spin-state temperature gives rise to an enhancement of the structure in the computed spectrum. Appropriate values for the resolution were determined by comparison of the calculated and observed fine rotational structure under conditions when the overall spectrum was well matched; in general, the apparent resolution was found to correspond to 1.30 - 1.35 times the nominal value for a given slit width, as determined from the angular dispersion of the monochromator. For consistency, this factor was applied throughout the analysis of the zero- and low-helium data and the resolution was varied to achieve a fit only in the case of the high-helium spectra. The only effect of increasing or decreasing the resolution is to slightly decrease or increase the value of the rotational temperature required to achieve a good match between experimental and

TABLE A-I

EXPERIMENTAL AND COMPUTATIONAL PARAMETERS
FOR INDIVIDUAL EXPERIMENTS

Experiment Number	P_{He} mt	Flows, Std ℓ min^{-1}			Parameters of Calculated Spectrum		
		Ar	N_2	O_2	T, K	FWHM, μm	σ, %
335612	2	6	0.05	6	120	0.035	3.5
028706	0	3.6	0.4	4.0	180	0.035	3.6
028707	0	3.6	0.4	4.0	180	0.035	3.5
028708	3	3.6	0.4	4.0	80	0.035	3.1
028710	2	3.6	0.4	4.0	110	0.035	2.8
028711	2	3.6	0.4	4.0	120	0.035	3.5
032702	0	3.6	0.4	4.0	180	0.035	3.6
033702	0	3.6	0.4	4.0	180	0.035	3.4
033703	0	3.6	0.4	4.0	180	0.020	3.5
034702	0	3.6	0.4	4.0	180	0.035	3.2
034704	0	4.9	0.1	5.0	140	0.035	3.1
034705	0	0	4.4	3.2	100	0.035	6.4
035702	15	3.6	0.4	1.5	40	0.030	2.3
035703	15	3.6	0.4	0.4	40	0.018	3.5
035705	8	1.0	0.25	0.6	40	0.035	4.3
257702	1.4	3.6	0.4	4.0	120	0.035	4.3
257711	12	3.6	0.4	4.0	60	0.018	4.6
269703	5	3.6	0.4	4.0	70	0.027	3.2
269704	4.5	3.6	0.4	4.0	70	0.018	7.4
269705	4.3	3.6	0.4	4.0	70	0.035	5.1
269706	10	3.6	0.4	4.0	40	0.027	2.5

TABLE A-I (Cont'd)

Experiment Number	P_{He} mt	Flows, Std ℓ min^{-1}			Parameters of Calculated Spectrum		
		Ar	N_2	O_2	T, K	FWHM, μm	σ, %
283707	0	3.6	0.4	4.0	180	0.027	5.5
283708	0	3.6	0.4	4.0	180	0.027	3.9
286703	0	3.6	0.4	4.0	180	0.035	4.2
286705	0	3.7	0.2	4.0	200	0.035	3.3
286706	0	3.9	0.1	4.0	180	0.035	2.9
286708	0	3.9	0.1	4.0	180	0.035	4.1
287705	3.0	3.8	0.1	4.0	100	0.027	2.3
287706	3.2	3.8	0.1	4.0	90	0.027	2.2

TABLE A-II

DERIVED RELATIVE POPULATIONS FOR INDIVIDUAL EXPERIMENTS

Experiment Number	$N_{(1)}$	$N_{(2)}$	$N_{(3)}$	$N_{(4)}$	$N_{(5)}$	$N_{(6)}$	$N_{(7)}$	$N_{(8)}$	$N_{(9)}$	$N_{(10)}$	$N_{(11)}$	$N_{(12)}$
335612	2.23	0.71	1.23	1.15	1.05	1.00	0.86	0.74	0.52	0.29	0.27	0.18
028706	2.43	1.42	1.28	1.53	1.36	1.00	0.94	0.93	0.73	0.39	0.24	0.23
028707	2.46	1.42	1.26	1.51	1.38	1.00	0.86	0.97	0.71	0.35	0.22	0.37
028708	1.80	0.89	1.14	1.11	1.09	1.00	0.90	0.78	0.49	0.31	0.14	0.12
028710	1.85	1.02	1.09	1.26	1.14	1.00	0.94	0.81	0.48	0.35	0.18	0.05
028711	2.12	1.00	1.19	1.33	1.12	1.00	0.94	0.81	0.55	0.35	0.21	0.13
032702	2.00	1.22	1.03	1.29	1.31	1.00	0.75	0.79	0.56	0.32	0.14	0.19
033702	2.62	1.50	1.14	1.53	1.53	1.00	0.79	0.95	0.65	0.26	0.24	0.29
033703	2.16	1.24	0.94	0.89	1.16	1.00	0.99	0.76	0.40	0.27	0.24	0.04
034702	2.25	1.23	0.90	1.22	1.25	1.00	0.94	0.91	0.56	0.30	0.23	0.18
034704	1.90	0.98	0.86	1.11	1.12	1.00	0.96	0.87	0.57	0.34	0.24	0.14
034705	1.89	1.00	0.71	1.00	0.89	1.00	0.85	0.74	0.55	0.23	0.21	0.18
035702	0.86	0.62	0.88	1.13	1.25	1.00	0.74	0.39	0.14	0.09	0.02	-
035703	0.79	0.77	0.69	1.00	0.95	1.00	0.85	0.62	0.38	0.24	0.10	0.02
035705	1.24	0.51	0.60	0.77	0.86	1.00	0.97	0.68	0.43	0.27	0.08	-

TABLE A-II (Cont'd)

Experiment Number	$N_{(1)}$	$N_{(2)}$	$N_{(3)}$	$N_{(4)}$	$N_{(5)}$	$N_{(6)}$	$N_{(7)}$	$N_{(8)}$	$N_{(9)}$	$N_{(10)}$	$N_{(11)}$	$N_{(12)}$
257702	1.23	0.84	0.78	0.89	0.97	1.00	0.91	0.70	0.41	0.21	0.13	0.13
257711	0.54	0.12	0.48	0.71	0.96	1.00	0.81	0.53	0.29	0.15	0.01	-
269703	1.48	0.93	1.05	1.01	1.25	1.00	1.09	0.40	0.33	-	-	-
269704	1.88	0.94	1.09	0.95	1.21	1.00	1.00	0.59	0.54	0.22	0.43	-
269705	1.55	0.86	1.03	0.88	1.20	1.00	0.95	0.62	0.31	0.20	0.15	
269706	1.32	1.16	1.70	1.89	1.65	1.00	0.36	0.05	0.05	-	-	-
283707	1.43	1.13	0.98	1.11	1.13	1.00	1.08	0.87	0.57	0.43	0.50	-
283708	1.32	1.05	0.95	0.99	1.07	1.00	1.01	0.79	0.54	0.45	0.47	
286703	1.61	1.12	0.88	1.11	1.16	1.00	0.91	0.88	0.50	0.25	0.36	
286705	1.85	1.01	0.83	1.04	1.07	1.00	0.86	0.71	0.41	0.22	0.19	
286706	2.08	0.93	0.89	1.23	1.14	1.00	1.02	0.79	0.39	0.22	0.26	
286708	2.82	1.13	0.83	1.44	1.34	1.00	1.08	0.98	0.41	0.17	0.41	
287705	1.26	0.66	0.77	0.91	0.94	1.00	0.94	0.68	0.41	0.21	0.18	
287706	1.05	0.59	0.77	0.84	0.94	1.00	0.89	0.70	0.40	0.23	0.15	

computed spectra (with no significant changes in the predicted populations). Similarly, the spin-state temperature was found to have an insignificant (< 10%) effect on the "best-fit" relative population distributions, although fits determined with finite spin temperature (equal population of both spin-states) typically required a rotational temperature about 15 K lower than those with equal spin and rotational temperatures. Structural features of the computed spectra were not significantly different for the two cases. For these reasons the spin and rotational temperatures were taken to be equal throughout the analysis. The apparent rotational temperature was the only parameter which was varied to fit the observed spectra for the zero- and low-helium cases.

The computed matches to the spectra of Figs. A-1 to A-3 are shown in Figs. A-4 - A-6 respectively. In general, spectra with zero-helium background can be matched using apparent rotational temperatures near 180 K. As can be seen,a temperature of this magnitude provides extensive overlapping of the spectra of different vibrational levels. Spectra with low (1 - 5 mtorr) helium background require temperatures near 90 K for a good fit. High-helium spectra require very low (~ 40 K) rotational temperatures to achieve a fit. In this case, because only a few rotational levels are significantly populated, little overlap between the $v \pm 1$ P and R branches and the adjacent bandcenters occurs. The quality of the computed matches has a tolerance of, at most, about ± 15 K for the temperature value; this amount of variation has < 5% effect upon the derived population distribution.

The derived populations for the lowest lying vibrational levels are affected by the presence of underlying background radiation near 5.2 μm. This background emission decreases in intensity with increasing helium pressure, perhaps due to collisional quenching effects, is present when the oxygen counterflow is cut off, and is not present when the nitrogen flow through the discharges is stopped (higher resolution scans, 0.0008 m,

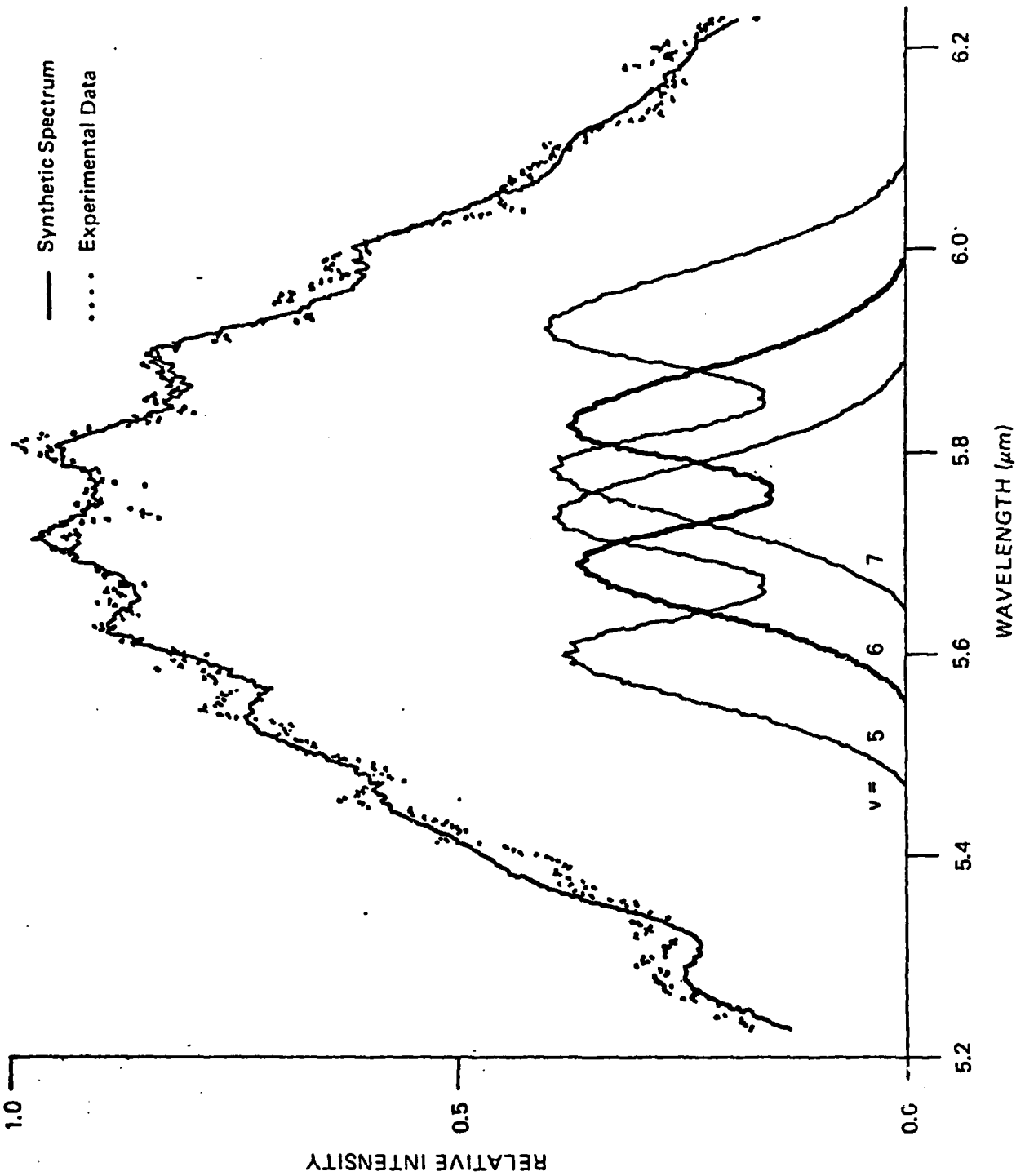

Fig. A-4 Comparison of synthetic and experimental spectrum, experiment 286706 (see Tables A-I and A-II).

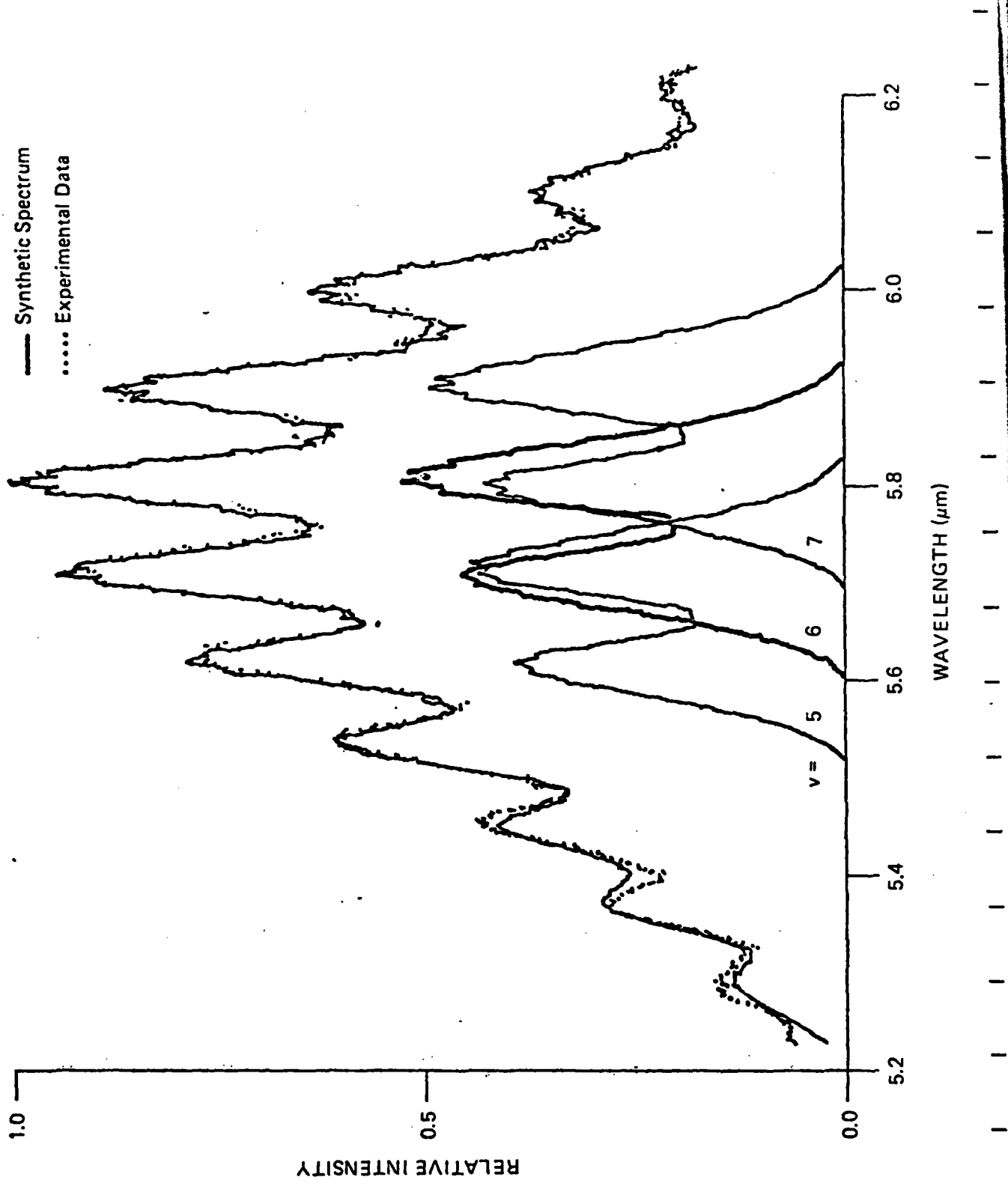

Fig. A-5 Comparison of synthetic and experimental spectra, experiment 287706 (see Tables A-I and A-II).

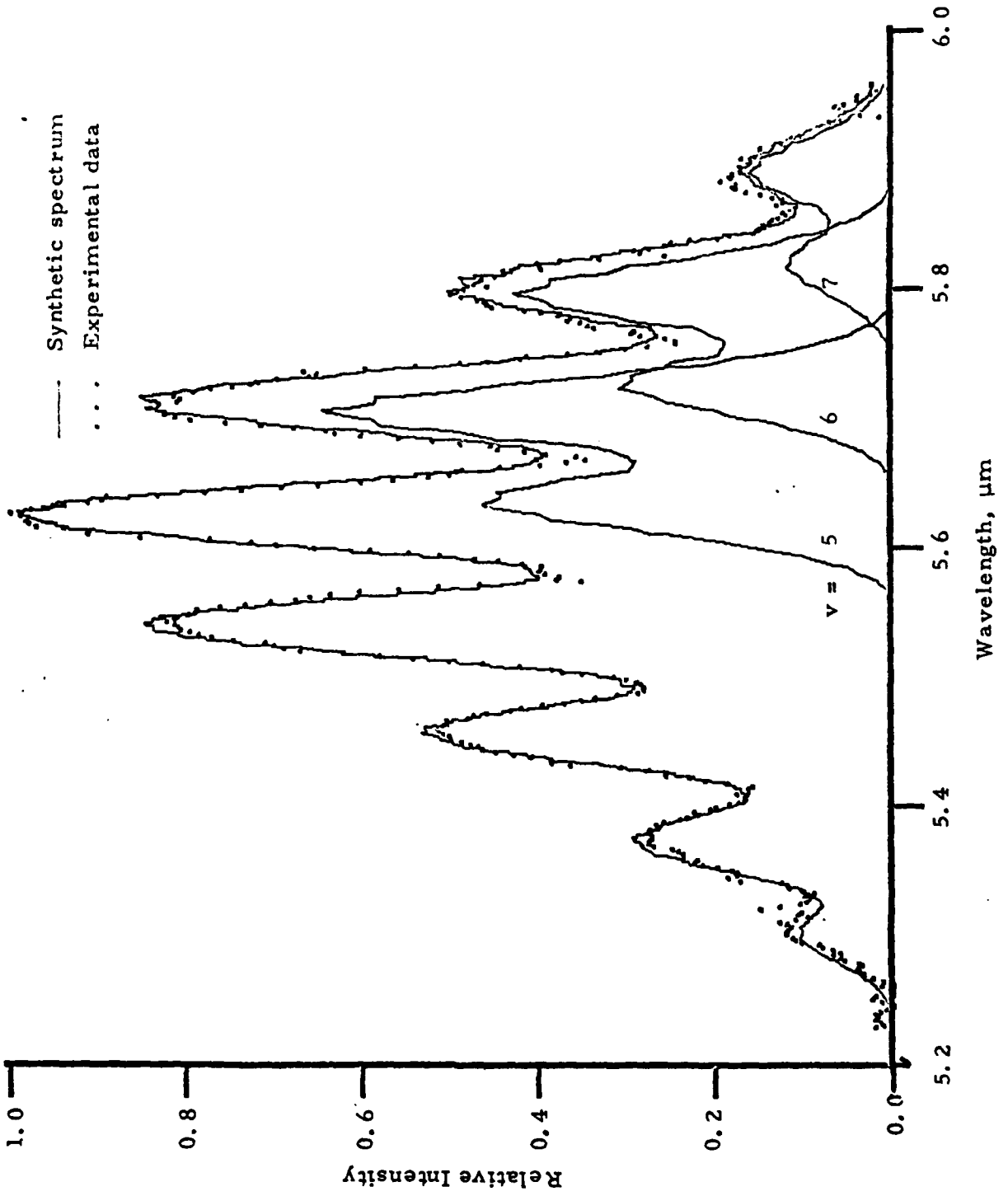

Fig. A-6 Comparison of synthetic and experimental spectra, experiment 269706 (see Tables A-I and A-II).

indicate that the spectrum of the background emission is similar to that of an inverted $^2\pi$ hydrogenic molecule; however, the band center frequency and rotational separation do not match calculated OH frequencies[1]).

In the zero-helium spectra, there are several sharp, experimentally reproducible structural features between 5.4 μm and 6.0 μm such that, while each feature can be approximately matched by synthetic spectra with slightly different temperatures, a close match of all the features at a single temperature cannot be achieved as it can for the low-helium case, cf. Figs. A-4 and A-5. This effect may be due to a non-Boltzmann rotational distribution; however, the resulting ± 15 K uncertainty in the "best-fit" temperature does nct affect the relative vibrational populations significantly. Simulation of the high-helium spectra presents a special problem. In the synthetic spectra, decreasing the temperature below 40 K causes an increase in intensity near the bandcenter due to an increase in the relative intensity of the low J lines which are unresolved from the Q branches. As a result, as the temperature is lowered, the apparent vibrational structure decreases. For this reason, a suitable match could only be obtained by decreasing the instrumental bandpass towards the nominal dispersion value. However, only five high-helium experiments have been analyzed, and trends in the results have not been clearly established.

3) Relative Vibrational Distributions

The individual relative vibrational distributions derived from the spectral fitting procedure are listed in Table A-II, and are plotted chronologically in Figs. A-7. Consecutive experiments tend to yield highly reproducible results, but there are some systematic fluctuations over long periods. Variation of the Ar, N_2, and O_2 flows over the ranges 0 - 6, 0.05 - 4.4, and 3.2 - 6 standard liter/min. (reaction zone partial pressures 0 - 2.1, 0.017 - 1.6, and 1.1 - 2.1 mtorr) have no effect upon the observed

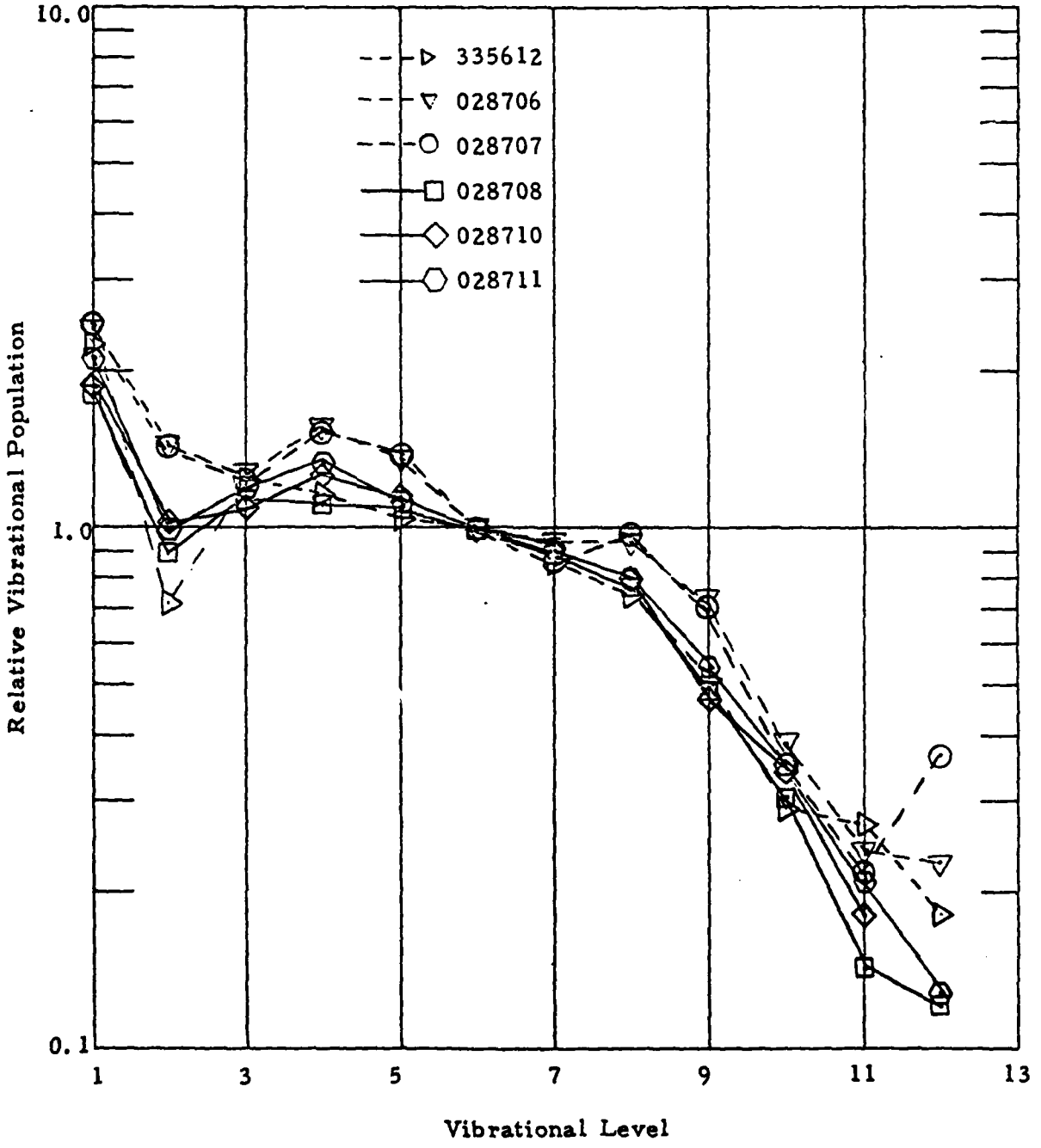

Fig. A-7a Derived relative populations for experiments listed above.

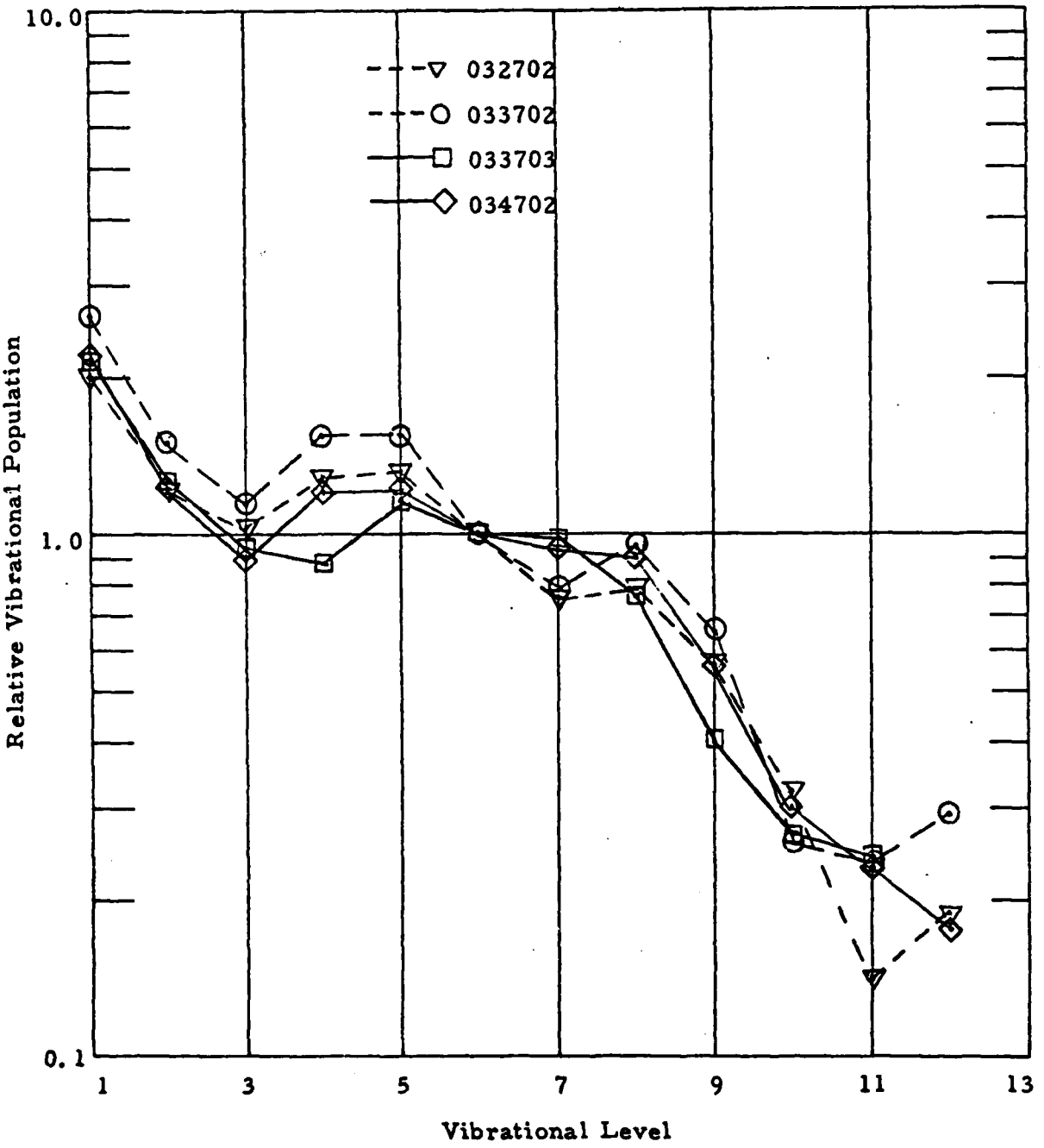

Fig. A-7b Derived relative populations for the experiments listed above.

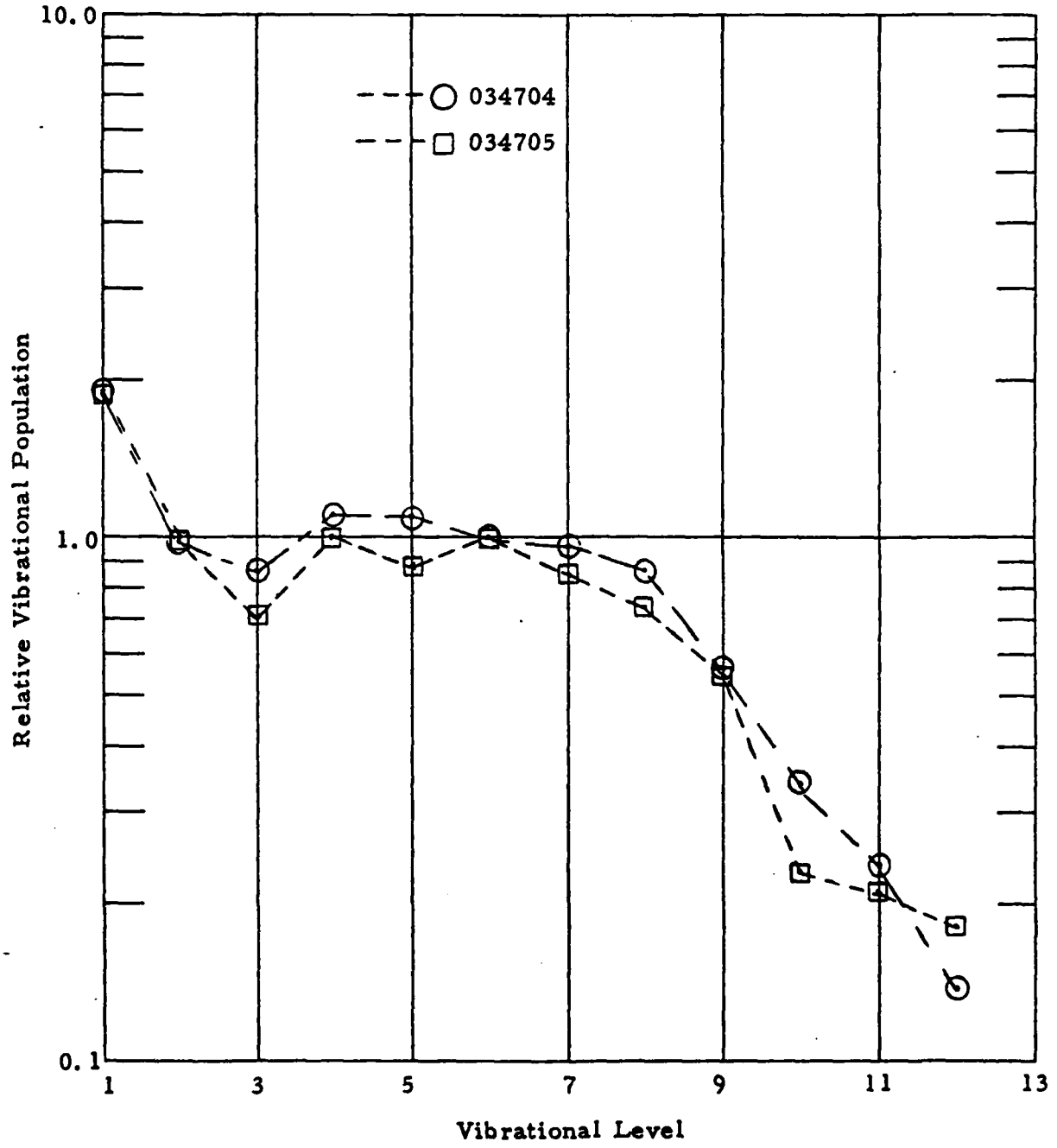

Fig. A-7c Derived relative populations for experiments listed above.

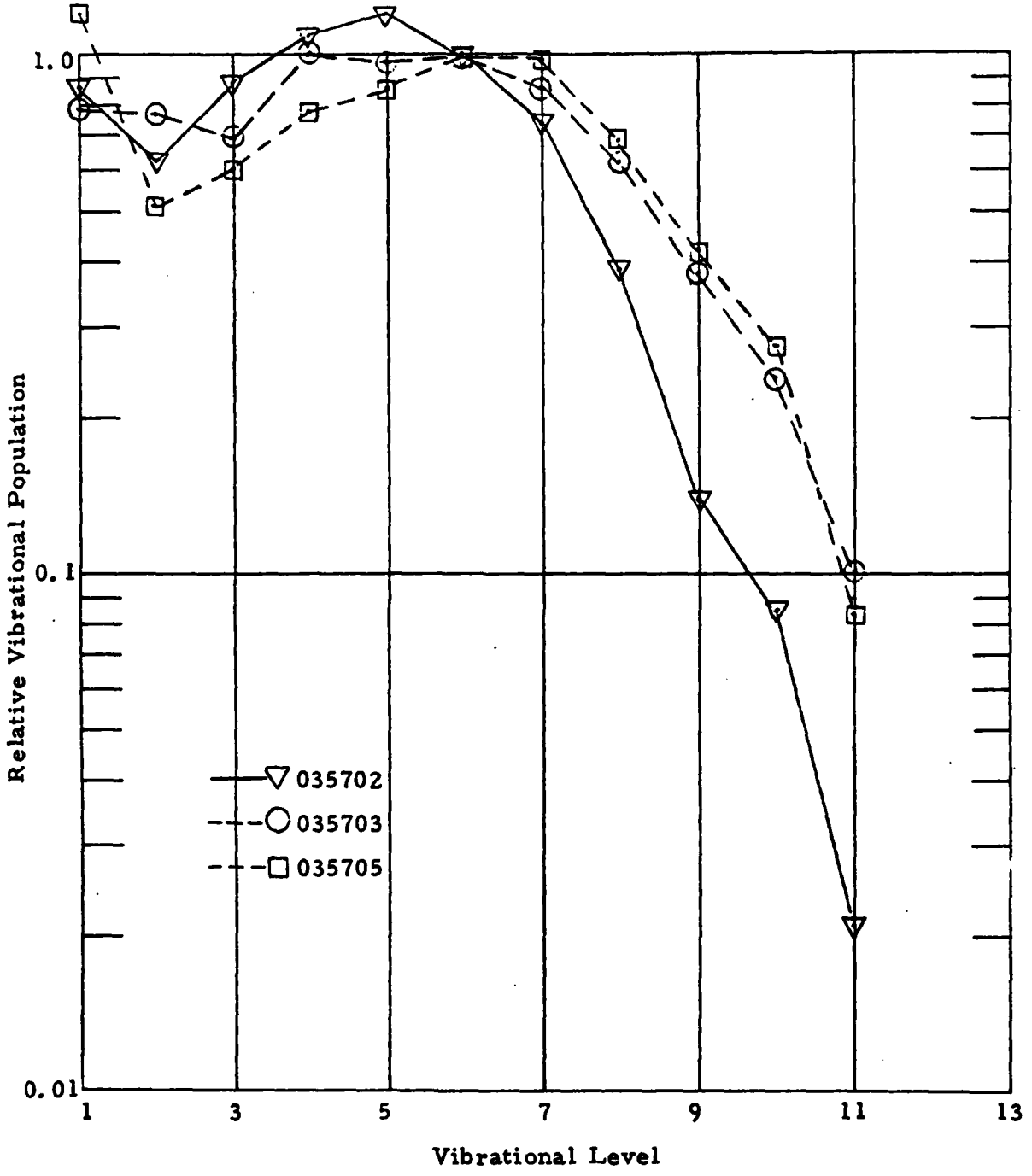

Fig. A-7d Derived relative populations for experiments listed above.

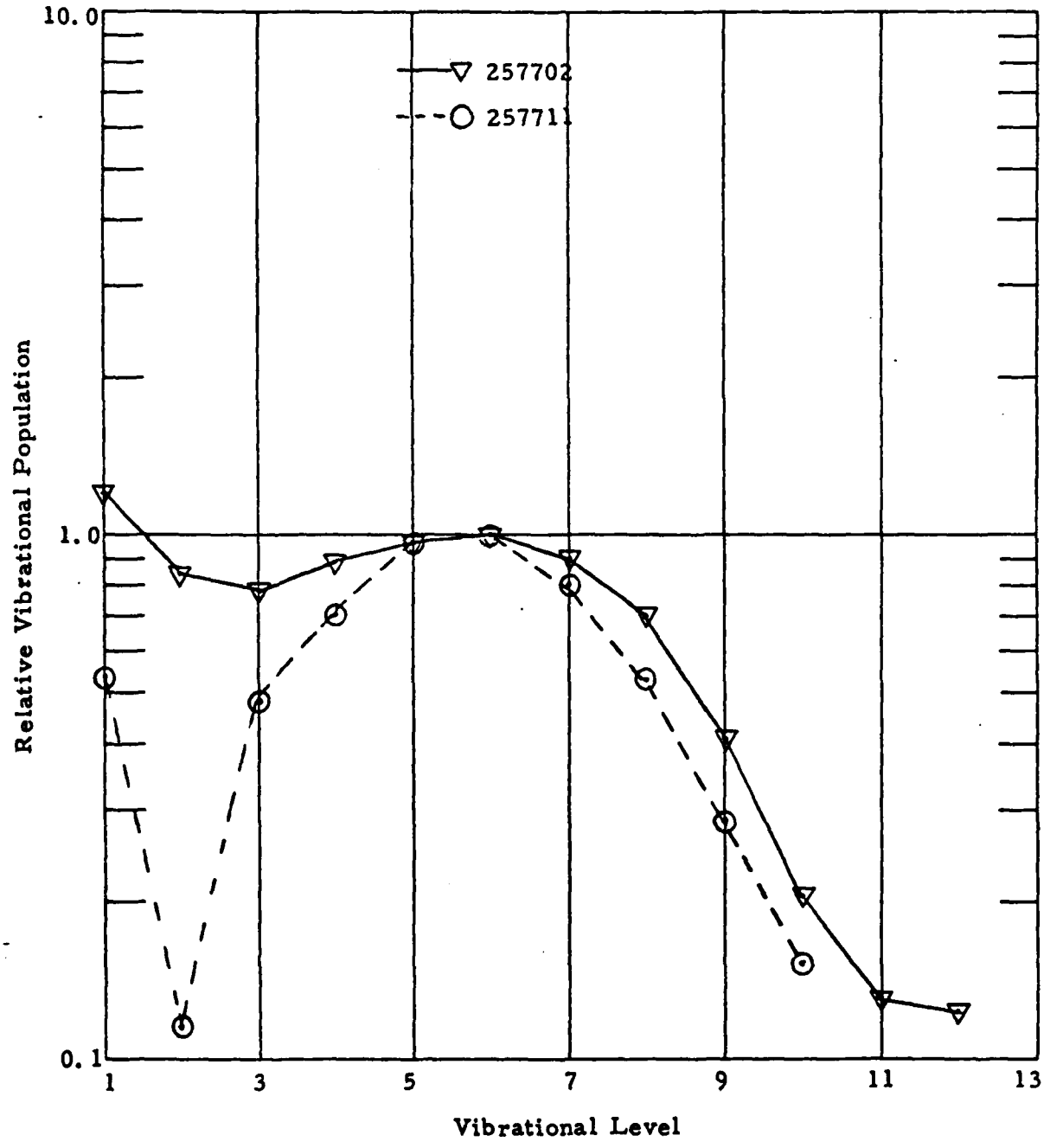

Fig. A-7e Derived relative populations for experiments listed above.

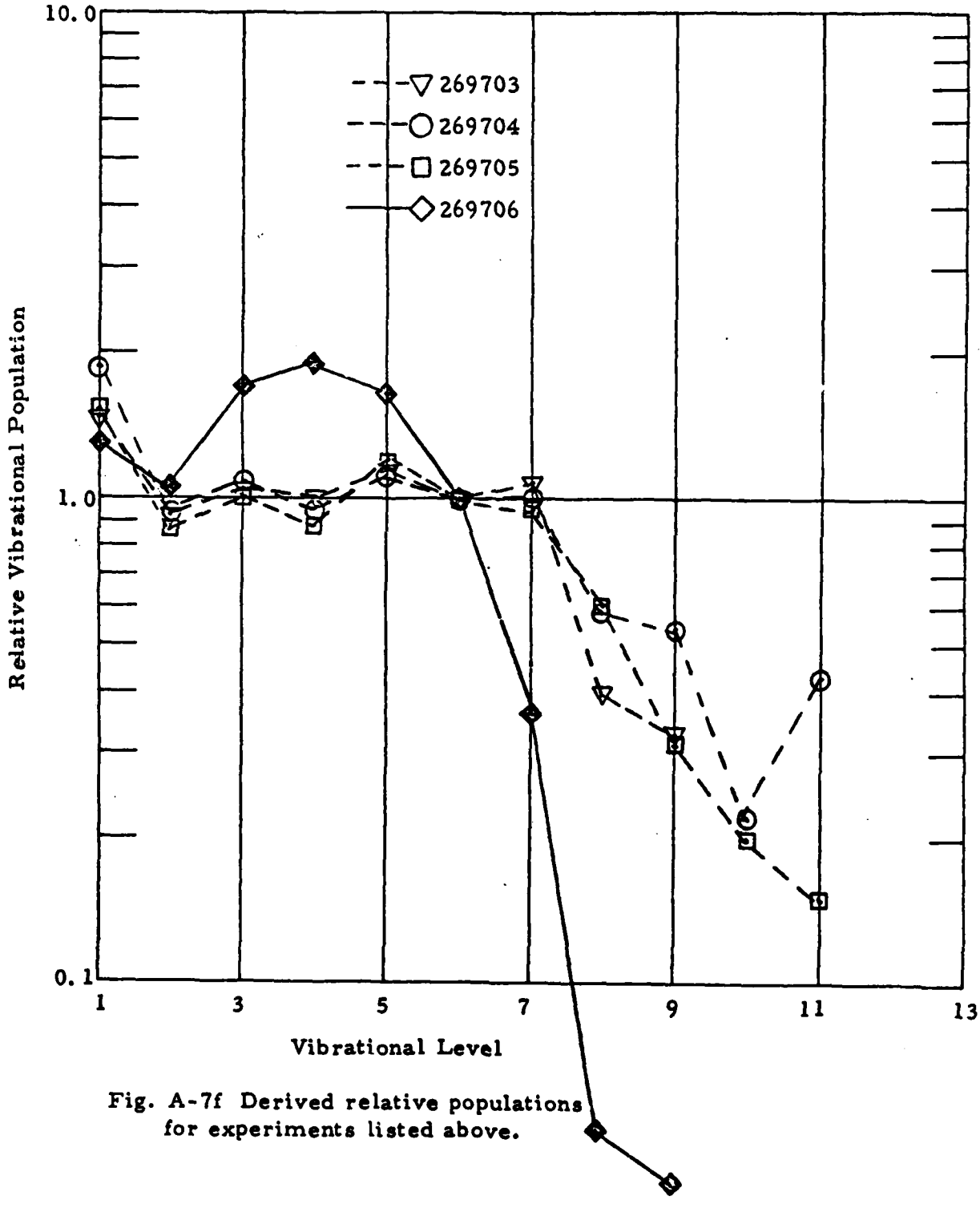

Fig. A-7f Derived relative populations for experiments listed above.

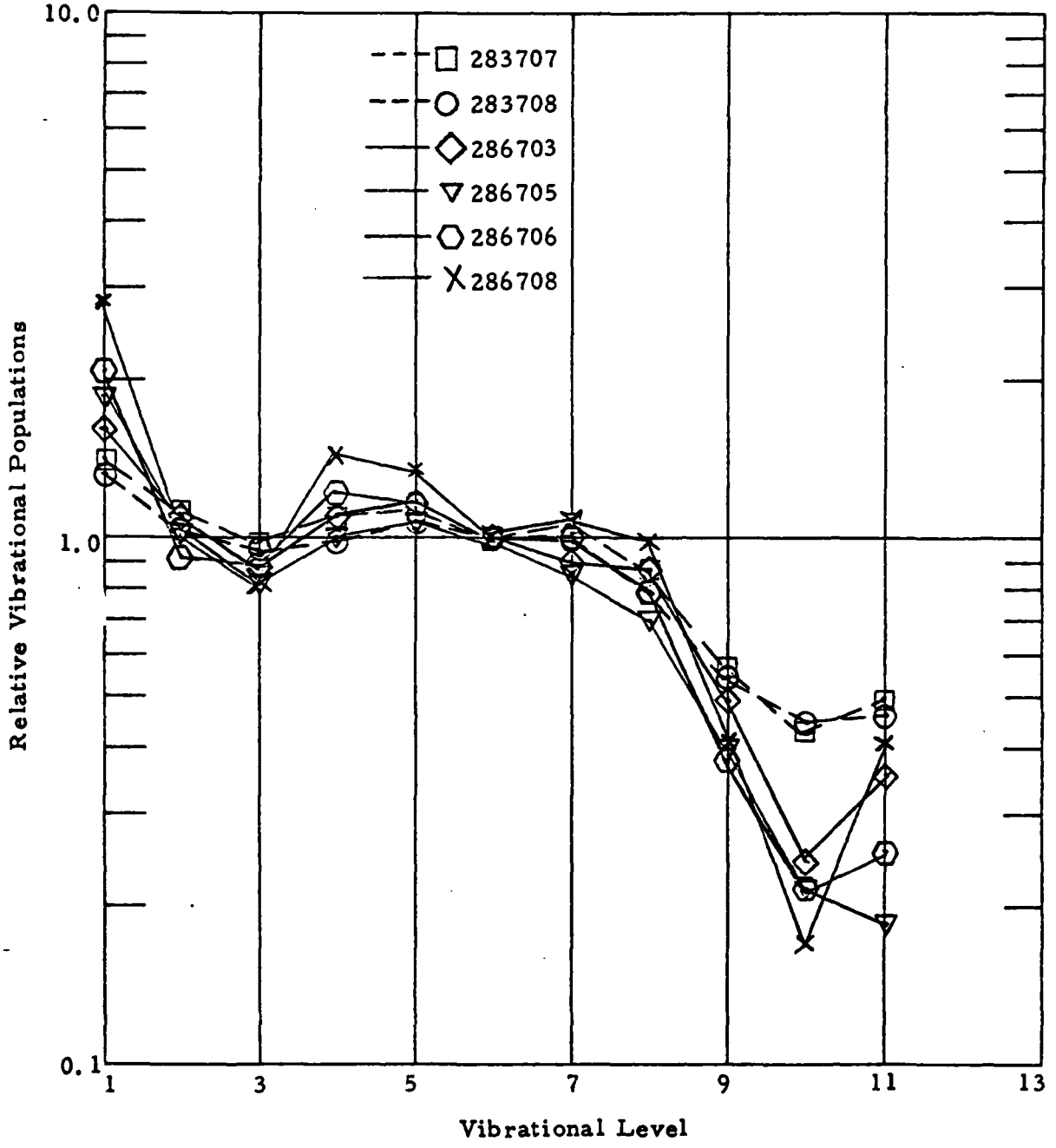

Fig. A-7g Derived relative populations for experiments listed above.

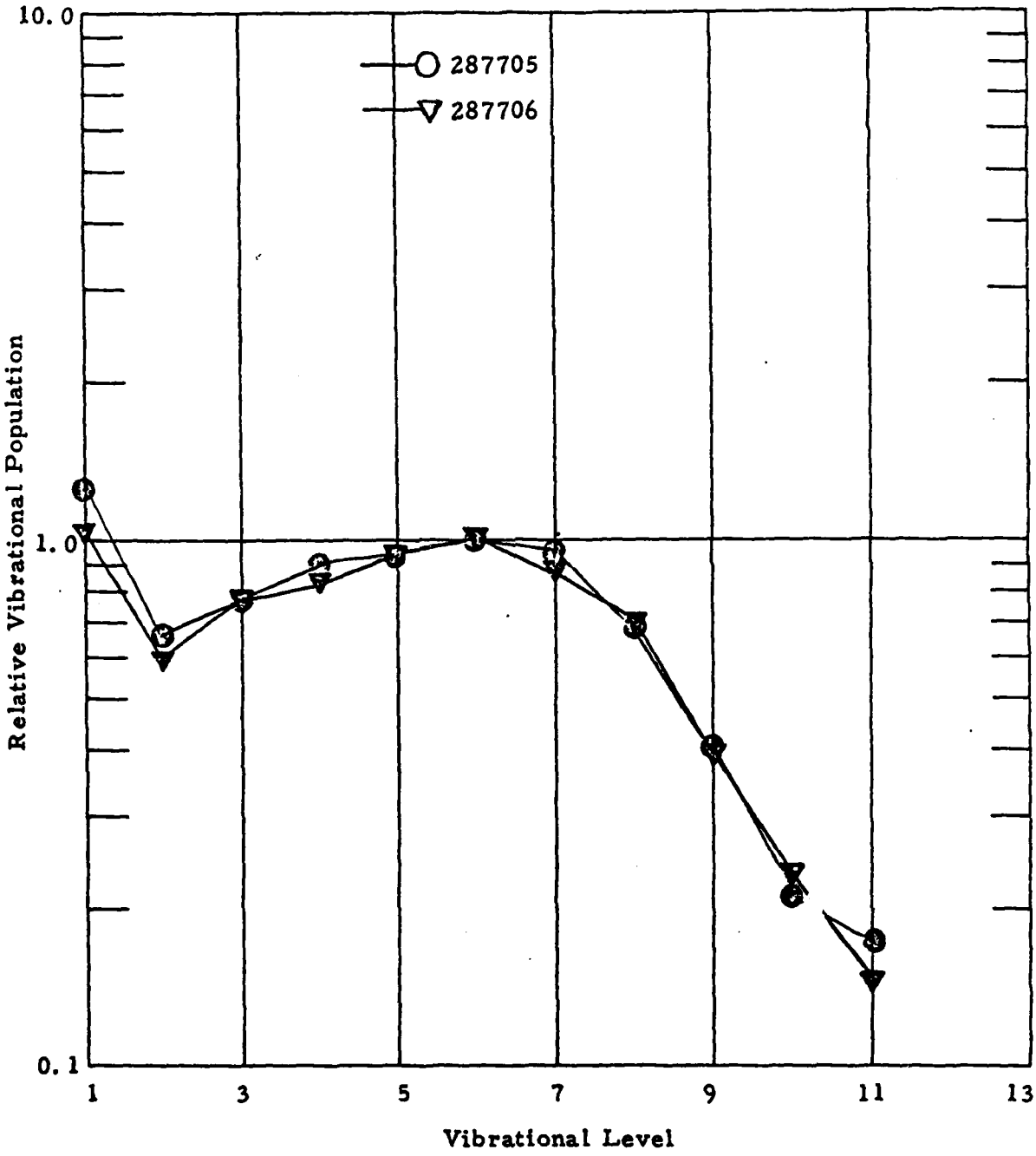

Fig. A-7h Derived relative populations for experiments listed above.

distributions outside of these systematic fluctuations. Variation of the static helium pressure up to ~ 5 mtorr also appears not to affect the observed distributions, but the five high-helium cases yield significantly different distributions both from the low helium cases and from each other. The high-helium distributions were taken to be affected by collisional relaxation; further interpretation must await a larger data base.

Average relative populations for the twelve zero-He spectra with similar flow conditions (i.e., excluding experiments 335612, 034704 and 034705, cf. Table A-I) and for all 24 experiments with less than 5 mtorr of helium are listed in Table A-III and are plotted for the latter case in Fig. A-8. The agreement of the values for the two cases to within one standard deviation indicates that any effect of up to 5 mtorr of helium upon the observed relative population distribution is undetectable within the systematic scatter of the data (~ 20%). The relative populations are likely to be overestimated for v = 1 due to the effect of the background emission near 5.2 μm. The relative population of v = 2 is underestimated due to coupling with the v = 1 level which it spectrally overlaps. Attempts to computationally remove the contribution of this radiation tend to reduce the v = 1 population to about the same level as for v = 2 - 7. The relative population of v = 12 should be considered to be an upper bound because the spectral intensity is close to the background level. Additionally, some of the spectra analyzed do not extend to sufficiently long wavelengths to include radiation from this level, thus reducing the statistical reliability of the deduced population.

The results of the analysis may be summarized as follows. As the static helium pressure increases, the apparent rotational temperature of NO decreases, as does the intensity of the background emission near 5.2 μm. Spectra for helium pressures of 0 and 1 - 5 mtorr have apparent rotational temperatures near 180 K and 80 - 120 K, respectively, but give rise to

TABLE A-III

AVERAGE RELATIVE POPULATIONS [≠]

V	N(v)/N(6), P_{He} = 0 mt (12 samples)	N(v)/N(6), P_{He} = 0-5 mt (24 samples)
1	2.0 ± 0.7	1.8 ± 0.6
2	1.2 ± 0.2	1.1 ± 0.2
3	1.0 ± 0.2	1.0 ± 0.2
4	1.2 ± 0.2	1.1 ± 0.2
5	1.2 ± 0.1	1.2 ± 0.2
6	1.0	1.0
7	0.9 ± 0.1	0.9 ± 0.1
8	0.9 ± 0.1	0.8 ± 0.1
9	0.5 ± 0.1	0.5 ± 0.1
10	0.3 ± 0.1	0.3 ± 0.1
11	0.3 ± 0.1	0.3 ± 0.1
12	0.2 ± 0.1	0.2 ± 0.1

[≠] The indicated uncertainty represents one standard deviation.

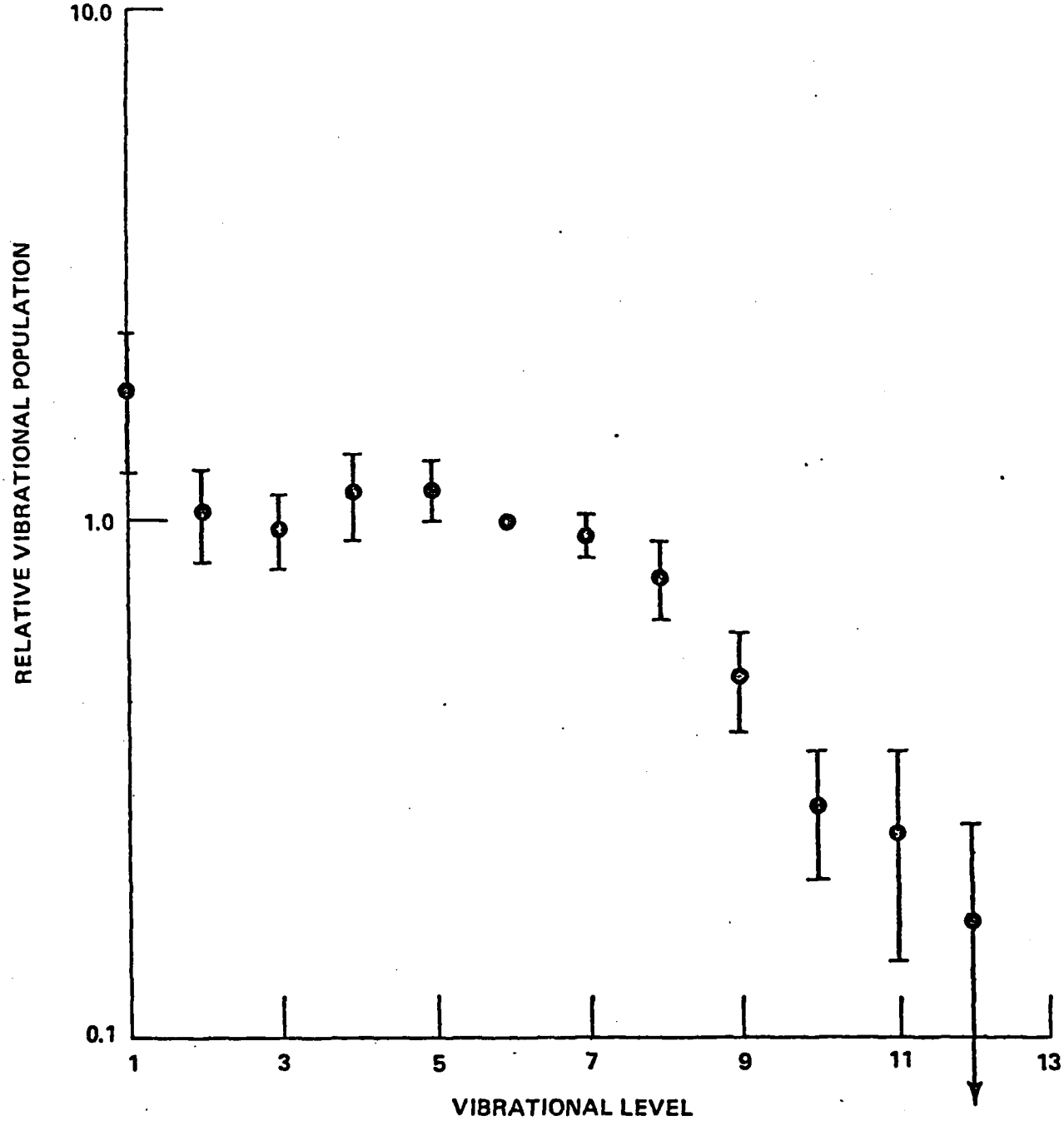

Fig. A-8 Average relative populations for 24 experiments with $P_{He} \leq 5$ mt. The error bars represent one standard deviation.

indistinguishable relative population distributions. These relative distributions are virtually unaffected by uncertainties in the parameters used in the computation.

REFERENCES

1. F. H. Mies, "Calculated Vibrational Transition Probabilities of OH ($X^2\pi$)", J. Molec. Spectrosc. 53, 150 (1974).

APPENDIX B

SURPRISAL ANALYSIS

1) General Description

Consider the exo-ergic, atom-diatomic, chemi-excitation reaction

$$A + BC \rightarrow AB(v) + C \quad , \tag{B-1}$$

having a total excess energy of E eV/molecule. The surprisal of the observed population distribution of AB can be defined as[1-4]

$$I(f_v') = - \ln[P(f_v')/P^o(f_v')] \quad , \tag{B-2}$$

$$\sum_{v'} P(f_v') = 1$$

$$\sum_{v'} P^o(f_v') = 1$$

where $P(f_v')$ is the observed relative vibrational population distribution and $P^o(f_v')$ is the prior nonspecific population distribution. The fraction of the total energy that is used for vibrational excitation is denoted by f_v'. It can be seen that linear plot of $I(f_v')$ as a function of f_v' implies that the reaction obeys an exponential gap law

$$P(f_v') = P^o(f_v') \exp[- \lambda_v(f_v')]/\exp \lambda_o \quad . \tag{B-3}$$

In this instance the parameter λ_v is a local measure of the deviation of $P(f_v')$ from the prior distribution $P^o(f_v')$ and a given value of λ_v is sufficient to

characterize the entire f_v' dependence of the observed distribution $P(f_v')$. In this sense λ_v^{-1} plays the role of a temperature like parameter. A population inversion corresponds to a negative value of λ_v, and thus a negative "vibrational temperature". If $\lambda_v = 0$, there is no surprisal regarding the distribution of available energy into the products' vibrational states. As will be shown, this implies that all final states are equally probable and that the available energy is distributed among the products vibrational states such that the entropy is maximized.

Since the prior distribution is a decreasing function of f_v', a negative value of λ_v indicates that the observed distribution varies more slowly than the prior distribution with respect to f_v'. This means that the reaction dynamics of the system tends to use the available energy to excite higher vibrational states rather than the lower ones, thus favoring a nonequilibrium population distribution. On the other hand, a positive value of λ_v indicates that the observed population distribution decreases more sharply than the prior distribution. This implies a disinclination of the system to utilize the available energy to excite higher vibrational states.

It should be noted that the interpretation of λ_v as "vibrational temperature" differs from the usual definition of the vibrational temperature. In contrast to the usual definition, appropriate for an oscillator in equilibrium with an infinite heat bath, the present definition does not imply that $P(f_v')$ must be a monotonic function of f_v'. Study of several chemical and inelastic energy transfer reactions have shown that even though $P(f_v')$ has a definite maximum, λ_v can be essentially constant.[1,2] This is due to the fact the reaction products are limited to a finite number of quantum states, and thus one has to consider the deviation of $P(f_v')$ from $P^o(f_v')$ and not from the density of states appropriate for an oscillator coupled to an infinite heat bath.

Lastly it can be noted that the denominator in Eq. (B-3), $\exp \lambda_o$, can be interpreted as a partition function, i.e., since

$$\sum_{v'=0}^{v^*} P(f_{v'}) = 1 \quad , \tag{B-1}$$

then by definition

$$Q_v = \exp \lambda_o = \sum_{v'}^{v'^*} P^o(f_{v'}) \exp (-\lambda_v(f_{v'})) \quad . \tag{B-4}$$

2) Determination of the Prior Distribution

The prior population distribution is derived from the assumption that at a given available total energy all final states are equally probable. This corresponds to maximizing the entropy change of the reaction. Consider the reaction of Eq. (B-1) where the product is a combination of an atom and a diatomic. If the atom is in a definite electronic state, the only quantum numbers for the products that can be resolved are the vibrational (v) and the rotational (J) numbers of the diatomic. The total density of states $\rho(E)$, of the diatomic for a given available total energy (E) is then given as[5]

$$\rho(E) = \sum_{v=0}^{v^*} \sum_{J=0}^{J^*(v)} (2J + 1)\, \rho_T(E - E_I) \quad , \tag{B-5}$$

where (2J + 1) is the rotational degeneracy factor (this factor appears because the angular momentum projection quantum number M is not determined) and

$\rho_T(E - E_I)$ is the density of translational states for the translational energy $E_T = E - E_I$. The internal energy of the diatomic is $E_I = E_v + E_R$. $J^*(v)$ is the highest value of J allowed by the conservation of energy at a given value of E and v, and v^* is the highest value of v allowed at a given E. In the vibrating rotor approximation

$$E_R = B_v \, hc \, J(J + 1) \quad , \tag{B-6}$$

where

$$B_v = B_e - \alpha_e(v + \tfrac{1}{2}) \quad , \tag{B-7}$$

and

$$E_v = vhc \, \omega_e[1 - x_e(v + 1)] \quad . \tag{B-8}$$

where ω_e and x_e are the vibrational constants of the molecule.

The prior distribution of vibrational-rotational states $P^o(v,J)$ can be written as

$$P^o(v,J) = (2J + 1) \, \rho_T(E - E_I)/\rho(E) \quad . \tag{B-9}$$

If one sums over all rotational states, one obtains the prior distribution of vibrational states $P^o(v)$,

$$P^o(v) = \sum_{J=0}^{J^*(v)} (2J + 1) \, \rho_T(E - E_I)/\rho(E) \tag{B-10}$$

In order to calculate $\rho_T(E - E_I)$, it is noted that for plane waves, if $\vec{k}$ is the wave vector, the density of momentum states in the space of $\vec{k}$ vectors is constant and equal to $(2\pi)^{-3}$. This is consistent with the orthogonality and closure relations for ket vectors $|k\rangle$.[6]

$$\langle k \,|\, k' \rangle = (2\pi)^3 \, \delta(\vec{k} - \vec{k}')$$

$$\int |\vec{k}\rangle \frac{d\vec{k}}{(2\pi)^3} \langle k| = 1 \qquad \text{(B-11)}$$

The number of states in the interval $\vec{k}$, $\vec{k} + d\vec{k}$ is therefore $d\vec{k}/(2\pi)^3$. Now if $\rho(E)$ is density of states, $\rho(E)\, d\Omega\, dE$ constitutes the number of states whose momentum is in the solid angle $\Omega, \Omega + d\Omega$ and whose energy $E = p^2/2m$ is in the band $E, E + dE$, thus

$$\frac{d\vec{k}}{(2\pi)^3} = \rho(E)\, d\Omega\, dE \quad . \qquad \text{(B-12)}$$

But

$$\vec{p} = \hbar\vec{k} \qquad \text{(B-13)}$$

and

$$d\vec{p} = p^2\, dp\, d\Omega \qquad \text{(B-14)}$$

therefore

$$\frac{d\vec{k}}{(2\pi)^3} = \frac{d\vec{p}}{(2\pi h)^3} = \frac{p^2\,dp}{(2\pi h)^3} = \rho(E)\,d\Omega\,dE \qquad \text{(B-15)}$$

or

$$\rho(E) = \frac{p^2}{(2\pi h)^3}\frac{dp}{dE} = A(E)^{1/2} \qquad \text{(B-16)}$$

where A is a constant.

Substituting Eq. (B-16) into (B-10) results in

$$P^o(v) = \sum_{J=0}^{J^*(v)} (2J+1)\,A_T(E - E_v - E_R)^{1/2}/\rho(E) \qquad \text{(B-17)}$$

Using the vibrating rotor (VR) approximation and replacing the summation over J with an integration over E_R results in

$$P^o(v) = \int_o^{E-E_v} \frac{A_T}{B_v\,hc}\,\frac{(E - E - E_R)^{1/2}}{\rho(E)}\,dE_R = \frac{2}{3}\frac{A}{B_v\,hc}\,\frac{(E - E_v)^{3/2}}{\rho(E)} \quad . \qquad \text{(B-18)}$$

Since

$$\sum_{v=0}^{v^*} P^o(v) = 1 \quad , \qquad \text{(B-1)}$$

$\rho(E)$ is given as

$$\rho(E) = \sum_{v=0}^{v^*} \frac{A}{B_v hc} \frac{2}{3} (E - E_v)^{3/2} \quad . \tag{B-19}$$

Hence in the VR approximation

$$P^o(v) = \frac{(E - E_v)^{3/2}}{\sum_{v=0}^{v^*} (E - E_v)^{3/2}} = \frac{(1 - f_v)^{3/2}}{\sum_{v=0}^{v^*} (1 - f_v)^{3/2}} \tag{B-20}$$

where $f_v = E_v/E$. Equation (B-20) was used to develop the prior distribution for NO used in the main text.

REFERENCES

1. R. B. Bernstein and R. D. Levine, "Role of Energy in Reactive Molecular Scattering: An Information-Theoretic Approach", in Advances in Atomic and Molecular Physics II", ed. by D. R. Bates and B. Bederson, (Academic Press, N. Y., 1975), pp. 216-297.

2. R. D. Levine and R. B. Bernstein, "Thermodynamic Approach to Collision Processes", in Modern Theoretical Chemistry, Vol. II: Dynamics of Molecular Collisions, Part B, ed. by W. H. Miller (Plenum Publishing Co., N. Y., 1975), Chapter 7.

3. I. Procaccio and R. D. Levine, "Vibrational Energy Transfer in Molecular Collisions: An Information Theoretic Analysis and Synthesis", J. Chem. Phys 63, 4261 (1975).

4. A. Ben-Shaul, R. D. Levine and R. D. Bernstein, "Entropy and Chemical Change. II. Analysis of Product Energy Distributions; Temperature and Entropy Deficiency", J. Chem. Phys. 57, 5427 (1972).

5. J. L. Kinsey, "Microscopic Reversibility for Rates of Chemical Reactions Carried Out with Partial Resolution of the Product and Reactant States", J. Chem. Phys. 54, 1206 (1971).

6. A. Messiah, Quantum Mechanics, Vol. II,(John Wiley and Sons, Inc., N. Y., 1966) pp. 736-738.

APPENDIX C

Auroral Production of $N(^2D)$ Atoms

As stated in the main text, the reaction between $N(^2D)$ and oxygen molecules can be an important source of vibrationally excited NO in the aurorally excited upper atmosphere. The auroral production efficiency for $N(^2D)$ atoms will be defined in this appendix so as to provice estimates of the number of vibrationally excited NO molecules created per ion pair in the E-region. Such predictions can later be coupled with a vibrational relaxation model in order to predict upper atmospheric NO vibrational band radiation signatures.

C-I $N(^2D)$ FORMATION

The dominant mechanisms for the formation of $N(^2D)$ atoms in the aurorally excited E-region are presently thought to be dissociative recombination of NO^+,

$$NO^+ + e \rightarrow a_1 N(^2D) + (1 - a_1) N(^4S) + O , \qquad C\text{-}1$$

ionic interchange reactions between nitrogen ions and atomic and molecular oxygen,

$$N_2^+ + O \rightarrow a_2 N(^2D) + (1 - a_2) N(^4S) + NO^+ \qquad C\text{-}2$$

$$N^+ + O_2 \rightarrow a_3 N(^2D) + (1 - a_3) N(^4S) + O_2^+ , \qquad C\text{-}3$$

and direct electron impact dissociation of N_2, encompassing the two reactions

$$e + N_2 \rightarrow e + a_4 N(^2D) + (2 - a_4) N(^4S) \qquad C\text{-}4$$

and

$$e + N_2 \rightarrow e + a_5 N(^2D) + (1 - a_5) N(^4S) + N^+ . \qquad C\text{-}5$$

The available experimental information on the branching ratios for reactions (C-1) - (C-5) is relatively sparse. The $N(^2D)$ production efficiency of reaction (C-1) has recently been measured in the laboratory[1] to be $a_1 = 0.76$. There appear to be no laboratory measurements of the branching ratios for reactions (C-2) and (C-3). Aeronomic estimates,[2] based upon a kinetic interpretation of thermospheric measurements of $N(^2D) - N(^4S)$ emission at 5200 Å, imply that a_2 and a_3 are near unity. The uncertainty in these estimates, particularly in the case of reaction (C-3) (see below), could be large and laboratory validation would be valuable.

There have been no laboratory measurements of the branching ratios for reactions (C-4), (C-5) and aeronomic modelers typically assume values of a_4 between 1 and 2 (see for example Refs. 2 through 4). Several recent studies may now be used to provide a firmer estimate for the production rate of $N(^2D)$ via reactions (C-4) and (C-5). The first of these is a detailed theoretical study of Porter et al[5] of electron/proton energy degradation in air (79% N_2, 21% O_2). In this analysis a painstakingly developed set of cross-sections for electron impact excitation of O_2/N_2 were used to specify species production efficiencies in electron irradiated air. It was found in this analysis that the production efficiency for the sum of N and N^+ ions rapidly asymptotes with increasing electron energy to 1.27/ion pair in air where, after adjusting the predictions for radiative cascade of highly excited nitrogen atoms to the ground or lowest metastable states, the production efficiencies of $N(^4S)$, $N(^2D)$, $N(^2P)$ and N^+ are predicted to be in the proportion .59/0.43/0.09/0.16. Thus, the analysis of Porter et al[5] implies that approximately 1/2 the nitrogen atoms produced by processes (C-4) and (C-5) will be formed in metastable states.

It should be noted that this result is specific to a 21% O_2/ 79% N_2 mixture, whereas the E-region atmospheric composition does exhibit large ambient oxygen atom concentrations. An electron energy deposition code developed by Peterson and co-workers[6] was exercised

to determine the potential effect of varying atmospheric composition on the efficiency for production of metastable nitrogen atoms. The most recent compilation[7] of excitation cross-sections for O_2, O and N_2 were used as input to this code, and energy allocation predictions were performed for a range of conditions corresponding to the composition of the standard atmosphere over the altitude range of 90-140 km. The computer model used did not yield a direct prediction of the metastable atom creation efficiency as output, but did provide relative ionization rates. Interestingly enough, it was found that for the altitude range considered the fractional production efficiency for N_2^+,[9] and N^+ varied only slightly, exhibiting an average value of approximately 0.75 per ion pair. Thus it may be inferred that the relative production rates for metastable atoms predicted for room air will also be reasonably valid for atmospheric conditions under which atomic oxygen concentrations can exceed those of molecular oxygen.

Zipf[8] has recently combined laboratory observations with auroral data of $N(^2P)$ radiative emission to provide estimates of 1.82, 1.38, 0.7 and 0.61 x 10^{-16} cm^2 for the relevant electron impact excitation cross-sections for $N(^4S)$, $N(^2D)$, $N(^2P)$ and N^+ production, respectively, at an electron energy of 100 eV. Scaling these cross-sections directly for ion pair production in air results in predicted excitation efficiencies for $N(^4S)/N(^2D)/N(^2P)/N^+$ of .57/0.34/0.23/0.18 atoms, respectively. Thus Zipf's analysis suggests that 0.57 metastable nitrogen atoms are created per ion pair in close agreement with the prediction of Porter et al,[5] although this latter analysis predicts a large proportion of the metastables to be in ^2D configuration. Furthermore, the total production rate of N and N^+ as deduced from Zipf's cross-sections is 1.32 per ion pair again in good agreement with the analysis of Porter et al.[5]

In the present analysis all nitrogen metastables have been treated as if they are in the ^2D configuration. The effect of this approximation on the following analysis is not anticipated to be large, inasmuch as the only important auroral sources of $N(^2P)$ appear to be

reactions (C-4) - (C-5), and even for these reactions $N(^2D)$ is predicted to be the dominant metastable produced. Based upon the results discussed above, a production efficiency of 0.55 $N(^2D)$ atoms per ion pair produced in air has been assumed for the direct electron impact dissociation of N_2, reactions (C-4) and (C-5); this value is taken to be invariant over the altitude range of 90-150 km.

From a modeling point of view, it is very convenient to discuss $N(^2D)$ production relative to the ion pair production rate, $-q_e$, and thus the reaction efficiencies of processes (C-1) - (C-3) will also be recast into production efficiency per ion pair in air. The positive ions created in electron irradiated air are dominantly those of atomic and molecular oxygen and nitrogen; however, in the E-region a number of ion/neutral charge exchange and interchange reactions occur on time scales short relative to electron-ion recombination, with the result that the primary E-region positive ions are found to be O_2^+ and NO^+ with NO^+ being the dominant of the two in auroral regions.[4,10,11] If NO^+ were the only positive ion then the rate of production of $N(^2D)$ via reaction (C-1) would be $a_1 = 0.76$ per ion pair. Since finite concentrations of O_2^+ will be present, the actual production rate will be given by the quantity $F_1\ a_1$ per ion pair, where F_1 is defined by

$$F_1 = (1 + k_a\ O_2^+/k_b\ NO^+)^{-1} \qquad \text{C-6}$$

where k_a, k_b are the rate constants for electron ion recombination of O_2^+ and NO^+, respectively. Note that for the E-region will typically be near unity, both because the quantity O_2^+/NO^+ will be less than one and because $k_b \approx 2\ k_a$.[11] The quantity F_1 can be evaluated directly either by using model predictions or, as in the present analysis, through the use of measured profiles of ionic concentrations.

With regard to the ionic interchange reaction (C-2), approximately 75% of the ion pairs created in electron irradiated air are in the form N_2^+/N^+, and Porter et al[5] predict that 0.16 N^+ are created per ion

pair; thus the production rate of N_2^+ is 0.59 per ion pair. The N_2^+ so formed will either react with oxygen atoms, reaction (C-2), or with oxygen molecules via

$$N_2^+ + O_2 \xrightarrow{k_2} O_2^+ + N_2 \ . \qquad \text{C-7}$$

Therefore the $N(^2D)$ production rate per ion pair due to reaction (C-2) may be specified by

$$F_2 = 0.59\ a_2\ (1 + k_7\ O_2/k_2 O)^{-1} \qquad \text{C-8}$$

where k_2 and k_7 have been measured to be $1.4 \times 10^{-10}\ (T/300)^{-0.44}\ cm^3/sec$[12] ($T < 1500$ K) and $5 \times 10^{-11}\ (\frac{300}{T})\ cm^3/sec$[13] ($T < 900$ K), respectively. It is to be noted that the contribution of reaction (C-2) to the total $N(^2D)$ production rate is controlled by the properties of the ambient atmosphere.

The last reaction to be considered, that between N^+ and oxygen molecules, reaction (C-3), does not significantly impact the analysis in that there are only 0.16 N^+ ions formed per ion pair in air. Reaction (C-3) has another branch,

$$N^+ + O_2 \rightarrow NO^+ + O \qquad \text{C-9}$$

and the best experimental information (see Ref. 13) suggests that branches (C-3) and (C-9) are equally probable. Since reactions (C-3) and (C-9) represent the dominant loss mechanism for N^+ in the E-region the assumption that a_3 is unity results in an estimated $N(^2D)$ creation rate of 0.08 per ion pair due to reaction (C-3).

C-II $N(^2D)$ Loss

Once $N(^2D)$ atoms are formed, they will subsequently either react to form vibrationally excited NO via

$$N(^2D) + O_2 \rightarrow NO + O \qquad \text{C-10}$$

or be lost by another means. Radiative decay of $N(^2D)$ is negligible given the long lifetime of this metastable state, $\sim 10^5$ sec,[14] and furthermore, $N(^2D)$ quenching by nitrogen molecules has been found to be a relatively inefficient process.[15,16] It appears that the only other important E-region loss mechanism for $N(^2D)$ atoms will be the reaction

$$N(^2D) + O \rightarrow N(^4S) + O \qquad \text{C-11}$$

and consequently the fraction of $N(^2D)$ atoms which ultimately react to form NO may be specified by

$$F_{NO} = \left(1 + \frac{k_{11}O}{k_{10}O_2}\right)^{-1} . \qquad \text{C-12}$$

The room temperature rate constant for reaction (C-10) is well defined having recently[15] been measured to be $(5.2 \pm 0.4) \times 10^{-12}$ cm^3/sec a value in reasonable agreement with that determined in earlier studies.[17,18] Furthermore, k_{10} has been found to exhibit a negligible temperature dependence over the range T = 237 - 365 K.

The magnitude of the rate constant of reaction (C-11) is more controversial. Davenport et al.[19] in an experimental study deduced that

$$k_{11} = 4 \times 10^{-12} \, e^{-250/T} \; cm^3/sec$$

where the activation energy was deduced from a limited data base spanning the temperature range of 31[illegible]-400 K. In contrast to this, Frederick and Rusch[2] performed a detailed analysis of the 5200 Å ($N(^2D) \rightarrow N(^4S)$) visible airglow data obtained on Atmosphere Explorer C and D during both day and night conditions and deduced that the rate constant for process (C-11) must be 4×10^{-13} cm^3/sec. Indeed they suggest that

use of the rate constant of Davenport et al.[19] would require the specification of a new, as yet unidentified, source of $N(^2D)$ in the upper atmosphere. Further studies of this rate constant will be required in order to clear up this discrepancy.

C-III NO Production Efficiencies

It can be seen from the previous two sections that the ultimate production efficiency for vibrationally excited NO will be a function of both the neutral and ionic composition of the disturbed atmosphere. For purposes of calculation a "typical" atmosphere has been defined to have the neutral properties of the 1976 U.S. Standard Atmosphere[20] and positive ion profiles corresponding to those measured in a specific IBC Class II aurora[10] (it is recognized that any given atmospheric scenario could provide significant variations from these "typical" properties however, it is not the purpose of this section to provide comprehensive sets of predictions for atmospheric NO production rates). The atmospheric properties so defined are listed in Table C.I. Also tabulated are the predicted fractions of $N(^2D)$ which will lead to NO formation, Eq. (C-12). This latter quantity has been evaluated for the values of the rate constant k_{11} given in Refs. 2 and 19, and as can be seen the discrepancy between these two can be quite significant for altitudes above 110 km.

The $N(^2D)$ production efficiencies calculated using this atmospheric model are listed in Table C.II. Both the individual contributions of reactions (C-1) through (C-5) and their sum are provided. It can be seen that the production efficiency varies only slightly, between 1.30 - 1.58 per ion pair over a span in altitude of 50 km. Also listed in Table C.II are the production rates for vibrationally excited NO per ion pair via reaction (C-10); predictions are provided for both values of the rate constant for reaction (C-11).[2,19] Again the disparity between these two sets of predictions becomes large at altitudes above 110 km.

TABLE C.I

"Typical" atmospheric properties in an IBC Class II aurora.

H,km	T,K	O_2,cm^{-3}	O,cm^{-3}	NO^+,cm^{-3}	O_2^+,cm^{-3}	F_{NO} (Ref.2)	F_{NO} (Ref.19)
140	560	5.7×10^9	2.7×10^{10}	2.0×10^5	8×10^4	0.73	0.30
130	470	1.4×10^{10}	4.6×10^{10}	2.4×10^5	1.2×10^5	0.81	0.41
120	360	4.4×10^{10}	9.3×10^{10}	2.8×10^5	1.2×10^5	0.86	0.56
110	240	2.6×10^{11}	2.3×10^{11}	2.3×10^5	4.5×10^4	0.93	0.81
100	195	2.2×10^{12}	4.3×10^{11}	0.6×10^5	1.3×10^4	0.99	0.96
90	187	1.5×10^{13}	2.4×10^{11}	(0.25×10^5)	(0.7×10^4)	1.00	1.00

( ) Extrapolated

TABLE C.II

$N(^2D)$ and NO production rates per ion pair.

H,km	$N(^2D)$ CREATION RATE/ION PAIR					NO* CREATION RATE/ION PAIR	
	REACTION C-1	REACTION C-2*	REACTION C-3	REACTIONS C-4,C-5	Σ	F_{NO}, (Ref.2)	F_{NO}, (Ref.19)
140	0.63	0.32	0.08	0.55	1.58	1.15	0.47
130	0.61	0.28	0.08	0.55	1.52	1.23	0.62
120	0.63	0.24	0.08	0.55	1.50	1.29	0.72
110	0.69	0.15	0.08	0.55	1.47	1.37	1.19
100	0.68	0.05	0.08	0.55	1.36	1.35	1.30
90	0.67	0.00	0.08	0.55	1.30	1.30	1.30

* $a_2 = 1.0$ applied

REFERENCES

1. D. Kley, G. M. Lawrence and E. J. Stone, "The Yield of $N(^2D)$ Atoms in the Dissociative Recombination of NO^+," J. Chem. Phys. 66, 4157 (1977).

2. J. E. Frederick and D. W. Rusch, "On the Chemistry of Metastable Atomic Nitrogen in the F-Region Deduced from Simultaneous Satellite Measurements of the 5200 Å Airglow and Atmospheric Composition," J. Geophys. Res. 82, 3509 (1977).

3. R. G. Roble and M. H. Rees, "Time Dependent Studies of the Aurora: Effects of Particle Precipitation on the Dynamic Morphology of Ionospheric and Atmospheric Properties," Planet. Space Sci. 25, 991 (1977).

4. Y. Kondo and T. Ogawa, "Odd Nitrogen in the Lower Thermospher Under Auroral Perturbations," J. Geomag. Geolectr. 28, 253 (1976).

5. H. S. Porter, C. H. Jackman and A. E. S. Green, "Efficiencies for Production of Atomic Nitrogen and Oxygen by Relativistic Proton Impact in Air," J. Chem. Phys. 65, 154 (1976).

6. L. R. Peterson, T. Sawada, J. N. Bass and A. E. S. Green, "Electron Energy Deposition in a Gaseous Mixture," Computer Phys. Comm. 5, 239 (1973).

7. C. H. Jackman, R. H. Garvey and A. E. S. Green, "Electron Impact on Atmospheric Gases I. Updated Cross-Sections," J. Geophys. Res. 82, 5081 (1977).

8. E. C. Zipf, "$N(^2P)$ and $N(^2D)$ Atoms" Their Production by E-Impact Dissociation of N_2 and Destruction by Associative Ionization, EOS Trans. AGU 59, 336 (1978). Also private communication, 1979.

9. W. Swider, "The D- and E-Regions," pp. 259-268 of Atmospheres of Earth and the Planets," D. Reidel Publ. Co., Dordrecht-Holland, 1975, ed. B. M. McCormac.

10. R. S. Narcisi, C. Sherman, L. E. Wlodyka and J. C. Ulwick, "Ion Composition in an IBC Class II Aurora 1. Measurements," J. Geophys. Res. 79, 2843 (1974).

11. W. S. Swider and R. S. Narcisi, "Ion Composition in an IBC Class II Aurora. 2. Model," J. Geophys. Res. 79, 2849 (1974).

12. M. McFarland, D. L. Albritton, F. C. Fehsenfeld, E. E. Ferguson and A. L. Schmeltekopf, "Energy Dependence and Branching Ratio of the $N_2^+ + O$ Reaction," J. Geophys. Res. 79, 2925 (1974).

REFERENCES (Cont.)

13. W. Lindinger, F. C. Fehsenfeld, A. L. Schmeltekopf and E. E. Ferguson, "Temperature Dependence of Some Ionospheric Ion-Neutral Reactions from 300-900 K," J. Geophys. Res. 79, 4753 (1974).

14. E. C. Zipf, Jr., "The Collisional Deactivation of Metastable Atoms and Molecules in the Upper Atmosphere," Can. J. Chem. 47, 1864 (1969).

15. D. Husain, S. K. Mitra and A. N. Young, "Kinetic Study of Electronically Excited Nitrogen Atoms $N(2\ ^2D_J, 2\ ^2P_J)$, by attenuation of Atomic Resonance Radiation in the Vacuum Ultra-violet," J. Chem. Soc. Farad. Trans. II 70, 1721 (1974).

16. T. G. Slanger and G. Black, "Quenching of $N(^2D)$ by N_2 and H_2O," J. Chem. Phys. 64, 4442 (1976).

17. C. L. Lin and F. Kaufman, "Reactions of Metastable Nitrogen Atoms," J. Chem. Phys. 55, 3760 (1971).

18. T. G. Slanger, B. J. Wood and G. Black, "Temperature Coefficients for $N(^2D)$ Quenching by O_2 and N_2O," J. Geophys. Res. 76, 8430 (1979).

19. J. E. Davenport, T. G. Slanger and G. Black, "The Quenching of $N(^2D)$ by $O(^3P)$," J. Geophys. Res. 81, 12 (1976).

20. U. S. Standard Atmosphere 1976, NOAA/NASA Report NOAA-S/T 76-1562, U. S. Government Printing Office, 1976.

APPENDIX D

EFFECT OF SLIT WIDTH ON OBSERVED BLACKBODY INTENSITIES

It has been empirically observed in past COCHISE measurements that blackbody and chemiluminescence intensities varied roughly as the 3/2 power of the spectrometer slit width (where the entrance and exit slits are placed at the same settings). This observation is contrary to the expectation that the observed intensity of continuum radiation should vary as the square of the entrance and exit slit width. The purpose of this appendix is to document measurements of intensity vs slit width at constant wavelength using the Electro Optics blackbody as a radiation source.

The results of four experiments are plotted in Fig. D-1. The intensity scale is arbitrary and is different for each experiment. If the intensity I varies with the slit width w as

$$I = C.w^{m} \qquad (D\text{-}1)$$

then plots of log I vs. log w, as shown in Fig. D-1, should have slope m. The data of 4/78 was obtained by cycling the slit setting up and down twice, thus generating four data points for each slit setting from 0.1 to 3 mm; the other three experiments have only one data point per slit setting. It can be seen that, although the reproducibility of readings is usually excellent, occasional gross errors of as much as a factor of 2 in intensity can be obtained due to inadvertent misalignment of the entrance and exit slits. Such misalignment will be reflected in spectral data as higher apparent resolution.

It can also be seen from Fig. D-1 that the data exhibit a reproducible transition from m = 2 to m = 3/2 behavior at w = 1mm. The 3/2- power

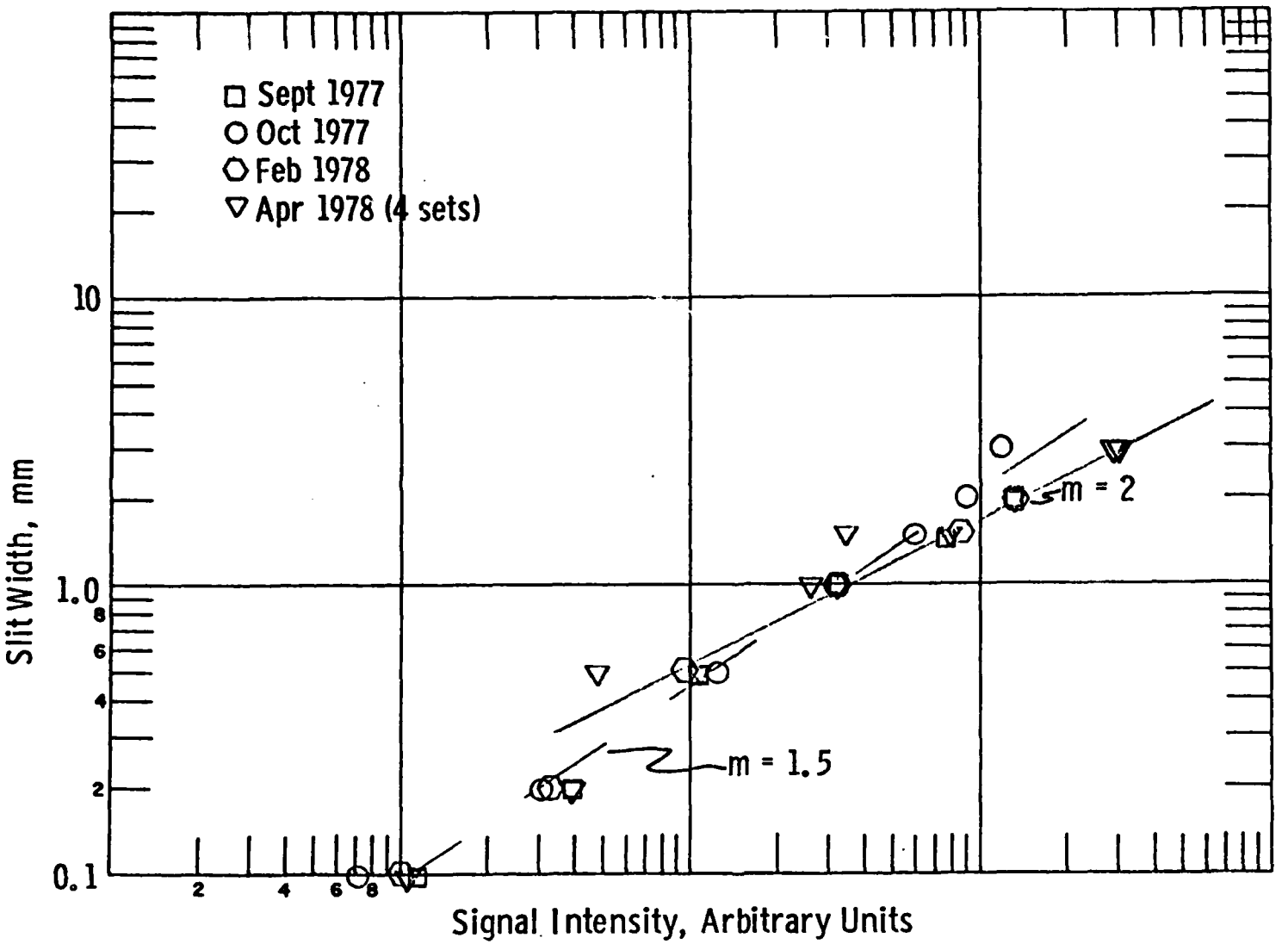

Fig. D-1. Effect of Slit Width on Observed Black Body Intensity. All measurements were made using the Electro Optics Black Body source (near 600K) at wavelengths near 5 μm. The observed intensities are normalized to a common value for 1 mm slits.

behavior for slit widths less than 1 mm is not understood, but it may be related to grating illumination patterns or to a slight misalignment of the spectrometer optical system at low temperature.

APPENDIX E

F-CENTER LASER PERFORMANCE CHARACTERISTICS

There exist three commercially available tunable laser sources in the infrared (SWIR): metal-salt diode lasers, parametric oscillators, and recently F-center lasers. Of these only the F-center laser (FCL) is capable of spanning the 2.2 - 3.3 μm spectral region. Diode lasers currently are capable of operation only at wavelengths longer than 2.9 μm, and at weak (0.25 mW cw) power levels in this region. Parametric oscillators operate in a pulsed mode, providing tunable radiation across the visible and out to 2.1 μm. Peak powers approaching a watt are possible for Nd:YAG pumped systems, but frequency stability is poor, 0.5 cm^{-1}. The lasing region of the F-center laser is especially interesting because the fundamental vibrational transitions of OH and NH as well as saturated carbon bonds absorb here. Additionally, overtone bands of CO_2, NO_2 and CH_4 occur in this bandpass. The FCL has output powers in the 3-30 mW range which will permit accurate absorption measurements, fluorescence pumping experiments, and laser induced reaction studies (including dissociation) to be carried out. Future technological breakthroughs should permit expansion of the lasing region to 0.8 - 4.0 μm. FCL's are commercially available only from Burleigh Instruments Inc.

The FCL operates on a four level homogeneously broadened system. The pump laser populates a level which rapidly decays non-radiatively to the upper laser level (with a long radiative lifetime). Lasing occurs to an excited level which rapidly decays to ground state (allowing cycle propagation). In this manner a population inversion may be continuously maintained during pumping. Operation is somewhat similar to solid state crystal lasers. Doped crystals are colored with an impurity which when cooled, can be readily photodissociated. These excited F-centers migrate through the crystal to the dopant sites, forming the active lasing sites. Temperature

is kept low to optimize fluorescence quantum yields (minimizing non-radiative losses from upper laser level). Reactivation is necessary once the crystal has returned to room temperature. Repeated cycling should not result in significant degradation of laser performance. No light should strike the room temperature crystal, because F-center migration to non-active sites will gradually reduce gain in the medium.

The laser cavity design is based on an astigmatically compensated three mirror scheme which has found much use in visible dye laser work. The pump laser enters the cavity through a beamsplitter and is focussed by one of the folding mirrors into the crystal gain medium. The external alignment of the pump beam by steering mirrors is the critical alignment during setup. Crystal height and angle is optimized by rotation of the cassette which contains the three crystals which are necessary for complete spectral coverage of the 2.2 - 3.3 μm region. Conversion efficiency in the crystal is a nearly constant 30%, with the rest being degraded to heat or providing visible output colinear with the IR radiation. The krypton laser 647.1 nm line will pump all three crystals, but pump frequency optimization at a given IR output frequency must be performed in the lab. Other lines (568, 531 nm) pump the short λ crystals more efficiently. Lasing occurs on a single longitudinal mode; several modes may oscillate well above threshold, with a mode separation of $\sim$ 1.5 GHz (.05 cm^{-1}). Frequency selection occurs at the third optical element, a grating which couples its zeroth order out of the cavity and its first order as feedback. In this arrangement with a retroflector, the angular dispersion of the output is minimized (1/4 milliradian over entire region) and spatial position is kept invariant. Use of a temperature controlled, piezo-electrically tunable, intra-cavity etalon permits a single frequency operation. Etalon tuning results in discrete frequency jumps of 0.01 cm^{-1}, continuous frequency tuning is achieved by varying the laser cavity length (moving the folding mirror) while simultaneously scanning the

etalon. The laser frequency width at any given time is $\sim$ 1 MHz (3×10^{-5} cm^{-1}) which is considerably narrower than Doppler linewidths. The necessary optics and voltage drives have been purchased from Burleigh to permit operation in this mode. A vibration isolation table and a 1W Spectra Physics Krypton laser (amplitude stabilized) have also been purchased. Assembly and check out of the system remains to be performed.

APPENDIX F

"COCHISE: Laboratory Spectroscopic Studies of Atmospheric Phenomena with High-Sensitivity Cryogenic Instrumentation"

John P. Kennealy and Francis P. Del Greco
Optical Physics Division
Air Force Geophysics Laboratory
Hanscom Air Force Base
Massachusetts 01731

George E. Caledonia and Wilson T. Rawlins
Physical Sciences Inc.
30 Commerce Way
Woburn, MA 01801

Abstract

The design of the COCHISE facility, a cryogenic apparatus used for laboratory studies of high altitude infrared excitation phenomena, is presented. The basic design concept is the extensive reduction of thermal background radiation through cryogenic (20 K) cooling of the entire reaction volume and detection system. Vibrationally excited molecules (e.g., NO, O_3, CO) are formed in a low-pressure (~ 3 mtorr) environment by interaction of a flowing reactant gas with discharge-produced radical and/or metastable species; the resulting infrared radiation is detected in the absence of interference from relaxation and surface effects. A long-path optical system and cryogenic monochromator permit high sensitivity for vibrationally excited species (~ 10^6 molecules cm^{-3}) and excellent spectral resolution (~ 2 cm^{-1}) over the spectral range 2-16 μm. The design and operation of the facility are described in detail. Specific applications of the facility to investigations of infrared atmospheric phenomena are also discussed.

Introduction and Design Concepts

The COCHISE facility at the Air Force Geophysics Laboratory is a cryogenic apparatus designed for partial simulations and detailed experimental studies of high altitude IR excitation phenomena, particularly chemi-excitation and excitation transfer processes. Infrared emission spectroscopic experiments designed to investigate gas phase excitation phenomena operating in the upper atmosphere require: (1) high sensitivity to the relatively weak molecular radiation from the excited species under investigation; (2) high spectral resolution to allow conclusive spectral analysis; and (3) specificity to the excitation process under investigation, i.e., freedom from interference due to radiative, collisional and surface relaxation processes. These conditions work against each other; the achievement of condition (3) necessitates the use of low pressures and/or low product yields, which results in low product radiation levels and increases the difficulty of achieving conditions (1) and (2). Furthermore, the limitation of IR detection sensitivity by thermal background radiation in the field of view severely inhibits spectrally resolved observations of IR radiation from important atmospheric species such as NO, CO_2, and O_3. Previous IR chemiluminescence methods have been highly successful in studies of chemiexcitation in hydrogen halides at wavelengths less than ~ 5 μm.[1] However, these methods are usually limited in scope by the presence of room temperature thermal background; for example, at 10 μm, the spectral radiance from typical vibrationally excited species at a column density of 10^8 cm^{-2} (representative of such experiments) is about nine orders of magnitude less than that from a room temperature blackbody.

The improvement in IR detectivity due to a cryogenic background is shown in Fig. 1. Since the limiting noise mechanism is the statistical fluctuation in the photon flux associated with the detector's environment, the detectivity of the system is inversely proportional to the square root of that flux. The results plotted in Fig. 1 are normalized to the detectivity at 293 K. Although considerable enhancement in detectivity is obtained with an 80 K background, the effects of background radiation can be virtually eliminated by cooling the entire simulation chamber and detection system to temperatures below 40 K. As a further benefit of cryogenic temperatures, rapid cryopumping of atmospheric gases can be attained near 20 K, and radiation leakage from the external vacuum system can be eliminated by complete optical isolation of the reaction/detection system during the experiments.

The COCHISE facility is designed to take full advantage of the benefits of cryogenic operation. The experimental direction taken in the development of the COCHISE facility has been to reduce the temperature of both the reaction chamber and the spectroscopic system to ~ 20 K to gain the advantages of cold background and cryopumping. A state-of-the-art infrared detector and a cryogenic scanning monochromator are coupled to a long-path reaction cell to allow spectrally resolved detection of IR radiation (2-22 μm) from emitting species at concentrations as low as 10^6 molecules cm^{-3}. The techniques of discharge flow and arrested relaxation are combined to allow mixing of the reacting species in the field of view at steady-state pressures near 3 mtorr, such that the excited products are formed and observed under nearly single collision conditions. The high-speed cryopumping of the reaction vessel removes the excited species from the field of view of the detection system before

radiative or collisional relaxation can occur, and eliminates complications normally encountered due to back-diffusion of species after collisions with chamber surfaces.

The achievement of the extreme thermal isolation and sensitivity requirements of the COCHISE facility demanded laboratory adaptations of techniques and infrared spectroscopic technology originally developed for space applications. The purpose of this paper is to describe the detailed design and operation of the COCHISE apparatus. In the following section, an overall description of the apparatus will be given, followed by more detailed descriptions of various key components. In the final section, some specific applications of the facility to relevant atmospheric problems will be discussed.

Apparatus Description

A schematic of the entire COCHISE apparatus is given in Fig. 2. The reaction chamber and detection system are enclosed within a cryogenic thermal shroud, which is in turn enclosed by a main vacuum chamber to provide thermal insulation. All surfaces within the shroud, with the exception of selected optical components and reagent gas lines, are held at temperatures near 20 K; this allows rapid cryopumping of all reagent and background gases except He and H_2. The reagent gases enter the reaction cell through four sets of opposing jets (see also Fig. 3) and interact along the centerline of the cell; the resulting radiation is collected by a mirror and lens, and focused onto the entrance slit of a grating monochromator system. The data processing, temperature control, and system housekeeping are performed by an external computer. The various components of the apparatus are described in more detail below.

Thermal isolation and control system

The cryogenic portion of the apparatus is thermally isolated inside a cylindrical main vacuum chamber ~ 3 m long and ~ 1.5 m in diameter (cf. Fig. 2); the thermally insulating vacuum enclosure is maintained at ~ 10^{-8} atm by a conventional LN_2-baffled diffusion pump system. The light-tight aluminum shroud, ~ 1.25 m in diameter, is surrounded by a multilayer thermal blanket of aluminized mylar in order to provide insulation from the 300 K thermal radiation of the outer wall. The shroud, reaction cell, and detection system are cooled to ~ 20 K by a closed-cycle gaseous helium refrigeration system (Cryogenic Technology, Inc.). Component temperatures are monitored and controlled to within ± 0.5 K in various locations by sensors and heaters which are coupled to a PDP-8/E computer (Digital Equipment Corp.). All of the services for the experiments, e.g. cryogenic coolant, microwave power, reagent gas flows, and diagnostic instrumentation, are introduced through a number of access ports; all diagnostic and control devices are mounted externally. The thermal system thus permits operation under a wide range of conditions for a variety of applications.

Reaction cell and reagent gas lines

A schematic of the reaction chamber is given in Fig. 3. The copper reaction cell is cylindrically symmetric, 60 cm long, 40 cm in diameter, with 2 cm thick walls, and is designed to have a surface temperature uniform within ± 0.1 K so that the cryopumping speed can be carefully controlled. The reagent gases are metered into either the discharge sidearms or the opposing counterflow sidearms through a two-stage heat exchanger. Up to three gases can be mixed prior to introduction to the discharge cavities; two gases can be separately mixed for the counterflow. Reagent gas temperatures downstream of the heat exchangers are usually maintained at 80-100 K.

Just prior to entering the reaction cell, gases in the sapphire discharge tubes are ionized, dissociated, and internally excited by four modified McCarroll-Evenson[2] microwave discharge cavities (Opthos Instruments) powered by Raytheon PGM-10 power supplies (2450 MHz, 100 W). Typical operation is at 50-90% of maximum power with duty cycles of 100% or 50% at 25 Hz, creating steady-state conditions while the discharges are on; all four discharges are driven by a single pulse generator to insure synchronous operation within a few microseconds.

Flow conditions in the reaction cell have been modeled for a range of experimental conditions[3]. Briefly, the reagent gases undergo free expansion into the reaction cell and interact in an axisymmetric stagnation region along the centerline of the cell; gas density variations along the cell axis are predicted to be < 10%. Pressures in the sidearms and raction zone, as determined by an MKS Baratron capacitance manometer, are ~ 1 torr and ~ 3 mtorr, respectively, for a typical total flow rate of ~ 8 standard l/min. The corresponding gas residence times are ~ 2 msec from the discharge cavity to the expansion region and ~ 0.3 msec within the field of view.

The chemiluminescent reactions occur primarily in the stagnation region where the opposing flows meet. The resulting IR radiation is viewed by the detection system through a 3" f/7 AR-coated Ge lens; the resulting field of view is roughly columnar along the cell axis such that only radiation occurring within ~ 4 cm of the axis is observed. A polished Al mirror at the far end of the cell enhances the collection efficiency of the system. The spectral response of the optical system is routinely calibrated with a variable temperature blackbody source imbedded behind a small aperture in the center of the mirror.

Spectral detection system

The detection system is isolated from the reaction system by an Al bulkhead with a 3" AR-coated Ge window in the center. Radiation from the reaction cell passes first through one of a series of order-sorting filters deployed by a solenoid-driven rotating filter wheel, then through an optional 25 Hz tuning fork chopper (American Time Products, Type 140), and finally into a cryogenic grating monochromator, where it is dispersed and focused onto a liquid helium cooled detector.

Cryogenic monochromator. In the selection of a cryogenic spectrometer system for the COCHISE facility, a scanning grating monochromator proved to be the most straightforward, reliable, and economical approach which would satisfy the sensitivity requirements of planned experiments. Because great difficulty was anticipated in achieving the requisite twelve order-of-magnitude reduction of thermal background flux on the detector, in this application it was felt that the multiplex advantage of Fourier spectroscopy might exacerbate those problems more than it would improve sensitivity. The instrument chosen was a 0.5 m asymmetrical Czerny-Turner system (Minuteman Laboratories #305 CM), constructed on an Invar frame to minimize defocusing and distortion at low temperatures. Independently adjustable entrance and exit slits are 2 cm tall and can be varied from 0.1 to 3.0 mm in width. The entire assembly is housed within a light-tight Al enclosure and is held at ~ 20 K during normal operation.

Two interchangeable replica gratings are employed. For wavelengths below 8 μm, a grating blazed at 3 μm with 150 lines/mm allows a nominal first-order reciprocal dispersion of 0.013 μm/mm in the exit slit plane; for longer wavelengths, a grating blazed at 10 μm with 75 lines/mm provides a reciprocal dispersion of 0.027 μm/mm. Thus, for a slit width of 0.5 mm, the resolution element is ~ 2.6 cm^{-1} at 5 μm and ~ 1.4 cm^{-1} at 10 μm. Both gratings are 6.4 cm square, which gives the instrument an aperture ratio of f/6.9.

Cryogenic infrared detector. The IR detector and preamplifier are housed in a single package. The detector element is an arsenic doped silicon cube, 3.0 mm on an edge (Santa Barbara Research Center); an f/0.25 parabolic reflector behind the cube permits collection of virtually all radiation passing through the monochromator exit slit. The contiguous preamplifier unit (Electro-Dynamics Laboratories, Utah State University) utilizes an integrated JFET operational amplifier (Burr-Brown 3521 R) in a direct-coupled negative-feedback operational scheme that has previously been successfully applied to ultra-high impedance cryogenic detectors.[4] The detector is maintained at 5-7 K through thermal strapping to an internally located, externally filled liquid helium vessel, while the pre-amplifier is maintained at 200 K by a proportional control system; under these conditions, the detector is sensitive to 1.2-22 μm radiation and has a peak Noise Equivalent Power of ~10^{-16} $W/Hz^{\frac{1}{2}}$.

Signal processing. The detector output is processed by synchronous phase-sensitive detection to discriminate against random-phase background noise. The radiation reaching the detector is modulated either by pulsing the microwave discharges with a 50% duty cycle square wave or by using the tuning fork chopper with the discharges operating CW; the pulsed discharge method has the advantage of discrimination against stray radiation which is not directly linked to species produced in the discharge plasma. The chopper is primarily used to modulate the radiation from the internal blackbody source during calibration measurements.

The ac detector output passes through a bandpass amplifier (PARC Model 113) and into a lock-in amplifier (PARC Model 124) which is synchronized either to the chopper pick-up coil or to the external pulse generator used to pulse the microwave discharges. The final demodulated signal is digitally filtered, displayed, and stored in real time by the PDP-8/E computer. The combination of grating scan rate, electronic time constant, and digital filtering rate for a given spectral scan is carefully chosen so that there are at least seven averaged data points and three electronic time constants per spectral resolution element; these criteria ensure that the apparent spectral detail is indeed limited by the instrument resolution.

Applications

The spectral responsivity of the COCHISE facility, as determined from calibrations with the internal blackbody source, is plotted as a function of wavelength in Fig. 4. A detailed absolute calibration of the system geometry is extremely complicated due to radial variations in both the optical collection efficiency and the concentrations of emitting species. As a result, the absolute responsivity values indicated on the ordinate of Fig. 4 were estimated for on-axis radiation only, and thus represent upper limits which are probably within a factor of two of the true values. The relative responsivity shown in Fig. 4 is accurate within ~ 30% over the entire wavelength range. For a molecular species with a band width of ~ 0.24 μm and a transition probability of ~10 sec^{-1} (typical values for the species encountered in these studies), the detection limit (S/N = 1) corresponding to a responsivity of 10^5 volt/watt cm^{-2} sr^{-1} μm^{-1} is approximately 3×10^6, 1.5×10^6, and 0.9×10^6 molecules cm^{-3} at 2.7, 3.3 and 10.6 μm, respectively; thus the ultimate detection limits indicated by Fig. 4 for such species are ~ 1×10^7 molecule cm^{-3} near 3 μm, ~ 2×10^7 molecule cm^{-3} near 5 μm, and ~ 1×10^6 molecule cm^{-3} near 10 μm.

The versatility of the apparatus is illustrated by the spectra in Figs. 5 and 6. Fig. 5 shows a CO ($\Delta v = 1$) spectrum observed when a discharged N_2/Ar mixture interacts with a counterflowing CO/O_2 mixture. The vibrational structure is completely resolved, with contributions evident from at least five vibrational levels, and even the rotational structure is partially resolved.[3]

Fig. 6 shows an O_3 ν_3 - band spectrum observed from the interaction of a discharged O_2/Ar mixture with counterflowing O_2. Although emission from the first vibrational level is the dominant feature, contributions from higher levels up to $v = 6$ are evident at longer wavelengths. The O_3 emissions observed in the COCHISE facility represent the first spectrally resolved observations of the higher vibrational levels of O_3.[5]

Similar measurements of radiation from chemiexcited NO have been carried out at 5.4 μm[6] and at 2.7 μm. Infrared chemiluminescence from NO and O_3 are processes of fundamental interest in the understanding of the radiation balance of the upper atmosphere.[7] The unique capabilities of the COCHISE facility permit detailed investigations of these processes which would be impossible to perform on a more conventional, non-cryogenic apparatus.

Acknowledgments

The authors wish to express their appreciation to Francis X. Robert and Arthur Corman of AFGL, Professors William M. Moore and Clair Wyatt of Utah State University, and Raymond Moore of Arthur D. Little, Inc. for their assistance in the development of the COCHISE facility. Major capital funding and support was provided by the Air Force Office of Scientific Research and by the Defense Nuclear Agency.

References

1. B.E. Holmes and D. W. Setser, "Energy Disposal in Unimolecular and Bimolecular Reactions," in Physical Chemistry of Fast Reactions, Vol. 3, edited by I.W.M. Smith, Plenum Publishing Co., London (1977).

2. B. McCarroll, "An Improved Microwave Discharge Cavity for 2450 Mhz," Rev. Sci. Instr. 41, 279 (1970); F. C. Fehsenfeld, K.M. Evenson and H.P. Broida, "Microwave Discharge Cavities Operating at 2450 MHz", Rev. Sci. Instr. 36, 294 (1965).

3. G. E. Caledonia, B. D. Green, G. A. Simons, J. P. Kennealy, F. X. Robert, A. Corman and F. P. Del Greco, "COCHISE Studies I: Fluid Dynamical and Infrared Spectral Analysis," Air Force Geophysics Laboratory TR-77-0281, Environmental Research Paper #619, 9 December 1977.

4. C. L. Wyatt, "Infrared Helium-Cooled Circular-Variable Spectrometer, Model HS-1," Final Report AFCRL-71-0340, Contract No. F19628-67-C-0322, Electro-Dynamics Labs., Utah State University, Logan, Utah, Sept. 15, 1971; C. L. Wyatt and D. J. Baker, "Rocket Launch of an LWIR Spectrometer Into an Aurora," Internal Report, Electro-Dynamics Labs., Utah State University, June 30, 1973.

5. W. T. Rawlins, G. E. Caledonia, J. P. Kennealy, and F. P. Del Greco, "Observations of IR Emission from Chemi-excited O_3" Paper M63, presented at the 1979 Spring Meeting of the American Geophysical Union, Washington, D.C., Abstract in EOS 60, 336 (1979).

6. J.P. Kennealy, F.P. Del Greco, G.E. Caledonia and B.D. Green, "Nitric Oxide Chemi-excitation Occurring in the Reaction between Metastable Nitrogen Atoms and Oxygen Molecules," J. Chem. Phys. 69, 1574 (1978).

7. J. P. Kennealy and G. E. Caledonia, "A Model of Upper Atmospheric Nitric Oxide IR Radiation," Paper SA79, presented at the 1979 Spring Meeting of the American Geophysical Union, Washington, D.C., Abstract in EOS 60, 338 (1979); T. C. Degges, A. T. Stair, Jr., R. M. Nadile, and E. R. Hegblom, "Altitude Dependence and Spectral character of Atmospheric Ozone Long Wavelength Infrared Emission," ibid. Paper SA81.

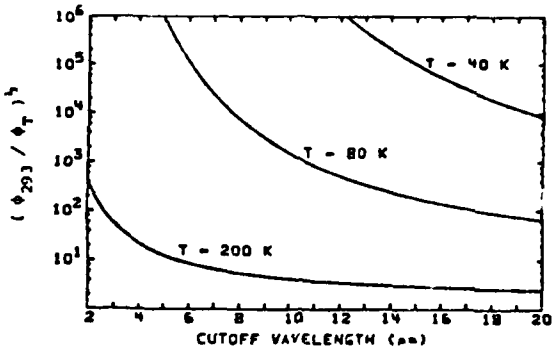

Fig. 1. Cold background detectivity improvement

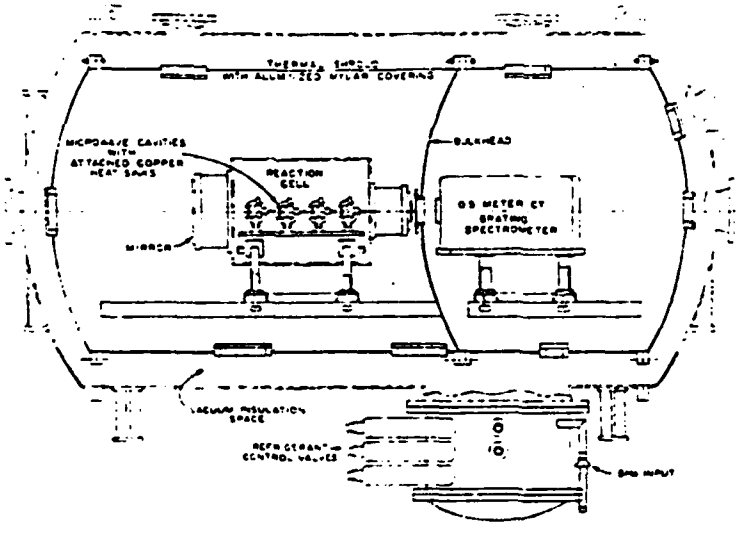

Fig. 2. Schematic of COCHISE facility

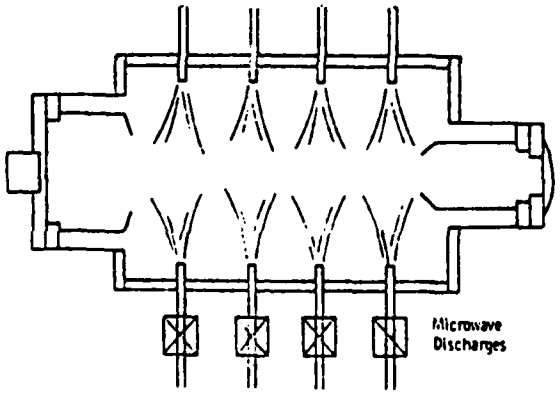

Fig. 3. Schematic of COCHISE reaction chamber

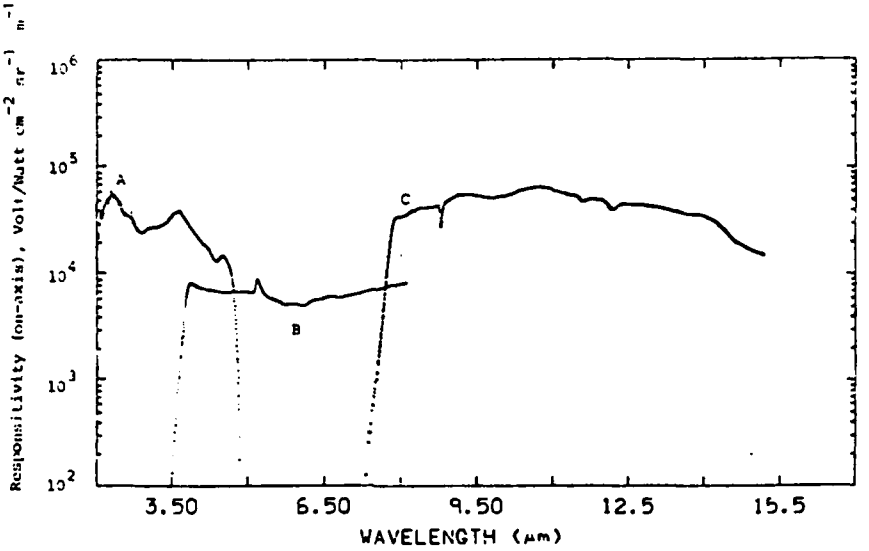

Fig. 4. Approximate spectral responsivity of COCHISE optical system. Curve A: 2 μm cut-on, long wavelength pass filter; 3 μm grating; 380 K blackbody source. Curve B: 4 μm cut-on, long wavelength pass filter; 3 μm grating; 380 K blackbody source. Curve C: 8 μm cut-on, long wavelength pass filter; 10 μm grating; 535 K blackbody source. A BaF_2 window in the exit slit limits the response for $\lambda \geq 14$ μm.

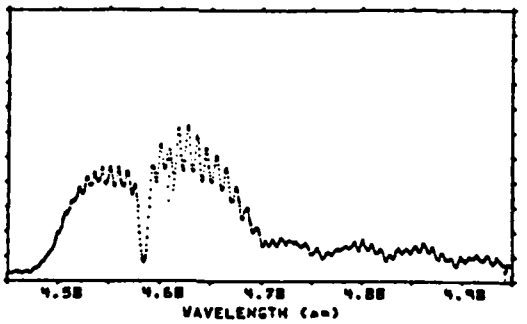

Fig. 5. CO ($\Delta v = 1$) fluorescence observed from the interaction of active nitrogen with a CO/O_2 mixture.

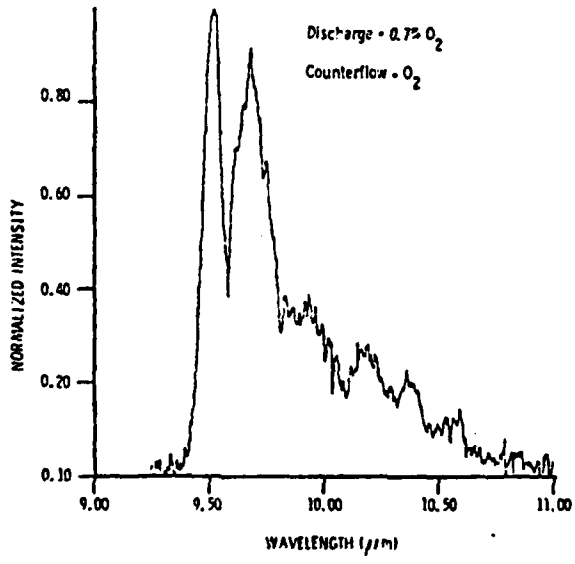

Fig. 6. O_3 chemiluminescence observed from interaction of a discharged O_2/Ar mixture with O_2

APPENDIX G

REMOTE INFRARED MONITORING OF SELECTED TRITIATED MOLECULES

10 December 1976 - 10 December 1977

B. D. Green, G. Wilemski and G. E. Caledonia

Formerly

PSI TR-110

I. INTRODUCTION

The purpose of this study is to provide a preliminary evaluation of the potential for remote monitoring of tritiated molecular species in the atmosphere through use of optical techniques. The tritiated species of specific interest to this analysis are limited to HT, HTO, CT_4 and CT_2H_2. The effort provided to develop this evaluation was broken into two distinct parts; (a) a review of the optical properties of the subject species and, (b) an examination of the manifold of remote monitoring techniques.

One requires both spectroscopic and radiative data in order to properly specify the optical properties of a molecule. The spectroscopic constants are used to determine the spectral position of allowed transitions whereas band and/or line strengths are required in order to specify the magnitude of the radiative emission or absorption of the transitions. A detailed literature review was performed in order to define the data base for the spectroscopic/radiative properties of the relevant tritiated species. The reference sources utilized included the files of the Defense Documentation Center, Physics Abstracts back to 1937, Chemical Abstracts to 1970, the Science Citation Index and texts and other sources available at the libraries of the Massachusetts Institute of Technology and the Air Force Geophysics Laboratory. Reference was also made to bibliographies of EPA publications and inquiries were also directed to relevant organizations such as IRIS, DASIAC, etc.

The results of this review are presented in Section II. As will be seen little information on the infrared bands of the subject molecules was available. Because of this a variety of isotopic scaling laws/relationships were employed to specify the desired molecular properties. Details of these analyses may be found in Section II.

Once armed with the spectral properties of the molecules, a review of remote monitoring techniques was undertaken, It became evident relatively early in the program that the subject molecules did not possess any ground state bands/transitions which fell in the near ultraviolet or visible portions of the spectrum and thus emphasis was placed on remote monitoring techniques which would utilize the infrared vibration/rotation bands of the molecules. (This of course did not preclude the use of visible radiation sources inasmuch as Raman scattering was considered as a potentially viable technique.)

A variety of monitoring techniques both passive and active, double and single ended were considered in some detail. Each technique was applied to a specific monitoring scenario in order to define the minimum detectable concentrations of the subject molecules which could be monitored using available, "off the shelf" detection equipment and generic collection optics. In this manner an optimum monitoring technique was determined. The details of this analysis may be found in Section III.

The summary and conclusions of this study may be found in Section IV. Also presented in this section are recommended verification steps to be taken prior to final development of a remote monitoring program. Lastly, if the concentration of tritiated species to be determined is below minimum detectable levels (i.e., by remote monitoring), it may be required to "capture" a gas sample for later laboratory analysis. Therefore, a brief review of the capability of various laboratory spectroscopic techniques is also provided.

II. SPECTROSCOPIC/RADIATIVE DATA

The vibration-rotation energy levels of any molecule can be expressed as a power series in the vibrational and rotational quantum numbers. The coefficients appearing in these expansions are determined most accurately from experiment. For diatomic molecules these parameters are: the harmonic frequency ω_e; the anharmonicity constants $\omega_e x_e, \omega_e y_e$, etc; the rotational constant Be, De, etc; the vibration-rotation interaction constants α_e, β_e, etc. Polyatomic molecules have analogous sets of constants for each normal vibrational mode, and often have additional constants that take into account perturbations of the energy levels arising from Coriolis interactions, Fermi type resonances, etc.

Each vibrational level has associated with it a set of rotational levels. The set of transitions between rotational levels of two different vibrational levels comprises a particular vibration-rotation band. There are three different possible branches or kinds of transitions within a band depending on how the rotational quantum number J changes. A transition in which J decreases by 1 ($\Delta J = -1$) is said to belong to the P branch. These transitions occur at lower frequencies then the band center frequency, ν_0. Lines belonging to the R branch have $\Delta J = 1$ and lie at frequencies higher than ν_0. The Q branch contains those transitions for which $\Delta J = 0$ and consists of very closely spaced lines, all at nearly the same frequency ν_0. All bands contain P and R branches but not necessarily a Q branch, whose presence is determined by conditions involving the change of electronic and/or vibrational angular momentum. The situation is schematically illustrated in Fig. 1.

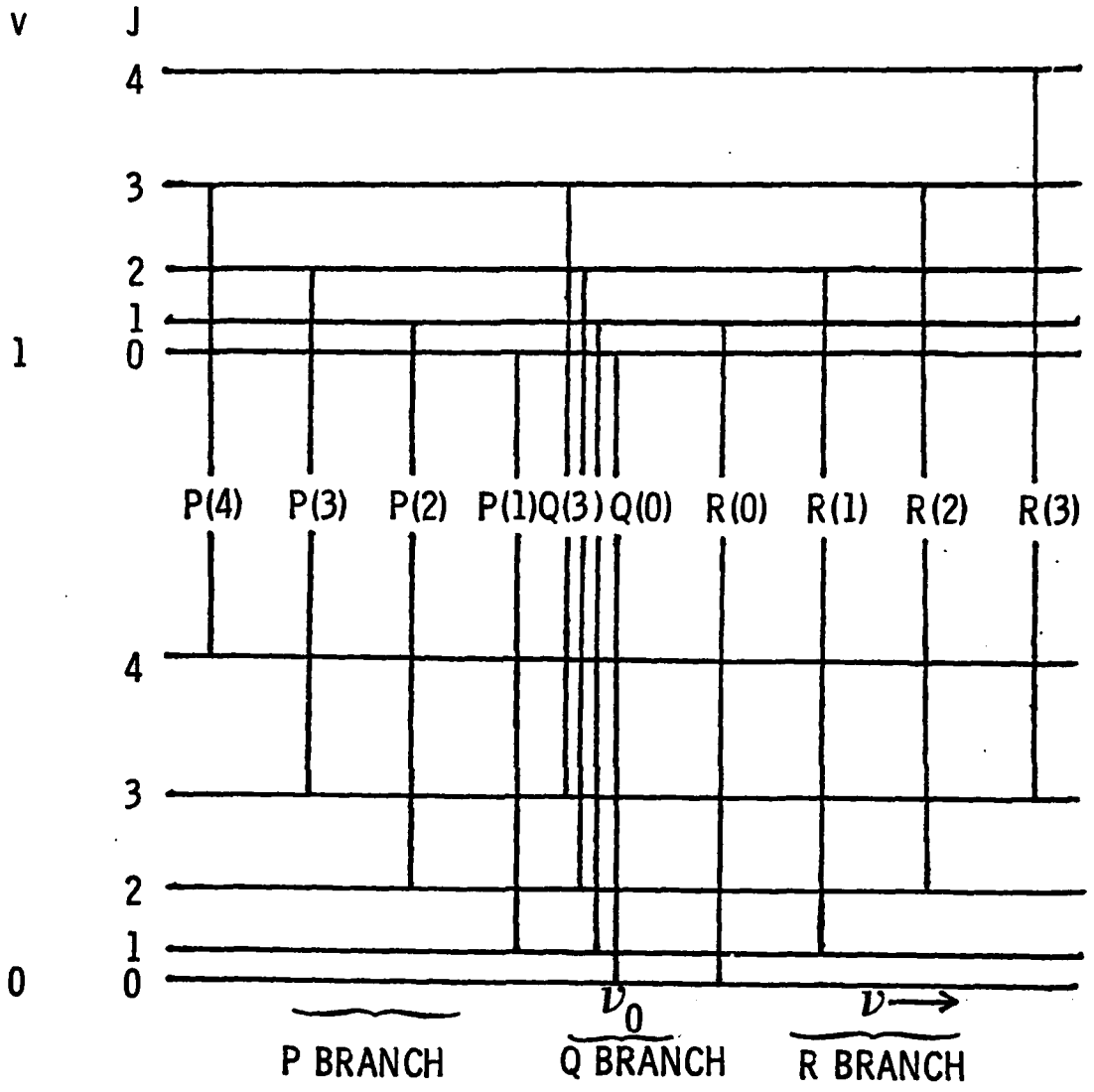

Fig. 1 Schematic energy level diagram illustrating P, Q, and R branches of the vib-rotational spectrum. Frequency, ν, increases to the right; v and J are the vibrational and rotational quantum numbers. For clarity, the rotational spacing is greatly exaggerated relative to the 1-0 vibrational spacing.

The intensity or strength of a spectral line or band can be determined experimentally using the relation[1]

$$S = \frac{1}{n\ell} \int \ln(I_o(\nu)/I(\nu))d\nu \qquad (1)$$

Here S is the intensity in units of cm/molecule, ν is the frequency in units of cm^{-1}, I_o and I are the incident and transmitted radiation fluxes at ν, n is the number density (molecules/cm^3) and ℓ is the path length in cm. The integral is to be performed over the extent of the line or band. We will use the symbol S to denote both the line intensity and the band intensity; its meaning will be clear from the context. An equivalent, practical definition of the band intensity is the sum of the intensities of all the lines in a band.

Regarding the theoretical foundation for S, the important point to note is that S is always proportional to a characteristic frequency ω and to the square of the dipole transition moment $\mathcal{R}$ (explicity defined later) which measures the strength of the transition: $S \alpha \omega \mathcal{R}^2$. More explicit theoretical formulas for S will be given later as needed.

The effects of isotopic substitution are several-fold. First, the frequencies of the fundamentals will shift to greater or lesser extent. This effect can be very large when D or T is substituted for H. Second, in many instances the full symmetry of the original molecule will be destroyed. As a result, degeneracies of vibrational bands may then be removed and previously forbidden bands may become allowed. Finally, the original allowed bands will often change in intensity from isotopomer to isotopomer, even for molecules of the same symmetry. This effect, however, is usually not very pronounced - the changes are generally less than an order of magnitude.

We can illustrate these effects using the molecules of interest in this report: As will be explained later, both HT and HD (Tables I - III) only have (very weak) infrared spectra at all because of isotopic substitution; H_2 is totally inactive in the infrared under normal conditions. Isotopic shifts in frequencies for these molecules are pronounced.

For water and its isotopomers (Tables IV - VIII), all three fundamentals are infrared active, so the principal effect is the change in frequencies of the vibrational bands from isotopomer to isotopomer. Perhaps the most significant of these is the large separation (1000 cm^{-1}) of the ν_1 and ν_3 bands of HOT and HOD compared to the partial overlap of the same bands seen in HOH, DOD and TOT. Also worth noting is the increase in intensity of the ν_1 band for HOT and HOD compared to that in the fully symmetric molecules.

In the methane series (Tables IX - XIII), the fully symmetric isotopomers show large frequency shifts, but only small changes in intensity for the various bands. By contrast, the spectrum of CH_2T_2 compared to that of CH_4 is replete with striking examples of isotope effects. In CH_4, the totally symmetric vibration ν_1 is infrared inactive; the ν_2 vibration is doubly degenerate but is only weakly allowed through a Coriolis interaction with ν_4; both the ν_3 and ν_4 vibrations are triply degenerate and are strongly infrared active. In CH_2T_2, on the other hand, only ν_{2b} is still inactive; the other bands are moderately to substantially split demonstrating the removal of degeneracy because of the lower symmetry of CH_2T_2. Many bands also show a considerable shift in frequency, and all are roughly comparably strong in intensity.

More examples of isotope effects and a deeper treatment of many of these topics can be found in the useful survey of Pinchas and Laulicht.[2] In the following sections, the existing data base for the molecules of interest is summarized and necessary theoretical details are presented.

A. Hydrogen Isotopomers

1) Spectroscopic Constants.

Energy levels for a diatomic vibrating rotor, HT is this case, can be calculated from the formulae[3]

$$E(v, J) = G(v) + B(v)J(J+1) + D(v)J^2(J+1)^2 + \ldots . \quad (2)$$

$$G(v) = \omega_e(v+\tfrac{1}{2}) - \omega_e x_e(v+\tfrac{1}{2})^2 + \omega_e y_e(v+\tfrac{1}{2})^3 + \omega_e z_e(v+\tfrac{1}{2})^4 + \ldots . , \quad (3)$$

$$B(v) = B_e - \alpha_e(v+\tfrac{1}{2}) + \gamma_e(v+\tfrac{1}{2})^2 + \ldots . \quad (4)$$

$$D(v) = D_e + \beta_e(v+\tfrac{1}{2}) + \ldots . \quad (5)$$

where v and J are the vibrational and rotational quantum numbers respectively.

In the absence of experimental values for the spectroscopic constants of HT, theoretical estimates were made using standard isotopic scaling relations[3] and very recent values[4] for H_2. These are listed in Table I, which also includes, for comparative purposes, some results for HD. In making these estimates, possible small differences between the Dunham coefficients[5] and the more familiar constants used here have been neglected. The limitations of the isotopic scaling relations make it unlikely that HT line positions calculated with the constants in Table I are reliable to better than $\pm 0.5\ cm^{-1}$. This uncertainty will increase with higher v and J values.

The line positions for HT were computed from the formula[3]

$$\nu = \nu_o + [B(v') + B(v'')]m + [B(v') - B(v'')]m^2 - 4D_e m^3 , \quad (6)$$

where the band center ν_0 is given by

$$\nu_0 = G(v') - G(v'') , \quad (7)$$

and m = J + 1 for the R branch and -J for the P branch. Values of the frequencies of the fundamental and first overtone bands of HD and HT are listed in Table II. Individual line frequencies may be found in Table III.

TABLE I

SPECTROSCOPIC CONSTANTS OF H_2, HD, HT (cm^{-1})

Constant	H_2[4]	HD[8]	HT*
ω_e	4403.566	3812.29	3596.6
$\omega_e x_e$	123.8573	90.908	82.622
$\omega_e y_e$	1.87269	0.504	1.0203
$\omega_e z_e$	-0.173514	---	-0.0772
B_e	60.8904	45.663	40.619
α_e	3.16997	2.003	1.727
γ_e	0.155932	0.03972	0.0694
D_e	0.046573	0.02667	0.0207

*calculated

Other comparable values for HD can be found in Ref. 3, 13, 14.

TABLE II

BAND CENTERS FOR HT, HD (cm^{-1})

Species	ν_{1-0}	ν_{2-0}
HD[8]	3632.15	7086.88
HT*	3434.1	6710.3

*calculated

2) Line Intensitites.

In the absence of experimental work, we have estimated line strengths for HT using measured dipole transition moments for HD reported by McKellar[6] and a theoretical scaling argument due, in part, to Herzberg.[7,8]

That HT and HD are very weakly active in the infrared can be understood in terms of a breakdown of the Born-Oppenheimer approximation. In any homopolar, unsymmetrically-isotopically-substituted diatomic molecule the center of positive (or negative) charge and the center of mass are no longer coincident. As the center of charge oscillates about its equilibrium position, the electronic motion lags slightly in keeping up. This phase difference in the motions of the positive and negative charge centers produces a small polarity in the molecule which does not average to zero because of anharmonicity and vibration-rotation effects. Thus these kinds of molecules have very small "permanent" dipoles and transition moments that are anomalous in their origin

Herzberg[7,8] suggests that the intensity of the vibrational band of such a molecule will be proportional to the square of the separation of the centers of charge and mass δ. Furthermore when the usual isotope sum rule[9,10] for intensities is applied to this case, the intensity ratio is found to vary inversely as the square of the quotient of the harmonic frequencies ω_e^{HD}, ω_e^{HT}. Combining these two results, we obtain

$$\frac{S_{HT}}{S_{HD}} = \left(\frac{\delta_{HT}}{\delta_{HD}}\right)^2 \left(\frac{\omega_e^{HT}}{\omega_e^{HD}}\right)^2 \qquad (8)$$

where S is the band intensity,

$$\delta = \frac{m_1 - m_2}{2(m_1 + m_2)} \quad , \tag{9}$$

and m_1 and m_2 are the masses of the appropriate nuclei.

We can deduce this result for the intensity ratio from a somewhat more unified point of view in the following way. The physical argument given for the origin of the dipole moment and its change with vibration leads us to postulate that the transition moment $\mathcal{R}_{01}$ will be proportional to the expectation value for the deviation of the center of charge z from its equilibrium value z_e, i.e.,

$$\mathcal{R}_{01} \propto \langle \psi_0 | (z - z_e) | \psi_1 \rangle \quad , \tag{10}$$

where ψ_0 and ψ_1 are the wave functions for the vibrational ground and first excited states. For our purposes it should be adequate to use Morse wave functions for the anharmonic oscillator and ignore the vibration-rotation interaction. It is easy to show that

$$z - z_e = (r - r_e)\delta \tag{11}$$

where r and r_e are the internuclear separation and its equilibrium value. Then using the results of Heaps and Herzberg[11] for $\langle \psi_0 | (r - r_e) | \psi_1 \rangle$, we find

$$\mathcal{R}_{01} \propto r_e \left(\frac{B_e}{\omega_e}\right)^{1/2} \delta \tag{12}$$

AD-A111 827 PHYSICAL SCIENCES INC WOBURN MA F/G 17/5
LABCEDE AND COCHISE ANALYSIS II. VOLUME I.(U)
FEB 80 W T RAWLINS, L G PIPER, B D GREEN F19628-77-C-0089
UNCLASSIFIED PSI-TR-207A NL

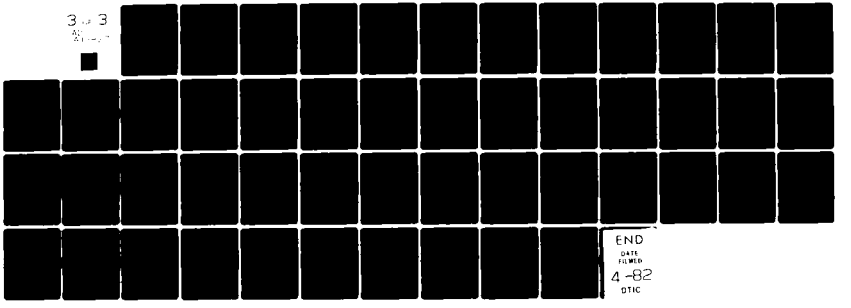

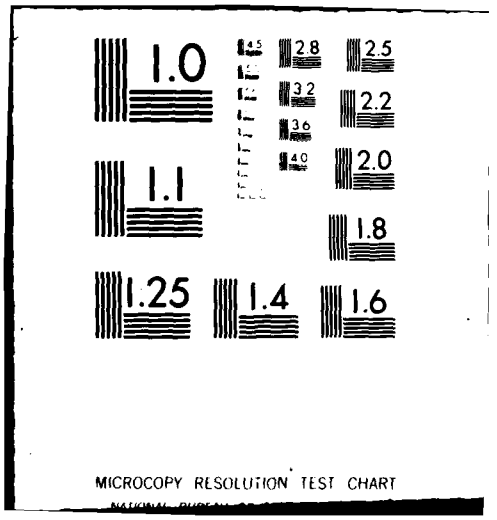
1.0
1.1
1.25
1.4
1.6
1.8
2.0
2.2
2.5
2.8
3.2
3.6
4.0
MICROCOPY RESOLUTION TEST CHART

With the isotopic scaling rule

$$\frac{B_e'}{B_e} = \left(\frac{\omega_e'}{\omega_e}\right)^2 \tag{13}$$

and the relation,

$$S \propto \omega_e \mathcal{R}_{01}^2 \tag{14}$$

we obtain the desired result, Eq. (8).

Using the appropriate values of the masses and ω_e's the ratio can be found:

$$\frac{S_{HT}}{S_{HD}} = 2 \quad . \tag{15}$$

Bunker[12], using a more fundamental, but complicated, approach for HD, suggests that the ratio should be 1.75, in good agreement with our simple calculation.

Line intensities for HD, listed in Table III, were calculated with the formula

$$S = \frac{8\pi^3}{3hc} \nu \frac{P_J}{2J+1} m \mathcal{R}^2(J) \tag{16}$$

TABLE III

LINE POSITIONS, INTENSITIES AND WIDTHS FOR HD, HT

HD				HT
Line[a]	ν[b] (cm^{-1})	S[c] $\times 10^{25}$ (cm/molecule)	FWHM[d] $\times 10^{3}$ (cm^{-1}/amagat)	ν(cal) (cm^{-1})
1-0 Band P(3)	3355.37*	0.679		3188.4
P(2)	3450.44	2.57		3272.7
P(1)	3542.93	3.90		3354.8
R(0)	3717.53*	8.29 (5.58)	8.6 ± 1.5	3510.6
R(1)	3798.45*	12.5 (19.4)		3583.2
R(2)	3874.36*	10.0		3651.6
R(3)	3944.72	4.20 (5.21)		3715.4
R(4)	4009.10	(1.04)		3774.0
2-0 Band P(1)	6997.67	1.10		6630.8
R(0)	7168.43	2.17	12.2 ± 2.0	6783.7
R(1)	7241.82	3.16		6850.5
3-0 Band R(0)	10445.47	0.555	15.0 ± 3.0	
R(1)	10511.46	0.733		
4-0 Band R(0)	13551.07	0.245	21.5 ± 1.5	

a This notation is used to designate the P or R branch and the J quantum number of the lower state.

b Frequencies are those of Durie and Herzberg[8], except for * values of McKellar[6].

c Calculated from McKellar's[6] results. Values in parentheses calculated from results of Bejar and Gush[15].

d Full width half maximum. Bejar and Gush[15] report a Doppler broadened line width of 0.026 cm^{-1}.

using McKellar's[6] reported values for $\mathcal{R}$. In this equation ν is the line center transition frequency in cm^{-1}, m = J or J + 1 for the P or R branches, and the fractional population of the J'th rotational level is given by

$$P_J = Q_R^{-1} (2J + 1)e^{-(hcB_e/kT)J(J+1)} \qquad (17)$$

where Q_R is the rotational partition function.

It is worth noting that the HD line intensities are 5 to 6 orders of magnitude weaker than "normal" vibration/rotation line intensities. Additionally, the constant B_e for HT differs by only 10% from the value for HD. Hence the rotational populations of these molecules will be nearly identical. In view of these two factors HT line intensities were estimated simply as twice the value of the corresponding HD line intensity, rather than from Eq. (16).

3) Line Widths.

McKellar[6] also reports several measured values of line widths for HD which can be used as estimates of HT lines. These values, however, are representative of H_2 broadening, not N_2 broadening which would be of greater value in atmospheric studies. The values are also listed in Table III.

B. Water Isotopomers

1) Spectroscopic Constants.

Only a limited amount of data exists for the tritiated water species, consisting principally of band center frequencies, ground state rotational constants and quartic distortion constants. The only upper state rotational

constants reported are for ν_2 in TOT. A summary is presented in Tables IV - VI. These data are not sufficient to permit estimation of line positions to better than a few cm^{-1}.

2) Integrated Band Intensities.

Measured intensities for a number of bands of HOH and HOD are summarized in the AFGL Atmospheric Absorption Line Parameters Compilation[16]. Predictions of the band strengths for the fundamental bands of HOT, HOD, TOT and DOD were made using these data in the manner described by Overend[1] and outlined below.

At temperatures low enough to prevent any appreciable population of upper vibrational levels, the following expression for the integrated intensity of the vib-rotation band holds[17]:

$$S = \frac{8\pi^3}{3hc}\,\bar{\nu}\,\left|\underset{\sim}{\mathcal{R}}\right|^2 \qquad (18)$$

Here $\bar{\nu}$ is an "average" frequency for the band in cm^{-1}, $\underset{\sim}{\mathcal{R}}$ is the dipole transition moment for the rotationless vibrational transition, and h and c are Planck's constant and the speed of light respectively. For $\underset{\sim}{\mathcal{R}}$, we may write more explicitly

$$\underset{\sim}{\mathcal{R}} = \langle \psi_v \left| \underset{\sim}{\mu} \right| \psi_v' \rangle \qquad (19)$$

where $\underset{\sim}{\mu}$ is the dipole moment operator and ψ_v, ψ_v', are wave functions for the initial and final vibrational states of the transition.

It is customary to expand $\underset{\sim}{\mu}$ in terms of the normal vibrational coordinates $\underset{\sim}{Q}$ of the molecule:

TABLE IV

GROUND STATE ROTATIONAL AND CENTRIFUGAL DISTORTION CONSTANTS OF HOT AND TOT (MHz)

	HOT	TOT
A	677849.04±0.17	338810.92±0.08
B	198197.49±0.13	145665.42±0.04
C	150462.41±0.13	100259.42±0.04
Δ_J	5.212±0.003	4.146±0.002
Δ_{JK}	48.523±0.023	-22.039±0.009
Δ_K	271.28±0.06	144.138±0.006
δ_J	1.4141±0.0005	1.6098±0.0007
δ_K	51.33±0.07	5.441.0.011

Taken from Ref. 22-24 where additional constants can be found. Comparable values have also been reported in Refs. 25-27, Ref. 27 also lists in cm^{-1} rotational constants for the ν_2 state of TOT: A = 11.982, B = 4.868, C = 3.316.

TABLE V

VIBRATIONAL CONSTANTS OF HOT AND TOT (cm^{-1})

	HOT	TOT
ω_1	2367.90	2298.76
ω_2	1370.17	1015.84
ω_3	3887.44	2436.91
x_{11}	-29.20	-15.19
x_{22}	-10.71	-6.70
x_{33}	-82.29	-17.81
x_{12}	-13.51	-6.14
x_{23}	-19.04	-7.23
x_{13}	-10.82	-60.25

Taken from Ref. 28. Some older ω values can be found in Ref. 29.

TABLE VI

BAND CENTER FREQUENCIES FOR WATER ISOTOPOMERS (cm^{-1})

Species	ν_1	ν_2	ν_3
HOH^{16}	3657.054	1594.736	3755.924
HOD^{16}	2723.687	1403.489	3707.459
DOD[a]	2671.69	1178.33	2788.05
HOT[b]	2299.780	1324	3716.577
TOT[c]	2237.154	995.37	2366.605

[a] Taken from Ref. 21, p. 470.

[b] ν_1 and ν_3 are from Ref. 25, ν_2 is from Ref. 29. Using Table V and the formula $\nu_2 = \omega_2 + 2X_{22} + 1/2\ X_{12} + 1/2\ X_{23}$ a calculated value is 1332.5 cm^{-1}.

[c] ν_1 and ν_3: Reference 30. ν_2: Reference 27.

$$\underset{\sim}{\mu} = \underset{\sim}{\mu}^0 + \sum_a \frac{\partial \underset{\sim}{\mu}}{\partial Q_a} Q_a + \ldots \tag{20}$$

where $\underset{\sim}{\mu}^0$ is the permanent dipole moment. Within the harmonic oscillator approximation we may combine Eqs. (18) - (20) to obtain

$$S \approx \frac{\pi}{3c^2} \left| \frac{\partial \underset{\sim}{\mu}}{\partial Q_a} \right|^2 \tag{21}$$

for a particular vibrational band. In obtaining Eq. (21) we have also put $\bar{\nu} = \omega_e$, an approximation which is well justified in the context.

The experimentally measured S values for the ν_1, ν_2 and ν_3 fundamentals of H_2O were used to evaluate the $\partial \underset{\sim}{\mu}/\partial Q_a$. The signs of these derivatives were chosen to correspond with those of Clough et. al.[18]. These derivatives are unfortunately not invariant with isotopic substitution. However they may be related to dipole derivatives with respect to the valence coordinates $\underset{\sim}{R}$. These latter derivatives may be determined using the equation

$$\frac{\partial \mu_\alpha}{\partial R_i} = \sum_a \frac{\partial \mu_\alpha}{\partial Q_a} \left(\underset{\sim}{L}^{-1}\right)_{ai} \tag{22}$$

which follows from the chain rule and the relation between the $\underset{\sim}{Q}$ and $\underset{\sim}{R}$ coordinates

$$\underset{\sim}{R} = \underset{\sim}{L}\ \underset{\sim}{Q} \tag{23}$$

In Eq. (22), α refers to a particular component (x, y, or z) of the dipole moment. Crawford[9] has shown how to relate $\partial\mu_\alpha/\partial R_i$ for two different isotopomers whenever a so-called "rotational correction" is required. His results have the form

$$\left(\frac{\partial \underset{\sim}{\mu}}{\partial R_i}\right)^{(2)} = \left(\frac{\partial \underset{\sim}{\mu}}{\partial R_i}\right)^{(1)} - \left(\underset{\sim}{\mu}^0 \times \underset{\sim}{\sigma}_i^{(1)}\right) \tag{24}$$

Here the x component of the vector $\underset{\sim}{\sigma}_i$ is defined as

$$(\sigma_i)_x^{(1)} = (\underset{\sim}{\beta}^{(1)}\ \underset{\sim}{A}^{(2)})_{1i} = -(\underset{\sim}{\beta}^{(2)}\ \underset{\sim}{A}^{(1)})_{1i} = -(\sigma_i)_x^{(2)} \quad . \tag{25}$$

With the correspondence ($2 \leftrightarrow y$), ($3 \leftrightarrow z$) holding, similar relations define the y and z components of $\underset{\sim}{\sigma}_i$. In Eqs. (24) and (25) the superscripts (1) and (2) refer to different isotopomers; the $\underset{\sim}{\beta}$ and $\underset{\sim}{A}$ matrices are discussed further by Crawford.[9]

The $(\partial\mu_\alpha/\partial R_i)$ are reassembled for use in Eq. (24) by means of the inverse equation

$$\left(\frac{\partial \mu_\alpha}{\partial Q_a}\right)^{(i)} = \sum_j \left(\frac{\partial \mu_\alpha}{\partial R_j}\right)^{(i)} L_{ja}^{(i)} \tag{26}$$

where, of course, the $\underset{\sim}{L}$ matrix for the appropriate isotopomer must be employed

This entire procedure is summarized as follows:

a) Determine $(\partial\mu_\alpha/\partial Q_a)$ from experimental S values for H_2O via Eq. (21).

b) Determine $(\partial\mu_\alpha/\partial R_i)$ from $(\partial\mu_\alpha/\partial Q_a)$ via Eq. (22).

c) Determine $(\partial\mu_\alpha/\partial R_i)$ for different isotopomers via Eq. (24).

d) Calculate S using Eqs. (21) and (26).

The $\underset{\sim}{G}$ and $\underset{\sim}{L}$ matrices needed for these calculations (as well as the harmonic frequencies used below) were obtained from S. A. Clough.[19] The results of these calculations are presented in Table VII. In the case of HOD, the calculated and measured values compare very well.

TABLE VII

INTEGRATED BAND INTENSITIES FOR WATER ISOTOPOMERS

$S \times 10^{18}$ (cm/molecule)

Species	ν_1	ν_2	ν_3
HOH[a]	0.362	10.6	7.99
HOD[a]	2.24	8.97	5.0
HOD[b]	2.13	9.09	4.64
DOD[b]	0.340	5.64	4.86
HOT[b]	1.78	9.17	4.78
TOT[b]	0.361	3.97	3.85

[a]Measured, Ref. 16.

[b]Calculated.

We should note that because of the limitations of the harmonic oscillator approximation, we are only determining effective values of $\partial\mu_\alpha/\partial Q_a$. Although these are admittedly useful in making theoretical estimates of band intensities for other isotopomers, they should not be expected to be as physically meaningful, nor to agree precisely in magnitude, with values obtained from more sophisticated analyses[18,20] that use more accurate wavefunctions. The differences between the effective quantities and their "true" values must surely play a substantial role in the debate over the bond-moment hypothesis, but this factor seems to have been neglected in previous discussions[21] of this problem.

As an additional check on the internal consistency of the intensity calculations we have also computed the F-sums defined by Crawford.[9] Within the limits of the harmonic oscillator approximation, these sums, suitably corrected for "rotation" as above, should be isotopically invariant. The F-sum is defined by

$$\Sigma_F \equiv \sum_a \frac{S_a}{\omega_a^2} \quad , \tag{27}$$

where ω_a is the harmonic frequency associated with the a'th vibrational band and the sum extends over all vibrations of the same symmetry. The sum rule derived by Crawford[9] for a pair of isotopomers can also be written as

$$\Sigma_F^{(1)} = \Sigma_F^{(2)} - \frac{\pi}{3c^2} \sum_a \left[\left(\frac{\partial \underset{\sim}{\mu}}{\partial Q_a} \right)^{(2)} - \underset{\sim}{\Delta}_a^{(2)} \right] \cdot \Delta_a^{(2)} \omega_{a2}^{-2} \quad , \tag{28}$$

or still further as

$$\Sigma_F^{(1)} = \frac{\pi}{3c^2} \sum_a \left| \left(\frac{\partial \underset{\sim}{\mu}}{\partial Q_a}\right)^{(2)} - \underset{\sim}{\Delta}_a^{(2)} \right|^2 \omega_{a2}^{-2} \quad , \tag{29}$$

where

$$\underset{\sim}{\Delta}_a^{(i)} = \sum_j \left(\underset{\sim}{\mu}^0 \times \underset{\sim}{\sigma}_j^{(i)}\right) L_{ja}^{(i)} \quad . \tag{30}$$

Equation (28) is obviously the preferred form to use whenever independent experimental intensity data exist for both isotopomers. The F-sum calculations are summarized in Table VIII. The agreement is excellent, indicating that the calculated values should be reliable to about 10 - 15%.

TABLE VIII

F-SUMS[a] FOR WATER ISOTOPOMERS

Pands	HOH	DOD	TOT	HOD	HOT
$\nu_1 + \nu_2$	3.925	3.924	3.922		
ν_3	0.5140	0.5139	0.5146		
$\nu_1 + \nu_2 + \nu_3$	4.439			4.540 4.560[b]	4.437

[a] All values x 10^{24}. HOH values calculated from Eq. (27) with measured S values. Remaining values are corrected for "rotation" as in the r.h.s. of Eq. (28) or (29).

[b] Calculated from Eq. (28) using measured S values in Σ_F^{HOD}.

C. Methane Isotopomers

1) Spectroscopic Constants.

The data here is very sparse. For several vibrations not even the band center frequencies have been measured. The equilibrium values of some of the constants have been reported; only one upper state rotational constant has been reported, that for ν_3 of CT_4. Tables IX - XII summarize the situation.

2) Integrated Band Intensities.

No measured band intensities for the tritiated methane isotopomers have been reported. Theoretical estimates of these quantities have been provided by Sverdlov[31] using the valence-optical theory of infrared intensities. This theory is similar in spirit to the method outlined in Section B, but differs in the choice of effective parameters to be determined as well as in some mathematical details. The results of Sverdlov's calculations are presented in Table XIII.

In conclusion the spectroscopic/radiative properties of these tritiated species had to be specified almost completely by theoretical techniques. Furthermore only bandstrengths have been provided for HTO, CT_4 and CT_2H_2 inasmuch as a theoretical definition of the linestrengths of these molecules is well beyond the scope of the present program. A proper definition of the molecular linestrengths would be required for the successful application of most techniques for remote monitoring. These would perhaps best be provided by experiment rather than theory.

TABLE IX

SPECTROSCOPIC CONSTANTS[a] FOR CT_4 (cm^{-1})

ω_1	1817	x_{11}	-64.6
ω_2	909.5	x_{12}	0
ω_3	1990	x_{13}	-65.0
ω_4	880	x_{14}	0
Be	1.751[b]	x_{22}	0
B_0	1.733[b]	x_{23}	-15.0
$(B_{0010}-B_0)$	-0.009	x_{24}	-11.2
ζ_3	0.252 (0.26)[b]	x_{33}	-17.5
ζ_4	0.24[b]	x_{34}	-12.0
		x_{44}	-6.0

[a]B and ζ values are from Ref. 32; ω's and x's from Ref. 33.

[b]Calculated.

TABLE X

HARMONIC FREQUENCIES[a] OF CH_2T_2 (cm^{-1})

ν_1	ν_{2a}	ν_{2b}	ν_{3a}	ν_{3b}	ν_{3c}	ν_{4a}	ν_{4b}	ν_{4c}
1906	1467	1285	3149	3153	1991	899	1038	1244

[a]Ref. 33

TABLE XI

ROTATIONAL CONSTANTS[a] FOR CH_2T_2 (cm^{-1})

A_e	B_e	C_e
3.75	2.63	2.19

[a]Ref. 33

TABLE XII

BAND CENTER FREQUENCIES (cm^{-1}) FOR METHANE ISOTOPOMERS

Band	3			1	2		4		
CH_4	3018.92[a]			2916.5[b]	1533.29[c]		1305.91[d]		
CD_4	2258.6[e]			2107.8[e]	1092.2[e]		996.0[f]		
CT_4[g]	1937.0			(1738.2)	(894.9)		858.0		
Band	3a	3b	3c	1	2a	2b	4a	4b	4c
CH_2D_2	2975.48[h]	3012.26[h]	2234[i]	2139[j]	1436[i]	1329[i]	1033[i]	1090[i]	1236.35[k]
CH_2T_2[g]	(2976)	3033	1932	(1852)	1426	(1255)	(879)	1005	1203

[a]Reference 34.

[b]Reference 35.

[c]Reference 36.

[d]Reference 37.

[e]Reference 38.

[f]Reference 39.

[g]Reference 33. Values in parentheses are calculated

[h]Reference 40.

[i]References 41 and 42.

[j]Reference 43. See also p. 26 of Reference 42.

[k]Reference 43.

TABLE XIII

BAND INTENSITIES[a] FOR METHANE ISOTOPOMERS

Band	3			1	2		4		
CH_4[b]	12.1				0.0891		5.87		
CH_4[c]	13.3			0	0		5.84		
CD_4[d]	6.0			0	0.045		3.59		
CH_4[d]	3.62			0	0.03		2.71		
Band	3a	3b	3c	1	2a	2b	4a	4b	4c
CH_2D_2[e]	5.80		2.30					3.57	
CH_2D_2[c]	2.30	4.35	2.04	0.93	0.73	0	0.86	1.35	1.84
CH_2T_2[c]	2.29	4.32	1.19	0.48	0.91	0	0.58	1.15	1.86

[a] $\times 10^{18}$; units: cm/molecule.

[b] Measured: Reference 44.

[c] Calculated: Reference 31.

[d] Calculated: ν_3, ν_4: Reference 31; ν_2: uncertain application of isotope sum rule using $S(\nu_2)$ for CH_4.

[e] Measured: Reference 43.

III. REMOTE MONITORING CONSIDERATIONS

Schematic absorption spectra of these molecular bands are displayed in Figs. 2, 4 and 6. Low resolution plots of the total vertical atmospheric transmission with molecular transition band centers drawn in for hydrogen, water, and methane isotopomers are shown in Figs. 3, 5, and 7 respectively. These spectra are taken from the Handbook of Geophysics and Space Environments.[45] A schematic of the HT absorption spectrum is presented in Fig. 2. As for HD, the HT overtone ($0 \rightarrow 2$) is only a factor of four weaker than the fundamental ($0 \rightarrow 1$) transition bandstrength. The predicted spectra are given for two instrumental resolutions, 0.01 μm and 0.1 μm. To simulate a grating instrument, a triangular slit function, constant in wavelength, is convolved with the nascent line shapes. For the lowest resolution scan, the overtone P and R branches are unresolved. It can be seen in Fig. 3, that the HT fundamental falls in the spectral region of atmospheric water vapor absorption (the ν_3 band), and a more accurate determination of the exact relative location of HT and HOH vibration-rotational lines would be needed to determine the optimum wavelength for HT detection. The HT overtone, although weaker, falls in a less severely attenuated atmospheric region.

In Fig. 4, the schematic spectra for HOH and HOT are given. The near degeneracy of the ν_3 and ν_1 bands in HOH is altered in HOT. As can be seen the HOT ν_1 band is shifted by nearly 2 μm and also gains sufficient bandstrength to provide for significant absorption. The integrated bandstrengths used are those given in Table VII. The HOT bandshape estimates are made from modified HOH rotational distributions and symmetry considerations. The ordinate scales are both normalized to the same value, corresponding to a two e-fold attenuation at the peak of the HOH ν_2 P branch. In Fig. 5 it is seen that the shifted HOT ν_1 band falls in a spectral

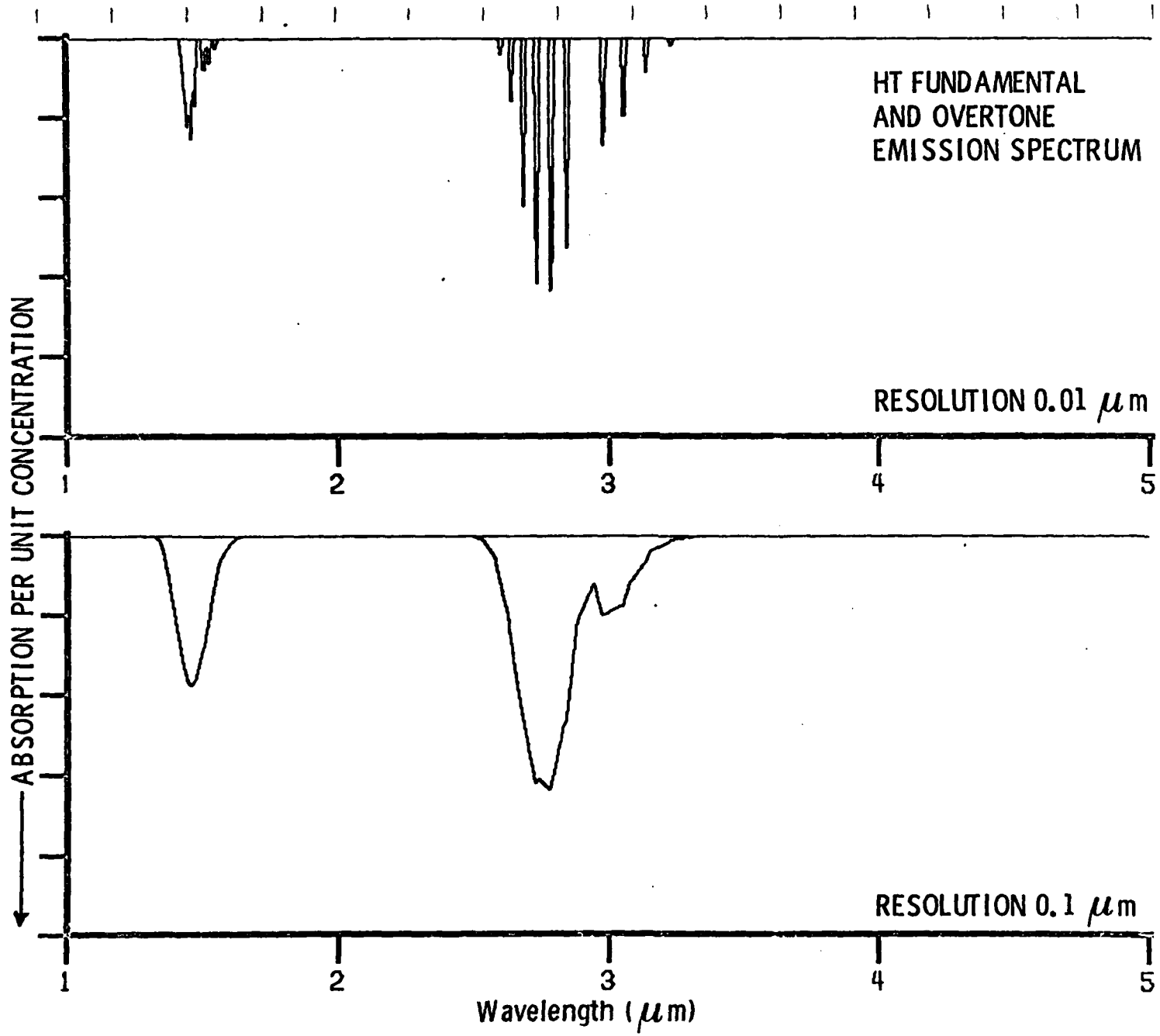

Figure 2. Schematic of HT Absorption Spectrum for Two Resolutions

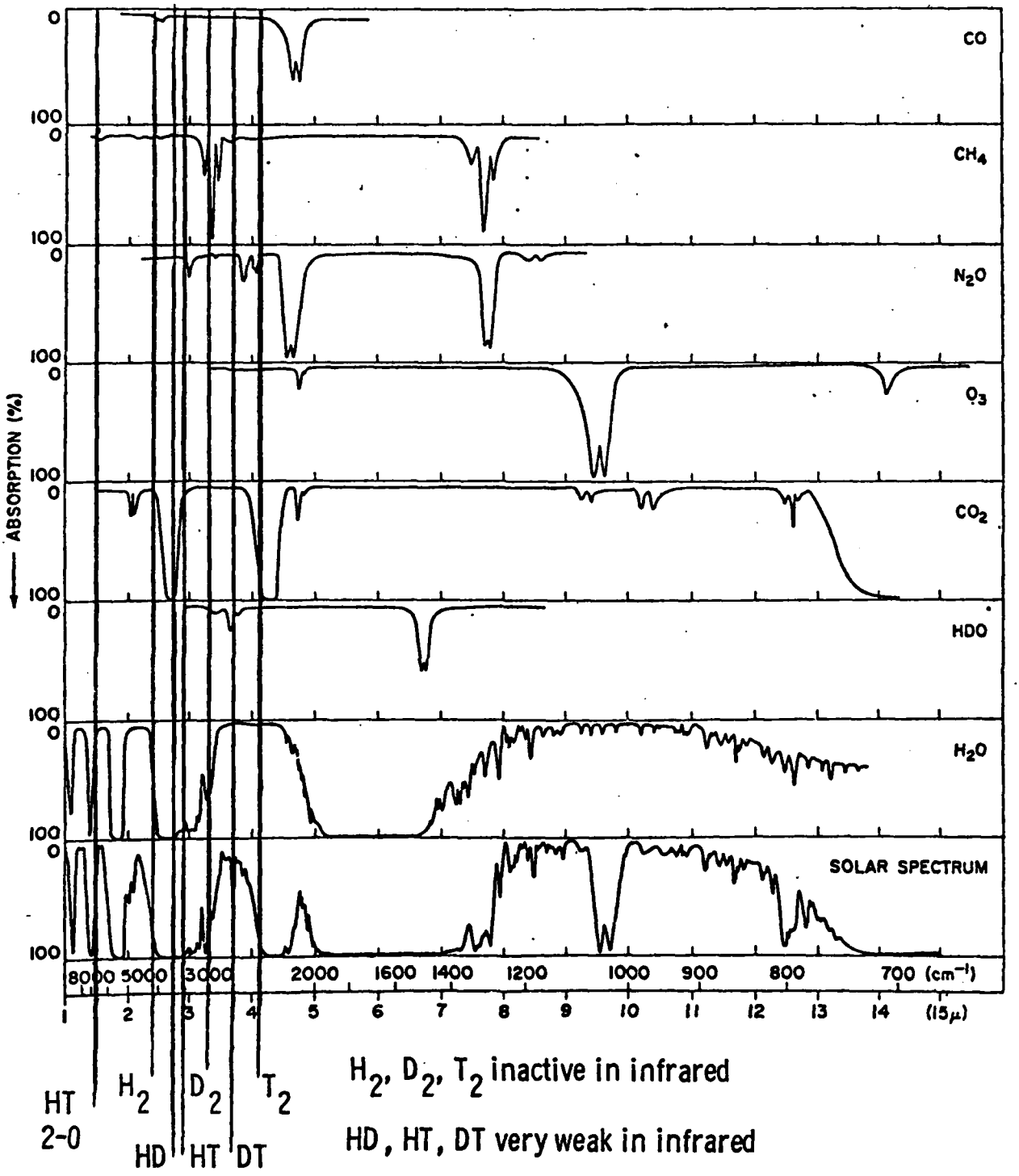

Figure 3. Bandcenters of the Transitions of Hydrogen Isotopomers Drawn for Comparison with Relative Atmospheric Transmission

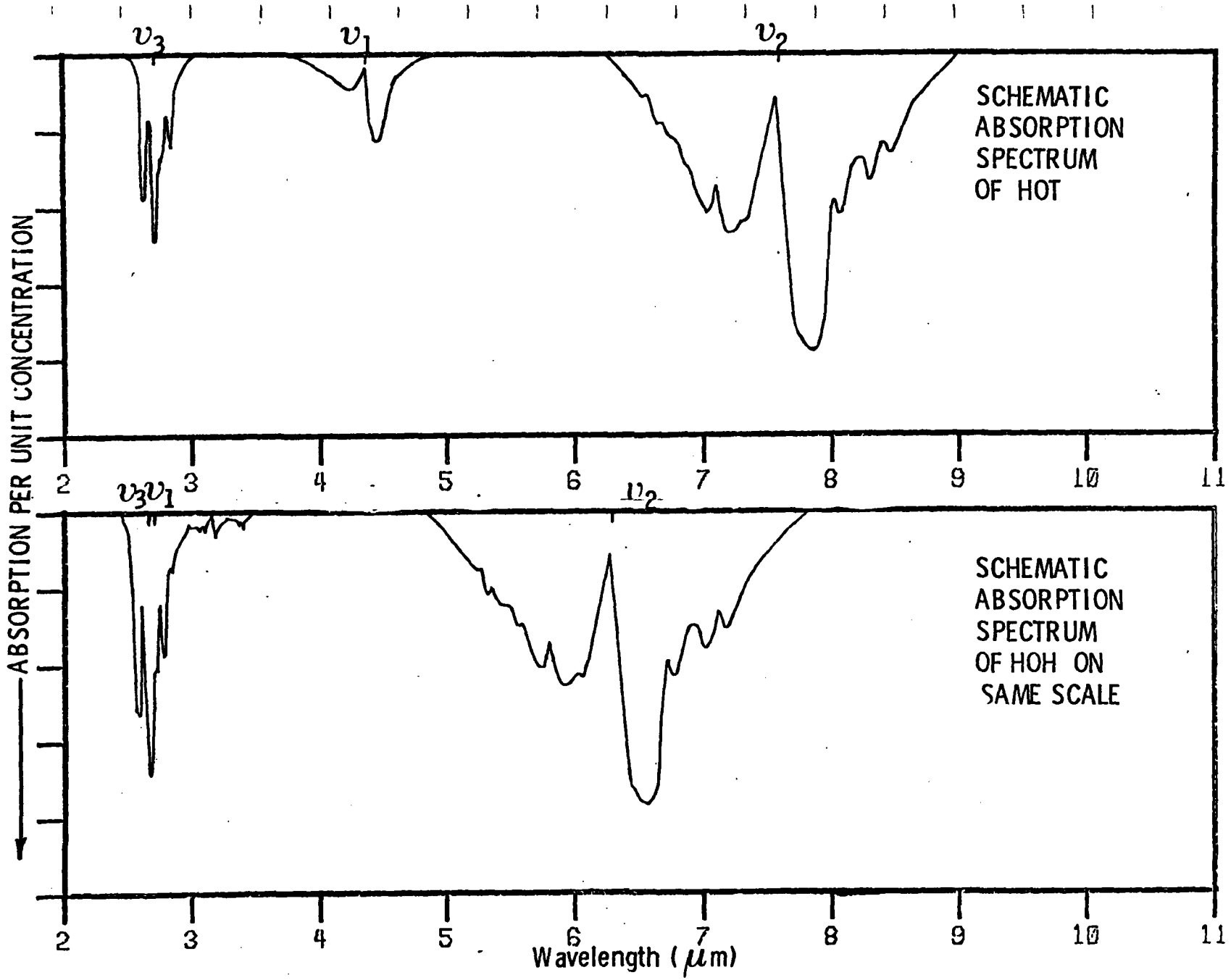

Figure 4. Comparison of HOH and HOT Absorption Spectra

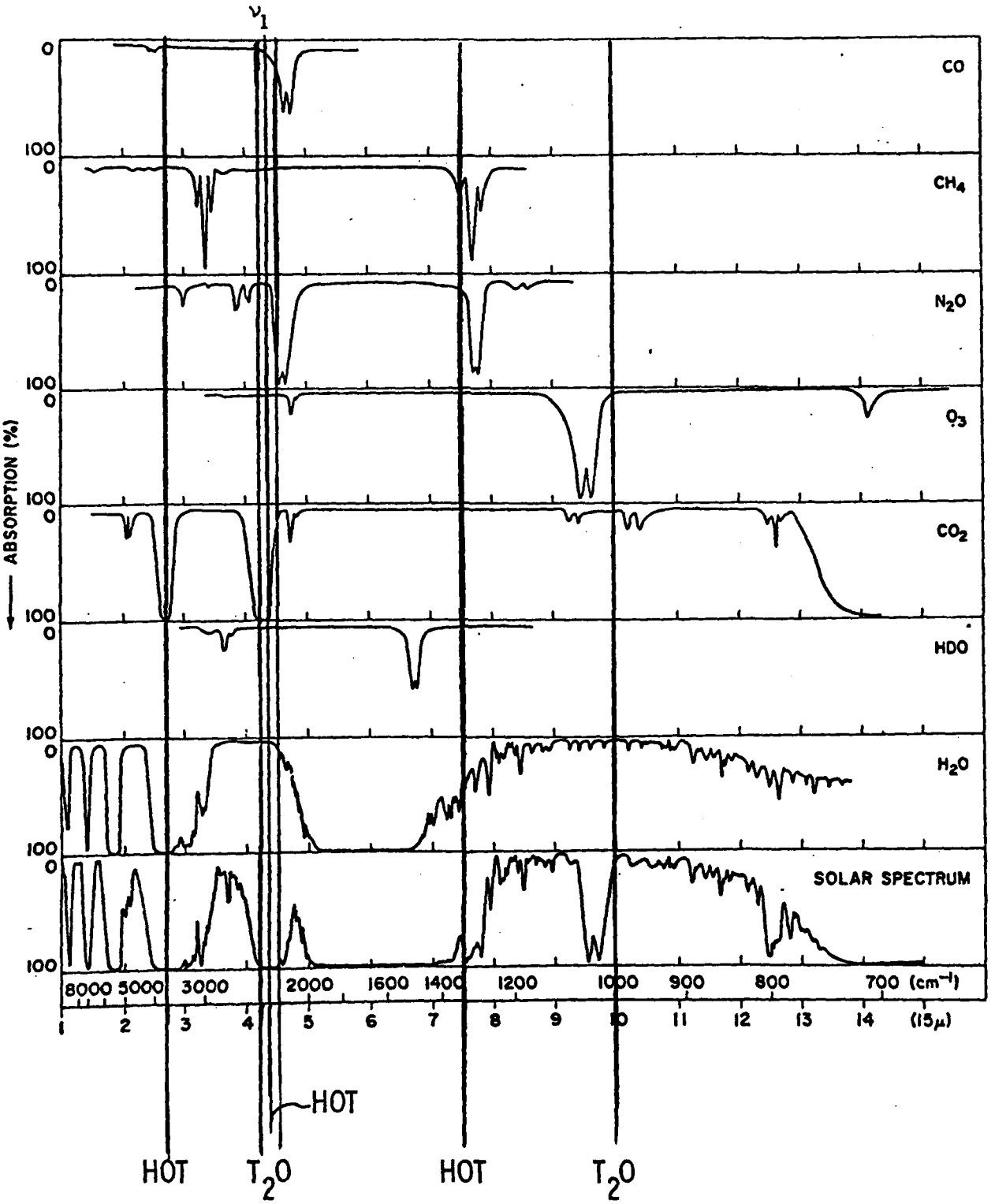

Figure 5. Water Isotopomer Bandcenter Locations Drawn for Comparison With Relative Atmospheric Transmission

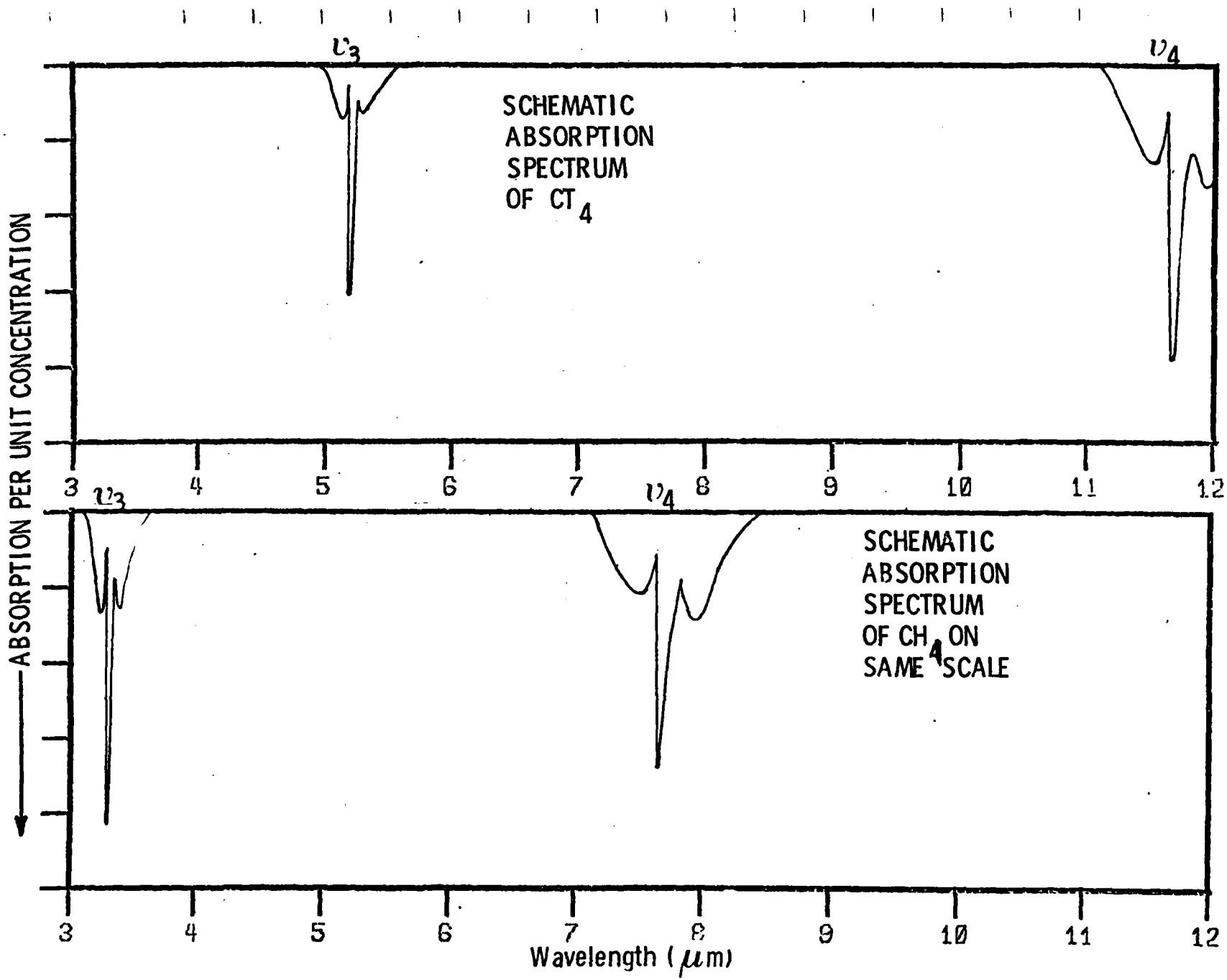

Figure 6. Comparison of CH_4 and CT_4 Absorption Spectra

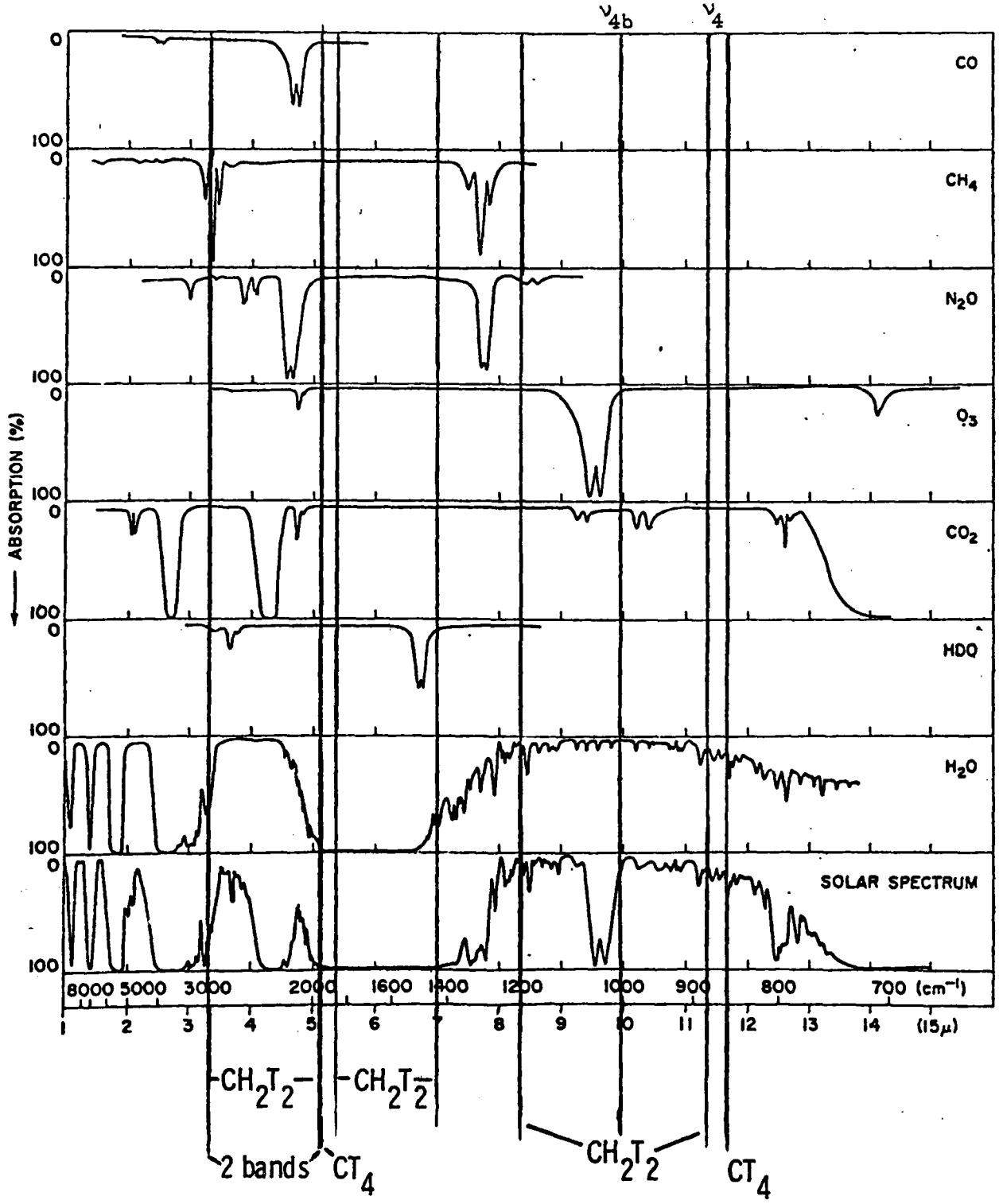

Figure 7. Methane Isotopomer Bandcenter Locations Drawn for Comparison With Relative Atmospheric Transmission

region affected by atmospheric CO_2 absorption. The HOT ν_2 band, which is significantly red-shifted from the atmospheric water absorption band, may suffer some interference with the methane ν_4 band, however the HOT ν_2 P branch lines appear to be the most likely candidates for interference-free transmission.

In Fig. 6 the predicted CH_4 and CT_4 vibrational spectra are presented, again both are normalized to the same scale. Because molecular symmetry is not disturbed, the molecular bandshapes are only red-shifted for CT_4 (due to increased molecular mass). The relative bandstrengths used are those listed in Table XIII. The CT_4 ν_4 vibrational band is shifted into a spectral region of good atmospheric transmission as is shown in Fig. 7. The CH_2T_2 transition centers of Table XII are also drawn in Fig. 7. It can be seen that the ν_{4b} band, centered at 1005 cm^{-1}, falls in an atmospheric region relatively free from interference (O_3 should not be present in significant quantities at low altitudes).

A systematic assessment of monitoring techniques was conducted to determine the most promising method for the remote detection of these tritiated species at very low concentrations in the atmosphere. Observation of the molecules either by their thermal emission or by their absorption signatures in broad background radiation would provide for a single position passive detection capability. Active remote monitoring techniques using broadband incoherent sources rapidly lose sensitivity as distance and spectral resolution are increased because of source intensity limitations. On the other hand lasers, with their narrow frequency bandwidth, high intensities and small beam divergences, fulfill all necessary criteria as remote monitoring sources.

Laser absorption techniques require a remote co-operative target, either a detector, a mirror (retroflector) or a topographical feature which may be used as a reflector (buildings or even trees). The necessity of a

detector or mirror located on the opposite side of the monitored region results in a loss of flexibility. Use of topographical features as retroflectors permits single-ended operation at the expense of returned signal level. Elastic scattering from molecules (Rayleigh scattering) and atmospheric particulates (Mie scattering) has been used to provide the return signal at the laser frequency for a single-ended system. This scattering is a slowly varying function of wavelength and sharper molecular absorption features would be resolvable in this return signal as the laser is tuned in wavelength. The elastic scattering, which is usually considered as a beam attenuation factor, acts as the diffuse retroflector for this differential absorption of back scattering (DABS) technique. Fluorescence, the subsequent reemission of the radiation absorbed by the molecule, may be detected by monitoring at the excitation wavelength only (direct fluorescence) or by monitoring the radiation emitted in the whole vibrational band. This fluorescence is emitted isotropically into 4π steradians , and thus the technique does not require a reflector. (Note all the above laser techniques require a radiation source which can be tuned into resonance with molecular absorption lines.)

Two non-resonant techniques were also considered, Raman scattering and coherent anti-Stokes Raman Scattering (CARS) or four-wave mixing. In the inelastic Raman process the laser radiation is isotropically scattered by the molecules , and thus the technique is single ended. The frequency shift from the incident radiation is approximately the molecular vibrational frequency. (Rotational structure is also present.) Thus a single laser excitation frequency will give rise to species specific shifted radiation. Resonance Raman scattering relies on enhanced scattering cross-sections by wavelength tuning the probe laser into near-resonance with a molecular electronic transition. Because none of the species of interest has an electronic transition in the near ultraviolet or visible,

this technique is not applicable. A CARS monitoring apparatus would employ two lasers, separated in frequency by the molecular vibrational frequency, and a complex optical sending system. The scattered radiation signal is collimated and forward scattered, necessitating a double-ended system.

The final technique considered was passive and single-ended, relying on the molecular thermal emission but utilizing heterodyning. Specifically, if frequency and intensity stabilized laser radiation is incident on the detector along with the thermal line radiation, and the laser is in near-resonance with the molecular emission a considerable improvement in the minimum detectable signal can be obtained through monitoring the beat frequencies occurring at the difference in frequencies of the two incident sources.

An in depth comparison of the techniques cannot be made without adopting a specific measurement scenario. All the above techniques can be viable for certain specific monitoring conditions. For example the sky background radiation, which forms the radiation source for passive absorption, often limits active resonance techniques and this radiation is a function of solar position, azimuthal angle and meteorological conditions. The altitude at which the species are to be monitored will determine molecular lineshapes and quenching times. Source velocity could doppler-shift the spectrum. Measurement uncertainties are a function of signal to noise and integration times. Additionally, the high power, accurately tunable laser source, which might be required for successful use of many of these techniques, will not necessarily be available. Tunable infrared diodes do not have sufficient power. Parametric oscillator linewidths are too broad. Technological improvements are expected, but collection efficiency and level of detection sophistication are inversely dependent on the tunable source intensity.

To reduce the number of variables as much as possible and permit comparison of the relative merits of the various methods, a uniform observation scenario and detection system have been chosen. Specifically the molecules will be remotely monitored in a "cloud" 1 km in thickness, 1 km away. The will be no source or "cloud" velocity and observation will be horizontal or slightly upwards. The "cloud" temperature will be 305°K but otherwise the cloud will have the same optical transmission and scattering characteristics as the normal sea-level atmosphere, with of course, the addition of the tritiated species.

Because the tritiated species do not have accessible electronic transitions, all the resonant processes considered are restricted to the infrared vibration-rotation transitions, whose frequencies have been presented in Section II. Even the visible-UV Raman and CARS techniques display shifts corresponding to these vibrational frequencies.

The fraction of the integrated species bandstrengths, listed in Section II, which will be found in a strong rotational line was calculated using the molecular rotational spacing and temperature. These integrated linestrengths were converted into absorption cross-sections, σ, using the relation

$$\sigma(\text{cm}^2/\text{molecule}) = S_J(\text{cm-molecule}^{-1})/b(\text{cm}^{-1}) \quad , \qquad (31)$$

where b is the expected pressure broadened linewidth at a pressure of one atmosphere. The values of S_J, σ, and the frequency ranges of interest for the tritiates are listed in Table XIV.

The detection system was chosen to have a 10^{-6} sr field-of-view unless otherwise stated, with a 10^{-4} μm bandpass in the visible, 10^{-2} μm bandpass in the infrared, and collection optics of 1 m^2 area. The detector

TABLE XIV

INDIVIDUAL LINE INTENSITIES

Molecule	Transition	S_J (cm-molecule^{-1})	σ (cm^2/molecule)	Frequency (cm^{-1})
HT	$R_2(1)$	6.4×10^{-25}	6.4×10^{-23}	6850
HOT	ν_2 , P(5)	1.4×10^{-19}	6.8×10^{-18}	~1320
CT_4	ν_4 , R(7)	1.1×10^{-19}	1.9×10^{-18}	~880
CH_2T_2	ν_{4b} , R(6)	5.4×10^{-20}	1.0×10^{-18}	~1035

for visible light was assumed to have 30% efficiency. Infrared signals were monitored by a Ge:Hg detector in the 6 - 12 μm region ($D^* \sim 10^{10}$ cm Hz$^{1/2}$ Watt^{-1}) and by PbS detector in the near IR($D^* = 4 \times 10^{11}$). A prototype tunable infrared laser system is assumed with 10^{-2}W power (1 kW peak power, 10^{-6} second pulse length and 10 Hz repetition rate). Finally, no interferences between molecular absorbers are taken into consideration in the minimum detectable concentration determinations. (It is assumed an interference free line can be found.)

Passive absorption techniques rely on a remote radiation source, either the sun, diffuse sky radiation, or earthshine. Differential absorption of the broad source spectrum occurs in the "cloud" by the species of interest. Dispersive instruments are confined to low resolution operation to gain sufficient signal intensity[46]. Interferometric detection[47,48] and non-dispersive correlation techniques[49-51] with high throughput have been successfully employed. A correlation mask technique using the sun as the remote source was capable of ppb level detection of absorbers in the near UV[50]. In the infrared down-looking earthshine measurements

provide the optimum signal. CO has been detected at 40 ppb-km by a gas filter correlation instrument and at 250 ppb-km by an interferometer[47]. The predicted sensitivities of these schemes have been adapted to tritiate detection using appropriate absorption cross-sections, detector sensitivities, source radiances and observation angle for this scenario. The predicted minimum detectable concentrations (MDC) are listed in Table XV. The sensitivity is inversely proportional to the pathlength through the cloud.

TABLE XV

MDC VALUES IN ppb

Technique	HT	HOT	CT_4	CT_2H_2
ABSORPTION	6×10^4	0.56	2	3.8
DABS	6×10^4	8.5	43	49
PASSIVE ABSORPTION	8.5×10^6	45.	400	570
HETERODYNE DETECTION OF EMISSION	--------	3.9×10^3	4.4×10^3	8.9×10^3
CARS	$10^4 - 10^5$	$10^4 - 10^5$	$10^4 - 10^5$	$10^4 - 10^5$
RAMAN	2.1×10^6	4.3×10^6	4.9×10^6	9.8×10^6

FLUORESCENCE - All species excessively large

Passive detection of emission similarly suffers intensity problems unless the molecular emitters are at a considerably elevated temperature. For the present scenario, normal detection schemes are unable to monitor the weak molecular emission in the presence of a broad spectral background. The detection system sensitivity may be increased by several orders of magnitude by using a laser as a local oscillator and mixing both the laser radiation and the remote emission on the detector (heterodyning). The dominant component of the amplified signal will be the difference frequencies between the local oscillator optical frequency and the remote emission (both background and signal). Only beat frequencies within the 1 MHz - 1 GHz bandpass (emission near-resonant with the local oscillator) will be amplified. The detector noise equivalent power of a radiometer using a photoconductive detector is

$$\text{N.E.P.} = \left(\frac{2h\nu}{\eta}\right)\left(\frac{B}{\tau}\right); \text{ Watts} \qquad (32)$$

where $h\nu$ is the photon energy, η is the mixer quantum efficiency, B is the amplification network bandpass and τ is the post detection integration time.[52] The laser local oscillator must be tunable and frequency stabilized; power requirements are minimal, being only tens of milliwatts. This technique then requires only that the molecular emission exceed the sky background radiance at line center. The line center emission is

$$I_{CL} = \frac{S_J}{b}\bar{N}_R L R_{BB}(\nu, T) \geq I_{sky}(\nu) \qquad (33)$$

where S_J is the vibrational-rotational line intensity, $\bar{N}_R$ is the average concentration of radiators, L is the length over which emission occurs, and R_{BB} is the blackbody radiance at the frequency of interest for 305°K. The

sky background radiance, $I_{sky}(\nu)$, for near-horizontal observation[45] is set equal to the centerline emission intensity in order to determine the minimum detectable $\bar{N}_R$. The field-of-view of the radiometer is optimized as 10^{-3} str for a 1 mm^2 infrared detector[53]. Radiometer direction can easily be chosen such that the "cloud" fills its field-of-view. The predictions for the MDC of each of the tritiated species using the S_J values of Table XIV, is given in Table XV. At HT emission wavelengths, the sky radiates much like a 300°K blackbody and detection is impossible. The $(\bar{N}_R)_{min}$ are calculated using Elsassar's radiation transfer function[54]. Note that at MDC levels the emitters are no longer optically thin and intensity does not scale linearly with concentration. The HOT radiation scales as $\sqrt{N}$ near MDC level. The tritiated methanes emission scale as $N^{0.6-0.7}$. As radiator concentration increases, the fractional radiative transfer scales as $\sqrt{N}$, complicating remote emitter concentration determination.

The laser absorption schemes considered would involve monitoring of the returned signal as laser frequency is varied. Atmospheric scattering will slowly vary as the laser is tuned, but the sharp molecular absorption features should be resolvable in the quasi-constant background. Inter-pulse frequency variation is the method considered here. If atmospheric transmission fluctuations are prohibitive, longer pulse durations with frequency modulation during the pulse may be required to achieve return signal stability.

The absorption technique return signal may be specified by the equation

$$I_{sig} = (I_L e^{-2\alpha_s R})(e^{-2\sigma \bar{N} D}) \frac{A_d}{A_b(R^2)} r \zeta(\nu) \qquad (34)$$

where I_L is the laser intensity, $A_d/A_b(R^2)$ is the fraction of the beam returned to the detector, r is the reflectivity of the reflector, $\zeta(\nu)$ is the detector efficiency, $\alpha_s(\nu)$ is the atmospheric attenuation due to scattering

(km^{-1}) and R is the distance to the region of interest. The term in the second bracket is the degree of absorption by the tritiated species where D is the "cloud" thickness.

The two terms in brackets predict beam fall off due to atmospheric and "cloud" attenuation, with $\sigma(\nu)$ being a much more rapidly varying function of frequency than $\alpha_s(\nu)$. A 1% signal change between on and off resonance pulses is taken as the smallest detectable absorption. This determines the MDC as long as I_{sig} is more than a factor of 100 greater than the detector N. E. P. The return signal power fall off is due to atmospheric attenuation and geometric beam spread. For the prototype laser with a mirror retroflector (double-ended system), $I_{sig} > 100$ N. E. P. for $R < 6$, 4, 5 and 4 km for HT, HOT, CT_4, and CT_2H_2 respectively, using the atmospheric attenuations[55] at the most likely detection frequency. For the present scenario, this technique is not power limited and the MDC is independent of R:

$$-\ell n \frac{I}{I_o} = 0.01 = 2\Delta\sigma \int_o^D N(x)dx = \sigma \bar{N}_{min} D \qquad (35)$$

where $\Delta\sigma$ is the change in molecular absorption coefficient between the two measurements. Only the average absorber concentration in the "cloud" can be obtained by this method. The $\bar{N}_{min}$ values are listed in Table XV. Note that a single-ended system using topographical reflectors becomes signal limited at ranges of 1 - 3 km depending on the reflectivity of the topographical target[56,57]. If sufficient signal is returned, $\bar{N}_{min}$ will be unchanged from the values deduced for a double-ended system.

When atmospheric elastic backscatter is used as the reflector (DABS), the effective reflectivity becomes

$$r_{eff} = \alpha_s(\nu)\, L \tag{36}$$

where L is the range observed by a gated detector. For the present scenario, the detector is gated on for a few μseconds, observing only backscatter which has passed through the whole cloud. The atmospheric backscatter is isotropic and the return signal is specified by

$$I_{sig} = (I_L\, e^{-2\alpha_s R})(e^{-2\sigma \tilde{N} D})\quad \alpha_s(\nu) L \frac{A_d}{4\pi R^2}\, \zeta(\nu) \tag{37}$$

where $A_d/4\pi R^2$ is the fraction of the scattered radiation reaching the collection optics. For similar laser powers, atmospheric backscatter results in a much lower returned signal than a reflector. Consequently, the range at which this method becomes very signal limited is less than 1 km. The Mie particulate scattering coefficient is a function of visibility and weather conditions. A laser power one hundred times higher than previously considered is required to permit detection of the tritiates under marginally signal limited conditions. The DABS MDC levels are listed in Table XV. Still higher laser powers would permit these values to approach the MDC levels of pure absorption. Heterodyne detection of DABS, requires a considerable increase in system complexity. A second cw laser, also frequency stabilized, is used as the local oscillator. Both lasers must be simultaneously tuned through a molecular absorption line while maintaining a constant frequency difference.[58]

For the case of fluorescence techniques in the infrared, the radiative lifetimes are long compared to typical laser pulse durations, thus requiring the use of long gating times (large background levels). Furthermore competition occurs between re-emission of the absorbed energy and energy transfer to other molecules through collisions. The collisional fluorescence efficiency, φ, is the fraction of the excited molecules which fluoresce.

For a pressure of one atmosphere φ is calculated to be 1.6×10^{-7} for HOT and 4.5×10^{-6} for CT_4 and CT_2H_2 from vibrational relaxation data for water and methane. φ is taken as unity for HT. When fluorescence from the whole vibrational band is monitored, the detection system bandpass must be increased. If direct fluorescence is used, only a small fraction of the total fluorescence is observed. The returned fluorescence signal is

$$I_{sig} = (\sigma\varphi\bar{N}D)(I_L e^{-2\alpha_s R})(e^{-\sigma\bar{N}D}) \frac{A_d}{4\pi R^2} \zeta(\nu) \qquad (38)$$

where the first term in brackets is the effective remote fluorescent source intensity. The minimum detectable signal level is taken to be equal to the sky background level. The combination of wide detection system bandpass, isotropic scattering, and low fluorescence efficiency eliminate fluorescence as a practical technique is this comparison.

The Raman scattering cross-section increases as ν^4, so a blue or ultraviolet laser source should be employed to enhance the small Raman cross-sections as much as possible. The Raman scattered, frequency-shifted signal is weaker than the atmospheric elastic scattering and therefore detection system discrimination against the laser frequency must be great. All modes of HT, HOT, CT_4, and CT_2H_2 are Raman active. The returned Raman signal is of the form

$$I_{sig} = (\sigma_R\bar{N}D)(I_L e^{-2\alpha_s R}) \frac{A_d}{4\pi R^2} \zeta(\nu) \qquad (39)$$

where the first term in brackets is the effective remote Raman signal source. The largest Raman cross-sections, σ_R, for the methane isotopomers are calculated to be 7×10^{-30} cm^2 str^{-1} for $CT_4(\nu_3)$ and $3.5 \times$

10^{-30} cm^2 str^{-1} for $CT_2H_2(\nu_3)$.[31] The HT and HOT cross-sections are estimated from the hydrogen isotopomers as 1.6×10^{-29} cm^2 str^{-1} and 8×10^{-30} cm^2 $str^{-1}(\nu_3)$ respectively. Atmospheric attenuation is ~ one km^{-1} in the near UV.[59] I_L is taken as 0.3J, assuming a doubled ruby laser source at 347 nm, with a gated detection system. Raman scattering is instantaneous and the detection gating is chosen to observe only Raman scattering from the cloud.[60,61] The MDC values in Table XV are calculated neglecting Raman signal interferences and Rayleigh background levels; they are taken as the concentration at which the Raman signal is equal to the sky background signal.

The final method considered, CARS, would be the most difficult to implement. It offers the advantages of higher conversion efficiency than the Raman process, and the output is collimated, not isotropically scattered. Two lasers are required, a pump laser at frequency ω_p, and a Stokes laser at ω_s. Their frequency difference must be the vibrational frequency, ν_o, of the tritiated molecule. The molecule is driven up to a virtual state by E_p and back down (stimulated emission) to $\nu_o = 1$ by E_s. The E_p field then drives the molecule up to a slightly higher virtual state from which re-emission occurs at $\omega_a = \omega_p - \omega_s + \omega_p$. A schematic of the process is shown in Fig. 8.

The non-linear effect arises from the dipole induced in the medium by the laser fields[60], i.e.,

$$\mu_I \propto \chi^{(3)} E_p E_s E_p \qquad (40)$$

where $\chi^{(3)}$ is the third order susceptibility. Equation (40) can be more explicitly written as

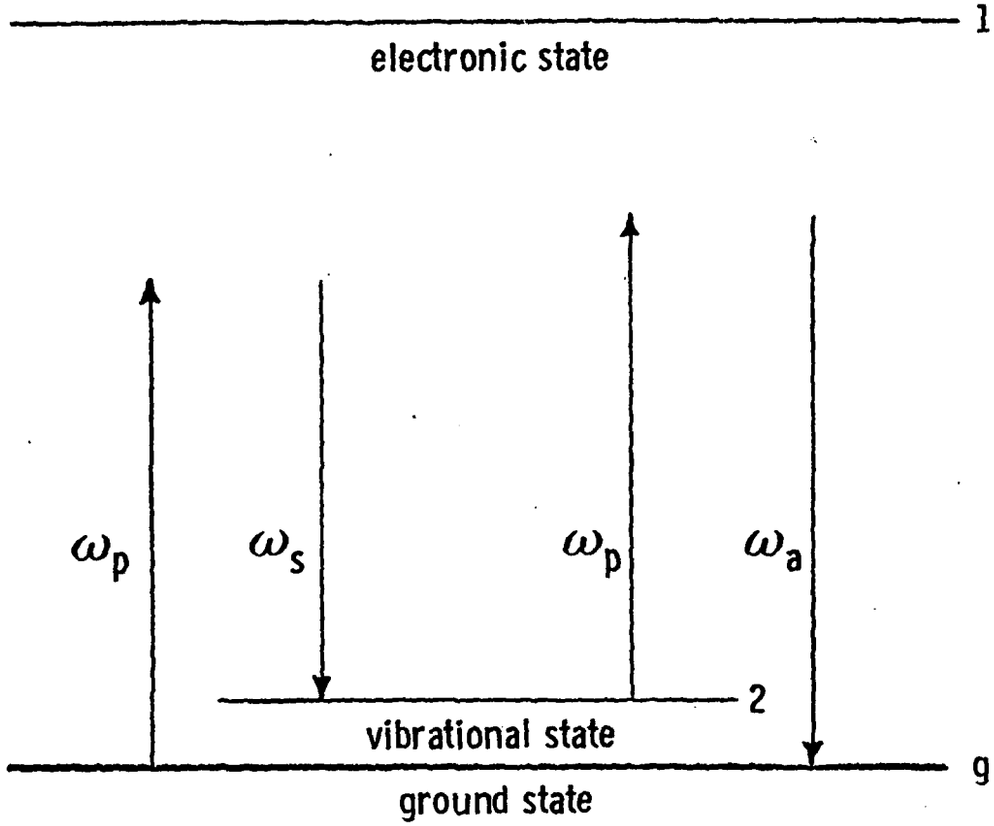

Figure 8. Schematic of CARS Pumping Mechanism

$$\mu_I \propto \frac{\mu_{g1}\mu_{12}\mu_{21}\mu_{1g}E_pE_sE_p}{\hbar^3(\omega_{1g}-\omega_p)(\nu_o-\omega_p+\omega_s)(\omega_{1g}-\omega_a)} \tag{41}$$

where μ_{xy} is the transition moment between states x and y in Fig. 8, and ω_{1g} is the frequency of the transition to state 1. As $\omega_p - \omega_s$ approaches ν_o the denominator approaches zero, and the induced dipole is resonantly enhanced. The ω_a emission is blue shifted from ω_p by ν_0 and hence is called anti-Stokes. Emission at ω_a is permitted at all angles, but occurs preferentially along a direction corresponding to minimum wave vector defect. The magnitude of the wave vector is

$$\left|\vec{k}\right| = \frac{2\pi\omega\eta}{c} \tag{42}$$

where η is the index of refraction of the medium at ω. The wave vector defect, $\vec{\Delta k}$, is then

$$\vec{\Delta k} = \vec{k}_a - (\vec{k}_p - \vec{k}_s + \vec{k}_p) \tag{43}$$

and the power in E_a, the anti-Stokes emission, falls off as $(\text{sinc}\ \vec{\Delta k})^2$. Knowledge of η, at the ω values chosen, permits prediction of the relative angular separation of pump, Stokes, and anti-Stokes beams which will maximize output power. Figure 9 displays this vector addition.[61] The pump and Stokes beams will not be co-linear, and the anti-Stokes beam will be forward scattered at yet a different angle, necessitating a double-ended detection system.

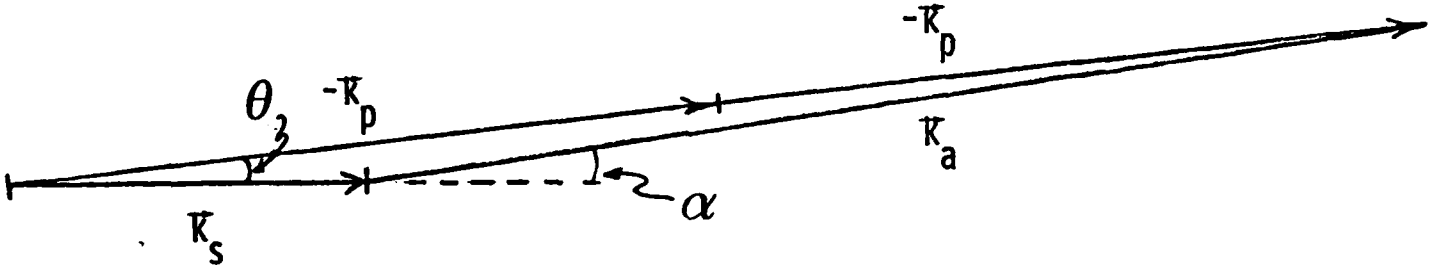

θ is angular separation of pump and Stokes beams

α is angular separation of Stokes and output beams

$\alpha > \theta$, $\Delta\bar{K} = 0$

Figure 9. Wavevector Addition for Four-Wave Mixing

The power in the anti-Stokes beam is

$$I_a \propto \frac{N^2 L^2}{A_p^2} I_p^2 I_s (\chi^{(3)})^2 \left[\frac{\sin(\Delta\vec{k}L/2)}{\Delta\vec{k}L/2}\right]^2 \tag{44}$$

where A_p is pump beam area, and L is the interaction length. The optical quality of the interacting beams must be very good inasmuch as wavefront distortion and index of refraction fluctuations will affect the wavevector matching and destroy the output beam coherence (collimation). For the present scenario the CARS signal is

$$I_{sig} \propto \frac{N^2 L^2}{A_p^2} I_p^2 I_s (\chi^{(3)})^2 \left[\text{sinc}\left(\frac{\Delta\vec{k}L}{2}\right)\right]^2 e^{-2\alpha_s R} \frac{A_d}{A_a} \zeta(\nu) \tag{45}$$

where A_a is the area of the anti-Stokes beam at the detector. It has been determined experimentally that interferences due to normal atmospheric constituents limit ultimate detection sensitivities to the 10 - 100 ppm level.[62] However pure species detectability levels are very low $\sim 10^{-10}$ atmosphere.[60]

From the summary of MDC levels for the various techniques presented in Table XV, it appears that no method will be capable of detecting HT concentrations less than 10 ppm. The absorption techniques permit ppb level detection of water and methane isotopomers in the cloud, orders of magnitude more sensitive than any of the other methods considered. Use of remote reflectors (mirrors, topographical targets) appears more feasible than DABS for current laser technology.

The absorption monitoring technique appears to be most apropos to present interests and is now applied to a more specific scenario. The volume to be monitored is taken to be the exhaust from the stack exposed to a 12 knot

crosswind. The plume, as a first approximation, grows conically downwind. The monitoring system is double-ended, observation is along the plume axis with source (or reflector) at the stack and the other element one km downstream. Since the plume is growing, the tritiate concentration is varying along the plume axis, but the absorption technique will measure only the integrated concentration along the optical path, which may then be related to the stack exhaust rate. With a 12 knot wind it takes 200 seconds to form a one km plume. A schematic of this monitoring scenario is given in Fig. 10. It is assumed that the initial plume radius is about one meter, and the growth angle of the plume is 0.1 radian.

The plume area at any point downstream, x, is

$$A(x) = \pi(r_i + x \sin\theta)^2 \tag{46}$$

and the tritiated density may be related to the initial density, N_i, by

$$N(x) = \frac{N_i A(0)}{A(x)} = \frac{N_i r_i^2}{(r_i + x \sin\theta)^2} \tag{47}$$

The integrated line density along a one km path is

$$\int_0^D N(x)dx \approx \frac{N_i D}{1 + \frac{\sin\theta}{r_i} D} \simeq 0.01\ N_i D \text{ (molecules/cm}^2\text{)} \tag{48}$$

where D is one km. The total concentration in the plume is $N_s A_s D$ (which is deposited in 200 seconds) where the subscript means at the stack exit.

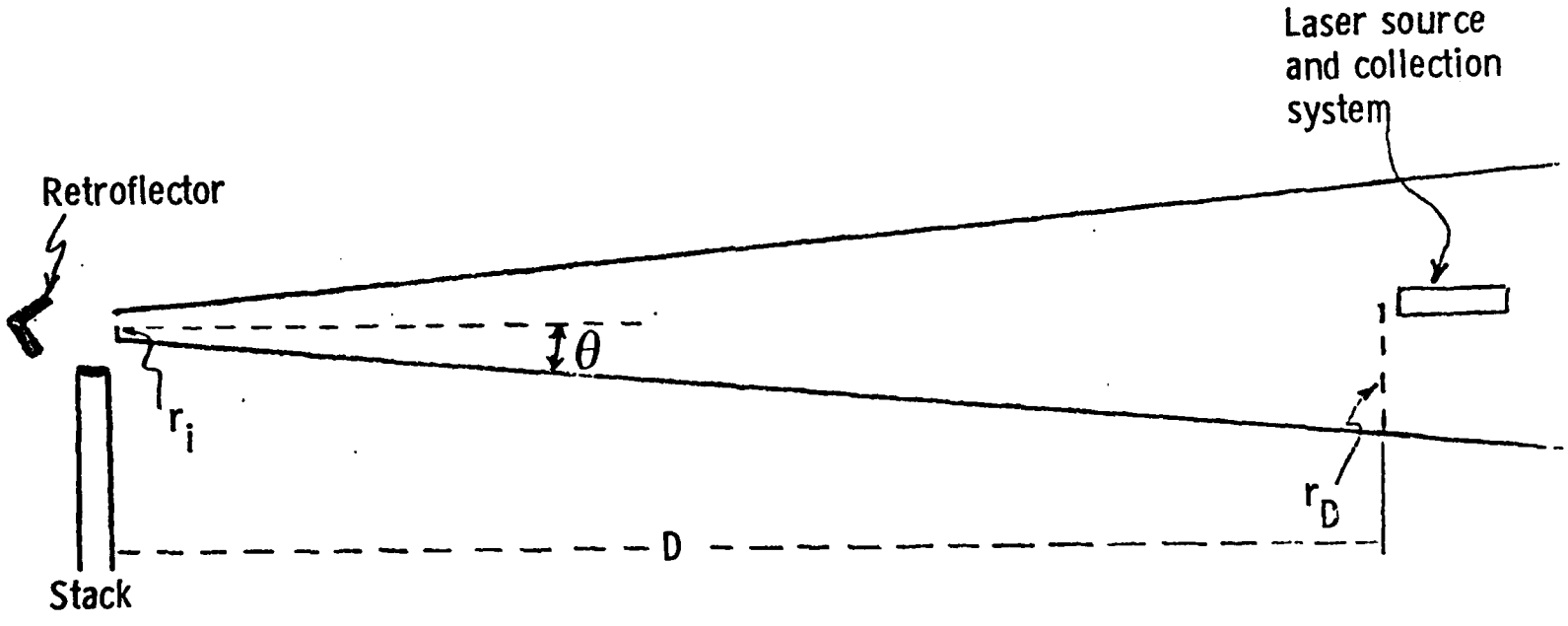

$D = 1\,Km,\ r_i = 1m,\ r_2 = 100m$

Figure 10. Visualization of Absorption Monitoring Technique for the Stack Plume Scenario

If we assume that A(0) is approximately the stack area, then the tritiate exhaust rate can be related to the detected line density,

$$\dot{N}_{TRIT} = \frac{N_s A_s D}{200} \frac{\text{molecules}}{\text{sec}} = \frac{N_i A(0) D}{200} = \frac{A(0) \int_0^D N(x)dx}{2} \qquad (49)$$

Making use of Eq. (35) for large return signal conditions results in

$$0.01 = 2\Delta\sigma \int_0^D N(x)dx = 0.02\,\Delta\sigma\,(N_i)_{min} D = \frac{4\Delta\sigma}{A(0)} (\dot{N}_{TRIT})_{min} \qquad (50)$$

Using the optimum cross-sections in Table XIV, values of N_{min} and $\dot{N}_{min}$ are calculated for the tritiates. These values are listed in Table XVI, for $A(0) = 3\ m^2$, and 1% minimum detectable signal change. Also shown are the corresponding minimum flows of radioactivity.

TABLE XVI

MINIMUM DETECTABLE CONCENTRATIONS FOR WIND DRIVEN PLUME

Molecule	$(N_i)_{min}$ ppb	$\dot{N}_{min}$ (grams/sec)	$\dot{C}_{min}$ (curies/sec)	Radiation at 1 km Downwind C_{min}/m^2	Time Required to exceed Maximum Quarterly Exposure (Inhale; $1 m^2$ area)
HT	3×10^6	7.8	4.1×10^4	1.3	2.4 msec
HOT	28	3.7×10^{-4}	3.9×10^{-1}	1.2×10^{-5}	260 sec
CT_4	100	1.6×10^{-3}	5.6	1.8×10^{-4}	17 sec
CH_2T_2	190	2.5×10^{-3}	5.3	1.7×10^{-4}	18 sec

The tritiate concentration one km downwind has dropped 4 orders of magnitude below the stack concentration and is at the 10 ppt level for the minimum detectable line densities of water and methane isotopomers. It should be noted that the absorption techniques do not become signal limited for ranges < 4 - 6 km and only a reflector is required at the stack; the source and collection optics may be several kilometers downwind.

IV. SUMMARY AND OVERVIEW

In conclusion the properties of the infrared vibration/rotation bands of HT, HOT, CT_4 and CT_2H_2 have been specified, and a manifold of optical remote monitoring techniques has been reviewed in order to define that method which best allows the observation these tritiated species at minimal concentrations in the atmosphere. The optimum monitoring technique has been found to be an active absorption method utilizing a tunable laser source with a retroflector. Minimum detectable concentrations have been specified for generic monitoring conditions and in one instance these concentrations have been related to minimum detectable exhaust stack tritiate mass flow rates. General equations which relate these minimum detectable concentrations to monitoring conditions, such as atmospheric properties and source and detector capabilities, have also been provided.

If the predicted minimum detectable concentrations are sufficiently low to prompt a further feasibility study it is suggested that the detailed line to line structure of these tritiates be measured in the laboratory. The proposed monitoring technique requires tuning on and off one transition in the vibration/rotation band of the molecule, and assumes that there will be no accidental interfering absorption by standard atmospheric species. Transition linewidths at pressures near one atmosphere are typically of order 0.1 cm^{-1}, and thus the spectral positions of both tritiate and possible interfering atmospheric molecules should be measured to at least this resolution. Such high resolution measurements can be performed using a laboratory absorption cell and state-of-the-art Fourier transform spectrometers. Furthermore, accurate values of the transition line strengths can also be provided by such measurements. (The species concentration is linearly proportional to the line strength of the monitored transition and only band strengths have been estimated in the present analysis.) The

results of this study could be used to define the optimum transitions to be monitored and to design a validating field test program. A harder look at the deleterious effects due to atmospheric and background variations could also be provided at that time.

It should be emphasized that no remote monitoring technique capable of monitoring "small" concentrations of HT has been identified. If it is desired to determine the concentration of HT, or to determine concentrations of the other tritiates at levels below those specified in Section III, it may be required to capture a sample of the contaminated gas for later analysis in the laboratory.

The state of the art in laboratory spectroscopic measurements has recently been described by Reid and co-workers[63]. In their studies an optimally designed multiple pass White cell with a tunable diode laser source has been used to measure CO concentrations as small as one in 10^{12}. This sensitivity would suggest that such a system could be used to measure HOT, CT_4 or CT_2H_2 concentrations of order 10 parts per trillion and HT concentrations of a part per million.

Hanst[64] has recently taken the novel approach of increasing the relative concentration of contaminant in the test sample via a process of selective cryogenic "distillation". In this technique molecular species such N_2, O_2, H_2O and CO_2 are removed from the sample gas by taking advantage of cryogenic cooling/ condensation phenomena and the remaining contaminant enriched distille is then probed by means of high resolution fourier transform spectroscopy. It would probably be quite difficult to eliminate species such as H_2O and CH_4 cryogenically without also eliminating their tritiated isotopomers, however it would appear possible to develop a sample highly enriched in HT by such techniques. This species could then perhaps be studied with a technique such as CARS.

One alternate technique has been considered for determination of the total tritium concentration in the sample. This would involve monitoring

the vibrational band emission of a species such as OT which could result from a chemiluminescent reaction such as

$$T + O_3 \rightarrow OT^* + O_2 \qquad (51)$$

The Q branch of OT($v = 1 \rightarrow 0$) transitions would fall at 4.50 μm and radiation from higher vibrational transitions would be degraded to the red into a relatively "clear" portion of the spectrum. The tritium atoms could be formed by introducing hydrogen atoms into the sample and taking advantage of isotopic exchange reactions with the contaminant tritiated molecules. It should be emphasized that this concept is only in the embryonic stage but could prove valuable if alternate techniques for determining HT concentration prove inadequate.

V. ACKNOWLEDGEMENTS

The authors with to acknowledge useful discussions with Mr. J. P. Kennealy and Dr. S. A. Clough of the Air Force Geophysics Laboratory.

VI. REFERENCES

1. Overend, J., in Infrared Spectroscopy and Molecular Structure, ed. by M. Davies, (Elsevier, Amsterdam, 1963) p. 345.

2. Pinchas, S. and Laulicht, I., IR Spectra of Labelled Compounds (Academic Press, New York 1971).

3. Herzberg, G., Spectra of Diatomic Molecules (Van Nostrand, New York, 1950), Chapter III.

4. JANAF Thermochemical Tables, Supplement #47, March 31, 1977.

5. Reference 3, p. 109.

6. McKellar, A. R. W., Can, J. Phys. 52, 1144 (1974).

7. Herzberg, G., private communication (1977).

8. Durie, R. A. and Herzberg, G., Can.J. Phys. 38, 806 (1960).

9. Crawford, Jr., B. L., J. Chem. Phys. 20, 977 (1952).

10. Wilson, Jr., E. B., Decius, J. C. and Cross, P. C., Molecular Vibrations (McGraw-Hill, New York, 1955). p. 191.

11. Heaps, H. S. and Herzberg, G., Z. Phys. 133, 48 (1952).

12. Bunker, P. R., J. Molec. Spectrosc. 46, 119 (1973).

13. Brannon, P. J., Church, C. H. and Peters, C. W., J. Molec. Spectrosc. 27, 44 (1968).

14. Stoicheff, B. P., Can, J. Phys. 35, 729 (1957).

15. Bejar, J. and Gush, H. P., Can. J. Phys. 52, 1669 (1974).

16. McClatchey, R. A., Benedict, W. S., Clough. S. A., Burch, D. E., Calfee, R. F., Fox, K., Rothman, L. S. and Garing, J. S., AFCRL Atmospheric Absorption Line Parameters Compilation, AFCRL-TR-73-0096, 26 January 1973.

17. Penner, S. S., Quantitative Molecular Spectroscopy and Gas Emissitivities, (Addison-Wesley, Reading MA, 1959) pp. 138-143, 153, 161.

18. Clough, S. A., Beers, Y., Klein, G. P. and Rothman, L. S., J. Chem. Phys., 59, 2254 (1973).

19. Clough, S. A., private communication (1977).

20. Flaud, J. M. and Camy-Peyret, C., J. Molec. Spectrosc. 55, 278 (1975).

21. Sverdlov, L. M., Kovner, M. A. and Krainov, E. P., Vibrational Spectroscopy of Polyatomic Molecules, Israel Program for Scientific Translations (John Wiley, New York, 1974) pp. 149-155.

22. DeLucia, F. C., Helminger, P., Gordy, W., Morgan, H. W. and Staats, P. A., Phys. Rev. 8, 2785 (1973).

23. Cook, R. L., DeLucia, F. C. and Helminger, P., J. Molec. Spectrosc. 53, 62 (1974).

24. Helminger, P., DeLucia, F. C., Gordy, W., Staats, P. A. and Morgan, H. W., Phys. Rev. 10, 1972 (1974).

25. Fayt, A. and Steenbeckeliers, G., C. R. Acad. Sc. Paris 275B, 459 (1972).

26. Bellet, J., Steenbeckeliers, G. and Stouffs, P., C. R. Acad. Sc. Paris 275B, 501 (1972).

27. Carpenter, R. A., Gailar, N. M., Morgan, H. W. and Staats, P. A., J. Molec. Spectrosc. 44, 197 (1972).

28. Khachkuruzov, G. A., as reported in Ref. 21, p. 471.

29. Staats, P. A., Morgan, H. W. and Goldstein, J. H., J. Chem. Phys. 24, 916 (1956).

30. Steenbeckeliers, G., private communication via L. S. Rothman (1977).

31. Reference 21, pp. 171-179.

32. Jones, L. H. and Goldblatt, M., J. Molec Spectrosc. 2, 103 (1958).

33. Jones, L. H. and McDowell, R. S., J. Molec. Spectrosc. 3, 632 (1959).

34. Bobin, B. and Fox, K., as reported in Reference 16, p. 48.

35. Bermejo, D., Escribano, R. and Orza, J. M., J. Molec. Spectrosc. 65, 345 (1977).

36. Dang-Nhu, M., as reported in Ref. 16, p. 48.

37. Michelot, F. and Fox, K., as reported in Ref. 16, p. 48.

38. Shepherd, G. G. and Welsh, H. L., J. Molec. Spectrosc. 1, 277 (1957).

39. Kaylor, H. M. and Neilsen, A. H., J. Chem. Phys. 23, 2139 (1955).

40. Deroche, J. C. and Guelachvili, G., J. Molec. Spectrosc. 56, 76 (1975).

41. Wilmshurst, J. K. and Bernstein, H. J., Can. J. Phys. 35, 226 (1957).

42. Hiller, Jr., R. E. and Straley, J. W., J. Molec. Spectrosc. 5, 24 (1960).

43. Deroche, J. C., J. Phys. (Paris) 34, 559 (1973).

44. Armstrong, R. L. and Welsh, H. L., Spectrochim.Acta 16, 840 (1960).

45. Handbook of Geophysics and Space Environments, S. L. Valley, ed. (McGraw-Hill: New York, 1965), Ch. 10.

46. Hirschfeld, T. B., Optical Engineering 13, (1), 15 (1974).

47. Goldstein, H. W., et. al., Second Joint Conference on the Sensing of Environmental Pollutants, Washington D. C., 10-12 December 1973 (ISA: Pittsburgh, 1973), p. 17.

48. Schindler, R. A., Applied Optics 9, (2), 301 (1970).

49. Acton, L. L., Griggs, M., Hall, G. D., Ludwig, C. B., Malkmus, W., Hesketh, W. D. and Reichle, H., AIAA Journal 1, (7), 899 (1973).

50. Barringer, A. R., et. al., Second Joint Conf. Sens. Env. Poll., op. cit., p. 25.

51. Walter, Jr., H. and Flanigan, D., Applied Optics 14, (6), 1423 (1975).

52. Menzies, R. T., Applied Physics Letters 22, (11), 592 (1973).

53. Mandel, L. and Wolf, E., Journal Optical Society of America 65, (4), 413 (1975).

54. Reference 17, p. 44.

55. McClatchey, R. A. and Selby, J. E. A., Atmospheric Attenuation of Laser Radiation From 0.76 To 31.25 μm, AFCRL Report No. AFCRL-TR-74-003 (January 1974).

56. Henningsen, T., Garbuny, M. and Byer, R. L., Applied Physics Letters 24, (5), 242 (1974).

57. Byer, R. L., Optical and Quantum Electronics 7, 147 (1975).

58. Kobayasi, T. and Inaba, H., Optical and Quantum Electronics 7, 319 (1975).

59. Kildal, H. and Byer, R. L., Proc. of I.E.E.E. 59, 1644 (1971).

60. Tolles, W. M., Nibler, J. W., McDonald, J. R. and Harvey, B. A., Applied Spectroscopy 31, 253 (1977).

61. Begley, R. F., Applied Physics Letters 25, (7), 387 (1974).

62. Regnier, P. R., Moya, F. and Taran, J. P. E., AIAA Journal 12, (6), 826 (1974).

63. Reid, J., Shewchun, J., Garside, B. K. and Ballik, E. A., presented at 1977 Annual Meeting Optical Society of America, Toronto, Canada, October 1977, see. J. Opt. Soc. Amer. 67, 1363 (1977).

64. Hanst, P. L., presented at the 1977 International Conference on Fourier Transform Spectroscopy, University of South Carolina, June 20-24, 1977.


DA
FILM